Superradiant phenomena

Lessons from and for Bose–Einstein condensates

Luca Giacomelli

Ph.D. thesis submitted to Dipartimento di Fisica
Università degli studi di Trento

Superradiant phenomena

Lessons from and for Bose–Einstein condensates

Luca Giacomelli

A dissertation submitted to the
Dipartimento di Fisica
Università di Trento

In fulfilment of the requirements for the Degree of
Philosophiæ Doctor in Physics

Under the Supervision of
Dr. Iacopo Carusotto
Prof. Massimiliano Rinaldi

Dottorato di Ricerca XXXIII ciclo
4 March 2021

Supervisors:

Dr. Iacopo Carusotto

Prof. Massimiliano Rinaldi

Members of the committee:

Prof. Vitor Cardoso - Instituto Superior Técnico (Lisbona)

Prof. Nicolas Pavloff - Université Paris–Saclay

Prof. Luciano Vanzo - Università di Trento

A Giulia,
All'ufficio 338,
A via dei Mille 41.

Contents

Introduction

▪ The conceptual framework: analogies and toy models

Analogies are fundamental in the way we think about anything and consist in a transfer of information from a subject to another. It is a cognitive process and a *poetic* mean that also naturally found its way into scientific thinking, where concepts and processes pertaining a particular situation are used to consider and understand new problems from an intuitive point of view. Even when studying a well solved scientific problems it is usual to resort to analogies with more familiar settings, depending on one's expertise and familiarity.

Besides being used as a *qualitative* comparison tool, analogies in physics can be made *quantitative*, that is a formal mathematical mapping between two different physical systems. This is the case of Analogue Gravity [1], a research field that aims at finding condensed matter *analogues* of the physics of curved spacetimes as described by General Relativity that may provide new perspectives on open problems of gravitational physics. In this case the analogy relies in the parallelism between the propagation of sound in a non-uniform medium and the behaviour of fields in a curved spacetime and is formally expressed by the fact that sound, under appropriate approximations, can be described with the Klein–Gordon equation associated to a Lorentzian metric describing a curved spacetime. The resulting *acoustic metric* depends on the properties of the medium (typically a fluid) in which the sound is propagating, but is not determined by the Einstein equations, so that the analogy is not with the equations governing spacetimes, but with the ones describing the propagation of fields in a fixed spacetime. In other words Analogue Gravity provides an analogy of the physics of fields in a curved spacetime.

One can hence try to construct configurations in which the resulting acoustic metric replicates a solution of the Einstein equations of general relativity, thus obtaining a laboratory-sized model of, for example, a black hole spacetime that can be probed in a way that is not possible for *real* astrophysical black holes. Unfortunately exact analogues of general-relativistic spacetimes are typically difficult (when not impossible) to construct, but interesting things can already be said by simply considering *toy models* of curved spacetimes.

Toy models are another important conceptual tool in physics, corresponding to a simplified description of a physical system focusing on replicating qualitatively some behaviour with the least possible amount of details. The aim of a toy model is usually to extract the essential ingredients of some phenomenon typically happening in a com-

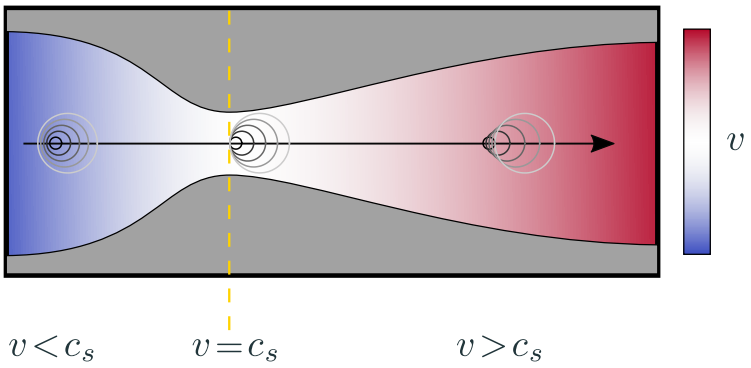

Figure 1: A de Laval nozzle is a tube shaped in such a way that the gas passing through it is accelerated to supersonic speeds. For sound propagating in the gas this is analogous to the horizon of a black hole.

plex setting; formally this corresponds to isolating the minimal mathematical structures responsible for the phenomenon. This is done by performing simplifications that may also not correspond to any physical system (for example considering a reduced number of spatial dimensions), but that make the problem easier to analyze. In doing this, one is constructing an idealized version of the phenomenon, that can then be recognized in more complex settings; in some sense, one is *defining* the phenomenon.

This toy-model approach can also be used in Analogue Gravity, that is instead of focusing on replicating the solutions of General Relativity one can think about simplified spacetimes displaying the phenomena one is interested in. The great advantage given by the analogy with respect to the purely theoretical consideration of these *toy spacetimes* is that these models can be physically built in a laboratory. To get an idea of how interesting *acoustic spacetimes* can be built with a moving fluid consider the de Laval nozzle depicted in Figure 1, that is a tube designed to accelerate a gas passing through it and bring it to a supersonic speed. The circles indicate successive wavefronts of the sound emitted by a point source in different points. When the fluid velocity is subsonic sound can propagate in all directions, but when it becomes larger than the speed of sound the waves cannot anymore move upstream and are *trapped* inside the region of supersonic flow. This is similar to the behaviour of light near the event horizon of a black hole, so that this configuration is called a *dumb hole*.

A prototypical example of the effects one can study in dumb holes is Hawking radiation, a phenomenon that raised many fundamental conceptual issues since its very discovery [2]. The possibility to observe this effect in a laboratory is what brought Unruh to introduce the idea of Analogue Gravity [3] and, since that seminal idea, Hawking radiation in gravitational analogues was object of intense study, that also lead to its experimental observation [4, 5]. This also brought to a general definition of *Hawking effect* [6], not restricted to gravitational physics, in the spirit of what we discussed above.

While analogies are built through similarities, part of their interest in the present context comes from the differences between the systems they connect. In fact, even

if the gravitational analogy allows to predict the occurrence of, for example, Hawking radiation in the analogue from its occurrence in gravitational systems, the explanation in terms of the physics of the analogue may be very different, providing an alternative picture for the peculiar phenomena of curved spacetimes in a different language. Besides this, the analogy usually relies, as we will see, on some large-scale approximation in the analogue system, so that the gravitational analogy is not exact and a breaking of the *emergent Lorentz symmetry* is present at small scales; this allows to test the effects of an underlying short-distances physics on the phenomena predicted for (Lorentz invariant) curved spacetimes. This has been a very important topic regarding Hawking radiation, related to the fundamental trans-Planckian problem, that is to the arbitrarily large frequencies involved in Hawking's original derivation. Moreover, analogue models provide examples of physical systems that on *large scales* can be described geometrically, but also whose microphysics is usually well known; the analogy can hence provide ideas for the still unknown microscopic (quantum) physics of gravity.

Besides this promising flow of information from the analogue system to the gravitational one, the *arrow of the analogy* also points in the other direction, that is the knowledge of the physics occurring in a gravitational context can provide new perspectives and predictions on the one of the system providing the analogue.

▪ The physical phenomena: superradiance

The work presented in this Thesis is an application of the concepts and methods we just delineated to another intriguing phenomenon concerning black holes: *superradiance*. The effect was predicted as an amplified reflection of radiation impinging on a rotating black hole, and is closely related to the possibility of *negative energies* (from the perspective of an asymptotic observer) in a region around the event horizon called *ergoregion*. This was first exploited by Penrose to propose a mechanism to extract energy from a rotating black hole [7].

Even since its first conception [8, 9], it has been known that superradiance is not restricted to black holes; the first derivation by Zel'dovich concerns in fact the scattering of electromagnetic waves on a rotating cylinder of conducting material. The effect has been widely studied in and out of gravitational physics [10] making it a very general phenomenon based on the extraction of energy from the object on which the radiation is scattering. This can usually be pictured as a scattering process in which *negative energy waves* are transmitted, leaving an extra *positive energy* to the reflected wave.

Through the gravitational analogy superradiance is expected in realizations of toy models of rotating spacetimes. A widely considered configuration is the one based on a vortex such as the one of a *draining bathtub* [11]; the scattering of surface gravity waves in water on such a vortex was recently used to obtain the first experimental evidence of superradiant scattering [12].

Besides amplified scattering, various dynamical instabilities are also associated to superradiance. Dynamically stable amplified scattering is obtained if the amplified radiation and its transmitted partner are removed from the system. In black hole spacetimes

this job can be provided asymptotically by the infinite external space and internally by the event horizon that, working as a one-way membrane, automatically evacuates everything that enters it. When these *boundary conditions* of the system are changed, dynamical instabilities can emerge [10]: for example by putting a rotating black hole in a confining geometry one obtains a so-called *black hole bomb*, or by removing its horizon the so-called *ergoregion instability* occurs, as happens for example in rapidly spinning stars.

Despite the impressive advances in the understanding and investigation of superradiance, some intriguing open points remain. The most fundamental is perhaps the role of dissipation, such as the one provided by an horizon, that is often regarded as a necessary ingredient. We just said that removing absorption implies the emergence of dynamical instabilities, but does this preclude the possibility of amplified scattering as is sometimes suggested? Another open point is the effect of the short distance physics on superradiant effects; we saw that this was a main topic in the study of Hawking radiation in analogues, while it has been hardly considered for superradiance.

The first aim of this work is to address these questions, and, as a wider scope, to obtain a clearer, more intuitive and more *general* picture of superradiance. We attempt at this by proposing new and conceptually simpler toy-model spacetimes, with the usual advantage in analogue models that they can be realized for experimental investigations.

Even if the vortex spacetimes, and more in general rotation, permitted many important steps in the approach to superradiance, the cylindrical geometry of these systems only allows a limited tuning, so that it is difficult to separate the different elements of the spacetime and their role in superradiant phenomena. Here we propose a new kind of analogue toy model, providing the possibility of a local tuning of the flow velocity of the fluid and thus a larger freedom in the control of the features of the resulting spacetime. In this way we obtain a comprehensive understanding of the basic superradiant phenomena and of the related dynamical instability mechanisms.

With particular attention to role of dissipation, we will show that superradiance can be understood as mode conversion at the edge of an ergoregion. This implies that the absence of absorption in the system prohibits superradiance as a *stationary* and dynamically stable process, but does not prevent amplified scattering as a *transient* phenomenon involving finite-width packets of waves. A related question is also if an horizon does in general provide the necessary dissipation to assure stable scattering, as is usually considered the case in black holes spacetimes. We will instead show that this is not a general feature of horizons and depends on their smoothness.

Our analogue model also has the interesting feature of being the *quantitative analogue* of another physical system: a relativistic charged and massive scalar field coupled to an electrostatic potential. Superradiance for this kind of field is known as the *bosonic Klein paradox* [13] and instabilities associated to electrostatic potential boxes are known as the *Schiff–Snyder–Weinberg (SSW) mechanism* [14]. These examples, given their simplicity, are actually toy models, for example the SSW effect was first derived with a toy model for nuclear physics in mind, that was in turn used as toy models for rotating spacetime in [15]. Our simple analogue spacetime is hence a first viable realization of these toy

models in a laboratory.

▪ The system: atomic Bose–Einstein condensates

The platform we chose for our studies are atomic Bose–Einstein condensates (BECs) [16]. These quantum fluids are interesting to construct analogue models of gravity because of the good theoretical understanding that was built in the last decades and because of the remarkable control that has been reached experimentally[1]. In the context of Analogue Gravity, these advances were recently used to propose [17, 18] and realize a series of experiments that led to the observation of analogue Hawking radiation in an effectively one-dimensional condensate [4, 5].

Particular tools for the manipulations of atoms that we are interested in exploiting are periodic potentials [19] and, especially, synthetic gauge potentials [20], that are techniques to make neutral atoms behave as if they were charged and coupled to an electromagnetic field. The feature of these tools that we will exploit is that they can be used to induce in a BEC velocity fields that are *rotational* (that is with a non-vanishing curl). This circumvents the standard requirement of irrotationality that is made in the derivation of the gravitational analogy and allows the building of what we call a *planar ergosurface*.

Other features of BECs that make them intriguing from the point of view of Analogue Gravity are the superluminal dispersion relation of acoustic excitations, that allows for a study of the influences of the short-wavelength physics, and the low temperatures allowing the quantum features of sound of sound to emerge, that are an opportunity to investigate very quantum aspects of field theories in curved spacetimes (such as Hawking radiation). We will exploit both these facts and will show how a superluminal dispersion relation can lead to the suppression of superradiance at high frequencies and how the quantum nature of fluctuations determines a spontaneous pair creation in the modes involved in superradiant scattering, expected to happen in rotating spacetimes and related to Hawking emission.

Our results summarized up to now exploit the flow of information from the analogue model to the gravitational case, i.e. these are lessons *from* Bose–Einstein condensates for the understanding of superradiant phenomena. We already said that also the opposite arrow of the analogy can be interesting. Here we will adopt this perspective to reconsider the problem of the stability of quantized vortices in BECs and to investigate peculiar instabilities occurring in non-uniformly flowing BECs resembling hydrodynamic parallel shear flows. Through the gravitational analogy we will understand the physics at play and will predict surprising phenomena; these are hence lessons from superradiance *for* BECs.

The irrotationality of the flow of a condensate implies that vortices can only occur with a quantized circulation, displaying a purely rotating velocity field. Thinking about

[1] Interestingly, the concept of dilute weakly-interacting BEC was first introduced by Bogoliubov as a toy model of real, strongly-interacting superfluids such as Helium, and only later their relatively simple description was found sufficient for an experimentally achievable system.

them in terms of the analogue spacetime they provide shows that they display ergoregion instabilities, modified by the microscopic physics of the condensate in a similar way we find for our toy model. This perspective provides a new way to look at the known features of quantized vortices in different geometries and allows to prove the poorly understood fact that vortices with multiple quanta of circulation are dynamically unstable in an infinite condensate, and to make new predictions of unexpected behaviours.

Finally, we consider a configuration analogous to our planar ergosurface, but without external *tricks* to obtain rotational velocity fields. Considering two parallel channels in which a BEC flows with different speeds, a line of quantized vortices will develop in the region of transition between the two flows. We will see that this configuration displays instabilities analogous to the Kelvin–Helmholtz instability of shear layers in hydrodynamics, that are however surprisingly suppressed for high enough relative velocities and replaced by an instability analogous to the SSW effect. This last topic summarizes the many connections delineated in this Thesis between different physical contexts, involving gravitational systems, relativistic charged fields, BECs and fluids.

▪ Structure of the thesis

In closing this Introduction, we summarize the structure with which the above mentioned topics are presented in this Thesis. The first two chapters are introductory and summarize known results that we will need in the following of the work:

- In Chapter 1 we give an introduction to Analogue Gravity in Bose–Einstein condensates. We first discuss the description of atomic BECs, starting from the mean field Gross–Pitaevskii equation and with particular attention to the characterization of the linear stability of stationary solutions and other properties of small amplitude (acoustic) fluctuations. We then show how a description of sound via an *acoustic metric* emerges in a BEC and discuss *acoustic black holes* starting from examples of black hole spacetimes in general relativity. We then give a comparison of the Bogoliubov and the Klein–Gordon problems by showing different representations and by analyzing the associated dispersion relations. Finally, we review an example of an Analogue Gravity study of a gravitational phenomenon, that is Hawking radiation in BECs and associated dynamical instabilities, that were object of recent experimental investigations.

- In Chapter 2 we give an introduction to superradiant phenomena. We start from some examples coming from the physics of non-gravitational systems, that show how superradiance is a phenomenon occurring in many physical contexts. We then pass to black holes and discuss the Penrose process to extract energy from a rotating black hole with a particle decaying into photons. After this we show two examples of superradiance in black holes: the scattering of acoustic fluctuations in the vortex geometry and the one of a charged field on a Reisser–Nordtröm black hole. Finally we summarize the essential aspects of superradiant dynamical instabilities in black holes and we show how the so-called Schiff–Snyder–Weinberg

(SSW) effect for a charged Klein–Gordon field is a good toy model for these instabilities.

The following chapters contain instead original work, some of which has already been published and some of which will be object of future publications:

- In Chapter 3 we present the idea of a *planar ergosurface* constructed using a rotational flow for a BEC. Two methods are proposed to obtain such a configuration: the use of a synthetic vector potential and the one of a periodic lattice potential. After showing how a synthetic vector potential can expand the set of possible acoustic metric, we consider superradiant scattering from a planar ergosurface obtained by applying such a potential. The analysis is performed with an analytical and graphical study of dispersion relations and with numerical calculations. We highlight the exact mapping of this configuration to the bosonic Klein paradox and the effects of a superluminal dispersion relation. The work presented in this first part of the Chapter was published in the preprint [21] and is currently under review. We then apply a semi-analytical input-output approach to the Bogoliubov problem in the vector-field-induced planar ergosurface. This allows to predict amplification factors for superradiant scattering and to treat the quantum effect of spontaneous pair production in the superradiant modes, that is characterized through density-density and momentum correlations of the fluctuations. We finally show how physics analogous to the one of the planar ergosurface can be obtained with periodic potentials used to change locally the dispersion relation of the atoms. These last two topics are still unpublished and will be object of future articles.

- In Chapter 4 we address superradiant instabilities obtained by changing the boundary conditions around a planar ergosurface. We concentrate for simplicity on the configuration obtained with a synthetic vector potential field, that is simpler because of its constant density. We show the result of numerical simulations of the Gross–Pitaevskii equation showing dynamically unstable behaviours. These are better characterized by numerically studying the spectra of the corresponding Bogoliubov problem, showing that these instabilities are an analogue version of the SSW effect, modified by superluminal effects. Dynamical instabilities are then studied by matching the Bogoliubov modes at the interface; this approach also provides a proof of the dynamical stability of the planar ergosurface. The role of dissipation in superradiance is then discussed, showing that the presence of superradiant dynamical instabilities does not prevent the possibility of amplified scattering. Finally, the role of horizons is investigated; by adding a third region to our setup we include an acoustic horizon, thus reproducing schematically the structure of a rotating black hole. Horizons are shown to avoid superradiant (ergoregion) instabilities only if they are smooth enough to prevent sizable reflection of fluctuations. The work presented in this Chapter included in the already mentioned work [21].

- In Chapter 5 we use the concepts presented in the previous chapters to study

the stability properties of quantized vortices in effectively-two-dimensional condensates. After a brief introduction to vortices in trapped condensates we analyze a doubly quantized vortex in an infinite BEC and show, with the combination of an infinite-size limit procedure and of a simulation of outgoing boundary conditions, that it is dynamically unstable in an otherwise homogeneous condensate. This result is then extended to vortices of higher quantizations, whose instabilities turn out to be ergoregion instabilities of the resulting acoustic geometry, modified by the effects of superluminal dispersion. Related to these phenomena, a surprising dynamical instability of a singly quantized vortex in an inhomogeneous geometry is discussed. Finally, we use quantized vortices to provide another example of superradiant scattering in a dynamically unstable system. The work of this Chapter was published in [22].

- In Chapter 6 we consider BECs moving with flows analogous to the one of a planar ergosurface, but for rotational velocity fields, with the idea to study the effect of the superradiant mechanisms presented in the previous Chapters on the dynamics of a nontrivial interface between two parallel flows. This interface is constituted by an *array of vortices* that is shown to display different instability mechanisms depending on the relative velocity of the flows. This is first demonstrated with GPE numerical calculations, showing significantly different behaviours for relative velocities below and above two times the speed of sound. Using a decomposition in Bloch waves, we numerically study the spectra of linear excitations, that well characterize the two instability regimes. The one for lower velocities is analogous to the Kelvin–Helmholtz instability of parallel flows in hydrodynamics, the other one is instead an instability of the SSW kind for finite systems and displays instead a continuous emission of phonons from the vortex array in an unbound system; we call this regime *radiative instability*. A third instability regime for small velocity is also found. The work presented in this Chapter will be object of a future publication.

- Finally, in the Conclusions we summarize the main results presented in this Thesis and sketch some possible future developments.

Chapter 1

Analogue gravity in Bose–Einstein condensates

Starting with an idea by Unruh [3], Analogue Gravity is based on the fact that sound fluctuations in a moving perfect fluid can be described *geometrically* as a massless scalar field obeying a Klein–Gordon equation in a curved-spacetime metric. The usefulness of this peculiar connection relies in the possibility to *experimentally* and *conceptually* address the formalism and the predictions of field theories in curved spacetimes, most famously Hawking radiation, whose validity is subject to conceptual issues and for which experimental evidence is presently not available.

Since its first conception, this research programme has gathered a wide number of different ideas and platforms to reproduce the physics of curved spacetimes: from classical and quantum fluids to optical systems and lattice models. We focus here on the case of atomic Bose–Einstein condensates (BEC) and refer to the comprehensive review [1] for a full catalogue of models.

Among the other possibilities one is particularly close to atomic BECs: quantum fluids of light [23]. Photons can show properties similar to fluids of matter when confined in one direction in an optical cavity, that has the effect of giving the photon an effective mass, and in a nonlinear medium, providing an effective photon-photon interaction. The resulting two-dimensional system has been shown to undergo Bose–Einstein condensation and the description of this state of the photon fluid is very similar, except for the driven-dissipative nature of the system, to the one we are now going to introduce for the atomic counterpart. Another alternative is given by light propagating in a bulk Kerr nonlinear medium, that under the paraxial approximation is described by an equation analogous to the mean field Gross–Pitaevskii equation for condensed atoms [24]. Our discussion can hence be easily transposed to these other platforms.

Configurations based on Bose–Einstein condensates were first proposed as gravitational analogues in [25–27]. The choice of these *quantum fluids* is convenient for many reasons. From the experimental point of view the control over these systems has gotten better and better in these 25 years since the first realization of condensates in the laboratory [28, 29] and now a rich tuning of the system's parameters can be performed, thus

allowing the engineering of configurations aimed at specific Analogue Gravity problems. From the theoretical point of view the description of these systems is very well known and tested, thus providing a system that on *large* scales falls in the gravitational analogy, but also whose microphysics, playing the role of the unknown short-scales physics of gravity, is under control. Moreover the low temperatures allow the emergence of very quantum features of the fluctuations, allowing investigations on very *quantum* features of field theories in curved spacetime (see also [30]). Similar considerations also hold for fluids of light, whose use as platforms for analogue gravity is currently under active consideration [31–35].

The aim of this Chapter is to introduce Analogue Gravity in BECs, starting from the main theoretical tools for the description of the condensates we will need in the following of our work. The derivation of the *acoustic metric* for the description of sound through the gravitational analogy is then reviewed and acoustic black holes are introduced in analogy with the solutions of general relativity. Subsequently, a detailed formal and physical comparison between the properties of fluctuations in BECs and the ones of the corresponding curved-spacetime Klein–Gordon description is made. The Chapter is closed with an exposition of the important and guiding example of Hawking radiation in BECs.

1.1 The basic equations of Bose–Einstein condensates

We review here some basic physics of the weakly interacting Bose gas in the condensed state. The main theoretical approaches we are interested in are the mean field description of the condensate, giving the famous Gross–Pitaevskii equation (GPE), and the linear Bogoliubov–de Gennes equations (BdG) for fluctuations around steady states, to which we will also refer as the Bogoliubov problem.

After a summary of the main properties of these approaches, we will show how from the GPE we obtain the equations for a perfect fluid in the so-called *hydrodynamic limit* and from the BdG we obtain, in the *long-wavelength limit*, a metric description of sound through a Klein–Gordon (KG) equation in curved-spacetime.

The presentation on Bose–Einstein condensates will here be limited to our needs, for comprehensive expositions refer to the standard textbooks [16,36,37]. The basic tools we will use stem from a treatment of the condensate as a coherent state with a well-defined phase, that in the thermodynamic limit is equivalent to a fixed-number state, and from a description of non-condensed atoms that does not conserve the overall number. A more rigorous number-conserving treatment was developed in [38], that however goes beyond our present scope.

1.1.1 The Gross–Pitaevskii equation

The system we have in mind is an interacting gas of bosons in which the average distance between particles d is much larger than the interatomic forces range r_0. In this case the gas is said to be *dilute* and one can neglect interaction processes involving

more than two particles. Moreover, since the particles are in average very far from each other, one can describe them with the asymptotic wavefunctions of their scattering problem, with momenta $p \ll \hbar/r_0$. The relevant quantity to describe their interaction is the scattering amplitude, that at such small momenta becomes independent of energy and is dominated by the s-wave scattering length a, that is hence the single parameter characterizing interactions. In addition, the gas is said to be *weakly interacting* if $|a| \ll d$.

The Hamiltonian involving only two-body interactions can be written in terms of the position-space atomic field operators $\hat{\Psi}(\mathbf{r})$ as

$$\hat{H} = \int \mathrm{d}\mathbf{r} \left(\frac{\hbar^2}{2M} \nabla\hat{\Psi}^\dagger(\mathbf{r}) \nabla\hat{\Psi}(\mathbf{r}) \right) + \frac{1}{2} \int \mathrm{d}\mathbf{r}\mathrm{d}\mathbf{r}' \; \hat{\Psi}^\dagger(\mathbf{r}')\hat{\Psi}^\dagger(\mathbf{r}) V(\mathbf{r}'-\mathbf{r})\hat{\Psi}(\mathbf{r}')\hat{\Psi}(\mathbf{r}), \quad (1.1)$$

where M is the atomic mass. $V(\mathbf{r})$ is the interatomic potential, that in *real* systems contains a sharp short-range behaviour that is difficult to treat and complicates the use of perturbation theory even at small energies.

However, in a dilute gas only momenta $p \ll \hbar/r_0$ are involved in the scattering processes and the actual short-range shape of the potential is hence not important: what matters is that the potential gives the correct large-distances scattering behaviour. It is hence convenient to replace the physical potential V with an effective potential $V_{\mathrm{eff}}(\mathbf{r})$ (Fermi pseudo-potential) providing the same scattering length a. This corresponds to considering only the zero-momentum component of the (effective) potential $V_0 = \int \mathrm{d}\mathbf{r} \; V_{\mathrm{eff}}(r)$, whose value is related to the scattering length calculated in the so-called Born approximation $a = \frac{M}{4\pi\hbar^2} V_0$. This constant potential in momentum space corresponds in coordinate space to a contact potential

$$V_{\mathrm{eff}}(\mathbf{r}, \mathbf{r}') = g\delta(\mathbf{r} - \mathbf{r}'), \quad (1.2)$$

where we defined the interaction coupling constant

$$g := V_0 = \frac{4\pi\hbar^2 a}{M}. \quad (1.3)$$

From the Hamiltonian (1.1) with this contact potential, and also including the possibility of an external trapping potential, one obtains the Heisenberg equation for the field operator

$$i\hbar \frac{\partial}{\partial t} \hat{\Psi} = [\hat{\Psi}, \hat{H}] = \left(-\frac{\hbar^2 \nabla^2}{2M} + V_{\mathrm{ext}} + g\hat{\Psi}^\dagger\hat{\Psi} \right) \hat{\Psi}. \quad (1.4)$$

The crucial step is now to substitute the quantum field operator $\hat{\Psi}(\mathbf{r}, t)$ with a scalar field $\Psi(\mathbf{r}, t)$, a recipe that is called Bogoliubov prescription. The meaning of this substitution is related to the fact that, for a large number of particles and in the absence of interactions, at zero temperature the atoms will condense and will occupy the same single-particle state. In the presence of interactions this in not exactly true but the hypothesis of weak interactions allows to use this (Hartree–Fock) approximation, in which correlations among particles are not considered. The *depletion* of the condensate due

to interactions can hence be neglected and one is left with the famous *Gross–Pitaevskii equation* (GPE)

$$i\hbar\frac{\partial}{\partial t}\Psi(\mathbf{r},t) = \left(-\frac{\hbar^2\nabla^2}{2M} + V_{\text{ext}}(\mathbf{r}) + g\left|\Psi(\mathbf{r},t)\right|^2\right)\Psi(\mathbf{r},t) =: H_{GP}\Psi(\mathbf{r},t), \tag{1.5}$$

describing a dilute, weakly interacting Bose gas at zero temperature in terms of a macroscopic scalar *order parameter* $\Psi(\mathbf{r},t)$, normalized to the total number of atoms $\int \mathrm{d}\mathbf{r}\ \left|\Psi\right|^2 = N$.

Equation (1.5) can be also obtained by imposing the stationarity condition to the action

$$\delta\left(-i\hbar\int \mathrm{d}\mathbf{r}\mathrm{d}t\ \Psi^*\partial_t\Psi + \int\ \mathrm{d}tE\right), \tag{1.6}$$

where the energy functional is

$$E = \int \mathrm{d}\mathbf{r}\ \left(\frac{\hbar^2}{2M}\left|\nabla\Psi\right|^2 + V_{\text{ext}}\left|\Psi\right|^2 + \frac{g}{2}\left|\Psi\right|^4\right), \tag{1.7}$$

obtained by taking the expectation value of the quantum Hamiltonian on the Hartree–Fock product state under the same assumptions that led to the GPE.

With a variational principle applied to the energy functional with the constraint that the total number of atoms is conserved, that is minimizing

$$E' = E - \mu\int \mathrm{d}\mathbf{r}\left|\Psi\right|^2, \tag{1.8}$$

one obtains the time-independent GPE

$$\left(-\frac{\hbar^2\nabla^2}{2M} + V_{\text{ext}} + g\left|\Psi_0(\mathbf{r})\right|^2 - \mu\right)\Psi_0(\mathbf{r}) = 0. \tag{1.9}$$

Analogously to the Schrödinger equation this is the equation for stationary solutions of the shape

$$\Psi(\mathbf{r},t) = \Psi_0(\mathbf{r})e^{-i\mu t/\hbar}, \tag{1.10}$$

where, instead of the energy of the solution, we have the Lagrange multiplier μ that is the chemical potential $\mu = \frac{\partial E}{\partial N}$.

It is also interesting now to consider a density-phase representation of the order parameter

$$\Psi(\mathbf{r},t) = \sqrt{n(\mathbf{r},\mathbf{t})}e^{i\Theta(\mathbf{r},t)}. \tag{1.11}$$

In terms of n and Θ the GPE (1.5) can be expressed by a pair of equations, the first being the *continuity equation*

$$\frac{\partial n}{\partial t} = -\nabla\cdot\left(n\frac{\hbar\nabla\Theta}{M}\right), \tag{1.12}$$

expressing the conservation of matter and from which one can can see that the gradient of the phase determines the velocity of the condensate

$$\mathbf{v} = \frac{\hbar \nabla \Theta}{M}. \tag{1.13}$$

that has hence a vanishing curl. The second equation is

$$\hbar \frac{\partial \Theta}{\partial t} + \frac{(\hbar \nabla \Theta)^2}{2M} + gn + V_{\text{ext}} - \frac{\hbar^2}{2M} \frac{\nabla^2 \sqrt{n}}{\sqrt{n}} = 0, \tag{1.14}$$

that can be expressed in terms of the velocity (1.13) as

$$M \frac{\partial \mathbf{v}}{\partial t} + \nabla \left(M \frac{v^2}{2} + gn + V_{\text{ext}} - \frac{\hbar^2}{2M} \frac{\nabla^2 \sqrt{n}}{\sqrt{n}} \right) = 0. \tag{1.15}$$

This equation is analogous to the Euler equation for an ideal fluid subject to an external force $\mathbf{f}_{\text{ext}} = -n \nabla V_{\text{ext}}$, except for the last term that is the only one left in which $\hbar$ enters explicitly. This term has the role of an additional pressure and is hence referred to as *quantum pressure* V_q.

This last term can be neglected if density variations occur over large enough length scales. In particular if these variations occur over a length scale λ, the quantum pressure term is proportional to $V_q \propto \xi^2/\lambda^2$, where ξ is the so-called *healing length* of the condensate

$$\xi = \frac{\hbar}{\sqrt{Mgn}}, \tag{1.16}$$

that can be interpreted as the length scale over which the microscopic physics of the condensate becomes important. Away from this regime, for $\lambda \gg \xi$, we are left with the equations of an inviscid, barotropic and irrotational fluid. We will call this the *hydrodynamic approximation*.

1.1.2 Elementary excitations: the Bogoliubov problem

A picture of the dynamical properties of condensates can be obtained with a linearized analysis of the Gross–Pitaevskii equation, in which one considers small deviations of the order parameter from a stationary configuration satisfying equation (1.9). This approach, besides showing the emergence of sound excitations and allowing a linear stability analysis of the stationary states, gives insight regarding the non-condensed particles.

Let us consider a stationary solution $\Psi_0(\mathbf{r})$ of the GPE and a perturbation of this state

$$\Psi(\mathbf{r}, t) = e^{-i\mu t/\hbar} \left[\Psi_0(\mathbf{r}) + \delta\psi(\mathbf{r}, t) \right]. \tag{1.17}$$

Inserting this equation in (1.5) and keeping only linear terms in $\delta\psi$ and $\delta\psi^*$ one obtains

$$i\hbar \partial_t \delta\psi = \left[-\frac{\hbar^2}{2M} \nabla^2 + V_{\text{ext}} - \mu \right] \delta\psi + 2g \left| \Psi_0 \right|^2 \delta\psi + g\psi_0^2 \delta\psi^*. \tag{1.18}$$

Notice that this equation is not strictly speaking linear in $\delta\psi$ since it also involves its complex conjugate. To end up with a linear problem one could take as variables the real and imaginary parts of $\delta\psi$ or, as we will do, is to consider $\delta\psi$ and $\delta\psi^*$ as formally independent variables and write the linear problem for the two-component vector

$$|\delta\psi\rangle = \begin{pmatrix} \delta\psi \\ \delta\psi^* \end{pmatrix} = \begin{pmatrix} u_{\delta\psi} \\ v_{\delta\psi} \end{pmatrix}. \tag{1.19}$$

We can hence rewrite equation (1.18) as

$$i\hbar\partial_t \begin{pmatrix} \delta\psi \\ \delta\psi^* \end{pmatrix} = \begin{bmatrix} H_{GP} + g|\Psi_0|^2 - \mu & g\Psi_0^2 \\ -g\Psi_0^{*2} & -\left(H_{GP} + g|\Psi_0|^2 - \mu\right) \end{bmatrix} \begin{pmatrix} \delta\psi \\ \delta\psi^* \end{pmatrix} =: \mathcal{L} \begin{pmatrix} \delta\psi \\ \delta\psi^* \end{pmatrix}. \tag{1.20}$$

This is the *Bogoliubov (or Bogoliubov–de Gennes) problem* for the elementary excitations of a condensate. A generic solution of this problem can be decomposed in eigenmodes satisfying

$$\mathcal{L} \begin{pmatrix} u_i \\ v_i \end{pmatrix} = \hbar\omega_i \begin{pmatrix} u_i \\ v_i \end{pmatrix}. \tag{1.21}$$

Since the matrix in (1.20) is not hermitian, the eigenfrequencies ω_i will not in general be real. If an eigenfrequency has a positive imaginary part the corresponding mode amplitude will exponentially grow in time. This behaviour is called a *dynamical instability*.

The Bogoliubov problem is however σ_3-pseudo-hermitian, that is

$$\sigma_3\mathcal{L}^\dagger\sigma_3 = \mathcal{L}. \tag{1.22}$$

This implies that the non-positive-definite inner product

$$\langle\psi|\,\sigma_3\,|\phi\rangle = \int \mathrm{d}\mathbf{r}\ \psi^\dagger(\mathbf{r})\sigma_3\phi(\mathbf{r}) = \int \mathrm{d}\mathbf{r}\left[u_\psi^*(\mathbf{r})u_\phi(\mathbf{r}) - v_\psi^*(\mathbf{r})v_\phi(\mathbf{r})\right] \tag{1.23}$$

is conserved on the evolution, so that we can define the norm of an eigenmode

$$\|\phi\|_B := \langle\phi|\,\sigma_3\,|\phi\rangle\,, \tag{1.24}$$

that can be positive, negative or zero. Property (1.22) also implies that, since $\mathcal{L}$ and its adjoint are related by a unitary transformation, if ω_i is an eigenfrequency, also ω_i^* will be, so that complex-frequency modes come in pairs and are called *pseudo-degenerate*. Moreover, the following orthogonality relation between eigenmodes holds

$$(\omega_i - \omega_j^*)\,\langle\phi_j|\,\sigma_3\,|\phi_i\rangle = 0, \tag{1.25}$$

from which one can see that eigenmodes relative to different eigenfrequencies are orthogonal and that modes with a complex frequency have vanishing norm.

A second symmetry of the $\mathcal{L}$ matrix is

$$\sigma_1\mathcal{L}\sigma_1 = -\mathcal{L}^*, \tag{1.26}$$

which implies that if $(u_i, v_i)^T$ is an eigenmode with eigenfrequency ω_i, then $(v_i^*, u_i^*)^T$ is an eigenmode with eigenfrequency $-\omega_i^*$, the two modes have opposite norms. This is a doubling of the modes that is actually not physical but depends on the choice (1.19) we made of treating the fluctuation field and its complex conjugate as independent variables. This expands the space of solutions of the linear problem and the physically relevant result is obtained by taking a linear combination between the spinor components of the form

$$\delta\psi_i(\mathbf{r}, t) = \mathcal{A}_i u_i(\mathbf{r}) e^{-i\omega_i t} + \mathcal{A}_i^* v_i^*(\mathbf{r}) e^{+i\omega_i t}, \tag{1.27}$$

giving the overall fluctuation on the order parameter. This shows that the two modes connected by the symmetry (1.26) are the same physical mode of complex amplitude $\mathcal{A}_i$.

We call this property *particle-hole symmetry* since, as we will see multiple times in the rest of this thesis, we can think of negative-norm modes as antiparticles. To obtain a complete description of the fluctuations one can hence construct a basis by considering only the modes with one sign of the norm. As we will see, it is instead sometimes more convenient to consider only positive frequencies and keeping modes of both norms; this provides an equally good basis of the space of fluctuations.

- An example: the uniform condensate

Before discussing instabilities let us consider the simplest example of a condensate of uniform density at rest, described by the real order parameter $\Psi_0 = \sqrt{n}$. In this case the eigenmodes will be plane waves of the shape $|\phi_k\rangle = e^{i\mathbf{k}\cdot\mathbf{r}} (u_\mathbf{k}, v_\mathbf{k})^T$. The Bogoliubov matrix (1.20) at fixed momentum $\mathbf{k}$ becomes (using $\mu = gn$)

$$\mathcal{L}_\mathbf{k} = \begin{bmatrix} \frac{\hbar^2 k^2}{2M} + gn & gn \\ -gn & -\left(\frac{\hbar^2 k^2}{2M} + gn\right) \end{bmatrix}, \tag{1.28}$$

whose eigenvalues are

$$\hbar\omega_\mathbf{k} = \pm\sqrt{\frac{\hbar^2\mathbf{k}^2}{2M}\left(\frac{\hbar^2\mathbf{k}^2}{2M} + 2gn\right)}. \tag{1.29}$$

This is the famous Bogoliubov dispersion relation for the elementary excitations of a uniform BEC, that is completely real for repulsive interactions $g > 0$. The plus sign refers here to positive-norm modes, while the minus refers to the particle-hole-symmetric negative-norm modes.

This dispersion law goes from a linear behaviour $\omega \propto k$ at small momenta $k \ll \xi^{-1}$ to a quadratic one $\omega \propto k^2$ at the opposite regime. The proportionality factor between wavenumber and frequency at small momenta is the speed of sound

$$c_s = \sqrt{\frac{gn}{M}}, \tag{1.30}$$

that coincides with the one calculated in the hydrodynamic fashion from the compressibility of the condensate. The presence of a *sonic* behaviour at small momenta, besides

being fundamental for the superfluidity of BECs, is crucial for the gravitational analogy, that works exactly only in this *long-wavelength limit*.

1.1.3 Energetic and dynamical instabilities

It is useful to consider the energy of Bogoliubov fluctuations. One can insert a fluctuation around a stationary state (1.17) in the grand canonical energy functional (1.8). We can than expand the energy functional in terms of increasing order in the fluctuations $E = E^{(0)} + E^{(1)} + E^{(2)}$. The first-order term vanishes because the functional is stationary on a stationary state, the second-order term is hence the first contribution to energy due to the fluctuations and has the shape

$$E^{(2)} = \int \mathrm{d}\mathbf{r} \left[\frac{\hbar^2}{2M} |\nabla \delta\psi|^2 + (V + 2g|\Psi_0|^2 - \mu)|\delta\psi|^2 + \frac{g}{2}(\Psi_0^*)^2 \delta\psi^2 + \frac{g}{2}\Psi_0^2 (\delta\psi^*)^2 \right] \tag{1.31}$$

This can be conveniently written with the vectorial convention as

$$E^{(2)} = \frac{1}{2} \langle \delta\psi | \, M \, | \delta\psi \rangle \,, \tag{1.32}$$

where the matrix

$$M := \begin{bmatrix} H_{GP} + g|\Psi_0|^2 - \mu & g\Psi_0^2 \\ g\Psi_0^{*2} & H_{GP} + g|\Psi_0|^2 - \mu \end{bmatrix} \tag{1.33}$$

is essentially the Bogoliubov matrix without the minuses in the second row, i.e. $\mathcal{L} = \sigma_3 M$. By expanding the vectors $|\delta\psi\rangle$ in terms of eigenmodes of the Bogoliubov matrix (1.21) the second order energy variation becomes

$$E^{(2)} = \frac{1}{2} \sum_{k,l} \langle \phi_k | \, M \, | \phi_l \rangle = \frac{1}{2} \sum_{k,l} \langle \phi_k | \, \sigma_3 \mathcal{L} \, | \phi_l \rangle = \sum_k \langle \phi_k | \, \sigma_3 \, | \phi_k \rangle \, \hbar\omega_k \tag{1.34}$$

where the sum runs over the eigenfrequencies of the Bogoliubov matrix. One can see that the energy of an eigenmode is not simply given by its frequency, but is also proportional to its norm. This implies that the modes connected by the particle-hole symmetry (1.26), having both opposite frequency and opposite norm, have the same energy.

In the previous section we introduced the concept of dynamical instability associated with the non-hermiticity of the Bogoliubov problem. From the properties listed above we can see that complex-frequency modes emerge as couples of zero-norm modes with complex conjugate frequencies, a growing one and a decaying one. Given that the energy of a mode is proportional to its norm we can see that dynamically unstable norms have zero energy.

A second notion of instability is *energetic instability*, that is the existence of eigenmodes with a negative energy. According to (1.34) this can happen if a positive-norm mode has a negative frequency or if a negative-norm mode has a positive one; these two

kinds of modes are related by the particle-hole symmetry. The presence of an energetic instability signals that the stationary solution around which we calculated the fluctuation modes does not correspond to a minimum of the energy functional and hence the energy of the condensate can be decreased by populating this mode.

Increasing the amplitude of an energetically unstable mode is hence a process that does not conserve the energy and is only possible if some dissipation is present within the system, for example, at finite temperatures, the presence of thermal atoms to which the extra energy can be transferred. Dynamically unstable modes instead, after being populated by some fluctuation, can grow without the need of external degrees of freedom since they carry zero energy. The growth of dynamically unstable modes is hence typically faster than the one of an energetically unstable one, since this last one relies on external fluctuations.

Even if the linear theory predicts an exponential growth in time of the dynamically unstable modes, this does not of course occur indefinitely. At some point the mode amplitude will enter a regime in which the perturbation theory is no more a good description and nonlinear effects requiring the full GPE start being important. Dynamical instabilities are often related to a significant change in the stationary state around which the linearization is made, that may be thought as a change of *phase* in analogy to spontaneous breaking of symmetries in field theories. We will see an example of this when dealing with multiply quantized vortices in Chapter 5.

- Two simple examples of energetic and dynamical instabilities

A first simple and important example of *energetic instability* is the one that occurs when a uniform condensate is moving with a supersonic speed. This is an expression of Landau's criterion for superfluidity, according to which frictionless flow for a fluid is possible if there is not the possibility of creating excitation in an energetically favourable way, that is if there are no energetic instabilities [16,39]. Landau provided the definition of a critical velocity, in terms of the dispersion relation of excitations, above which superfluidity breaks down since the fluid begins to be subject to friction.

How this applies to a BEC can be easily understood by studying the Bogoliubov problem for a condensate of uniform density that is moving with a uniform flow. Take for simplicity one spatial dimension and a condensate stationary order parameter

$$\Psi_0(t,x) = \sqrt{n} e^{iKx} e^{-i\mu t/\hbar}, \tag{1.35}$$

that has a uniform velocity $v = \hbar K/M$ associated to it. By taking fluctuations of the shape

$$\Psi(x,t) = e^{-i\mu t/\hbar} e^{iKx} \left(\sqrt{n} + \chi(x,t)\right) \tag{1.36}$$

and considering plane waves as we did in the derivation of (1.28) we can easily obtain the dispersion relation

$$\hbar\omega_k = \hbar v k \pm \sqrt{\frac{\hbar^2 k^2}{2M}\left(\frac{\hbar^2 k^2}{2M} + 2gn\right)}. \tag{1.37}$$

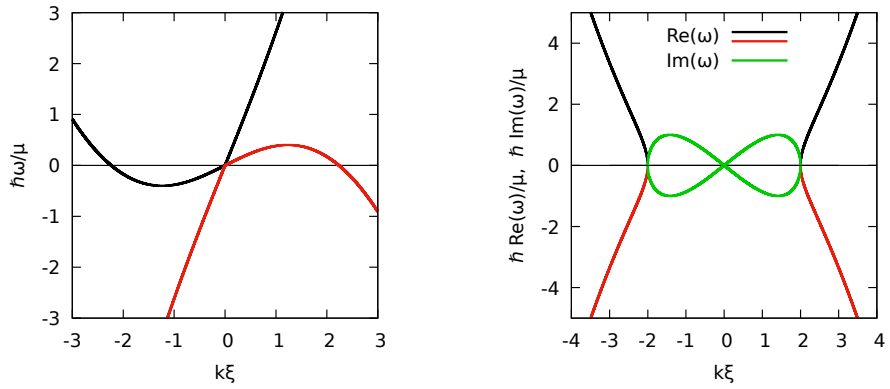

Figure 1.1: Examples of instabilities. On the left the dispersion relation of excitations in a uniformly moving condensate, in which energetic instabilities emerge when the flow is faster than the speed of sound (here $v = 1.5\, c_s$). On the right the Bogoliubov dispersion relation of a uniform condensate with an attractive interaction displaying dynamical instabilities. Black, red and green lines correspond respectively to positive-, negative- and zero-norm modes.

The choice (1.36) corresponds to measuring momenta with respect to the condensate momentum and the frequencies with respect to the chemical potential. The term added to the Bogoliubov dispersion relation is hence a Doppler shift due to the change of reference frame.

The effect of such a shift, as can be seen in the left plot of Figure 1.1, is to *tilt* the dispersion relation. If the velocity is larger than the speed of sound $c_s = \sqrt{gn/M}$, part of the negative-norm branch of the dispersion relation (corresponding to the minus in the dispersion relation) raises to positive frequencies, or, equivalently, part of the positive-norm branch lowers to negative frequencies. According to what we discussed above, the modes laying on these parts of the dispersion curves have a negative energy and are thus *energetically unstable*.

A simple example of *dynamical instability* can instead be obtained by considering a uniform condensate at rest but with an *attractive* interaction constant $g < 0$. The analysis is identical to the one performed in the derivation of the Bogoliubov dispersion relation (1.29) and also the eigenvalues are the same. This time however they are not all real, in fact for

$$\frac{\hbar^2 k^2}{2M} < 2\,|g|\,n \tag{1.38}$$

they are purely imaginary. This is shown in the right plot of Figure 1.1, where green lines indicate zero-norm pseudo-degenerate imaginary eigenvalues, corresponding to a dynamically unstable modes and their decaying partners. Interestingly, the depicted dispersion relation is similar to the one of a tachyonic field, that is a field with an imaginary mass.

Uniform condensates with attractive interaction are hence dynamically unstable with respect to sufficiently low-momentum perturbations, causing the collapse of the gas. It

is interesting to comment, as done in [37], that this does not preclude the experimental realization of condensates with attractive interactions: if one puts such a condensate in a confining geometry in which the lowest possible momentum is above the instability condition (1.38), no dynamically unstable modes appear. The system is hence stabilized by the discrete spectrum of excitations; we will see in Chapter 5 that a similar stabilization takes place for multiply quantized vortices in harmonic traps.

- Interplay between energetic and dynamical instabilities

Dynamically unstable modes can physically be interpreted as the continuous simultaneous creation of excitations with opposite energies. This interpretation is supported by the fact that dynamically unstable modes can emerge in a dynamically stable system by the approaching in frequency of two modes of opposite energies when some parameter is varied.

This can be seen, as was done for example in [40], by considering a variation of some parameter of the system that causes a dynamically stable linear problem specified by $\mathcal{L}$ to change as $\mathcal{L}' = \mathcal{L}+\delta\mathcal{L}$. Assume that the new eigenmodes of the system will be determined simply by a reduced basis of two eigenmodes $|\phi_1\rangle$ and $|\phi_2\rangle$ of the original matrix $\mathcal{L}$ with *close* real eigenfrequencies $\omega_{1,2}$. We can hence look for new eigenstates of the shape $|\phi\rangle = a_1 |\phi_1\rangle + a_2 |\phi_2\rangle$ by projecting the new eigenvalue equation via the inner product (1.23) (i.e. by applying $\langle\phi_i| \sigma_3$ on the left). By defining $\delta\mathcal{L}_{ij} := \langle\phi_i| \sigma_3 \delta\mathcal{L} |\phi_j\rangle = \delta\mathcal{L}^*_{ji}$ one obtains

$$\begin{bmatrix} \omega_1 + \|\psi_1\|_B \delta\mathcal{L}_{11} & \|\psi_1\|_B \delta\mathcal{L}_{12} \\ \|\psi_2\|_B \delta\mathcal{L}^*_{12} & \omega_2 + \|\psi_2\|_B \delta\mathcal{L}_{22} \end{bmatrix} \begin{pmatrix} a_1 \\ a_2 \end{pmatrix} = \omega \begin{pmatrix} a_1 \\ a_2 \end{pmatrix}. \tag{1.39}$$

The resulting new eigenvalues are

$$\begin{aligned} \omega_\pm =& \frac{\omega_1 + \|\psi_1\|_B \delta\mathcal{L}_{11} + \omega_2 + \|\psi_2\|_B \delta\mathcal{L}_{22}}{2} \\ & \pm \sqrt{\left(\frac{\omega_1 - \omega_2 + \|\psi_1\|_B \delta\mathcal{L}_{11} - \|\psi_2\|_B \delta\mathcal{L}_{22}}{2}\right)^2 + \|\psi_1\|_B \|\psi_2\|_B \, |\delta\mathcal{L}_{12}|^2}, \end{aligned} \tag{1.40}$$

from which one can see that the eigenvalues can change in a relevant way only if the difference $\omega_1 - \omega_2$ is not large compared to the magnitude of the perturbations $\delta\mathcal{L}_{ij}$. This justifies our truncation of the eigenmodes basis to two element since only close eigenvalues matter for the mixing.

Now, if the two modes have the same sign of the Bogoliubov norm the argument of the square root in (1.40) is always positive and the two eigenvalues undergo an avoided crossing, that is they approach each other until their separation becomes comparable with the linear problem perturbation $\delta\mathcal{L}$ and then move away from each other.

If instead the two modes have have opposite-signed norms the argument of the square root can become negative and hence the two new eigenfrequencies will have the same real part and develop opposite imaginary parts. The opposite-normed modes are hence becoming pseudo-degenerate giving rise to a dynamically unstable mode and its decaying

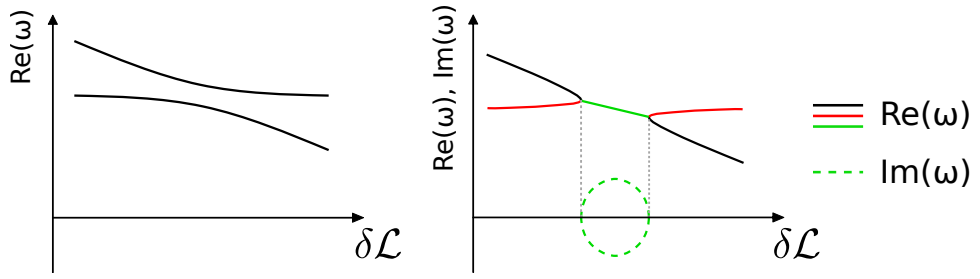

Figure 1.2: Possible behaviours of neighboring eigenvalues when a parameter of the linear problem is changed. On the left avoided crossing for eigenfrequencies relative to modes of the same norm. On the right coalescence of opposite-normed modes in a couple of pseudo-degenerate modes signaling dynamical instability. Black lines indicate positive-norm modes, red lines negative-norm ones and green lines modes with a vanishing norm.

partner. A pictorial representation of these two behaviour depending on the relative sign of the norms is given in Figure 1.2.

That this is mechanism is essential for the emergence of dynamical instabilities in condensates was shown for example in [41]. Moreover it is possible to define an energetic instability as a negative eigenvalue of the matrix (1.33). In this sense it can be shown that dynamical instabilities can be present only if there is also an energetic instability; the converse is not true and energetically unstable but dynamically stable systems can occur. The interplay between energetic and dynamical instabilities will be a Leitmotiv of this work.

The structure of the Bogoliubov problem and these behaviours are much more general than the present case of BECs and depend on the symplectic nature of the problem that is shared with Hamiltonian systems [42,43], where the norm is known as Krein signature. Another occurrence of this structure is the Klein–Gordon equation [15,44], we will discuss this after introducing the gravitational analogy in Section 1.4.

1.1.4 Quantization of fluctuations

One of the interesting features of Bose–Einstein condensate is the quantum nature of fluctuations, that is also relevant for analogue models of gravity since they allow to study *quantum* aspects of field theories in curved spacetimes.

Quantization of fluctuations is relatively easy if the system is dynamically stable, in fact modes with nonzero norm are normalizable. We will follow here the prescription of associating destruction operators to the u component of the Bogoliubov vectors and creation operators to the v components, keeping in mind that more rigorous approaches validating this procedure are available [38]. Under this prescription the *classical* fluctuation field (1.27) becomes

$$\hat{\delta\psi}(\mathbf{r},t) = \sum_k \left[u_k(\mathbf{r})\hat{b}_k e^{-i\omega_k t} + v_k(\mathbf{r})^* \hat{b}_k^\dagger e^{+i\omega_k t} \right], \tag{1.41}$$

with the commutation relations

$$\|\phi_k\|_B\|\phi_l\|_B\,[\hat{b}_k,\hat{b}_l^\dagger] = \|\phi_k\|_B\delta_{kl}, \tag{1.42}$$

that for positive-norm modes is the usual bosonic commutation relations, while for negative-norm ones implies that creation and annihilation operators are exchanged. This shows that negative-norm modes correspond to antiparticles (and that creating an antiparticle is equivalent to annihilating a particle) and to remember this it is convenient to redefine the ladder operators so that for negative-norm modes an annihilation operator is associated to the v component. We may hence rewrite the quantum fluctuation field as

$$\begin{aligned}\delta\hat{\psi}(\mathbf{r},t) = &\sum_{\|\phi_k\|_B>0}\left[u_k(\mathbf{r})\hat{b}_k e^{-i\omega_k t} + v_k(\mathbf{r})^*\hat{b}_k^\dagger e^{+i\omega_k t}\right]\\ &+\sum_{\|\phi_k\|_B<0}\left[u_k(\mathbf{r})\hat{b}_k^\dagger e^{-i\omega_k t} + v_k(\mathbf{r})^*\hat{b}_k e^{+i\omega_k t}\right].\end{aligned} \tag{1.43}$$

We already commented on the particle-hole symmetry and how positive and negative norm modes with opposite frequencies are the same physical mode, so that in the above sums one should keep only one mode for each particle-hole pair to avoid overcounting. One could simply select only the positive-norm modes, but we will see in the following that it is sometimes useful to construct a basis with modes of both norms.

The second-order energy correction (1.34) becomes the Hamiltonian of the quantum field. Choosing to construct a basis with positive-norm modes only, the Hamiltonian hence is [45]

$$\hat{H}^{(2)} = -\sum_k \int \mathrm{d}\mathbf{r}\,|v_k|^2 + \sum_k \hbar\omega_k\hat{b}_k^\dagger\hat{b}_k, \tag{1.44}$$

where the operators satisfy bosonic commutation relations $[\hat{b}_k,\hat{b}_l^\dagger]=\delta_{kl}$ and $[\hat{b}_k,\hat{b}_l]=0$. If one had chosen to also keep negative-norm modes, they would have entered the sum of equation (1.44) with a minus. The first term comes instead from commutations between the operators in the expansion process starting from the energy functional and is an estimate of the contribution of quantum fluctuations to the ground state energy. While usually a small correction, this kind of corrections can become important and with a macroscopic effect in certain situations; for example quantum fluctuations can provide a repulsive correction to a gas with attractive interactions that can stabilize the collapse and form the so-called quantum droplets [46].

When dynamically unstable modes are present instead, quantization is less straightforward, since the norm of these modes vanishes. This is a solved problem in relativistic quantum field theories, see for example [15, 47], and was adapted to the BEC case in [26, 48]. The idea is that the orthogonality relation (1.25) does not impose for the Bogoliubov inner product between a mode of complex frequency ω_k and its pseudo-degenerate partner (of frequency ω_k^*) to vanish. We can hence associate to each mode k the dual mode $\bar{k}$ with $\omega_{\bar{k}} = \omega_k^*$, in terms of which the (non-constant) part of the

quantized Bogoliubov Hamiltonian can be written

$$\hat{H}^{(2)} = \sum_k \hbar\omega_k \hat{b}^\dagger_{\bar{k}} \hat{b}_k \tag{1.45}$$

with the commutation relations

$$[\hat{b}_k, \hat{b}^\dagger_l] = \delta_{\bar{k}l} \ , \qquad [\hat{b}_k, \hat{b}_l] = 0. \tag{1.46}$$

This means that for complex-frequency modes the canonical conjugate of the destruction operator is not its hermitian conjugate, i.e. the creation operator. A consequence is that creation and annihilation operators for complex-frequency modes commute, so that they are not creation and annihilation operators in the usual sense. The quantum field theory in the presence of dynamically unstable modes does hence not have a *particle interpretation*.

The meaning of this formalism can be understood by defining new operators

$$\hat{c}_k = \frac{\hat{a}_k + \hat{a}_{\bar{k}}}{\sqrt{2}} \ , \qquad \hat{c}_{\bar{k}} = i\frac{\hat{a}^\dagger_k - \hat{a}^\dagger_{\bar{k}}}{\sqrt{2}} \tag{1.47}$$

that satisfy ordinary commutation relations $[\hat{c}_k, \hat{c}^\dagger_k] = [\hat{c}_{\bar{k}}, \hat{c}^\dagger_{\bar{k}}]$ and are hence ordinary annihilation operators. The part of the Hamiltonian (1.45) involving complex-frequency modes can hence be written

$$\hat{H}_{k,\bar{k}} = \Re(\omega_k)\left[\hat{c}^\dagger_k \hat{c}_k - \hat{c}^\dagger_{\bar{k}} \hat{c}_{\bar{k}}\right] - \Im(\omega_k)\left[\hat{c}^\dagger_k \hat{c}^\dagger_{\bar{k}} + \hat{c}_k \hat{c}_{\bar{k}}\right]. \tag{1.48}$$

Notice that the imaginary part of the frequency is associated to production of pair of modes, reflecting the dynamical instability of the condensate.

This kind of construction for the Klein–Gordon equation (that we will connect with the Bogoliubov problem in the following of this Chapter) has also been used to treat the superradiant instabilities of rotating spacetimes [49] and the Schiff–Snyder–Weinberg effect [15]. These topics will be briefly presented in the following Chapter when discussing superradiant instabilities and will be a recurring topic in the rest of the work.

1.2 The acoustic metric

1.2.1 Intro: a geometric description of sound

Before proceeding with a derivation starting from the equations of Bose–Einstein condensates, let us give a very simple explanation of how we can describe sound propagation in a moving medium via a *relativistic* acoustic metric.

Consider a fluid flowing with a (possibly space dependent) velocity field $\mathbf{v}$ and suppose that sound propagates in it with a speed c_s. With respect to the laboratory sound propagates, if its wavevector has a direction $\hat{\mathbf{n}}$, according to

$$\frac{d\mathbf{x}}{dt} = c_s \hat{\mathbf{n}} + \mathbf{v}. \tag{1.49}$$

Requiring for $\hat{\mathbf{n}}$ to be a unit vector one obtains

$$c_s^2 dt^2 = (d\mathbf{x} - \mathbf{v}dt)^2 \tag{1.50}$$

or

$$-\left(c_s^2 - \mathbf{v}^2\right) dt^2 - 2\mathbf{v}\cdot d\mathbf{x}dt + d\mathbf{x}\cdot d\mathbf{x} = 0. \tag{1.51}$$

This clearly has the shape of a null line element in a relativistic language, that is $g_{\mu\nu}dx^\mu dx^\nu = 0$ with a metric of the shape

$$g_{\mu\nu} = \Omega(t,\mathbf{x}) \begin{bmatrix} -(c_s^2 - v^2) & -\mathbf{v}^T \\ -\mathbf{v} & \mathbf{I} \end{bmatrix}, \tag{1.52}$$

where $\Omega(t,\mathbf{x})$ is a *conformal factor* that cannot be obtained from this simple derivation. This is telling us that the propagation of sound in a moving medium can be described with the null geodesics of a Lorentzian metric (that are left invariant by a conformal transformation changing the overall factor of the metric).

This is the basic fact on which Analogue Gravity is based. We will see in the following how this idea finds a realization in the emergence of a Klein–Gordon equation for a (possibly quantum) scalar field in a curved spacetime.

1.2.2 The acoustic metric in a BEC

The argument we just summarized shows in general terms how the presence of a perturbation propagating with a fixed speed in a moving medium implies the possibility of a geometric description of sound in terms of a curved-spacetime metric. Here we show explicitly that this is possible for excitations in Bose–Einstein condensates. This follows essentially from the fact that their behaviour can be approximated with the one of a perfect fluid, thus recovering the classical result of Unruh [1, 3, 11].

Instead of taking fluctuations around a steady state of the shape (1.17), it is convenient to consider density and phase fluctuations in the hydrodynamic representation of the GPE of equations (1.12) and (1.15). This corresponds to considering a different factorization of the fluctuation field

$$\Psi(\mathbf{r},t) = e^{-i\mu t/\hbar}\Psi_0(\mathbf{r})\left[1+\varphi(\mathbf{r},t)\right] = e^{-i\mu t/\hbar}\sqrt{n}e^{i\Theta}\left(1 + \frac{n_1}{2n} + i\Theta_1\right), \tag{1.53}$$

where the total density and phase are $n = n_0 + n_1$ and $\Theta = \Theta_0 + \Theta_1$. The resulting linear equations are

$$\begin{cases} \partial_t n_1 + \nabla\cdot\left[n_1\mathbf{v} + n_0\dfrac{\hbar}{M}\nabla\Theta_1\right] = 0 & \text{(1.54a)} \\ \hbar\partial_t\Theta_1 + \hbar\mathbf{v}\cdot\nabla\Theta_1 + gn_1 - \dfrac{\hbar^2}{4M}\dfrac{1}{n}\nabla\cdot\left[n\nabla\left(\dfrac{n_1}{n}\right)\right] = 0, & \text{(1.54b)} \end{cases}$$

where the velocity is given by the background phase $\mathbf{v} = \hbar\nabla\Theta_0/M$. The last term of the second equation comes from the linearization of the quantum pressure term and is responsible for the deviation from the hydrodynamic behaviour. If we consider density fluctuations happening over large enough wavelengths $\lambda \gg \xi$ (*long wavelength limit*) we obtain an algebraic expression for the density variations

$$n_1 = -\frac{1}{g}\left(\hbar\partial_t\Theta_1 + \hbar\mathbf{v}\cdot\nabla\Theta_1\right), \tag{1.55}$$

that can be substituted in the first equation, so that we obtain a single equation for the phase fluctuations

$$-\left(\partial_t + \nabla\cdot\mathbf{v}\right)\frac{n_0}{Mc_s^2}(\partial_t + \mathbf{v}\cdot\nabla)\Theta_1 + \nabla\cdot\left(\frac{n_0}{M}\nabla\Theta_1\right) = 0. \tag{1.56}$$

By introducing $(3+1)$-dimensional coordinates $x^\mu = (t, x^i)$, with Greek indices spanning from 0 to 3 and Latin ones from 1 to 3, we can rewrite this equation as

$$\partial_\mu\left(f^{\mu\nu}\partial_\nu\Theta_1\right) = 0, \tag{1.57}$$

where Einstein summation convention for repeated indices is used and

$$f^{\mu\nu} = \frac{n_0}{c_s^2}\begin{bmatrix} -1 & -v^j \\ -v^i & (c_s^2\delta^{ij} - v^iv^j) \end{bmatrix}. \tag{1.58}$$

It is now convenient to bring this equation in the shape of a d'Alembertian for a curved spacetime

$$\Box\Theta_1 = \frac{1}{\sqrt{|g|}}\partial_\mu\left(\sqrt{|g|}g^{\mu\nu}\partial_\nu\Theta_1\right) \tag{1.59}$$

by identifying $f^{\mu\nu} = \sqrt{|g|}g^{\mu\nu}$ and inverting the resulting $g^{\mu\nu}$ one obtains the *acoustic metric*

$$g_{\mu\nu} = \frac{n_0}{c_s}\begin{bmatrix} -(c_s^2 - v^2) & -v^j \\ -v^i & \delta_{ij} \end{bmatrix}, \tag{1.60}$$

also expressed by the line element

$$ds^2 = \frac{n_0}{c_s}\left[-c_s^2dt^2 + (dx^i - v^idt)\delta_{ij}(dx^j - v^jdt)\right]. \tag{1.61}$$

Equation (1.59) shows how, in the long-wavelenght limit, phase fluctuations of a BEC follow the same equation as a minimally-coupled massless scalar field propagating in a $(3+1)$-dimensional Lorentzian geometry. This relativistic description comes from the finite and fixed speed of sound, that plays the role of the speed of light, and has nothing to do with the background physics of the condensate, that continues to live in a non-relativistic Galileian world.

This is the core idea of Analogue Gravity, in which fluid configurations are engineered so that the acoustic metric reproduces a general-relativistic spacetime of interest, so that the propagation of fields in this spacetime can be studied in an experimentally controllable and well-understood setting. Some comments on this research programme are in order.

First of all the acoustic metric (1.60) is determined by three scalar degrees of freedom, that is the phase of the condensate (giving the irrotational velocity), its density and the speed of sound (that can be tuned in a space-dependent way). A general Lorentzian metric has instead 6 degrees of freedom, so that the acoustic metric can, at best, simulate a subset of possible metrics. This limitation is however not so stringent because, even if many metrics of interest in general relativity cannot be reproduced, some simpler *toy model* metrics that show the same main characteristics can be obtained. In Chapter 3 we will also see how BECs can be used to extend the class of metrics that can be reproduced.

A relevant aspect of gravitational analogues in BECs is that the analogy is strictly true only in the long-wavelength limit, beyond which the superluminal shape of the Bogoliubov dispersion relation starts to matter. This is a drawback but also an occasion to study the effect of high-frequency dispersive effects on the physics of curved spacetimes. This has been a main topic in the investigation of analogue Hawking radiation, as we will briefly show in Section 1.5.

Another important point is the fact that here there are no *analogue Einstein equations*, that is we cannot simulate the dynamics of the solutions of general relativity but only the propagation of fields in a given curved background. This is however interesting enough, especially for the fact that fluctuations in BECs are *quantum*, so that one can directly investigate and probe aspects of quantum field theory in curved spacetimes. The relative simplicity of the physical system also allows to go beyond the physics of quantum fields in a fixed spacetime and study the *back-reaction* of quantum fluctuations on the geometry (see for example [50]).

Besides this a BEC analog model provides a *large-scale* metric description in a system whose small-scales (quantum) microphysics is well known, that is exactly what is missing in quantum descriptions of gravity. So, even if we are not reproducing directly Einstein equations, BEC analogue models can provide a playground in which the interplay between the macroscopic geometric description with the complex quantum microscopic many-body physics can be studied, possibly giving ideas for the more difficult gravitational case.

1.3 (Acoustic) black holes

Among the most interesting spacetimes to study there are black holes, that is vacuum solutions of the Einstein equations that display an event horizon, that is a surface from which nothing, not even light, can escape. In analogue acoustic spacetimes horizons, as well as other characteristics of black hole spacetimes, have a very intuitive nature in terms of the values of the flow velocity. This is because, differently from the case of

general relativity, the background laboratory gives a natural *absolute space* with respect to which it is easy to say what is moving and what is at rest.

In this Section we want to give some examples of black hole spacetimes in general relativity and their *toy model analogue* counterpart in an acoustic setup. We first show how the most famous black hole solution, the Schwarzschild solution, admits a representation in the shape of an acoustic metric. We then give a brief account of the Kerr rotating black hole as a useful reference for the acoustic case. We then see how the basic features of a rotating black hole can be reproduced acoustically with a flow in the shape of a draining vortex.

1.3.1 The Schwarzschild black hole in Painlevé–Gullstrand coordinates

Obtained only some months after the final development of Einstein theory of general relativity, the Schwarzschild geometry is an asymptotically flat static and spherically symmetric solution of the Einstein equations. It is the first and easiest example of a black hole and can be described by the line element

$$\mathrm{d}s^2 = -\left(1-\frac{2M}{r}\right)\mathrm{d}t^2 + \left(1-\frac{2M}{r}\right)^{-1}\mathrm{d}r^2 + r^2\left(\mathrm{d}\theta^2+\sin^2\theta\,\mathrm{d}\phi^2\right). \tag{1.62}$$

One can see that the metric components are singular in two points, i.e. $r=0$ and $r=2M$. By checking the Riemann tensor it turns out that the first one is also a *true* curvature singularity, while the one at $r_H=2M$ is only a coordinate singularity, corresponding to the so-called *event horizon*.

This spacetime has a Killing vector $t^\mu = \partial x^\mu/\partial t$ associated to the invariance under time translations (to which also an invariance under time reflections is added), that is a timelike vector field for the asymptotical Minkowski metric, but becomes spacelike for $r<r_H$. Static observers have a four velocity directed along t^μ, so that this fact implies that they are not possible inside the horizon.

Let us now consider a different shape of the Schwarzschild metric, that can be obtained by defining a new time coordinate

$$\mathrm{d}t_{PG} = \mathrm{d}t + \frac{\sqrt{2M/r}}{1-2M/r}\mathrm{d}r, \tag{1.63}$$

with which the line element (1.62) becomes

$$\mathrm{d}s^2 = -\mathrm{d}t_{PG}^2 + \left(\mathrm{d}r+\sqrt{\frac{2M}{r}}\,\mathrm{d}t_{PG}\right)^2 + r^2(\mathrm{d}\theta^2+\sin^2\theta\,\mathrm{d}\phi^2). \tag{1.64}$$

This is known as the *Painlevé–Gullstrand* line element and it is interesting to notice, as done in [11], that it has the same shape as the acoustic line element (1.61) with a radial only velocity $v_r=-\sqrt{2M/r}$.

Notice however that one cannot in general simply set both the density n_0 and the speed of sound c_s as constants, since the continuity equation $\nabla\cdot(n_0\mathbf{v})=0$ would not

be satisfied. Continuity requires $n_0 \propto r^{-3/2}$, so that the overall factor n_0/c_s in the acoustic metric will not be a constant. One can hence think of a fluid flow reproducing the Schwarzschild metric only up to a *conformal factor*; this is however good enough for many purposes since the causal structure is not changed.

The Schwarzschild metric expressed in the shape (1.64) has the interesting feature of having only one singularity at $r = 0$. The coordinate singularity has hence been removed and we can recognize the horizon as the points in which the Painlevé–Gullstrand *velocity* v_r becomes larger than one, that in the analogue corresponds to v_r becoming supersonic. We already saw in the Introduction how analogue horizons are related to supersonic flows and will discuss this more in the following.

1.3.2 Gravitational rotating black holes: the Kerr metric

The Kerr geometry is an asymptotically flat, stationary and axisymmetric vacuum solution of the Einstein equations describing a rotating neutral black hole. It is a much more complicated solution than static black holes (Schwarzschild and Reisser–Nordström, that will be briefly discussed in Section 2.4.2) and for this was obtained only in 1963 [51]. This spacetime has the Schwarzschild black hole as a particular case and is perhaps the most interesting arena in which superradiance has been predicted in general relativity.

A full discussion of this spacetime is out of the scope of this introductory chapter and we will only present some basic facts we will need. A nice introduction can be found in [52] and presentations can be found in many standard textbooks (for example [53,54]), with a particularly in depth discussion given in Chandrasekhar book [55].

In Boyer–Lindquist coordinates the Kerr metric is given by the line element

$$ds^2 = -\left(1 - \frac{2Mr}{\rho^2}\right) dt^2 - \frac{4Mar\sin^2\theta}{\rho^2}\, dt\, d\phi + \frac{\Sigma}{\rho^2}\sin^2\theta\, d\phi^2 + \frac{\rho^2}{\Delta}\, dr^2 + \rho^2\, d\theta^2, \quad (1.65)$$

where $\rho^2 = r^2 + a^2\cos^2\theta$, $\Delta = r^2 - 2Mr + a^2$ and $\Sigma = (r^2 + a^2)^2 - a^2\Delta\sin^2\theta$. Here M is the mass of the black hole and the parameter a is the ratio between its angular momentum and its mass.

This spacetime has two Killing vectors $t^\mu = \partial x^\mu/\partial t$ and $\phi^\mu = \partial x^\mu/\partial\phi$, reflecting the stationarity and the axial symmetry. It is interesting to consider static observers, that is observers that have a four-velocity proportional to the timelike Killing vector $u^\mu = (-g_{00})^{-1/2} t^\mu$, where the proportionality factor is necessary to have a properly normalized velocity. These observers cannot exist everywhere, in fact when

$$r_E(\theta) = M + \sqrt{M^2 - a^2\cos^2\theta} \quad (1.66)$$

the time-time component g_{00} of the Kerr metric vanishes and changes sign for smaller radii. Correspondingly, the four-velocity of a static observer becomes null and then spacelike, signalling the impossibility of having such an observer there. Beyond this limit g_{00} changes sign and the time-translation Killing vector becomes spacelike: in some sense here space *moves faster than light* with respect to an asymptotic observer.

The surface specified by (1.66) is the so called *static limit*, that we will call *ergosurface* since the region it surrounds is called *ergoregion*. This name comes from energy and is due to the fact that inside the ergoregion the conserved energy of a particle as measured from infinity $E = -p_\mu t^\mu$ can be negative. As we will see this is the crucial fact that allows energy extraction from black holes through the Penrose process (Section 2.3).

Although the only curvature singularity of the Kerr spacetime occurs for $\rho^2 = 0$, the coordinate singularities at $\Delta = 0$ correspond instead to the two horizons of the spacetime, occurring inside the ergoregion at $r_\pm = M \pm \sqrt{M^2 - a^2}$. The main characteristics of the spacetime are represented as circles on the equatorial plane $\theta = \pi/2$ in the left part of Figure 1.3.

It is important to make a clarification on the different types of horizons. An *event horizon* in an asymptotically flat spacetime is the boundary of the black hole region, from which it is impossible for anything to escape to (future) infinity. This is hence a global concept, for which we need to know the full future evolution of geodesics; this may be a problem for acoustic black holes in experimentally realizable settings.

Luckily for stationary spacetimes event horizons coincide with horizons defined in a local way. These rely on the concept of *trapped surfaces*, that are closed spacelike surfaces from which there are no *outgoing* geodesics, that is geodesics for which r increases[1]. Such surfaces are contained in a spacetime region whose boundary is the so-called *trapping horizon* or *apparent horizon* (see for example Section 5.1 of [54]). In stationary spacetimes the event horizon is also a trapping horizon. In particular in the Kerr spacetime both $r_\pm$ are trapping horizons, with r_+ being also the event horizon of the spacetime.

The inner horizon r_- is a new very peculiar feature of the spacetime. While inside the horizon of the Schwarzschild black hole (and between r_+ and r_- in the present case) nothing can move outward, this being expressed by the fact that the radial coordinate is timelike, inside the inner horizon of a Kerr black hole r is spacelike, so that moving in a direction of increasing r is again possible. The inner horizon can hence be crossed in the other direction and one enters *another copy* of the Kerr spacetime. This intriguing causal structure is however out of the reach of Analogue Gravity, since to describe in a regular way each crossing of r_- a change of coordinates is necessary and we saw that analogue spacetimes do not reproduce a full *geometry* but a metric in specific coordinates. We hence will not dedicate further attention to this interesting topic and refer the interested reader to [54].

As a last comment notice that in the static limit $a \to 0$ one recovers the Schwarzschild metric (1.62) for which there is only one horizon that also coincides with the ergosurface, so that there is no ergoregion.

[1] This fact is often expressed by saying that geodesics outgoing from the surface (a notion that can be defined formally) do not expand away but converge. For a clarifying discussion see for example Section 5.1.7 of [54].

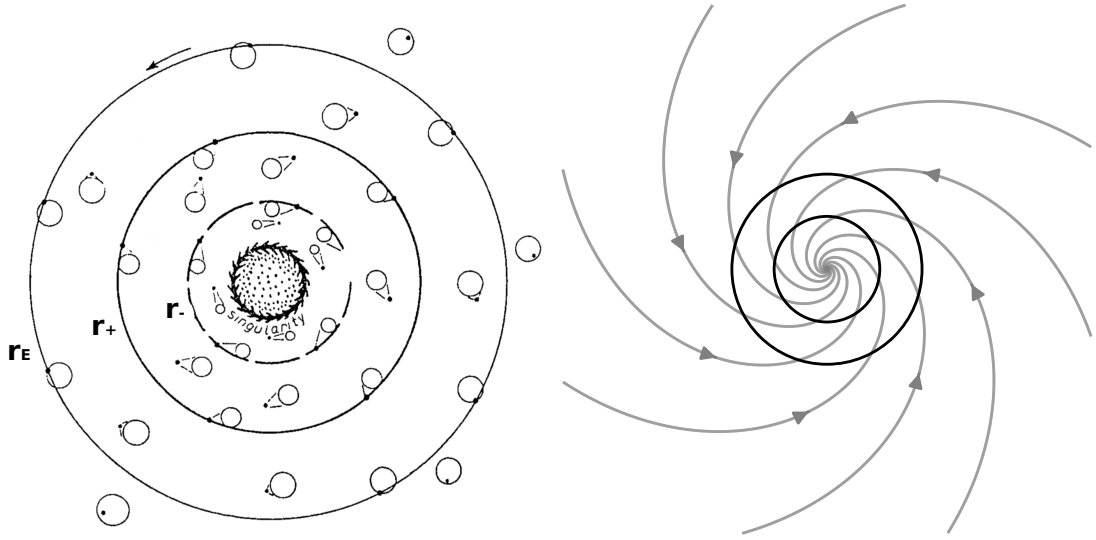

Figure 1.3: On the left a schematic representation of the equatorial plane of the Kerr spacetime (adapted from [56]) with the large circles indicating the important features of the spacetime: from the exterior the ergosurface, the event horizon r_+, the inner horizon r_- and the singularity. The small circles indicate the *wavefront* of light emitted from the dots. Outside the ergosurface light can propagate in all directions, inside the ergoregion instead it must travel in the direction of rotation but can still move to larger radii. At r_+ lightcones are tangent to the horizon and inside it light is forced to travel inwards. Finally, at r_- the cones are again tangent while inside it it is again possible to move in the direction of increasing radii. On the right streamlines of the flow of the vortex geometry (1.68). The outer circle indicates the ergosurface and the inner one the horizon. Notice that, despite being much simpler, the vortex geometry displays an ergosurface and an horizon similarly to the Kerr black hole.

1.3.3 Acoustic rotating black holes: the vortex geometry

Considering now the acoustic metric (1.60) one can think of tuning the fluid quantities so to obtain a black hole metric, that is one that includes an horizon. If the condensate flow is steady, the resulting spacetime will be invariant under time translations (i.e. stationary) and the associated Killing vector is $t^\mu = \partial x^\mu/\partial t = (1, 0, 0, 0)$. As we said in the case of the Kerr spacetime, an ergoregion is characterized by the Killing vector t^μ becoming spacelike, that is

$$g_{\mu\nu} t^\mu t^\nu = g_{00} = -(c_s^2 - v^2) > 0, \tag{1.67}$$

so that any region of supersonic flow $|v| > c_s$ is an ergoregion in the acoustic spacetime.

We said that in ergoregions particles (but also field modes) can have negative energies with respect to an observer at infinity. In acoustic spacetimes hence we can hence have negative-energy modes for our scalar field in regions where the background flow velocity

is supersonic. As we already said and will see multiple times in the course of this thesis, these modes are associated to Landau criterion for the breakdown of superfluidity above some critical frequency, that focuses exactly on negative-energy excitations.

For what concerns horizons instead, we already said that the most convenient notion is the one of a trapping horizon. The definition of a trapped surface becomes here simpler than the generally-covariant one based on the behaviour of geodesic bundles. In fact if a (closed) surface is such that the flow velocity has everywhere a normal component greater than the speed of sound, then sound waves cannot propagate outward and will be dragged by the fluid. We can here think in these terms because the laboratory provides an absolute space with respect to which we can say if the sound is moving in some direction.

Since we will be interested in steady flows, the resulting acoustic metric will be stationary, so that the trapping horizon defined in this way is also the event horizon. We can hence for our purposes forget the distinction and talk simply of *acoustic horizons*.

The simplest way in which one can obtain an acoustic horizon is by considering a fluid in a narrow tube so that it is effectively one-dimensional. If this has a flow that passes from a subsonic to a supersonic velocity, the corresponding acoustic spacetime will have an horizon. This is a *minimal* example of acoustic black hole that can be seen as a toy model of the radial reduction of the Schwarzschild spacetime; we will consider again this kind of configuration in Section 1.5.

Let us now give an explicit example of a stationary and axially-symmetric acoustic spacetime in which the above mentioned features appear. We are interested in a *draining bathtub* type of flow, in which the fluid rotates and moves radially towards the center. For simplicity we consider a two dimensional and constant-density perfect fluid (or BEC in the hydrodynamic limit); the continuity equation and the fact that the velocity must be irrotational require a velocity field of the shape (in polar coordinates)

$$\mathbf{v} = \frac{A}{r}\hat{r} + \frac{B}{r}\hat{\phi}, \tag{1.68}$$

where A and B are two parameters. The acoustic metric for this configuration is characterized by the line element

$$ds^2 = -\left(c_s^2 - \frac{A^2+B^2}{r^2}\right)dt^2 - 2\frac{A}{r}dt\ dr - 2B dt\ d\phi + dr^2 + r^2 d\phi^2, \tag{1.69}$$

that we can bring in a shape more similar to the Kerr line element with the change of coordinates $dt' = dt + Ar/(r^2c_s^2 - A^2)$ and $d\phi' = d\phi + AB/(r^3c_s^2 - A^2 r)$:

$$ds^2 = -\left(c_s^2 - \frac{A^2+B^2}{r^2}\right)dt'^2 - 2B dt\ d\phi' + \frac{r^2c_s^2}{r^2c_s^2 - A^2}dr^2 + r^2 d\phi'^2. \tag{1.70}$$

The vanishing of the time-time component of the metric individuates the ergosurface

$$r_E^2 = \frac{A^2+B^2}{c_s^2}, \tag{1.71}$$

that correctly corresponds to the locus of points where the modulus of the velocity (1.68) becomes supersonic. The horizon is instead signalled by a coordinate singularity in

$$r_H^2 = \frac{A^2}{c_s^2}, \tag{1.72}$$

that, as expected, is the radius at which the radial component of the velocity becomes supersonic.

Although being much simpler, this analogue spacetime reproduces some of the most interesting features of the equatorial slice ($\theta = \pi/2$) of the Kerr black hole. It does not display an interior horizon and only has a point singularity, however it is an asymptotically flat spacetime with an horizon surrounded by an ergoregion. A sketchy comparison of the vortex geometry with the Kerr one is given in 1.3. Although we cannot expect to make *quantitative* predictions about real rotating black holes by studying this model, the main conceptual ingredients are the same, so we can get a *qualitative* understanding of some of the physics occurring outside of the horizon.

It is worth to stress again that, although we started from BECs, we have here considered the equations of a perfect fluid, so from the point of view of the condensate physics we worked in the *hydrodynamic limit*, in which there is no quantum pressure and elementary excitations all move at the speed of sound. We talk about what happens beyond this limit (that will be a main topic of the rest of the thesis) in the following Section.

1.4 The Bogoliubov and Klein–Gordon problems

In the previous Sections we derived the gravitational analogy starting from the Bogoliubov problem for a moving condensate and performing the long-wavelength limit, from which we obtained a Klein–Gordon equation for a massless scalar field in curved spacetimes. In this Section we want to give a detailed comparison of the properties of the Klein–Gordon equation with of the Bogoliubov problem, that we will see show the same spectral structure.

The main physical difference between the two equations relies instead in the dispersion relation of the fluctuations, that has the peculiar Bogoliubov shape (1.29) for the Bogoliubov problem in an uniform condensate and becomes instead simply linear with the long-wavelength approximation, corresponding to the Klein–Gordon equation.

1.4.1 Formal comparison

Let us consider again the factorization of fluctuations (1.53) that we used in deriving the gravitational analogy

$$\Psi(\mathbf{r},t) = e^{-i\mu t/\hbar}\Psi_0(\mathbf{r})\left[1+\varphi(\mathbf{r},t)\right] = e^{-i\mu t/\hbar}\sqrt{n}e^{i\Theta}\left(1+\frac{n_1}{2n}+i\Theta_1\right). \tag{1.73}$$

With an approach similar to our first exposition of the Bogoliubov problem we consider the linear problem for the two-component vector $(\varphi, \varphi^*)^T$

$$i\hbar\partial_t \begin{pmatrix} u_\varphi \\ v_\varphi \end{pmatrix} = \begin{bmatrix} D + gn & gn \\ -gn & -D^* - gn \end{bmatrix} \begin{pmatrix} u_\varphi \\ v_\varphi \end{pmatrix} = \mathcal{L} \begin{pmatrix} u_\varphi \\ v_\varphi \end{pmatrix}, \tag{1.74}$$

where

$$D = -\frac{\hbar^2}{2M}\frac{1}{n}\nabla\cdot(n\nabla) - i\frac{\hbar^2}{M}\nabla\theta\cdot\nabla = D_n + iD_\Theta. \tag{1.75}$$

Again, the non positive-definite inner product conserved on the evolution is

$$\langle\varphi|\psi\rangle_B = \langle\varphi|\sigma_3|\psi\rangle = \int d\mathbf{r}\left[u_\varphi^*(\mathbf{r})u_\psi(\mathbf{r}) - v_\varphi^*(\mathbf{r})v_\psi(\mathbf{r})\right]. \tag{1.76}$$

We want to compare this with the Klein–Gordon equation in the acoustic metric (1.59), that in the simple case of constant background density and speed of sound takes the simple shape

$$\nabla^2\phi - \frac{1}{c_s^2}\left(\partial_t + \mathbf{v}\cdot\nabla\right)^2\phi = 0. \tag{1.77}$$

It is useful to rewrite this equation as a system of first-order in time ones [57] by defining the conjugate momentum

$$\pi = -\frac{1}{c_s^2}(\partial_t + \mathbf{v}\cdot\nabla)\phi, \tag{1.78}$$

so that the equation takes the form

$$\partial_t \begin{pmatrix} \phi \\ \pi \end{pmatrix} = \begin{bmatrix} -\mathbf{v}\cdot\nabla & -c_s^2 \\ -\nabla^2 & -\mathbf{v}\cdot\nabla \end{bmatrix} \begin{pmatrix} \phi \\ \pi \end{pmatrix}. \tag{1.79}$$

The associated conserved inner product is

$$\langle\phi_1|\phi_2\rangle_{KG} = i\int \delta\mathbf{x}\ \left[\pi_1^*\phi_2 - \phi_1^*\pi_2\right]. \tag{1.80}$$

Let us compare this with the formulation of the Bogoliubov problem (1.54a) in terms of the density and phase variations. This can obtained in matrix form with the change of variables

$$\widetilde{n}_1 = \frac{M}{\hbar}\frac{n_1}{n} = \frac{M}{\hbar}(\varphi + \varphi^*); \qquad \Theta_1 = \frac{\varphi - \varphi^*}{2i}, \tag{1.81}$$

that give

$$\partial_t \begin{pmatrix} \Theta_1 \\ \widetilde{n}_1 \end{pmatrix} = \begin{bmatrix} -\mathbf{v}\cdot\nabla & -\frac{\hbar^2}{4M^2}\frac{1}{n}\nabla(n\nabla) - c_s^2 \\ -\hbar^2\frac{1}{n}\nabla(n\nabla) & -\mathbf{v}\cdot\nabla \end{bmatrix} \begin{pmatrix} \Theta_1 \\ \widetilde{n}_1 \end{pmatrix}. \tag{1.82}$$

Notice how, for a constant density and for the desired velocity field, if we neglect, with respect to c_s^2, the term involving spatial derivatives in the second element of the first row, we exactly obtain the Klein–Gordon problem (1.79). This is exactly the long-wavelength

limit we used in the derivation of the acoustic metric and this additional term in the Bogoliubov problem is responsible for the dispersive effects at higher frequencies as we will see in a moment.

In terms of the fields (1.81) the Bogoliubov inner product (1.76) becomes

$$\langle\varphi|\psi\rangle_B = i\frac{\hbar}{M}\int d\mathbf{x}\,[\delta\widetilde{n}_\varphi\delta\Theta_\psi - \delta\Theta_\varphi\delta\widetilde{n}_\psi]\,, \tag{1.83}$$

that has the same (symplectic) shape of the Klein–Gordon inner product (1.80) so that all the considerations about norm and energy we made also hold true for the Klein–Gordon equation. The two degrees of freedom that emerge in BECs excitations from the mixing of positive and negative frequencies are here a consequence of the second order in time of the Klein–Gordon equation [57].

This comparison shows how the spectral properties we discussed for the Bogoliubov problem can directly transfer to the Klein–Gordon one. This common mathematical structure is also shared in general by Hamiltonian systems.

Finally, let us rewrite problem (1.82) in terms of the fields u_φ and v_φ after taking the hydrodynamic approximation:

$$i\hbar\partial_t\begin{pmatrix}u_\varphi\\ v_\varphi\end{pmatrix} = \begin{bmatrix}\frac{D_n}{2}+iD_\theta+gn & -\frac{D_n}{2}+gn\\ \frac{D_n}{2}-gn & -\left(\frac{D_n}{2}-iD_\theta\right)-gn\end{bmatrix}\begin{pmatrix}u_\varphi\\ v_\varphi\end{pmatrix}. \tag{1.84}$$

Notice that with respect to the full dispersive problem (1.74) here the derivatives are distributed in all the matrix elements. This formulation of the Klein–Gordon problem in *Bogoliubov language* will be useful to understand the role of dispersive effects in the configurations we will consider.

1.4.2 The dispersion relations

The dispersion relation gives the functional dependence of the energy of excitations on their momentum. As such it only makes sense in uniform systems in which the excitations have a plane-wave shape and the wavenumber $\mathbf{k}$ is conserved. However it can also give useful insight in the physics of a system that varies spatially slow enough to allow a local expansion in momentum (eikonal approximation).

The dispersion relations for the different problems can be obtained, as we did in deriving equation (1.37), by considering uniform systems (with constant density and uniform velocity) and considering fluctuations in the shape of plane waves. The dispersion relation can then be obtained solving for the eigenvalues of the matrices we introduced in the previous Section.

For example for a constant-density condensate with uniform velocity $\mathbf{v}$ the diagonalization of the matrix in (1.74) gives the modified Bogoliubov dispersion relation

$$\hbar\omega = \hbar\mathbf{v}\cdot\mathbf{k} \pm \sqrt{\frac{\hbar^2k^2}{2M}\left(\frac{\hbar^2k^2}{2M}+2gn\right)} = \hbar\mathbf{v}\cdot\mathbf{k} \pm \hbar c_s\sqrt{\frac{k^2}{2}\left(2+\frac{\xi^2k^2}{2}\right)}, \tag{1.85}$$

where $\xi = \sqrt{\hbar^2/(Mgn)}$ is, as above, the healing length of the condensate. Notice that the choice of having the phase of the condensate as an overall factor in the expression for the fluctuation field (1.53) corresponds, as we already commented about (1.37), to *measuring* the momenta with respect to the condensate momentum. The extra term involving the velocity in (1.85) is hence a Doppler shift.

Performing the same procedure on the matrices of equations (1.79) or (1.84) we obtain the dispersion relation for the corresponding Klein–Gordon problem

$$\omega = \mathbf{v} \cdot \mathbf{k} \pm c_s \left|\mathbf{k}\right| . \tag{1.86}$$

This can be directly compared with the second expression in (1.85) to show that the Bogoliubov dispersion relation differs substantially for momenta $k \gtrsim \xi^{-1}$, for which the dispersion relation deviates from a linear behaviour.

A graphical comparison of the two dispersion relations for a one-dimensional configuration is given in Figure 1.4 where the solid lines indicate the Bogoliubov dispersion relation and the dashed lines the Klein–Gordon one. Here black lines indicate positive-norm modes and red lines negative-norm ones; it is easy to notice the redundancy of one of the two norms to describe all the modes. In the case of a supersonic velocity one can see that the negative-norm branches rise to positive frequencies (equivalently the positive-norm ones lower to negative frequencies), so that negative energy modes are present.

This is an example of Landau's criterion of superfluidity [16, 39] according to which above some critical frequency energetic instabilities develop in superfluids; here the critical speed is the speed of sound. Remembering, as we said in Section 1.3.3, that in analogue spacetimes ergoregions correspond to regions of supersonic flow, we have here another interpretation of the negative-energy modes occurring in those portions of the spacetime.

Since the slope of the dispersion curves indicates the group velocity of the modes one from Figure 1.4 we can see that in the Klein–Gordon case all the excitations of a branch move with the same velocity, that with respect to the lab frame is $v \pm c_s$. For the Bogoliubov dispersion instead the group velocities are larger than the speed of sound for $k \gtrsim \xi^{-1}$; these are called *superluminal* corrections to the Klein–Gordon equation.

This poses a difficulty in the definition of an horizon (and of an ergosurface) in BEC analogues. In a one-dimensional configuration such as the one sketched in the upper part of Figure 1.4 the point in which the flow velocity matches the speed of sound is an horizon. Beyond this point, as one can see in the right panel, for the Klein–Gordon problem all the excitations have a group velocity directed downstream, as one would expect for a real horizon. For the Bogoliubov case however also excitations with upstream velocities are present, so that the sonic point is not really an horizon. Moreover, for high enough frequencies this is not even an ergoregion since no negative-energy modes are present.

One could define *frequency-dependent* horizons and ergoregions by comparing the flow velocity with the speed of the modes at that frequency. In this way a *rainbow metric* is obtained, in which the positions of the horizons and the ergosurfaces depend on the frequency. We will use this kind of spacetime elements when discussing superradiance

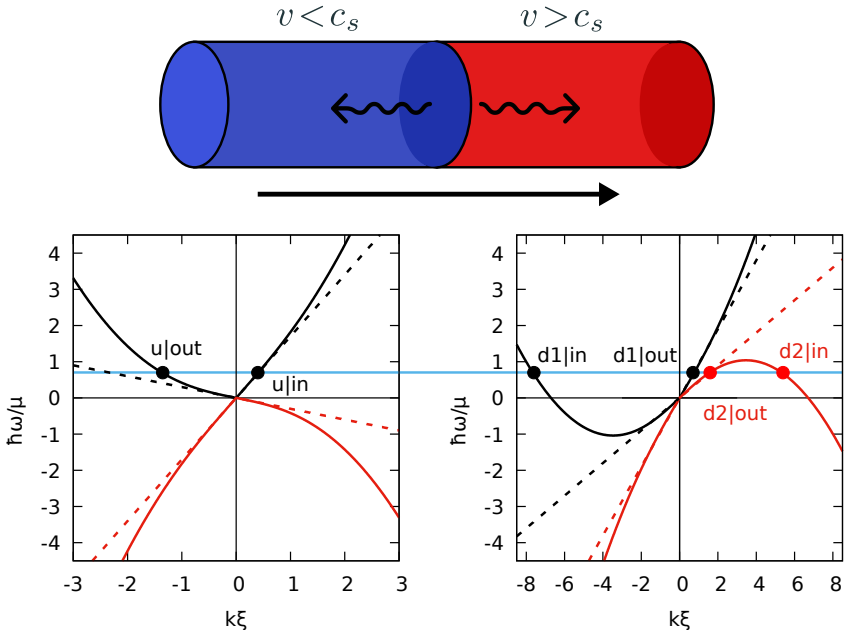

Figure 1.4: The top drawing is a schematic representation of a *minimal* black hole: a condensate flows in a tube and the flow velocity and the speed of sound are such that two regions of subsonic and supersonic motion are present. The point of transition between the two is an horizon, from which one expects emission of Hawking pairs, indicated with wiggly lines. The two panels on the bottom show the Bogoliubov dispersion relation (solid lines) in the two regions. The black lines correspond to positive-norm modes, the red lines to negative-norm ones. The dashed lines are the corresponding Klein–Gordon dispersion. Scattering processes occur at fixed frequency, the horizontal blue line is an example, individuating the relevant modes on the dispersion curves.

and horizons in our setups.

Notice that the *dispersive* nature of the Bogoliubov dispersion law is related to the fact that is of higher order in k, so that at fixed ω there will be in general four modes (possibly of complex wavenumber) instead of the two of the Klein–Gordon equation. As an example look at the intersections of the blue line of Figure 1.4 with the dispersion curves: inside the horizon there are four solutions for the Bogoliubov case, two of which ($d1|in$ and $d2|in$), not present in the Klein–Gordon case, are at large momenta and move upstream.

1.5 A prototypical example: Hawking radiation in BECs

Hawking radiation [2, 58] is one of the most famous effects of quantum field theories in curved spacetimes. The prediction is that black holes emit at the quantum level

radiation with a thermal spectrum at future infinity with a temperature

$$k_B T = \frac{\hbar\kappa}{2\pi}, \tag{1.87}$$

where κ is the surface gravity of the black hole, that can be interpreted as the force per unit mass necessary for an observer at infinity to hold a particle stationary at the event horizon and that for the Schwarzschild black hole has the value $\kappa = 1/(4M)$. This emission can be understood as quantum pair creation at the horizon and was historically derived after the realization that ergosurfaces could lead to spontaneous emission of particle pairs.

The original idea of fluid analogues by Unruh [3] was motivated by the possibility of observing black hole evaporation in the laboratory. In this case the surface gravity of the horizon is given in terms of the fluid quantities by

$$\kappa = \frac{1}{2}\frac{\partial(c_s^2 - v^2)}{\partial n}\bigg|_{\text{horizon}}. \tag{1.88}$$

We will not give a derivation of the Hawking effect in gravitational physics, for which many good introductory expositions are available (for example [59–61]), but we will focus on the realization in BEC analogues.

As we said in the previous Section, the presence of nonlinear dispersion relations poses a difficulty in defining ergoregions and horizons. This issue is related to the so-called *trans-Planckian* problem of Hawking radiation. In the original derivation of Hawking it is possible to see that if one follows the emitted radiation from the future infinity (where it is observed) back in time, this gets infinitely blueshifted. Hence it seems that Hawking result relies on the validity of quantum field theory in curved spacetimes up to arbitrarily high energies, for which there is no experimental evidence. In fact the microscopic physics of the spacetime beyond the Planck scale may be very different and contain deviations from the general-relativistic description.

One of the main interests of gravitational analogues has been to provide a framework in which to study possible deviations from the Lorentz-invariant physics of curved spacetimes. In particular, analogue models are systems in which a low-energy geometric description emerges from a well-known microscopic background. A possible way in which the microphysics comes into play is with modifications to the dispersion relations of the fluctuations at high(er) frequencies, exactly as we saw for the Bogoliubov dispersion. In that case the healing length ξ plays the role of an *analogue Planck length*.

Hawking radiation with such modifications has been widely studied [62–65] and has proven robust to dispersive effects, also maintaining its thermal nature in appropriate regimes. For a comprehensive discussion and complete references see [1].

In analogue black holes it is instructive to study Hawking radiation in terms of scattering of fluctuations at an acoustic horizon (for nice introductions see [66, 67]), that is a mechanism very different from the one occurring in the gravitational case. In the particular case of Bose–Einstein condensates it was shown that the microscopic mechanism of pair creation is conceptually the same even in configurations well outside the hydrodynamic limit [68–73].

1.5.1 A minimal black hole

As an example that will be useful as a conceptual reference also when discussing superradiant phenomena we consider now consider a *minimal* configuration displaying the spontaneous pair production associated to the Hawking effect. Consider a condensate flowing in a narrow *tube*, that is a condensate tightly confined in two directions so that the first *transverse* excited states have a high energy and can be neglected from the description. The dynamics of this *cigar-shaped* condensate can be described with a one-dimensional GPE (see Chapter 24 of [16]), and hence the excitations with a one-dimensional Bogoliubov problem.

Instead of considering a spatially-inhomogeneous flow velocity one can take a constant one and construct an acoustic horizon can be constructed by locally varying the speed of sound $c_s = \sqrt{gn/M}$. In BECs this can be obtained with a local variation of the interaction constant, that can be achieved by changing the transverse size of the condensate or the atom-atom scattering length with an external magnetic field (exploiting Feshbach resonance). In order to maintain the density homogeneous one should add an external potential assuring $V_{\rm ext}(x) + g(x)n = const = \mu$, so that the one-dimensional GPE has a plane wave stationary solution

$$\Psi_0(x) = \sqrt{n_0} e^{i(Mv/\hbar)x}. \tag{1.89}$$

Consider the case in which the speed of sound is constant, except for a region where it passes from being larger than the flow velocity to being smaller. Labelling with u and d the *upstream* and *downstream* regions sufficiently far from the transition region we have $c_d < v < c_u$. This configuration is sketched in the upper part of Figure 1.4, where we show a sharp transition between the two zones. Plots of the dispersion relations in the two uniform regions are shown with the relevant modes indicated by dots, named with *in* or *out* depending of if they mode towards or away from the horizon.

Consider a scattering process in which the mode $u|in$ (of frequency below the critical one for the existence of negative-norm modes) impinges on the transition region. The modes involved in the scattering are the ones that have the same frequency in the two regions, so that the wave will be reflected in the $u|out$ mode and transmitted in the positive-norm mode $d1|out$ and in the negative-norm one $d2|out$. Notice that the modes involved in this particular scattering are not qualitatively different from the corresponding ones of the Klein–Gordon dispersion, since the modes $d1|in$ and $d2|in$ do not come into play. As we already commented, instead of the negative norm mode we can equivalently consider the corresponding positive-norm negative-frequency one. The partial conversion of a positive-frequency mode to a negative-frequency one has been experimentally observed with surface waves on moving water [74] and is a classical analogue of the Hawking effect [75].

To understand why this is the case we can follow the scattering approach of [69], that we will extend to the superradiant case in Section 3.3, in which two bases for the fluctuations are introduced: the one of ingoing modes and the one of outgoing ones. The quantum field describing the fluctuations at a fixed frequency (below the critical

frequency for negative-norm modes) can be decomposed in terms of these modes as

$$\hat{\delta\psi}(\omega,x)=\sum_{I=u,d1}\left[u_{I|in}(x)\hat{a}_I(\omega)+v^*_{I|in}(x)\hat{a}^\dagger_I(\omega)\right]+\left[u_{d2|in}(x)\hat{a}^\dagger_{d2}(\omega)+v^*_{d2|in}(x)\hat{a}_{d2}(\omega)\right], \tag{1.90}$$

or the equivalent expression in terms of outgoing modes, whose operators we indicate with $\hat{b}$. Here u_I and v_I are the components of the Bogoliubov modes of the basis. Notice that, as in equation (1.43), for the negative-norm mode $d2$ creation and annihilation operators are exchanged.

The two bases are related by an input-output relation given by the scattering matrix

$$\begin{pmatrix}\hat{b}_u(\omega)\\ \hat{b}_{d1}(\omega)\\ \hat{b}^\dagger_{d2}(\omega)\end{pmatrix}=S(\omega)\begin{pmatrix}\hat{a}_u(\omega)\\ \hat{a}_{d1}(\omega)\\ \hat{a}^\dagger_{d2}(\omega)\end{pmatrix}. \tag{1.91}$$

We have now the basic ingredients of Hawking emission, that should in this setup emerge as emission of phonons in the $u|out$ mode. The emitted quanta in this mode per unit time can be computed using the input-output relation as

$$\langle\hat{b}^\dagger_u(\omega)\hat{b}_u(\omega)\rangle=|S_{uu}|^2\langle\hat{a}^\dagger_u(\omega)\hat{a}_u(\omega)\rangle+|S_{ud1}|^2\langle\hat{a}^\dagger_{d1}(\omega)\hat{a}_{d1}(\omega)\rangle+|S_{ud2}|^2\left(\langle\hat{a}^\dagger_{d2}(\omega)\hat{a}_{d2}(\omega)\rangle+1\right), \tag{1.92}$$

where the $+1$ in the last term comes from the commutation of the operators of the negative-norm mode. If we start from the vacuum of the ingoing modes (at zero temperature) all the expectation values of the right-hand side vanish and only the emission due to the vacuum quantum fluctuations remains:

$$\langle\hat{b}^\dagger_u(\omega)\hat{b}_u(\omega)\rangle=|S_{ud2}|^2. \tag{1.93}$$

This is the Hawking radiation in our setup. Its spectrum will depend on the way the horizon is shaped, the thermality of this spectrum is discussed in [72] with the conclusion that the low-frequency spectrum is not altered by dispersive effects. In the case of a sharp interface we are way outside of the hydrodynamic limit and the surface gravity is formally infinite; nonetheless an analytical approximate spectrum going as $1/\omega$ is found.

Even if the Hawking temperature in this kind of setups is typically too low to be observed, in a laboratory one can also access the interior of the horizon. A strategy to obtain experimental evidence of Hawking emission is hence to measure density correlations of fluctuations between the upstream and downstream regions, to find correlations between the modes $u|out$ and $d2|out$. This strategy was presented in [17] and numerically implemented in [18] and is at the basis of the experimental observations of spontaneous Hawking radiation in Bose–Einstein condensates [4, 5, 76].

1.5.2 Black-hole lasers

Although nonlinear dispersion at high frequencies seems not to alter substantially the Hawking effect at low frequencies the situation changes dramatically if also an inner horizon is present, such as the one of the Kerr spacetime (or of charged Reisser–Nordström

black holes). This was first noticed in [77], where it is shown that superluminal dispersion determines the occurrence of dynamical instabilities in black holes displaying an inner horizon, and was then extensively studied in BEC-based analogues [78–83].

This can be realized in our minimal black hole by adding another transition from supersonic to subsonic flow in the downstream region, creating a *white hole horizon*. What changes with respect to the Hawking emission case is that the fully dispersive modes $d1|in$ and $d2|in$ enter in the game since they can be populated with the reflection at the inner horizon, and not just by zero-point fluctuations. We can take the inner downstream region to have the same sound speed as the upstream one, and imagine again a scattering process starting with the mode $u|in$. After the modes $d1|out$ and $d2|out$ are transmitted from the outer horizon they scatter on the inner one and are transmitted to the $u|in$ mode (that is an outgoing mode beyond the inner horizon) and reflected on the $d1|in$ and $d2|in$ modes that go back at the outer horizon, where the exact same scattering happens. Hence the excitations between the two horizons continue to bounce back and forth.

Notice now that at each bounce the energy must be conserved and that negative-norm modes carry here negative energy. Considering for example the scattering of the $d2|in$ mode that comes beck to the outer horizon: to conserve the energy the amplitudes of the ingoing and outgoing modes must be such that

$$-\left|\mathcal{A}_{d2|in}\right|^2 = \left|\mathcal{A}_{u|out}\right|^2 + \left|\mathcal{A}_{d1|out}\right|^2 - \left|\mathcal{A}_{d2|out}\right|^2, \tag{1.94}$$

where the negative-norm modes' amplitudes must enter with a minus sign. This implies that

$$\left|\mathcal{A}_{d2|out}\right|^2 \geq \left|\mathcal{A}_{d2|in}\right|^2. \tag{1.95}$$

This happens also at the inner horizon, so that at each bounce the amplitude of the negative-norm mode increases. This behaviour is the signal of a dynamical instability that can be detected as a complex-frequency eigenmode of the Bogoliubov problem and takes the name of *black-hole laser*.

This instability was looked for experimentally in a cigar-shaped condensate as reported in [84]. The condensate was accelerated by moving a step potential through it by creating a pair of black hole and white hole horizons. An oscillating density modulation was observed to emerge between the two horizons and was attributed to self amplification of the quantum emission of Hawking radiation. Successive analyses of this experiment concluded however that the observed effect is not seeded by quantum fluctuations but is a predictable and deterministic effect triggered by the experimental setup [85] and that the same kind of result can be obtained in a system without interactions [86], being due to a linear interference, and is hence not related to black hole lasing. More recent experiments of the same group however brought new evidence of experimental observation of black hole lasing [87].

Taking a step back we can say that Hawking radiation is caused by the presence of an energetic instability confined in a region of the system, i.e. the inside of the horizon. By adding the inner horizon we are changing the boundary conditions of the problem so

that the energetically unstable modes have *closed orbits*, i.e. they are bound in region of the system and are coupled to the exterior only by positive-norm modes. This results in a dynamical instability for the self-amplification of the bounded mode [79]. This is a pattern that will accompany us throughout the rest of this thesis.

Besides this very general mechanism, another reasons in which this physics is interesting for the following of this work is that this mechanism was shown to be at the basis of the breakdown of a superfluid flow passing through a penetrable barrier [88]; this is an example of how feed-back of information from the analogue gravity perspective to fundamental questions of condensed matter physics, a perspective that we will adopt in Chapter 5.

1.6 Summary: from BECs to curved spacetimes

In this Chapter we introduced the main theoretical tools we will need to study Bose–Einstein condensates, with a particular attention to the elementary linear excitations around a stationary state of the Gross–Pitaevskii equation. We showed how from the Bogoliubov linear problem for these excitations a geometric description of sound propagation through a relativistic *acoustic metric* emerges in the hydrodynamic limit. For non-uniformly moving condensates having regions of supersonic flow, this acoustic metric can have the shape of a black hole metric of general relativity. Even if the solutions of the Einstein equations cannot in general be reproduced in these fluid analogues, interesting toy model acoustic spacetimes can be obtained, sharing the main interesting features of black holes such as horizons and ergoregions.

This gravitational analogy allows the study of field theories in curved spacetimes, also in their quantum aspects thanks to the low temperatures of Bose–Einstein condensates. We explained in detail how the Bogoliubov excitation field is related to the Klein–Gordon field and discussed that the differences between the two can be not a bug but a feature of the gravitational analogue. As a guiding example we reviewed some studies of Hawking radiation in a simple analogue black hole.

In the discussion we introduced two different concepts of instability that will be of capital importance in the following of this Thesis: *energetic* and *dynamical* instability. Energetic instability corresponds to the existence of negative energy modes, while dynamical instability is the presence of exponentially growing zero energy modes. With black hole lasing we saw a first example of the interplay between these two concepts, that we will see at play multiple times throughout this work.

We saw that energetic instabilities are at the basis of Hawking emission in Bose–Einstein condensates, and in the next Chapter we will see how the simultaneous presence of positive and negative energy modes is the fundamental ingredient of superradiant scattering. In closing this Chapter, it is interesting to notice that the amplification (1.95) of a negative-energy mode scattering on an acoustic horizon from the *inside* is based on the interplay between modes of different norm and is a first example of superradiance.

Chapter 2

Superradiance

At the end of the previous Chapter we saw how one can investigate Hawking radiation in analogue models, obtaining new perspectives on the phenomenon. This is related to the fact that the Hawking effect is a *kinematical* effect, that is it only relies on the propagation of fields in a curved geometry and not on the gravitational dynamics of the spacetime.

Another interesting phenomenon of the same kind is black hole superradiance, that is the amplified reflection of radiation scattering on a rotating or charged black hole. Anticipated by a prediction by Zel'dovich regarding the scattering of electromagnetic waves on a rotating conducting cylinder [8, 9] and by an observation by Penrose involving decaying particles around rotating black holes [7], the amplification relies on the *extraction* of energy from the black hole and, differently from Hawking radiation, is a classical effect. When the involved fields are *quantum* the phenomenon becomes a *spontaneous emission* of pairs that has historically been a precursor of Hawking pair production.

Despite being mainly investigated in black hole physics, superradiance is a very general phenomenon relying on the existence of *negative-energy states* that can store the extra energy associated to the amplification. As we saw in the previous chapter, the concept of negative energy is not restricted to relativistic systems, but emerge fairly commonly in quasiparticle descriptions of condensed matter systems.

In presentations of the phenomenon it is often highlighted how this amplification goes hand in hand with dissipation [10, 89], that is provided in black holes by the one-way membrane of the horizon, and is also sometimes claimed that no dissipation results in no amplification [90]. Addressing this point, the role of horizons and, more in general, the essential ingredients for superradiant scattering is one of the main motivation of our analogue gravity approach to this phenomenon.

In the present Chapter we wish to give an introduction to superradiant phenomena in the spirit of the recent review [10], providing a set of examples ranging from black holes to less extreme physical settings. During presentation we try to pinpoint the common features giving rise to the phenomenon and to highlight the main points we will address in the rest of this thesis. After focusing on some guiding example from physical

systems outside of general relativity, we summarize the work by Penrose on energy extraction from rotating black holes with particles. This serves as an introduction to some examples of superradiance in *gravitational* and *acoustic* black holes. Finally we address superradiant instabilities arising from self-amplification of radiation when the boundary conditions of the problem are changed.

2.1 Intro: some general-physics examples

Despite being the most famous and studied example, superradiance in black holes was actually preceded by many occurrences of amplified scattering in other areas of physics. We present here some examples that will also be useful in our analogue gravity approach to superradiance.

2.1.1 The bosonic Klein paradox

As a first and preciously simple example of superradiance we consider, as was first done in [91], a charged relativistic scalar field ϕ in one spatial dimension coupled to a spatially-dependent electrostatic potential $A_0(x)$; it will obey the Klein–Gordon (KG) equation

$$-\left(\frac{1}{c}\partial_t + i\frac{e}{\hbar c}A_0\right)^2\phi + \partial_x^2\phi - \frac{\mu^2 c^2}{\hbar^2}\phi = 0, \tag{2.1}$$

where e is the electric charge of the field, μ its mass and we take the electrostatic potential asymptotically constant with $A_0(x\to-\infty)=0$ and $A_0(x\to+\infty)=\bar{A}_0$.

Consider first the massless case $\mu=0$. We are interested in the stationary scattering problem for a plane wave coming from $y=-\infty$; the solution will be of the form $\phi(t,y)=e^{-i\omega t}\chi(y)$, so that the KG equation becomes (now taking $\hbar=c=1$)

$$\frac{d^2\chi}{dx^2} + (\omega - eA_0)^2\chi = 0, \tag{2.2}$$

with asymptotic solutions

$$\begin{aligned}\chi(y\to-\infty) &= e^{i\omega y} + \mathcal{R}e^{-i\omega y}\\ \chi(y\to+\infty) &= \mathcal{T}e^{ik_{tr}y},\end{aligned} \tag{2.3}$$

with $\mathcal{R}$ and $\mathcal{T}$ reflection and transmission coefficients and where the transmitted wavevector

$$k_{tr} = \omega - eA_0 \tag{2.4}$$

is determined from the dispersion relation $(\omega - e\bar{A}_0)^2 = m^2 + k^2$ by requiring for the group velocity $\partial_k\omega$ to be positive. Notice that the transmitted wavevector is positive for $\omega > e\bar{A}_0$ but negative for $\omega < e\bar{A}_0$.

A relation between the reflection and transmission coefficients can be obtained using the fact that the Wronskian $W(\chi_1,\chi_2) := \chi_1\chi_2' - \chi_1'\chi_2$ of two linearly independent

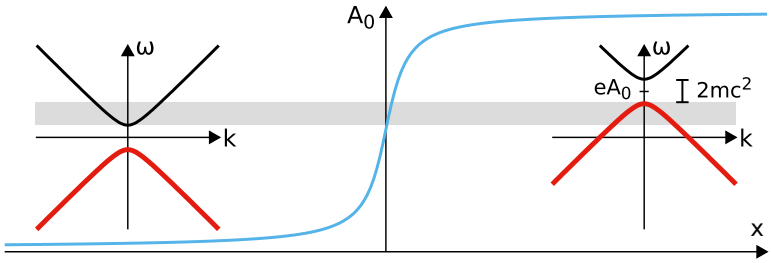

Figure 2.1: Dispersion relations of the massive Klein–Gordon equation minimally coupled to an electrostatic potential. The blue profile is the space-dependent potential considered in the Klein paradox case and the dispersion relations are the ones computed in the two asymptotic regions. Black lines correspond to positive-norm (particle) modes and red lines to negative-norm (antiparticle) modes. The gray region indicates the frequencies for which superradiant scattering is possible.

solutions is a constant because of the absence of first order terms in equation (2.2); the Wronskian can be interpreted as the *electric current* of the charged field. By taking $\chi_1 = \chi$ and $\chi_2 = \chi^*$ and computing W in the two asymptotic regions one obtains

$$1 - |\mathcal{R}|^2 = \frac{\omega - e\bar{A}_0}{\omega}|\mathcal{T}|^2. \tag{2.5}$$

For $\omega > e\bar{A}_0$ one has $|R|^2 < 1$, as in *standard* scattering. A more interesting result is found for

$$\omega < e\bar{A}_0, \tag{2.6}$$

for which the right-hand side becomes negative, hence $|\mathcal{R}|^2 > 1$ and the reflected wave has a larger amplitude than the ingoing one. This is clearly an example of *superradiant scattering*.

This phenomenon can be seen as a paradox if one thinks at the Klein–Gordon equation as describing a single particle, similarly to the Schrödinger equation. With this picture in mind where is the extra energy of the amplification coming from? The paradox is actually easily resolved from the relativistic point of view in which particles can be created and annihilated; as we are going to see now the effect is in fact due to creation of pairs of particles and antiparticles at the electrostatic potential step.

The massive case of equation (2.1) can be treated in a similar way, though the analytical result is slightly less transparent. More understanding of this phenomenon can be obtained from studying a graphical representation of the dispersion relation of the massive scalar field, that we show in Figure 2.1. Notice the presence of a mass gap and that the effect of the electrostatic potential is to shift the dispersion curves vertically.

In the massless case any amount of this vertical shift causes the negative-norm *antiparticle* modes to raise to positive frequencies. It becomes hence apparent that the superradiant condition (2.6) corresponds to the case in which *particle* modes are transmitted to *antiparticle* modes, whose current is opposite-signed. Hence the amplification

is not violating the conservation of energy because the transmitted particles have a *negative energy*, that compensates exactly for amplification.

From the graphical representation it is easy to understand that superradiant scattering in the massive case can occur only if the electrostatic field is strong enough to overcome the mass gap

$$e\bar{A}_0 > 2\mu c^2, \tag{2.7}$$

that is strong enough to create a particle-antiparticle pair. If this condition is met superradiant scattering can occur for

$$\mu < \omega < e\bar{A}_0 - \mu. \tag{2.8}$$

For $e\bar{A}_0 - \mu < \omega < e\bar{A}_0 + \mu$ one instead has total reflection because of the absence of modes for $x \to +\infty$, while for higher frequencies one has, as in the massless case, standard scattering.

Notice that the amplification relies on the bosonic nature of the field. Treating the analogous Dirac equation problem shows that $|\mathcal{R}|$ is always smaller than one. From the quantum perspective the amplified reflection is essentially a stimulated pair production in an external field, with the Pauli exclusion principle limiting fermionic amplification.

This example has been clarified and related to superradiance in [13]. Despite its simplicity the bosonic Klein paradox already has the main ingredients of superradiance and is hence a good guide in more complicated setups. The basic process can be seen to be amplification of radiation by transmission of radiation with the opposite energy, the different physical realization depend on how these negative energy modes become available. In Section 3.2.2 we will see how this physics appears naturally also with (synthetic) vector gauge potentials, that will provide an exact realization of this simple model.

2.1.2 Hydrodynamic tangential discontinuities

Wave amplification has also been predicted in the traditional field of hydrodynamics [92–94]. The phenomenon involves the scattering of acoustic or gravity waves at a *tangential discontinuity* of a compressible fluid, that is a surface at which some fluid quantities are discontinuous and through which there is no mass flux. As discussed in Landau's book [95] (chapter 84) this implies continuity of the pressure at the surface of discontinuity.

In Problem 2 of the same chapter the scattering of sound waves at such a discontinuity is studied. In particular an homogeneous compressible fluid is considered, with medium 1 (for $z > 0$) having a velocity v in the x direction and medium 2 (for $z < 0$) being at rest. A sound wave of wavevector $\mathbf{k}$, forming an incidence angle θ with the z axis and having an angle ϕ between its projection $\mathbf{q}$ on the xy plane and the x axis. The wavevector components are hence

$$k_x = q\cos\phi\,, \qquad k_y = q\sin\phi\,, \qquad k_z = \frac{\omega}{c_s}\cos\theta, \tag{2.9}$$

where $0 < \theta < \pi/2$.

In medium 2 the pressure variation wave will have the form

$$\delta p_2 = e^{i(k_x x + k_y y - \omega t)} \left(e^{i k_z z} + \mathcal{R} e^{-i k_z z} \right), \tag{2.10}$$

with $\mathcal{R}$ amplitude of the reflected wave. In medium 1 the refracted wave will have the shape

$$\delta p_1 = \mathcal{T} e^{i(k_x x + k_y y + \widetilde{k}_z z - \omega t)}, \tag{2.11}$$

where $\widetilde{k}_z$ is determined from the Doppler-shifted dispersion relation (analogous to the Klein–Gordon one (1.86))

$$(\omega - v k_x)^2 = c_s^2 (k_x^2 + k_y^2 + \widetilde{k}_z^2). \tag{2.12}$$

We can now impose the continuity for the pressure $\delta p_1(z = 0) = \delta p_2(z = 0)$ and for the vertical displacement of the discontinuity $\zeta_1 = \zeta_2$. This gives a solution for the waves amplitudes

$$\mathcal{R} = \frac{(\omega - v k_x)^2/\widetilde{k}_z - \omega^2/k_z}{(\omega - v k_x)^2/\widetilde{k}_z + \omega^2/k_z}, \qquad \mathcal{T} = \frac{2(\omega - v k_x)^2/\widetilde{k}_z}{(\omega - v k_x)^2/\widetilde{k}_z + \omega^2/k_z}, \tag{2.13}$$

where the sign of $\widetilde{k}_z$ must be chosen so that the group velocity of the refracted wave is directed away from the discontinuity

$$\frac{\partial \omega}{\partial \widetilde{k}_z} = c_s^2 \frac{\widetilde{k}_z}{(\omega - v k_x)} > 0. \tag{2.14}$$

Since the transmitted wavenumber is given by

$$\widetilde{k}_z^2 = \left(\frac{\omega}{c_s} \right)^2 \left[\left(1 - \frac{v}{c_s} \sin\theta \cos\phi \right)^2 - \sin^2\theta \right], \tag{2.15}$$

one can distinguish three kinds of reflection:

1. For $(v/c_s)\cos\phi < \operatorname{cosec}\theta - 1$ the transmitted momentum is real and $\omega - k_x > 0$, so that $\widetilde{k}_z > 0$ and from (2.13) we can see that $|\mathcal{R}| < 1$ and one has *ordinary* scattering in which the reflected wave is weaker than the incident one.

2. For $\operatorname{cosec}\theta - 1 < (v/c_s)\cos\phi < \operatorname{cosec}\theta + 1$ instead $\widetilde{k}_z$ is imaginary and what happens is total internal reflection with $|R| = 1$.

3. The most interesting case occurs however for $(v/c_s)\cos\phi > \operatorname{cosec}\theta + 1$, that can occur only for

$$v > 2c_s, \tag{2.16}$$

for which $\widetilde{k}_z$ is again real but negative. Then equation (2.13) predicts $|\mathcal{R}| > 1$, that is *superradiant scattering*.

This phenomenon bears many resemblances to the bosonic Klein scattering and, as we will see, to the scattering occurring at an ergosurface: an interpretation in terms of transmission of negative-energy sound waves was for example given in [94]. Notice however that, as underlined by Landau, this amplification mechanism comes together with the surface instabilities of hydrodynamic tangential discontinuities, such as the Kelvin–Helmholtz instability. Superradiant scattering in this context can hence be hidden exponentially increasing modes localized on the surface.

The configuration we propose in Chapter 3 for Bose–Einstein condensates subjected to synthetic vector potentials, does not have such surface instabilities, so that amplified scattering (and its quantum counterpart) is the only relevant mechanism. Surface instabilities and their relation to superradiant phenomena are instead studied in a different setup involving quantized vortices in Chapter 6.

2.1.3 Superradiance, dissipation and rotation

Besides the bosonic Klein paradox, the first example of superradiant scattering was provided by Zel'dovich in 1971 [8, 9]. He showed that a rotating cylinder made of absorbing material can amplify some modes of scalar or electromagnetic radiation. Leaving the detailed electromagnetic calculation aside (that can be found for example in [89]), Zel'dovich gives a simple general argument to show the emergence of superradiance.

Consider first a scalar field in an absorbing medium moving at velocity V along x. In the reference frame where the medium is at rest the KG equation is

$$\Box'\Phi - \mu^2\Phi + a\partial'_t\Phi = 0, \tag{2.17}$$

where a is the absorptivity of the medium. By changing to the frame in which the medium is moving the first two terms of the equation remain the same because of Lorentz invariance, while the absorption term becomes

$$\Box\Phi - \mu^2\Phi + a\gamma\left(\partial_t\Phi + V\partial_x\Phi\right) = 0, \tag{2.18}$$

where $\gamma = (1 - V^2)^{-1/2}$. By taking the field of the plane wave shape along the velocity direction $\Phi = \varphi(y, z)e^{-i\omega t + ik_x x}$, the equation becomes

$$\Box\varphi - k_x^2\phi - \mu^2\varphi - ia\gamma\left(\omega - Vk_x\right)\varphi = 0, \tag{2.19}$$

from which one can see that if

$$\omega < Vk_x \tag{2.20}$$

the absorption term changes sign and works hence as an *amplifier*. The field however has a linear dispersion relation $\omega = \mathbf{k}^2$, so that for the Klein–Gordon field, or for electromagnetic waves in a vacuum, this condition requires for V to be larger than the speed of light and is hence impossible to satisfy.

More in general the condition to obtain amplification is that the velocity of the medium from which the energy is drawn must exceed the phase velocity of the field.

Even if in a *plane geometry* in a vacuum this is impossible, things change if rotating configurations are considered.

By taking a cylinder of absorbing medium rotating with angular velocity Ω we can decompose the field as $\Phi = f(r)e^{-i\omega t+im\phi}$. Analogously to equation (2.19), the Klein–Gordon equation in the radial direction becomes

$$\Box_r \Phi - \frac{m^2}{r^2} - \mu^2 \Phi - ia\gamma\left(\omega - m\Omega\right)\Phi = 0, \tag{2.21}$$

where $\Box_r$ is the radial part of the d'Alembertian in polar coordinates. This time the absorption term changes sign for

$$\omega < m\Omega, \tag{2.22}$$

that is in principle possible to satisfy without the need of superluminal velocities. This reflects the fact that the angular phase velocity of the fluctuations is ω/m, that can be exceeded for large enough multipole momenta.

The observation of this phenomenon in a laboratory however requires high rotation frequencies for the absorbing object; moreover the centrifugal terms of the radial equation may make it difficult for the waves to arrive near the rotating object. A significant step towards the experimental feasibility was made only very recently in [96], where a scheme was proposed to observe Zel'dovich amplified scattering of electromagnetic waves by bringing radiation directly near the rotating object. An analogue version of this phenomenon has also been considered in fluids of light [97].

2.1.4 Other radiation-emission processes

Consider an object with internal structure, so that it can emit and absorb photons, moving in some medium. In the case of an emission of a photon the object's energy in the medium frame will change from E to $E' = E - \hbar\omega$ and its momentum from $\mathbf{P}$ to $\mathbf{P}' = \mathbf{P} - \hbar\mathbf{k}$. In the reference frame of the object its rest energy will hence go from $M = \gamma(E - \mathbf{v}\cdot\mathbf{P})$ to $M' = \gamma'(E' - \mathbf{v}'\cdot\mathbf{P}')$, where $\gamma = (1 - v^2/c^2)$. For a very massive object the recoil due to the emission will be very small and the change in rest energy can be approximated to

$$M' - M = -\gamma\hbar(\omega - \mathbf{v}\cdot\mathbf{k}) + \mathcal{O}(\mathbf{v}' - \mathbf{v}). \tag{2.23}$$

In a vacuum the dispersion relation of the photon is $\omega = c|\mathbf{k}|$ and hence the rest energy variation will always be negative when a photon is emitted. This is called ordinary Doppler effect [98,99] because the relation between the frequency of the internal transition and the one of the emitted photon is the usual Doppler shift $\omega_0 = \gamma(\omega - \mathbf{v}\cdot\mathbf{k})$.

A more peculiar process takes place if the object is in a dielectric medium of refractive index n and is moving with velocity $v > c/n$. In this case for a photon emitted with respect to $\mathbf{v}$ at an angle such that $\cos\theta > c/(nv)$ the right-hand side of (2.23) changes sign and the emission can occur together with an excitation of the object; this is called

the *anomalous Doppler effect*, happening when the following *Ginzburg–Frank condition* is satisfied

$$\omega - \mathbf{v} \cdot \mathbf{k} < 0. \tag{2.24}$$

Energetically this is possible because the emitted photon energy is negative in the object's frame, that is it *slows down* the medium motion. An analogue realization of the anomalous Doppler effect was considered in [100].

This process was linked to superradiance in [89], where it was shown that the anomalous Doppler effect implies the possibility of superradiance, that is radiation satisying the Ginzburg–Frank condition is superradiantly amplified by the object with internal structure, at the expense of its internal energy.

Another effect sometimes related to superradiance is the *Cherenkov effect*, in which a point charge moving in a dielectric with a velocity greater than the speed of light in that medium emits electromagnetic radiation. The occurrence of this emission can be seen from equation (2.23) with $M' - M = 0$, since a point charge does not have the internal structure to change its rest energy. In a dielectric $\omega = ck/n(\omega)$, where $n(\omega)$ is the refractive index, so that photons will be emitted only with an angle

$$\cos\theta_c = \frac{c/n(\omega)}{v}, \tag{2.25}$$

forming the so-called Cherenkov cone. The acoustic equivalent of this phenomenon is the emission of a Mach cone when a *small* defect moves supersonically inside a fluid.

This phenomenon is however not related to superradiance, at least not at the linear level of equation (2.23), since in the charge's rest frame the emitted radiation carries zero energy and the charge has no internal structure in which to *store* (positive or negative) energy. The emission on a cone can be in fact understood from an $\omega = 0$ cut of the Doppler-shifted dispersion relation dispersion relation (1.86), as was done for example for Bose–Einstein condensates in [101].

2.2 A general approach to superradiance

We said that superradiance is a very general phenomenon and as such it can be treated with a very general approach, applicable for example to fields in black hole spacetimes as well as to the electromagnetic waves of the Zel'dovich effect, as explained in [90].

Different physical systems share the fact that the equations describing the propagation of the field of interest can be put, with opportune field decompositions and change of coordinates, in a Schrödinger-like shape

$$\frac{d^2}{d\xi^2}\psi(\xi) + V_{\text{eff}}(\xi)\ \psi(\xi) = 0, \tag{2.26}$$

where V_{eff} is an effective potential that depends on the physical system and on the characteristics of the field (e.g. frequency or multipole momenta). The coordinate

$\xi \in (-\infty, +\infty)$ can be chosen so that the effective potential has constant values in the asymptotic regions, where we can expand ψ in plane waves

$$\psi(\xi) \to \begin{cases} \mathcal{I}e^{ik_{-\infty}\xi} + \mathcal{R}e^{-ik_{-\infty}\xi} & \text{as } \xi \to -\infty \\ \mathcal{T}e^{ik_{+\infty}\xi} + \mathcal{O}e^{-ik_{+\infty}\xi} & \text{as } \xi \to +\infty \end{cases}, \tag{2.27}$$

where $k^2_{\pm\infty} = V_{\text{eff}}(\pm\infty)$. The letters indicating the waves amplitudes explain the physical process we have in mind: an incident wave $\mathcal{I}$ comes from $-\infty$ and scatters on the potential by which it is partially reflected ($\mathcal{R}$) and partially transmitted ($\mathcal{T}$), while the wave of amplitude $\mathcal{O}$ is included to allow the possibility of some reflection of the transmitted wave. The association between the sign of the momentum and the *direction* of the wave has to be made according to the sign of the group velocity, as we did for the bosonic Klein paradox in Section 2.1.1.

As we did in that case, we can obtain a relation between the amplitude of these four waves from the conservation of the Wronskian between a solution and its complex conjugate $W(\psi, \psi^*) = \psi \frac{d}{d\xi}\psi^* - \psi^* \frac{d}{d\xi}\psi$. This constant value takes the asymptotic expressions $W(-\infty) = 2ik_{-\infty}(|\mathcal{I}|^2 - |\mathcal{R}|^2)$ and $W(+\infty) = 2ik_{+\infty}(|\mathcal{T}|^2 - |\mathcal{O}|^2)$, giving the equality

$$|\mathcal{R}|^2 = |\mathcal{I}|^2 - \frac{k_{+\infty}}{k_{-\infty}}\,(|\mathcal{T}|^2 - |\mathcal{O}|^2). \tag{2.28}$$

Let us consider the situation in which no wave *comes back* from $+\infty$, that is $\mathcal{O} = 0$, as for the bosonic Klein scattering. The result depends on the signs of the momenta of the asymptotic expansions: for $k_{+\infty}/k_{-\infty} > 0$ we have $|\mathcal{R}|^2 < |\mathcal{I}|^2$, as expected in *ordinary scattering*, while for $k_{+\infty}/k_{-\infty} < 0$ instead $|\mathcal{R}|^2 > |\mathcal{I}|^2$, that is superradiant scattering.

Consider now the case in which there is reflection for $\xi \to +\infty$, that is $\mathcal{O} \neq 0$. If a total reflection of the transmitted wave occurs than $|\mathcal{T}|^2 = |\mathcal{O}|^2$, and equation (2.28) tells us that $|\mathcal{R}|^2 = |\mathcal{I}|^2$, so that one is brought to conclude that nothing exciting happens and the field is simply totally reflected, as concluded in [90]. Actually, the situation is more subtle, as we discuss in the following, and raises the fundamental question on the role of boundary conditions for superradiant scattering.

2.3 The Penrose process

Let us now move to black hole physics and consider the first discovered example of energy extraction from black holes. Roger Penrose [7] showed that it is possible for a particle to enter the ergoregion of a Kerr black hole and decay into two photons, of which one is able to escape the ergoregion with an energy larger than the one of the incoming one. This is possible while conserving energy because the other photon, that then falls inside the horizon, turns out to have a negative energy (with respect to an observer at infinity), thus lowering the energy and angular momentum of the black hole.

We start by considering the motion of particles in the Kerr black hole spacetime (Section 1.3.2), that is on the behaviour of timelike and null geodesics. A comprehensive

exposition can be found in [55], here we focus only on some basic properties of the geodesics in the equatorial plane.

Given a spacetime described by the line element $ds^2 = g_{\mu\nu}dx^\mu dx^\nu$, the equations describing geodesics can be obtained from the Lagrangian

$$2\mathscr{L} = g_{\mu\nu}\frac{dx^\mu}{d\tau}\frac{dx^\nu}{d\tau}, \tag{2.29}$$

with τ an affine parameter along the geodesics. For the equatorial plane in the Kerr spacetime the Lagrangian is

$$2\mathscr{L} = \left(1 - \frac{2M}{r}\right)\dot{t} + \frac{4Ma}{r}\dot{t}\dot{\varphi} - \frac{r^2}{\Delta}\dot{r}^2 - \left[(r^2+a^2) + \frac{2Ma^2}{r}\right]\dot{\varphi}^2, \tag{2.30}$$

(dots indicate differentiation with respect to τ) whose independence from t and φ assures the conservation of the canonical momenta

$$p_t = \frac{\partial\mathscr{L}}{\partial\dot{t}} = \left(1 - \frac{2M}{r}\right)\dot{t} + \frac{2Ma}{r}\dot{\varphi} = const = E \tag{2.31}$$

$$p_\varphi = \frac{2Ma}{r}\dot{t} - \left[r^2 + a^2 + \frac{2Ma^2}{r}\right]\dot{\varphi} = const = -L \tag{2.32}$$

along the geodesics. These constant values are identified with the energy and the angular momentum.

The Hamiltonian turns out to be equal to the Lagrangian (this is due to the fact that $\mathscr{L}$ is only composed by *kinetic energy*) and, being independent on t, is a constant

$$2\mathscr{H} = E\dot{t} - L\dot{\varphi} - \frac{r^2}{\Delta}\dot{r}^2 = const = \delta_1. \tag{2.33}$$

Considering equation (2.29) one can see that $\delta_1 = 0$ for null geodesics and can be instead be chosen as $\delta_1 = 1$ for timelike ones by rescaling the affine parameter. This choice for massive particles implies that E has to be interpreted as the energy per unit mass.

Using the canonical momenta conservation and the constancy of the Hamiltonian one can obtain the equation governing the radial coordinate of the equatorial geodesics

$$r^2\dot{r}^2 = r^2E^2 + \frac{2M}{r}(aE - L)^2 + (a^2E^2 - L^2) - \delta_1\Delta. \tag{2.34}$$

To understand how energy extraction can be possible let us discuss the energy of particles at rest. From (2.34) with $\dot{r} = 0$ one obtains a second order equation in E with solutions

$$E = \frac{2MaL \pm \sqrt{\Delta}\sqrt{r^2L^2 + \delta_1 r[r(r^2+a^2) + 2Ma^2]}}{r(r^2+a^2) + 2Ma^2}, \tag{2.35}$$

where, since a particle at rest at infinity must have $E = 1$, we must choose the plus sign.

If we look instead for particles with a negative energy we must hence have $L < 0$ and that the first term in the numerator of (2.35) is in modulus larger than the second. This condition is equivalent to asking that

$$r - 2M < -\frac{r\Delta}{L^2}\delta_1, \tag{2.36}$$

that for massless particles requires $r < 2M$, so that we can conclude that negative-energies are only possible for counter-rotating particles inside the ergoregion.

Let us now turn to the Penrose process: imagine a particle starting at rest at infinity (so that $E^{(0)} = 1$) and arriving at a turning point ($\dot{r} = 0$) of its geodesic inside the ergoregion, where it decays into two photons. From equation (2.34) one obtains expressions for the angular momentum of the initial particle $L^{(0)}$ and of the two photons $L^{(1),(2)}$

$$L^{(0)} = \frac{-2Ma + \sqrt{2Mr\Delta}}{r - 2M} \tag{2.37}$$

$$L^{(1),(2)} = \frac{-2Ma \pm \sqrt{\Delta}}{r - 2M} E^{(1),(2)}. \tag{2.38}$$

Imposing now the conservation of energy $E^{(1)} + E^{(2)} = 1$ and angular momentum $L^{(1)} + L^{(2)} = L^{(0)}$ one obtains the energies of the two photons

$$E^{(1),(2)} = \frac{1}{2}\left(1 \pm \sqrt{\frac{2M}{r}}\right), \tag{2.39}$$

so that for $r < 2M$ (inside the ergoregion) one photon has a negative energy, while the other one has an energy greater than one, that is greater than the one of the incoming particle.

It is possible to show that the negative-energy photon is doomed to fall inside the horizon, causing a decrease of its mass and angular momentum, while the other one can exit the ergoregion, thus *extracting energy from the black hole.* The extracted energy is equal to minus the energy of the negative-energy photon and is hence larger when the splitting process happens at smaller radii, with the maximum value obtained when it occurs at the horizon r_+.

Notice that, as discussed in [10], while in the full Kerr spacetime the geodesic of the negative-energy photon must fall inside the horizon, energy extraction can be obtained also if the spacetime does not have an horizon; for examples in *ergostars*, that show an ergoregion without an horizon. The negative-energy particle is however necessarily confined inside the ergoregion because we saw that there are only positive-energy particles outside of it. The subsequent evolution of the process depends however on the details of the spacetime. This fact is related, as we will see, to the role of horizons (and more in general dissipation) for superradiance.

2.4 Superradiant scattering in black holes

Black hole superradiance is sometimes called *the Penrose process for waves* since it relies on the presence of negative energy modes of the field around the horizon to which the waves coming from infinity can transmit while being amplified in the reflection. Differently from the decay of a particle into photons, here the mechanism can be seen as a wave coming from infinity that, in the reflection, triggers the creation of a negative-energy wave going towards the horizon and of another one with an opposite (positive) energy being reflected together with the incoming wave that is responsible for the amplification. Superradiance can hence be seen as a *stimulated* version of the Penrose process.

Since our main focus is analogue gravity, we only focus on bosonic (zero spin) fields; for a complete description of higher-spin cases see [10]. Notice however that the bosonic nature of the field is essential to have amplified scattering. Intuitively speaking superradiance can be seen as the production of pairs of *quanta* of the field with opposite energies, with the amplification being due to multiple quanta being emitted in the *reflected mode*; for fermions Pauli exclusion principle forbids the production of many quanta in the same mode.

Superradiant scattering is a *classical* effect since it emerges from the study of a classical scalar field in a curved spacetime. There is however a quantum analog of the effect that consists in particle creation. The possibility was put forward by Zel'dovich [9] in his work on amplification of electromagnetic waves and was then predicted with the quantization of a scalar field in the Kerr spacetime [102,103]; these worked as precursors of the derivation of Hawking radiation. As for the Penrose process, superradiance can be seen as a stimulated version of this effect occurring at the classical level. We will investigate pair production associated to superradiance in an analogue configuration in Section 3.3.

In this Section we are going to show two examples of superradiant scattering in black holes. We first focus on rotating black holes and, instead of focusing on the rather complex mathematics of the Kerr spacetime, we present a calculation predicting superradiance in the vortex acoustic geometry. This provides an explicit example of the general procedure of Section 2.2, that we complement with an interpretation of the phenomenon in terms of dispersion relations, a tool that we are going to widely use in the rest of this Thesis. We then present superradiant scattering of charged radiation in a Reisser–Nordström (static and charged) black hole, that is essentially the occurrence of the bosonic Klein paradox in a black hole context.

2.4.1 Superradiance in rotating black holes: the vortex geometry

Superradiance in the Kerr black hole was anticipated by Zel'dovich [8,9] and worked out by Starobinskii [102, 104] for a scalar field. This work is based on the (surprising) separability of the equation for a scalar field in the Kerr geometry and was later expanded higher-spin fields by Teukolsky [105, 106]. For full references and discussion see [10].

Given our focus on analogue models of black holes, instead of reviewing the calculation for a scalar field in the Kerr spacetime we directly present the analogous one for sound in the vortex geometry of Section 1.3.3, that shares with the (equatorial slice of) Kerr black hole the main features important for superradiance.

Amplified scattering in gravitational analogues with the vortex geometry has been extensively studied theoretically [107–113], and was recently experimentally observed using gravity waves on water [12]. The calculation we now present was originally worked out in [107].

Consider the Klein–Gordon equation (1.59) in the $(2+1)$-dimensional vortex metric (1.69). Because of the rotational symmetry we can take a stationary and axisymmetric solution

$$\phi(t,r,\theta) = e^{-i\omega t}e^{im\theta}R(r), \tag{2.40}$$

where $\omega, m \in \mathbb{R}$. The Klein–Gordon equation for the radial function $R(r)$ turns out to be

$$\begin{aligned}\frac{1}{r}\left(1-\frac{A^2}{c_s^2r^2}\right)\frac{d}{dr}\left[r\left(1-\frac{A^2}{c_s^2r^2}\right)\frac{d}{dr}\right]R(r)+\\ +\left[\omega^2-\frac{2Bm\omega}{c_sr^2}-\frac{m^2}{r^2}\left(1-\frac{A^2+B^2}{c_s^2r^2}\right)\right]R(r)=0.\end{aligned} \tag{2.41}$$

Introducing the *tortoise coordinate* r^*

$$dr_* = \left(1-\frac{A^2}{c_s^2r^2}\right)^{-1}dr \implies r_* = r+\frac{|A|}{2c_s}\log\left|\frac{r-|A|/c_s}{r+|A|/c_s}\right|, \tag{2.42}$$

whose domain is the whole real axis, the horizon is pushed to $r_* \to -\infty$. It is also convenient to rewrite the radial problem in terms of $G(r_*) \coloneqq r^{1/2}R(r)$, so that equation (2.41) becomes

$$\frac{d^2G(r^*)}{dr^{*2}}+\left[Q(r)+\frac{1}{4r^2}\left(1-\frac{A^2}{c_s^2r^2}\right)^2-\frac{A^2}{c_s^2r^4}\left(1-\frac{A^2}{c_s^2r^2}\right)\right]G(r^*)=0, \tag{2.43}$$

where we defined

$$Q(r) \coloneqq \frac{1}{r^4}\left[(A^2+B^2-c_s^2r^2)m^2-2Bm\omega r^2+\omega^2r^4\right]. \tag{2.44}$$

This equation has a Schrödinger-like shape (2.26), so that we can use the approach of Section 2.2. In the asymptotic region $r^* \to +\infty$ the effective potential of equation (2.43) simply becomes

$$V_{\text{eff}}(r_* \to \infty) = \omega^2. \tag{2.45}$$

At the horizon instead we can substitute $1-A^2/(c_s^2r^2)=0$ and obtain

$$V_{\text{eff}}(r_* \to -\infty) = (\omega - m\Omega_H)^2, \tag{2.46}$$

where we defined the angular velocity of the horizon

$$\Omega_H := \frac{c_s B}{A^2}. \tag{2.47}$$

Imposing ingoing boundary conditions at the horizon as discussed in the previous section, relation (2.28) becomes

$$|\mathcal{R}|^2 = |\mathcal{I}|^2 - \frac{1}{\omega}\left(\omega - m\frac{c_s B}{A^2}\right)|\mathcal{T}|^2, \tag{2.48}$$

so that for

$$\omega < m\Omega_H \tag{2.49}$$

superradiance occurs.

It is interesting to notice that this condition for superradiant scattering is analogous to the Zel'dovich condition (2.22) and is of the same shape of condition (2.8) for the bosonic Klein paradox. In particular the radial field $G(r^*)$ expressed in function of the tortoise coordinate can be thought as a massless charged scalar field in a space-varying and asymptotically constant electrostatic potential, with asymptotic values $\frac{e}{\hbar}A(r_* \to +\infty) = 0$ and $\frac{e}{\hbar}A(r_* \to -\infty) = m\Omega_H$ given by the asymptotic expressions of the effective potential (2.45) and (2.46).

We can hence interpret the phenomenon, as we did for the bosonic Klein paradox, in terms of positive and negative energy modes and to do this it is instructive to look at this problem from the point of view of the dispersion relation of the field, as we will often do in the rest of this thesis. To this end suppose that the space variation of the vortex velocity is slow enough that it makes sense to consider, at each $\bar{r}$, the dispersion relation of a uniform system having a constant flow $\mathbf{v}(\bar{r})$.

An example is shown in Figure 2.2, where the first graph shows the radial dispersion relation at fixed azimuthal number $m = 3$ at $r \to \infty$ and the second graph the ones at radii closer to 0. The black curves are the positive-norm branches, the red ones the negative-norm ones, the black arrows show the direction of increasing r and the horizontal dotted line is the upper limit (2.49) on frequency to have amplification. The solid lines in the right panel correspond to the dispersion relations at the ergosurface and horizon radii.

One can see that the ergoregion corresponds to the radius at which the negative-norm branch raises to positive frequencies while the horizon to the limit at which there stops to be modes with positive group velocities. Also, beyond the horizon, instead of having just one ingoing mode per frequency, negative and positive norm modes coexist at the same frequency. Notice how the frequency limit for superradiance (dashed blue line) corresponds to the value above which negative-norm modes are only available inside the horizon, so that amplified reflection happens when it is possible to transmit, as in the Klein paradox case, only to negative-norm modes, that is for $\omega < \Omega_H$, and not if also positive-norm modes are available for partial transmission.

It is hence evident that the role of the horizon is to impose a boundary condition and this is why in conditions (2.49) and (2.54) the values of the angular velocity and of

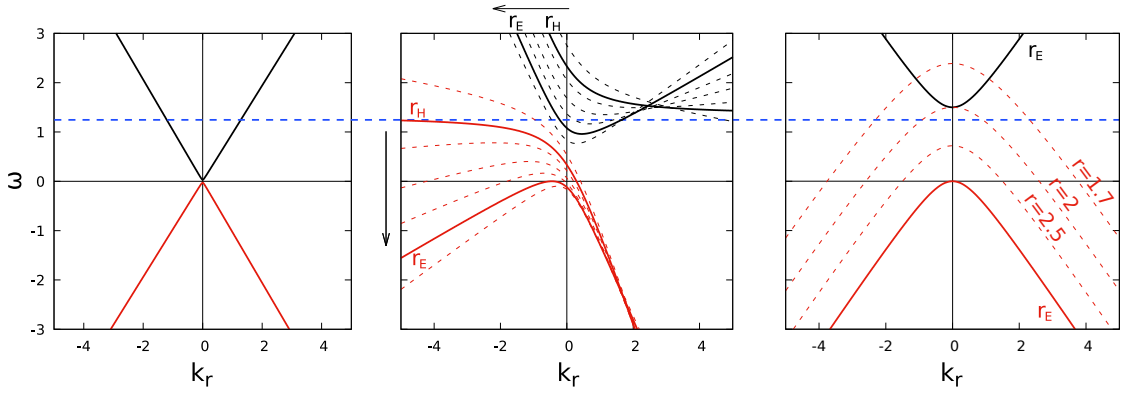

Figure 2.2: Left and central plots: dispersion relations of the Klein–Gordon equation for $A = 3c_s$, $B = 4c_s$ and $m = 3$ and different values of the radius, as if we were considering a uniform region with the velocity at that point. The left graph shows the asymptotic dispersion relation and the central graph the ones at radii around the horizon and the ergosurface with the black arrows indicating the direction of increasing r. Black (red) curves indicate positive (negative) norm modes. The solid lines in the central plot are the dispersion relations at the ergosurface and at the horizon. The horizontal blue dashed line indicates the upper bound (2.49) for superradiant scattering. Right plot: same kind of plot for the case with no radial flow $A = 0$. In this case there is no horizon but only an ergosurface at $r_E = 4$. For smaller values of the radius one can see that negative-energy are available, allowing amplified reflection also for frequencies higher than the blue dashed line.

the electrostatic potential at the horizon appear. If no horizon was present, for example in a vortex without a radial flow, according to this reasoning with dispersion relations, superradiance could be also possible for higher frequencies. This can be understood from the third plot of Figure 2.2, where the Klein–Gordon dispersion relation is plotted for the case with no radial flow. The horizon is now not present and one can see that for radii inside the ergoregion amplified reflection by transmission *only* to negative-energy modes is also possible for higher frequencies.

This last suggestion is again related to the fundamental question on the role of boundary conditions in superradiance and to the dynamical instabilities related to superradiance that we discuss in the next section.

As a last comment, notice that the transmission to multiple modes of different norms associated to no amplification resembles the scattering we described when discussing Hawking radiation in Section 1.5. This gives the hint that amplified scattering from the exterior of an horizon is not possible because of this mode structure. Remember however that superradiant scattering from the interior of the horizon is possible with the Bogoliubov superluminal dispersion for negative-energy modes. This is because in that case the ingoing negative-norm mode can only transmit to positive-energy modes, giving rise to a kind of *reverse superradiance* in which the negative energy is amplified.

2.4.2 Superradiance in static charged black holes

Superradiance can occur in black holes without rotation when the black hole is charged. Asymptotically flat and static black holes with a charge are described by the Reisser–Nordström solution of Einstein equations, whose line element has a simple form analogous to the Schwarzschild one

$$ds^2 = -f dt^2 + f^{-1} dr^2 + r^2 d\theta^2 + r^2 \sin^2\theta d\varphi^2, \tag{2.50}$$

but with

$$f(r) = 1 - \frac{2M}{r} + \frac{Q^2}{r^2} \tag{2.51}$$

and a background vector potential $A_\mu = (Q/r, 0, 0, 0)$, with M the mass of the black hole and Q its electric charge. This spacetime shows an event horizon at $r_+ = M + \sqrt{M^2 - Q^2}$ (and also an inner horizon at $r_- = M - \sqrt{M^2 - Q^2}$, analogous to the one of the Kerr spacetime we saw in Section 1.3.2).

Consider now a massless charged scalar field of charge q propagating in this metric. Its evolution is described by a Klein–Gordon equation in a curved spacetime with the addition of the minimal coupling to the electrostatic potential. Separating the different frequency ω and angular momentum l components of the charged field, the radial equation has the general Schrödinger-like shape (2.26) with the effective potential

$$V_{\text{eff}}(r) = \left(\omega - \frac{qQ}{r}\right)^2 - f(r)\left(\frac{l(l+1)}{r^2} + \frac{f'(r)}{r}\right). \tag{2.52}$$

The second term of this potential is due do the gravitational background, while in the first we can recognize the one due to the electrostatic coupling, as in the case of the bosonic Klein scattering (2.2). With the change of coordinates defined by $d\xi = -f^{-1}(r)\ dr$ the interval $r \in [r_+, \infty)$ is mapped to $\xi \in (-\infty, \infty)$, thus obtaining the general case of Section 2.2.

As discussed in [114, 115], the horizon (now at $\xi \to +\infty$) can be taken as a one-way membrane[1] so that no wave is coming back from the horizon and we can set $\mathcal{O} = 0$ in relation (2.28), that here becomes

$$|\mathcal{R}|^2 = |\mathcal{I}|^2 - \frac{\omega - qQ/r_+}{\omega}\,|\mathcal{T}|^2, \tag{2.53}$$

from which one can see that for

$$\omega < \frac{qQ}{r_+} \tag{2.54}$$

superradiance occurs.

It is interesting to notice the similarity with the result (2.5) we obtained for the Klein scattering, with the electrostatic field $\bar{A}_0$ here substituted by the value of the

[1] We will show in Section 4.3 that this does not seem to be a general property of horizons and depends instead on the details of the spacetime.

electrostatic field at the horizon. It seems hence that the nature of the phenomenon is the same in the two cases, and what gravity adds in the Reisser–Nordström case is *just* an open boundary condition provided by the horizon so that the effect can occur in a circular geometry. This is different from the rotating black hole case in which no charge degree of freedom is necessary and gravity also provides the negative-energy modes inside the ergoregion. In fact the Reisser–Nordström black hole has no ergoregion, but is surrounded by a region where the electrostatic potential is strong enough to make antiparticle modes available.

2.5 Superradiant instabilities

Superradiant amplification of radiation may be the source of dynamical instabilities if the geometry of the system is such that the amplification process happens in a reiterated way, for example if the amplified radiation is in some way amplified again.

A possibility is a fission-like process in which the radiation amplified by a rotating black hole is then further amplified by other rotating black holes in a cascading instability; this kind of process was however quantitatively excluded because the black hole cluster should occupy a volume smaller than its Schwarzschild radius [10, 116].

We are more interested in dynamical instabilities involving a single black hole (more correctly a single ergoregion). We know that rotating black holes display superradiant scattering that can be seen as due to an *energetic instability*. We also saw when discussing black hole lasers that changing the boundary conditions in an energetically unstable system can lead to dynamical instabilities given by the *trapping* and self amplification of negative-energy modes. Actually, the same can also happen with trapping of the positive-energy amplified modes. We can say that dynamically stable superradiant scattering occurs because the negative energy modes are *absorbed* by the horizon and the amplified positive-energy ones radiate away asymptotically. Here we discuss two cases in which one of these two conditions is not satisfied.

As we said in Section 2.2, the approach exploiting the conservation of the Wronskian seems to suggest that nothing particular happens with such a change of boundary conditions. This conclusion is however limited by the fact that we are restricting to stationary processes and real frequencies. These changes of boundary conditions lead instead to complex-frequency modes, such as those we discussed in the black hole case.

We will give here a qualitative exposition of superradiant instabilities in black holes, addressing the concepts we will need for the following of the work and referring to Section 5 of the review [10] for a full presentation.

2.5.1 Black hole bombs

A first possibility is that the radiation that is superradiantly amplified is fed back to the black hole by some reflecting boundary condition outside of the ergoregion, let us say by a mirror. In this case the positive-energy radiation trapped outside of the ergoregion grows exponentially, and with it its pressure on the mirror, that will at some

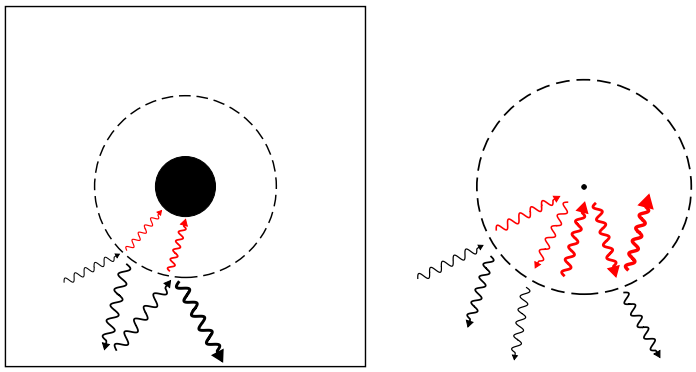

Figure 2.3: Schematic representation of superradiant instabilities in rotating spacetimes. On the left the black hole bomb mechanism, in which radiation on the outside of the ergoregion is unstable because of repeated amplification. On the left the ergoregion instability in which the negative-energy radiation is trapped inside the ergoregion because of the absence of the horizon providing a dissipation mechanism.

point *explode*. For this reason this kind of instability is called a *black hole bomb* [117]. This instability process is sketched on the left of Figure 2.3.

As explained in [10], the instability of rotating black holes in confining geometries can be understood in very general terms by considering a *small* absorber or amplifier in a confining box. The box supports stationary normal modes, that with some absorption become *quasinormal*, that is acquire a small imaginary part of the frequency and decay in time.

Considering the scattering of a wave with an initial amplitude A_0, after N interactions with the absorber its amplitude will be $A = A_0(1 - |a|^2)^N \sim A_0(1 - N\,|a|^2)$, with a the *small* absorption probability. In a time t the wave will interact $N = t/r_0$ times, where r_0 is the size of the confining box, so that the time-dependence of the wave amplitude will be

$$A(t) \sim A_0 \left(1 - \frac{|a|^2}{r_0} t\right) \sim A_0 \left(1 - e^{-(|a|^2/r_0)t}\right), \tag{2.55}$$

corresponding to a small imaginary part of the frequency.

In the case of rotating or charged black holes, for waves satisfying the superradiance conditions (2.49) or (2.54), the black hole works as an amplifier and $|a|^2 < 0$, as concluded from the Zel'dovich argument of Section 2.1.3. Thus the imaginary part of the frequency becomes positive, corresponding to a dynamical instability.

This kind of behaviour can be expected for both rotating and charged black holes, with the quantitative details of the instability process depend on the actual equations governing the radiation and on the mechanism providing the reflection. Putting a mirror around a black hole may seem a difficult thing to do, however sometimes *nature provides its own mirrors* [117].

One of such natural mirrors occurs in anti-de Sitter spacetimes, in which an observer at the origin measures a finite time for a light ray to reach the AdS boundary. Rotating

black holes in such backgrounds are hence unstable, at least if they are small enough with respect to the AdS *box size* [118, 119]. Larger black holes were instead found to be stable. The reason can be understood by thinking that the size of the confining geometry determines the lowest possible frequency of the radiation contained; if the box is too small the lowest excitation frequency will be higher than the upper bound for superradiant amplification.

An even more realistic and important mirror is the one provided for massive fields in asymptotically flat spacetimes by their own mass. In fact for a scalar field of mass μ the small frequencies $\omega < \mu$ are reflected by the lack of asymptotic propagating modes [120]. The resulting black hole bomb instability was found to be relevant on astrophysical scales for $\mu M \lesssim 1$, that for very massive black holes corresponds to an ultralight boson field. The importance of this kind of black hole bomb comes from the fact that such massive fields have been predicted in many extensions of the Standard Model of particle physics, so that the fact that such instabilities are unobserved imposes bounds of the masses of these beyond-the-standard-model particles.

2.5.2 Ergoregion instabilities

Let us consider instead the situation in which no confining geometry is present but the spacetimes displays an ergoregion but not an horizon. This can occur for the so-called *ergostars*, that is compact objects that rotate fast enough to *drag* the space as a Kerr black hole would.

In this case the negative-energy scalar field modes living inside the ergoregion cannot be absorbed by the horizon and will be trapped there. Since outside of the ergoregion only positive-energy modes are available, the coupling to these modes will determine an exponential increase of the negative-energy modes inside the ergoregion. This is called an *ergoregion instability*; a pictorial representation is given in the right panel of Figure 2.3.

This process was discovered in the Seventies [121, 122], but a complete description of the phenomenon has been given only recently (see Section 5.14 of [10] for a full treatment and complete references). The instability is related to the existence of long-lived modes inside the ergoregion that are responsible for the trapping of the negative-energy fluctuations. Notice that an horizon is not the only thing that can prevent the ergoregion instability, in fact if the star surface absorbs the scalar field radiation, the trapping of the negative-energy field modes is avoided [123].

Notice that the same kind of instability phenomenon can be expected for charged objects with no horizon but with an electrostatic field strong enough to create an *effective* ergoregion. A study of this kind of instability was only recently reported in [124], where a Reisser–Nordström spacetime with a mirror inside the effective ergoregion was considered, thus preventing the possibility of absorption from the black hole.

An *acoustic* configuration displaying this kind of instability is the vortex without a drain, that is the vortex geometry of Section 1.3.3 with no radial flow ($A = 0$). The resulting acoustic metric has an ergoregion and no horizon, so that with respect to the

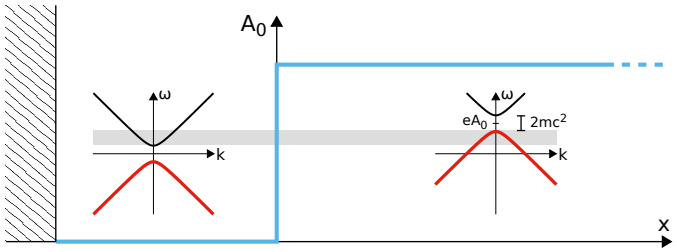

Figure 2.4: The bosonic Klein paradox setup, analogous to the one of Figure 2.1 with a reflecting boundary added on the left. This gives rise to the dynamical instabilities predicted in the SSW effect and analogous to a black-hole bomb instabilities.

superradiant scattering of Section 2.4.1 we cannot impose outgoing boundary conditions towards the center of the vortex. The ergoregion instability of this configuration was numerically studied in [125], where different kinds of reflecting boundary conditions were imposed at a finite radius. A situation in which this kind of acoustic geometry emerges spontaneously are quantized vortices in Bose–Einstein condensates [16], that display a purely rotating flow. Despite the deviation from the hydrodynamic regime, we show in Chapter 5, also by comparison with the results of [125], that these vortices display instabilities that are a modified version of ergoregion instabilities.

It is interesting to notice that, as for amplified reflection, also this kind of instabilities have been discovered in classical hydrodynamics [126]. This is an example of how Analogue Gravity brings together and gives new perspectives on classical results of different fields.

2.5.3 The bosonic Klein paradox turns unstable: the SSW effect

Remember that we introduced this chapter with a presentation of a charged scalar field in an electrostatic potential as a useful toy model for superradiant scattering. We also close the chapter with this simple model since it turns out to be a good reference also for what concerns superradiant instabilities. In particular, by changing the boundary conditions to the bosonic Klein paradox of Section 2.1.1 we can reproduce the instability mechanisms that we just discussed for black-holes.

Referring to the Klein paradox configuration, reproduced in Figure 2.4, we can think of the right region as the ergoregion, where negative-energy *antiparticles* are possible. By imposing a reflecting boundary condition on the left (as is the case in the Figure) we are in the situation of the black hole bomb instability, in which the positive-energy field modes are trapped and grow between the ergoregion and the asymptotic confinement. If instead the reflection is imposed on the right we are in the ergoregion instability case, that is we are removing the *dissipation* of negative-energy modes given by the open boundary condition on the right as it is removed in a black hole spacetime by having no horizon.

Notice that these configurations are essentially square potential boxes for a massive

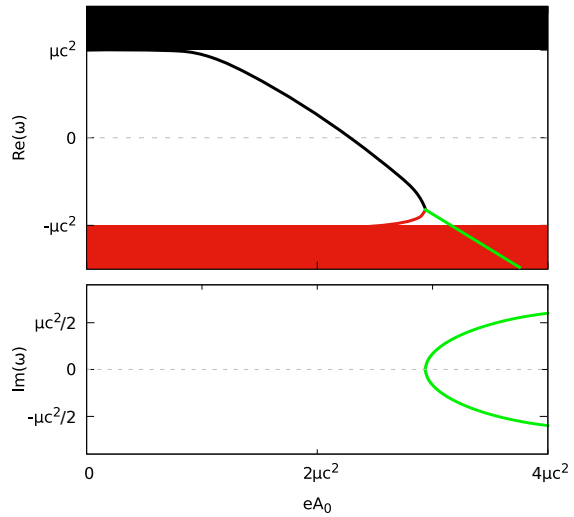

Figure 2.5: Representation of the Schiff–Snyder–Weinberg effect through the spectra of the configuration of Figure 2.4 for different depths of the potential. The black and red regions are respectively the particle and antiparticle continuous spectra of a massive charged Klein–Gordon field and are separated by the mass gap. When increasing the depth of an electrostatic potential box initially bound particle states enter the mass gap. When the potential is deep enough this bound state reaches the antiparticles continuum, where it can undergo the pseudo-hermitian *band sticking* generating dynamically unstable field modes.

charged Klein–Gordon field. Interestingly, the bound states in this kind of potentials were studied in 1940 by Schiff, Snyder and Weinberg [14], that took it as a simple model of a realistic potential of subatomic size. By taking a square box potential, analogous imposing a reflecting boundary condition at the left of the Klein paradox setup, they found that, for a not too deep potential, bound states for particles were formed, that is they found eigenenergies inside the mass gap of the field. By making the well deeper the energy of the bound state decreases until it approaches the antiparticle continuum, where a further eigenenergy appears inside the mass gap, emerging from the antiparticles continuum. By continuing the deepening of the potential these two states end up merging in a single band and developing an imaginary part of the eigenenergy. This behaviour of *band-sticking* is exactly what we described in the previous chapter as a consequence of the non-Hermiticity of the Klein–Gordon equation. In the right part of Figure 2.5 we give a pictorial representation of this physics, called the *Schiff–Snyder–Weinberg (SSW) effect*.

This effect has been thoroughly studied by Fulling [15, 127], that also connected it to rotating spacetimes by introducing a toy model metric (an acoustic metric *ante litteram*) mapping directly to the square potential for the charged scalar field via what he calls the *reduction of a gravitational problem to an electromagnetic one*.

In Chapters 3 and 4 we will see an explicit case of this mapping and also a *physical*

occurrence of the SSW effect in Bose–Einstein condensates, that can hence be used to simulate the physics of a quantum charged scalar field. The occurrence of these phenomena in a system whose physics is well known will allow us to better understand superradiance, for example by constructing specific setups that allow to disentangle the different ingredients of the phenomenon.

2.6 Which are the essential ingredients of superradiance?

After this introduction to superradiant effects, the remaining chapters deal with the actual original work of this thesis, that will on the one hand use analogue models to better understand superradiance and on the other hand use superradiance to better understand the systems providing the gravitational analogy. For the first of these aims we now summarize what is the current picture of superradiance that emerges from what we discussed in this introduction.

In the course of this chapter we tried to emphasize the most fundamental features of superradiance and we found that an essential ingredient is the presence of modes of the field in some part of the system in which the negative energy needed to compensate for the amplification can be dumped; for example in the Klein paradox the positive-energy *particle* waves are amplified by transmission to negative-energy *antiparticle* ones.

Another fundamental aspect of superradiance is the role of boundary conditions and of dissipation. We saw that general arguments can be made connecting superradiance to dissipation. This dissipation can be provided by an actual dissipative system, as in the Zel'dovich effect, but also by an unbound system assuring outgoing boundary conditions, as for example in the bosonic Klein paradox, for which left-going waves in the asymptotic right region were excluded. Open (or radiative) boundary condition can in fact be viewed as a dissipative element since the energy can escape outside [114, 128]. Formally this can be understood from the fact that a boundary condition requiring, for example, for a field to behave as a purely left-going plane wave $\phi \propto e^{ikx}$ is not invariant under Hermitian conjugation; the overall problem is hence non-Hermitian and does not conserve energy. In the case of black holes we saw that this kind of boundary condition are usually at play at the horizon, that works as a one-way membrane and is treated as a perfect absorber.

The question is now if dissipation is an essential ingredient of superradiance. We surely know that if open boundary conditions are removed from the system superradiant instabilities can develop, but does this prevent amplification as the general argument of Section 2.2 seems to suggest? In the language of black holes the question translates to: are horizons necessary for superradiance?

As presented up to now, with spatially unbounded plane wave solutions, superradiance is a stationary process. We will instead show with our toy-model approach of the next Chapter, that the absence of dissipation excludes superradiance as an equilibrium (stationary) process but not as a time-dependent one involving finite-width wavepackets. Dissipation is hence not necessary for superradiance and is only related to the *long-time*

dynamical stability of the system. Moreover, we are also going to see that horizons do not *in general* provide the necessary absorption to avoid instabilities.

The picture we will build of superradiance will then serve us for our second aim of applying the concepts learned from superradiance to understand some physics of Bose–Einstein condensates. From the point of view of superfluid physics it is natural, by looking at the vortex geometry here presented, to think about quantized vortices and ask if they display superradiance or superradiant instabilities and if these are related to the instabilities known in the literature. Another question coming from this exposition of superradiance is if the physics of hydrodynamic tangential discontinuities that we considered in Section 2.1.2 can be obtained in BECs and what is the interplay between the surface instabilities and superradiace in this setting.

Chapter 3

Superradiant scattering on a planar ergosurface

Superradiance in analogue gravity emerges naturally in vortex-like flows that, we saw, have the essential features of a rotating Kerr black hole: an ergoregion and an horizon. In such rotating configurations amplified scattering has been widely considered in different media, from water to quantum fluids to optical systems. This led to the first experimental evidence of superradiant scattering of gravity surface waves propagating in a tank of water having a draining vortex in the center [12].

In spite of these impressive advances, there are still a number of intriguing open points in our understanding of basic superradiance phenomena. The circular geometry of rotating systems and their limited tunability makes it difficult to disentangle the different microscopic mechanisms at play and build an intuitive picture of the overall process. The goal of this Chapter is to propose a new concept of analog model that allows a local tuning of the velocity profile and, thus, a wider flexibility in the design of the analog spacetime to be studied.

The idea is to exploit some of the remarkable technological tools available for the manipulation of cold atoms to induce a *rotational* velocity field $\nabla \times \mathbf{v} \neq 0$ in a Bose–Einstein condensate. This allows the construction of setups in which superradiance occurs in a simple and tunable geometry in which the ergoregion is simply a plane, as sketched in Figure 3.1.

This kind of configuration reminds tangential discontinuities in hydrodynamics, that we discussed in connection with superradiance in Section 2.1.2, but is here obtained without the surface instabilities typical of the hydrodynamic case and amplified scattering is hence the only physically relevant phenomenon. Moreover the quantum nature of the fluctuation field allows the investigation of the pair production associated to superradiant amplification.

We start the discussion with the most promising realization of our tunable geometry: the local change of the flow velocity with the inclusion of a synthetic vector potential coupled to the atoms of the condensate. After showing how this new degree of freedom changes the acoustic metric we analyze superradiant scattering on the *minimal* ergo-

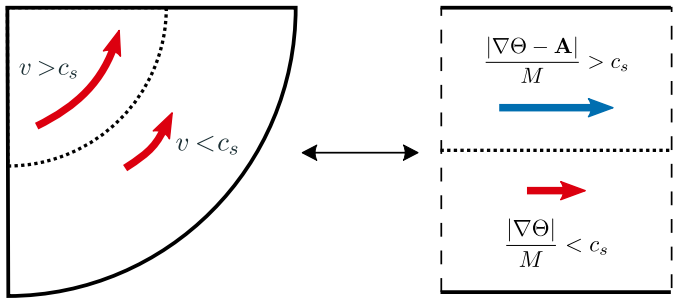

Figure 3.1: Schematic representation of the setup for the realization of an analogue ergosurface in a Cartesian geometry using a local tuning of the velocity. While in the vortex case the velocity field is fixed by the irrotationality constraint, in the right configuration the velocity is locally tuned with specific local designs of the system. The depicted case refers to the coupling of the condensate atoms to a synthetic vector potential, but a similar velocity field can be obtained with the inclusion of a lattice region changing the effective mass of the atoms.

surface of Figure 3.1 by studying the Klein–Gordon equation describing fluctuations in the long-wavelength limit. This problem can be exactly mapped to the bosonic Klein paradox of Section 2.1.1. We then consider the exact Bogoliubov dispersion relation and show that its superluminal behaviour at high momenta can determine the suppression of superradiant scattering when we move away from the long-wavelength regime. Our *analytical* predictions based on the study of dispersion relations are then confirmed with numerical simulations of the Gross–Pitaevskii equation. Subsequently we apply a scattering matrix approach to obtain a prediction for the superradiant amplification factors. This allows to address the phenomenon of quantum spontaneous pair creation at the ergosurface that is characterized via the density-density correlations in position space and the two-body correlation function in momentum space. Finally, we describe an alternative realization of a planar ergosurface that, instead of exploiting synthetic vector potentials, involves periodic trapping potentials for the atoms of the condensate.

The results of Sections 3.1 and 3.2 were addressed in [21] while the rest of this Chapter will be object of future publications.

3.1 Acoustic metric in the presence of a synthetic vector potential

The atoms usually considered to obtain Bose–Einstein condensates do not have an electric charge, so that the effective Hamiltonian describing them (1.1) is the one of neutral particles, that is there is no minimal coupling to a gauge field. It is however possible to generate *synthetic (or artificial) gauge fields* for neutral atoms, that is to tune the external potentials or to couple the internal states of the atoms so that the effective Hamiltonian of the atomic field has the shape of the one of a charged field minimally

coupled to a gauge field. This allows to mimick the physics of charged particles with neutral atoms and is interesting to reach regimes that are difficultly achievable with *real* charged particles [20, 129].

A simple realization of this concept can be obtained by rotating the system with an angular frequency Ω along some axis z [130]. The Hamiltonian in the rotating frame $\hat{H}'$ is related to the one in the laboratory frame by $\hat{H}' = \hat{H} - \Omega \hat{L}_z$. The additional term can can be rewritten as a combination of a centrifugal potential $V_c = -M\Omega r^2/2$ and a minimally-coupled vector potential $\mathbf{A} = M\Omega(y\mathbf{e}_x - x\mathbf{e}_y)$; this second *artificial* gauge field provides a uniform *artificial* magnetic field $B_z = 2M\Omega$.

In the last decades, several other strategies to induce space dependent gauge potentials have been experimentally demonstrated using combinations of static electromagnetic fields and microwave and/or optical Raman beams [20]. As a result, neutral atoms end up experiencing a minimal coupling to a vector potential that is formally analogous to the one of electrically charged objects and is responsible for all sorts of magnetic effects [131]. Even though we will restrict here to the case of atomic systems, similar constructions are also possible for optical systems, where synthetic magnetic fields for neutral photons are presently the subject of intense investigations [132].

A possible realization is based on coupling of internal states of an atom in such a way that the dressed states have a modified dispersion relation, in particular with a shifted position of the minimum in some direction [133, 134]. This is mathematically equivalent to having a vector potential in the direction of the shift, that can be varied in the other directions, making the vector potential space-dependent. We are interested here in the applications of these techniques to the atoms of a Bose–Einstein condensate, where synthetic vector potentials were demonstrated, for example, to create a vortex lattice [135] in a uniform artificial magnetic field.

In the mean field description of a BEC these situations can be accounted for by including additional terms to the GPE in the form of a vector potential $\mathbf{A}(\mathbf{r}, t)$ minimally coupled to the atomic momentum [1]. Putting all terms together, the GPE then reads [136]

$$i\hbar\partial_t\Psi = \left[\frac{(-i\hbar\nabla - \mathbf{A}(\mathbf{r},t))^2}{2M} + V(\mathbf{r}) + g\,|\Psi|^2\right]\Psi\,, \tag{3.1}$$

where $V(\mathbf{r})$ is the external trapping potential, g is the interaction constant and M is the bare atomic mass. In analogy to usual magnetism, the curl of the vector potential provides the *synthetic magnetic field* $\mathbf{B}$ experienced by the neutral atoms. Its time dependence contributes to the *synthetic electric field*. In what follows, we will focus our attention on static vector potentials with complex spatial profiles $\mathbf{A}(\mathbf{r})$ giving spatially inhomogeneous synthetic magnetic fields but no synthetic electric field.

To see how this modification of the GPE affects the resulting acoustic metric we follow the strategy of Section 1.2 and rewrite the GPE (3.1) in the superfluid hydrodynamic

[1] Note that depending on the microscopic scheme used to generate the synthetic vector potential, additional correction terms may arise [20]. For the sake of simplicity and generality, in the following we will work under the assumption that they are negligible.

form in terms of the modulus and the phase of the order parameter $\Psi = \sqrt{n}\, e^{i\Theta}$:

$$\begin{aligned} \partial_t n &= -\nabla \cdot \left[n \frac{(\hbar \nabla \Theta - \mathbf{A})}{M} \right] \\ \hbar \partial_t \Theta &+ \frac{(\hbar \nabla \Theta - \mathbf{A})^2}{2M} + gn + V - \frac{\hbar^2}{2M} \frac{\nabla^2 \sqrt{n}}{\sqrt{n}} = 0. \end{aligned} \tag{3.2}$$

Again, except for the last *quantum pressure* term in the second equation, these equations recover the continuity and Euler equations of a perfect fluid, with the difference that the synthetic vector field affects the expression of the velocity field in terms of the condensate phase

$$\mathbf{v} = \frac{\hbar \nabla \Theta - \mathbf{A}}{M} = \mathbf{v}_{\rm can} - \frac{\mathbf{A}}{M}. \tag{3.3}$$

The distinction between the *canonical velocity* $\mathbf{v}_{\rm can} = \nabla\Theta/M$ and the *physical velocity* $\mathbf{v} = \mathbf{v}_{\rm can} - \mathbf{A}/M$ in the presence of a vector potential has the crucial consequence [136] that the physical velocity field $\mathbf{v}(\mathbf{r})$ appearing in the hydrodynamic equations is no longer constrained to be irrotational as it occurs in textbook superfluid hydrodynamics.

The rest of the derivation of the acoustic metric we reviewed in Section 1.2 remains unvaried, so that in the hydrodynamic limit we find again that the phase fluctuations can be described by a Klein–Gordon equation in a curved spacetime specified by the acoustic metric (1.60)

$$g_{\mu\nu} = \frac{n_0}{c_s} \begin{bmatrix} -\left(c_s^2 - \mathbf{v}^2\right) & -\mathbf{v}^T \\ -\mathbf{v} & I \end{bmatrix}. \tag{3.4}$$

This time however the velocity entering the metric is (3.3), breaking thus the irrotationality constraint on the physical velocity field $\mathbf{v}$ that is typically taken as an hypothesis in the derivation of the acoustic metric [1].

As a key result of this section, the possibility of breaking the irrotationality constraint on the physical velocity field $\mathbf{v}$ by means of the synthetic vector potential dramatically expands the range of space-times that can be implemented in analog models and gives a novel degree of freedom in engineering configurations for the study of analogue gravity effects[2]. This new freedom will be at the heart of our approach to superradiance.

3.2 Superradiance from an isolated planar ergosurface

Let us start from the simplest case of a single planar ergosurface separating regions of sub- and super-sonic flow with a velocity directed along the x axis parallel to the interface. As it is sketched in Figure 3.1, the synthetic vector potential gives the possibility to break the irrotationality constraint and generate a rotational superfluid flow using

[2] A different expansion of the degrees of freedom in the acoustic metric unsing density-dependent gauge potential was recently developed in [137].

a two-dimensional BEC[3] in the form of a plane wave of wavevector $\mathbf{K}$ with a spatially uniform density. The rotational flow is induced by a jump in the x component of the synthetic vector potential, for instance from a vanishing value for $y < 0$ to a finite value A_x for $y > 0$ (right panel).

The translational invariance of this geometry along x offers crucial advantages from both the technical and the conceptual points of view. In particular, it guarantees that the k_x component of the momentum is conserved during the scattering process. This is in analogy to the angular momentum conservation in cylindrical geometries (left panel). In contrast to the cylindrical case where the flow displays a non-trivial radial dependence, the asymptotic regions of our geometry are however flat and homogeneous, which allows to expand the incident and scattered waves in a plane wave basis. Finally, in contrast to the cylindrical geometry, the ergosurface is in our case an infinite line and the ergoregion an unbounded half plane. Thanks to this simpler geometry, the superradiance process at the ergosurface can be isolated from additional geometrical features and the products of the superradiant amplification are automatically evacuated without the need of a horizon.

As we said in Section 2.1.2 geometrically similar flows can be studied in classical fluid mechanics, in which context tangential discontinuities are known to show amplification for sound and gravity waves. Differently from that case, as we are going to see in what follows, our system is instead immune to surface instabilities instabilities, which leaves us with a stationary configuration in which superradiant scattering is the main physical process.

3.2.1 Superradiant scattering in the hydrodynamic Klein-Gordon approximation

As a first step, we consider the problem in the hydrodynamic limit and we derive a prediction for the amplification by means of a scattering approach as the general one presented in Section 2.2 [90]. The impact of the superluminal features of the Bogoliubov dispersion will be discussed in Sec.3.2.3. In the configuration under examination, the acoustic metric has the form

$$g_{\mu\nu} = \frac{n_0}{c_s} \begin{bmatrix} -(c_s^2 - v_x^2) & -v_x & 0 \\ -v_x & 1 & 0 \\ 0 & 0 & 1 \end{bmatrix}, \tag{3.5}$$

where the total physical velocity $v_x = v_x(y)$ includes the synthetic vector potential and is oriented along x.

Because of the translation invariance along x we can look for solutions of the form $\Theta_1(t, x, y) = e^{ik_x x}\phi(t, y)$ with a well-defined x component of the wavevector $\mathbf{k}$. Note that

[3] For the sake of simplicity, similarly to the one-dimensional black hole of Section 1.5, here we consider a two-dimensional condensate, where the third dimension is frozen by a tight confinement and the dynamics can be described by a two-dimensional GPE of the shape (3.1) (see Chapter 23 of [16]). Generalization to the full three-dimensional case would make the discussion more cumbersome but would not involve any additional conceptual difficulty.

k is here the wavevector of the perturbation, to be distinguished from the one **K** of the underlying condensate. Under this Ansatz, the Klein–Gordon equation (1.60) reduces to a single differential equation for $\phi(t, y)$,

$$-\left(\frac{1}{c_s}\partial_t + i\frac{v_x}{c_s}k_x\right)^2 \phi + \partial_y^2\phi - k_x^2\phi = 0. \tag{3.6}$$

The analysis is further simplified if we restrict to cases where the flow velocity $v_x(y)$ has a y-dependence concentrated around $y = 0$, while sufficiently far from this interface it acquires constant asymptotic values $v_x(y) = v_x^{s,f}$ in the *slower* (s) region $y < 0$ and in the *faster* (f) one $y > 0$. These velocities are related to the atomic canonical momentum K_x and the synthetic vector potential by $v_x^s = \hbar K_x/M$ and $v_x^f = (\hbar K_x - A_x)/M$. For the sake of concreteness, we assume the velocities fulfill $0 \leq v_x^s < v_x^f$, but our results are straightforwardly extended to other configurations.

In particular, we look at the stationary scattering problem for an incident plane wave of frequency ω coming from $y = -\infty$. In this case, we can expand the solution in plane waves as $\phi(t, y) = e^{-i\omega t}\varphi(y)$ with $\varphi(y \ll 0) = e^{ik_y^s y} + \mathcal{R}e^{-ik_y^s y}$ and $\varphi(y \gg 0) = \mathcal{T}e^{ik_y^f y}$. Within each region, the wavevector $k_y^{s,f}$ along y is determined by the dispersion relations for the Klein–Gordon equation (1.86) in the two regions

$$\omega = v_x^{s,f}k_x \pm c_s\sqrt{k_x^2 + \left(k_y^{s,f}\right)^2}, \tag{3.7}$$

where the plus and minus signs refer to positive- and negative-norm modes. It is immediate to analytically see that, for subsonic flows $c_s > v_x$, for a given positive frequency $\omega > 0$, only positive-norm modes are available and their **k**-space locus has a closed, elliptic shape as shown by the solid lines in Fig. 3.2. For supersonic flows $c_s < v_x$, the locus consists instead of two hyperbolic branches of opposite norms (dashed lines in the same figure).

For given values of ω and k_x, the k_y values involved in the scattering process have to be chosen with the requirement that the group velocity $\mathbf{v}_g = \nabla_{\mathbf{k}}\omega$ of the incident and transmitted waves has a positive y component, so that the incident wave in the lower, slow region moves towards the interface and the transmitted wave in the upper, fast one moves away from it. For the same reason, the reflected wave in the lower region must be chosen in order for the group velocity to have a negative y component. The fact that the flow velocity is parallel to the interface guarantees that the wavevectors of the incident and reflected waves have opposite y components $\pm k_y^s$.

A concrete example of superradiant scattering process is given in Figure 3.2 for a case where the lower $y < 0$ region (solid lines) is subsonic and the upper $y > 0$ one (dashed lines) is supersonic, so the $y = 0$ interface is an ergosurface. The incident and reflected modes (filled and empty black dots) lie on a positive-norm (thin line) branch, while the transmitted mode (red dot) lies on a negative-norm (thick line) branch.

As explained in Section 2.2, in order to establish the superradiant amplification, we can consider the relation between the reflection and transmission coefficients stemming

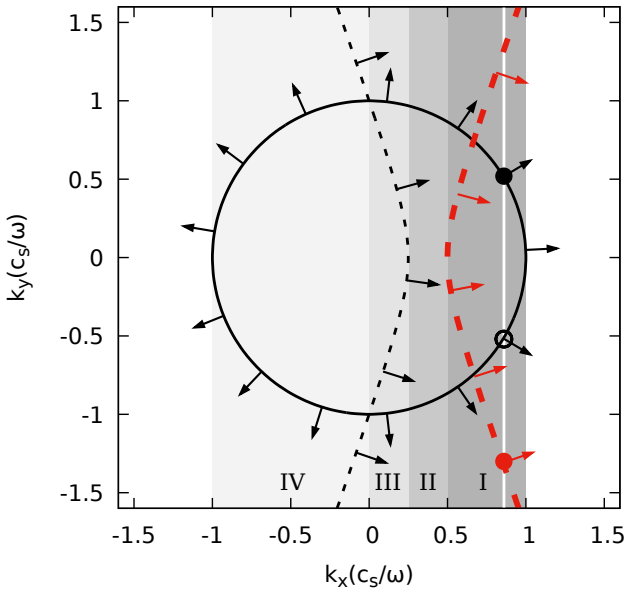

Figure 3.2: **k**-space locus of modes at a given ω for the Klein–Gordon equation in the *slow* lower $y < 0$ region (solid line) and the *fast* upper $y > 0$ region (dashed lines). The slow region is taken at rest $v_x(y < 0) = v_x^s = 0$ and the fast one is moving with supersonic speed $v_x(y > 0) = v_x^f = 3c_s$. The speed of sound c_s is the same on both sides. Positive norm branches are shown as thin black lines, negative norm branches are shown as thick red lines. For each mode the arrows indicate the direction of the group velocity $\mathbf{v}_g = \nabla_{\mathbf{k}}\omega$. The different levels of gray (I-IV) indicate the k_x intervals for which the different scattering processes occur (see text). The vertical white line in the darkest region (I) indicates an amplified superradiant scattering process, with the filled black dot indicating the incident mode, the empty black dot the reflected one and the red dot the transmitted one.

from the conservation of the Wronskian $W = \varphi(\varphi^*)' - \varphi'\varphi^*$ between the solution and its complex conjugate. This provides a relation

$$1 - |\mathcal{R}|^2 = \frac{k_y^f}{k_y^s} |\mathcal{T}|^2 \,. \tag{3.8}$$

between the reflection $\mathcal{R}$ and the transmission $\mathcal{T}$ amplitudes. From this relation it is immediate to see that the reflection coefficient exceeds one (i.e. the reflected wave is amplified) if the wavevectors k_y^s and k_y^f of the incident and transmitted waves have opposite signs. Given the form of our dispersion shown in Fig.3.2, this condition is naturally satisfied if the scattering process involves modes of opposite norms on the two sides. This is a sufficient condition for superradiant scattering to occur at an isolated ergosurface. A similar explanation for the amplification of waves at tangential discontinuities

in classical fluid mechanics was given in [94].

In addition to the superradiant amplified reflection discussed so far, other kinds of scattering processes can occur depending on the wavevector k_x, that is on the incidence angle from the lower region. The characterization of the different cases can be carried out by comparing the dispersion in the two regions as shown in Fig. 3.2 and keeping in mind the conservation of k_x at the interface [138]. The incident wavevector is to be chosen on the dispersion in the lower region (solid line).

For instance, superradiant scattering is restricted to the darkest region (I) where a single, opposite norm mode is available for transmission in the upper region (thick red dashed line). In the neighboring, slightly lighter region (II), the incident wave is completely reflected since there is no available mode to transmit into the upper region. In the next two, even lighter regions (III-IV), ordinary scattering occurs and the incident wave is partially reflected and partially transmitted into a same-norm mode (thin black dashed line), the incident energy being distributed among the two in an incident-angle-dependent way as it happens for refraction of electromagnetic waves at the surface of a dielectric. While in all other regions (I-III) the x component of the group velocity has the same positive sign in both the lower and upper regions, in region (IV) the incident and transmitted waves have opposite signs of the x component of the group velocity, leading to a negative refraction phenomenon [139]. In this case, the incident wave has a negative x component of the group velocity, but due to the drag by the moving fluid, the transmitted wave in the $y > 0$ region deviates its path towards the positive-x direction.

Whereas all other scattering process (II-IV) only involve positive norm modes and can also occur with non-uniform, yet everywhere subsonic velocity profiles, the superradiant process (I) crucially relies on the presence of a negative norm transmitted mode, which is only possible for a supersonic flow. To this purpose, it is worth noting that one cannot replace the change in the transverse velocity with a change in the local speed of sound, e.g. via a spatial modulation of the interaction constant as proposed in [17, 18] for the analogue Hawking radiation. Even though negative norm modes emerge in the upper, fast region, superradiant scattering can not occur since there are no k_x values for which states are simultaneously available on the positive-norm curve of the lower, slow region and on the negative-norm curve of the upper, fast region. This can be easily checked analytically. On a dispersion diagram such as Fig.3.2, it corresponds to the red thick dashed curve being always located to the right of the thin solid line.

As a final point, note how, in contrast to the cylindrical geometry, our translationally invariant (and thus Galilean invariant) geometry along x gives symmetric roles to the upper and lower regions. As a result, amplification does not depend on the way in which the interface is crossed. In particular, the same superradiant scattering process occurs for wavepackets hitting the interface from the upper, fast region.

3.2.2 Mapping to a 1D electrostatic problem

The acoustic spacetime emerging from our translationally-invariant, two dimensional setup offers a realization of the *rectilinear* model of the Kerr metric introduced in [15] as

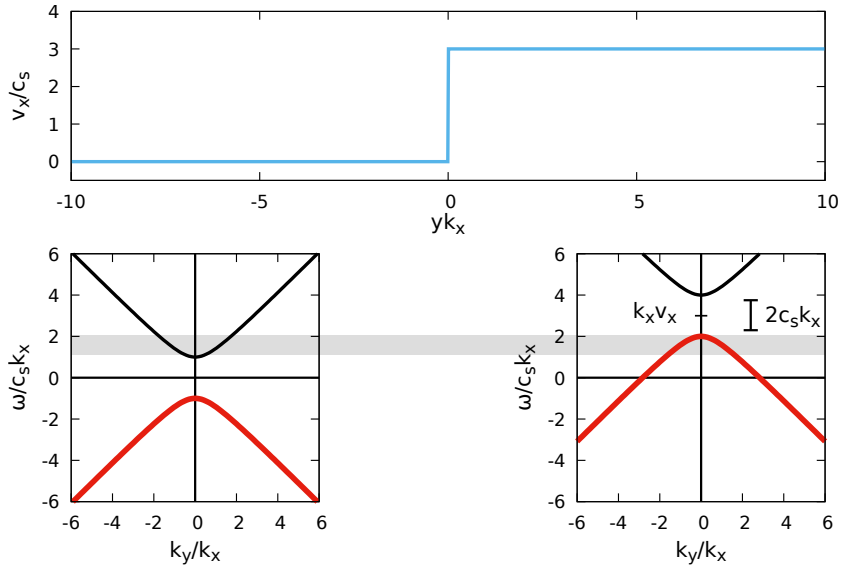

Figure 3.3: Schematic representation of the physical mechanism underlying the massive bosonic Klein paradox in our reduced problem along y. In the upper plot a step increase of the transverse velocity is shown, in the lower plots the Klein–Gordon dispersion relations at fixed k_x in the two regions. The condition for the amplification to occur is to have both particle and antiparticle modes available at the same frequency, as indicated by the light gray shading in the plot.

a toy model for the study of bosonic fields in rotating spacetimes. As it was explained there, in this case the problem of a massless neutral scalar field in the curved space-time can be reduced to a electrostatic problem in reduced dimensions. In this section, we take inspiration from these results to build an explicit link between our synthetic field configuration and the massive bosonic Klein paradox we introduced in Section 2.1.1. This suggests a further direction in which our atomic system can be used as a quantum simulator of a relativistic quantum field theory.

This link is easily understood by comparing the reduced one-dimensional Klein-Gordon equation for our analogue model (3.6) with the equation for a one-dimensional massive charged scalar field in an electrostatic potential A_0,

$$-\left(\frac{1}{c}\partial_t + i\frac{e}{\hbar c}A_0\right)^2\phi + \partial_y^2\phi - \frac{m^2c^2}{\hbar^2}\phi = 0. \tag{3.9}$$

Here, e is the charge, m is the mass of the field and c is the speed of light. The two equations are mapped into each other with the identifications

$$\frac{m^2c^2}{\hbar^2} \longleftrightarrow k_x^2 \qquad \frac{eA_0}{\hbar} \longleftrightarrow k_x v_x \qquad c \longleftrightarrow c_s \ : \tag{3.10}$$

the role of the scalar potential $A_0(y)$ is played by the transverse velocity $v_x(y)$ and both the mass m and the charge e are controlled by the value of the transverse momentum k_x.

This parallelism makes it evident that superradiance in our system is equivalent to the bosonic Klein paradox of Section 2.1.1, that is the amplified reflection of a bosonic field off an electrostatic potential step. In this analogy, the negative norm modes correspond to antiparticles, amplified reflection is associated to the transmission of antiparticles, and energy conservation corresponds to overall charge conservation. Because of the *particle-hole symmetry* of the Bogoliubov problem, the positive frequency, negative-norm modes are actually physically equivalent to positive-norm modes at negative frequencies for $-k_x$. This is consistent with our identification of the transverse momentum k_x with the charge of the particle in the reduced problem.

The condition for the superradiant process to happen can be derived by looking at the dispersion relations in the two asymptotic regions far from the potential step as shown in Figure 3.3 (analogous to Figure 2.1). These plots correspond to a different *cut* of the same dispersion relation studied in Figure 3.2: there, the **k**-space locus of modes at a given ω was shown. Here, we plot instead the dependence of ω on k_y for a given k_x. It is immediate to see that the effect of a constant transverse velocity is to rigidly shift the dispersion relation along the ω direction.

As a simplest example one can take the electrostatic potential $A_0(y)$ to be zero far in the $y < 0$ region and to tend to a positive constant A_0 far in the $y > 0$ region (upper plot). If this value is large enough to satisfy

$$eA_0 > 2mc^2\,, \tag{3.11}$$

transmission to antiparticles, and hence amplification of the reflected wave, can occur in the range of frequencies $mc^2 < \omega < eA_0 - mc^2$. The factor 2 in the condition (3.11) physically corresponds to the fact that a particle-antiparticle pair is generated during the scattering process and both the particle and the anti-particle have the same mass m.

Through the identifications (3.10), we can easily obtain from (3.11) a necessary condition for amplified scattering,

$$\Delta v_x > 2c_s \tag{3.12}$$

where Δv_x is the velocity jump across the interface, $\Delta v_x = v_x^f - v_x^s$. Quite remarkably, this condition shows that the presence of an analogue ergosurface separating sub- and super-sonic flows is not sufficient for superradiant scattering to occur, but a large enough velocity jump must be present.

While the parallelism with the Klein paradox has been rigorously established for a given k_x, it is important to keep in mind that the non-trivial form of the identifications in (3.10) make that our sound scattering process to have a completely different angular k_x-dependence from the one of a charged field hitting a scalar potential step at different angles. For instance, for $k_x = 0$ waves at normal incidence, the mass gap in the corresponding electrostatic problem vanishes. Since for a massless field there is no forbidden mass gap to overcome and every non-zero electrostatic field provides amplification within a suitable interval of incident frequencies, one could have expected amplification to occur for every small value of v_x. However, one must also remember

that for $k_x = 0$ also the charge vanishes in our identification, so the scalar potential has no effect and superradiant scattering is forbidden.

Finally, it is worth noting that condition (3.12) is the same result (2.16) derived in [95] for the hydrodynamic tangential discontinuity. Notice however that, because of the rotational velocity field, the metric treatment of that system (such as the one presented in [10]) is not a full description of the physics because of the presence of surface unstable modes.

3.2.3 The role of the superluminal Bogoliubov dispersion

Up to now we have considered the problem within the hydrodynamic approximation, where sound is described by a Klein–Gordon equation and hence displays a linear dispersion relation. In reality, the collective excitations in a uniform flowing BEC follow the Doppler-shifted Bogoliubov dispersion relation (1.85),

$$\hbar\omega = \hbar\mathbf{v}\cdot\mathbf{k} \pm \sqrt{\frac{\hbar^2 k^2}{2M}\left(\frac{\hbar^2 k^2}{2M} + 2gn\right)}. \tag{3.13}$$

That, as we said, is well linear and sonic at small momenta but then grows quadratically at higher momenta, i.e. becomes *superluminal*. The first term accounts for the Doppler shift of the frequency when moving from the fluid to the laboratory frame.

While the superluminal nature of the Bogoliubov dispersion is not expected to completely suppress the superradiance effects, important modifications may well appear. The first study of superradiant scattering for dispersive fields [140] focused on to the Klein paradox for a one-dimensional massless field. In what follows, we extend the study to the general two-dimensional case of a Bogoliubov dispersion. In the previous subsection we have seen how the transverse momentum k_x of the sound waves, besides giving the coupling with the background flow, also provides a mass term for the dimensionally reduced Klein paradox problem. We are now going to show how the main effect of the superluminal dispersion will be encoded in a modification to this mass term.

Within the one-dimensional perspective at a given k_x, having a finite frequency range for superradiance requires that the maximum of the negative norm branch in one region be higher than the minimum of the positive norm branch in the other region. Imposing this requirement on the Doppler-shifted dispersion relations (3.13) for velocities parallel to x implies that

$$\hbar\,\Delta v_x\,k_x - 2\sqrt{\frac{\hbar^2 k_x^2}{2M}\left(\frac{\hbar^2 k_x^2}{2M} + 2gn\right)} > 0, \tag{3.14}$$

where we have taken $\Delta v_x = v_x^f - v_x^s > 0$. This condition is satisfied for

$$0 < \frac{\hbar^2 k_x^2}{M^2} < \Delta v_x^2 - 4c_s^2, \tag{3.15}$$

which implies that, in contrast to the Klein–Gordon case, there is a maximum value of

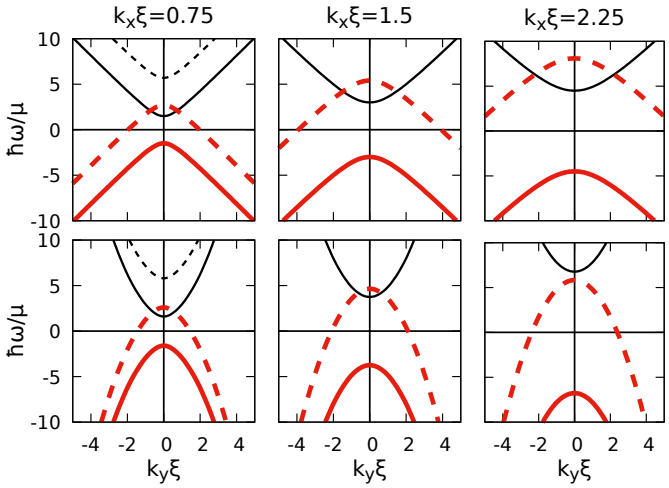

Figure 3.4: Constant-k_x cuts of the hydrodynamic Klein–Gordon (upper panels) and the Bogoliubov (lower panels) dispersion relations for increasing values of k_x (left to right). Solid lines refer to the slow region at rest with $v_x^s = 0$ and dashed lines to the fast region with $v_x^f = 2.8c_s$. Black (thinner) lines are the positive-norm branches, red (thicker) lines are the negative-norm ones. In the Klein–Gordon case, if the condition (3.12) is satisfied, superradiant scattering remains possible at all k_x thanks to the enduring intersection between the positive-norm branch in the slow region and the negative-norm one in the fast region (upper panels). In the Bogoliubov case, this intersection is only present for low or moderate values of k_x (bottom-left and bottom-center panels) and disappears for high enough values of k_x for which superradiant scattering is no longer possible (bottom-right panel).

the transverse momentum above which superradiance can no longer occur,

$$k_x^{\max} = \frac{\sqrt{\Delta v_x^2 - 4c_s^2}}{c_s}\,\xi^{-1}. \tag{3.16}$$

The dependence of this upper bound on ξ highlights the dispersive origin of the effect. As it is illustrated in Figure 3.4, this upper bound can be related to the nonlinear k_x-dependence of the effective mass gap in the reduced one-dimensional Bogoliubov problem. For small k_x, both the mass gap and the rigid upward shift of the dispersions given by the effective electrostatic potential grow linearly in k_x. For large k_x, the mass gap grows faster than the rigid shift, so the negative- and positive-norm modes eventually stop intersecting for large enough values of k_x.

Further light on this physics can be obtained by looking at the constant-ω cuts of the Bogoliubov dispersion relation (3.13) that are displayed in the different panels of Figure 3.5. Panel (a) shows how the main effect of the superluminal dispersion is to change the shape of the curves in the supersonic region: instead of the hyperbolic open shape of the Klein–Gordon case shown as dashed lines in Figure 3.2, they now have a closed, oval-like shape. For increasing ω, the oval corresponding to the positive norm modes

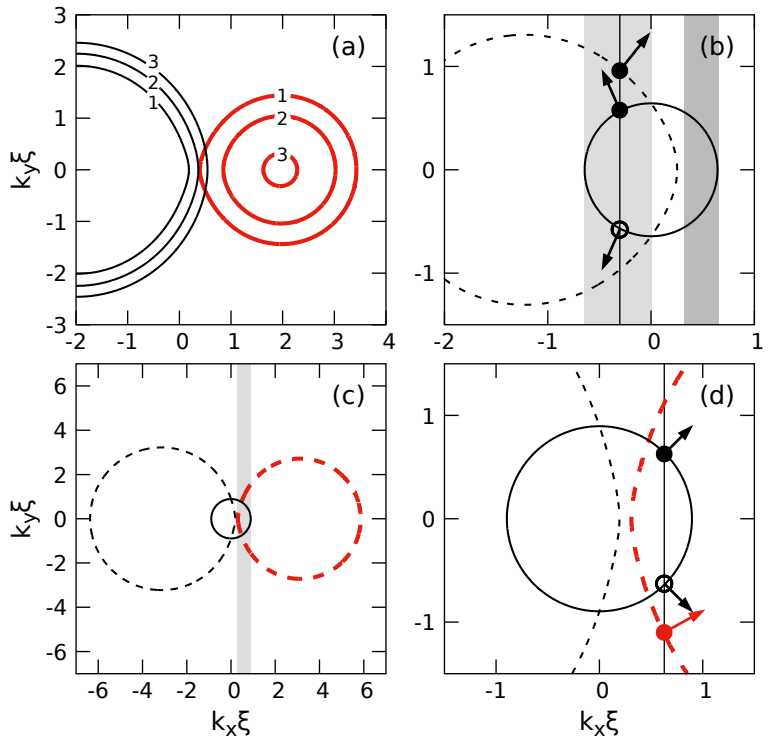

Figure 3.5: Cuts of the Bogoliubov dispersion relation at constant ω. Solid (dashed) lines refer to the slow (fast) region at $y < 0$ ($y > 0$). The speed of sound c_s is the same on both sides. Black (thin) lines are positive-norm modes and red (thicker) ones negative-norm ones. Arrows indicate the direction of the group velocity, that is outward for the black curves and inward for the red ones. (a) Cuts at different values of $\hbar\omega/Mc_s^2$ (indicated by the numbers on the curves) in a uniform region with a supersonic speed $v_x^f = 2c_s$: because of the superluminal dispersion these curves have an oval shape also in the supersonic case, rather than the hyperbolic one of the Klein–Gordon case. (b) Dispersions at $\hbar\omega = Mc_s^2$ in the two zones for a slow region at rest $v_x^s = 0$ and a fast region with a subsonic speed $v_x^f = 0.83\,c_s$. In the darker gray region one has total reflection while in the lighter gray one *negative refraction* occurs; the dots and the arrows indicate the modes involved in an example of such process and their group velocities. This process will be addressed in the GPE simulation shown in the lower panels of Fig.3.8. (c) Dispersions at $\hbar\omega = 1.5Mc_s^2$ for a slow region at rest $v_x^s = 0$ and a fast one with a supersonic speed $v_x^f = \pi c_s$: in the gray region superradiant scattering is possible. (d) A closeup of the same plot; the dots and the arrows indicate the modes involved in an example of such process and their group velocities. This specific process will be addressed in the GPE simulations shown in Fig.3.6 and in the upper panels of Fig.3.8.

expands, while the one corresponding to the negative norm ones shrinks and eventually disappears above some critical frequency.

Analogously to the Klein–Gordon case presented in Figure 3.2, the occurrence of superradiant scattering can be visualized from the intersection of both positive- and negative-norm curves with the vertical line at a fixed k_x: this happens in the gray region in panel (c) and an example of such process is displayed on a magnified scale in panel (d). As before, also other kinds of scattering behaviours can be recognized depending on parameters: in the darker gray region of panel (b) the incident wave gets totally reflected, while in the lighter gray region negative refraction occurs.

While these cases exhaust the possibilities for a velocity parallel to x, in Section 4.3 we shall see how even more complex scattering processes can occur once the flow can also acquire a y component.

3.2.4 GPE numerical calculations

In order to shine further light on superradiant scattering and confirm the predictions drawn from the graphical study of the analytical dispersion relations, we performed numerical simulations of the time dependent dynamics of the two-dimensional GPE (3.1). For the background condensate, we take a real and constant order parameter Ψ_0 and a spatially uniform interaction strength, so that the canonical velocity is zero and the speed of sound is spatially uniform and equal to $c_s = \sqrt{gm/M}$. We take the vector potential directed along x with $A_x(y < 0) = 0$ and $A_x(y \geq 0) = A_x$ constant, so to give a sudden jump in the physical velocity along x. In order to maintain the plane wave shape of the BEC at all times, we need to introduce an external potential jump $V(y \geq 0) - V(y < 0) = -A_x^2/(2M)$. We impose periodic boundary conditions in both directions and we ensure that the integration box is large enough for finite size effects to be irrelevant for the computational times of interest.

Among many other possible schemes that may be implemented, our choice of using a vector potential that is directed along x and only varies along y is beneficial from both the experimental and numerical point of view. Such a configuration could be, for instance, obtained by means of a pair of counterpropagating Raman laser beams directed along the $\pm x$ directions and a y-dependent magnetic field that varies the detuning of the atomic states [133].

Time evolution is numerically performed with a split-step pseudo-spectral method, in which we apply the propagator of the GPE as $e^{-iHt} \sim e^{-i\widetilde{V}t/2} e^{2iA_x(y)\,p_x} e^{-ip^2/2M} e^{-i\widetilde{V}t/2}$, where $\widetilde{V}$ contains all the terms multiplicative in position space such as the external potential. As usual, the kinetic energy is included in a multiplicative way in Fourier space for both x, y. Thanks to the specific form $A_x(y)$ of the vector potential considered here, also this latter can be included in the calculation as a multiplicative factor provided the Fourier transforms along x and y are performed separately and the vector potential is applied in between to the partially Fourier transformed wavefunction $\tilde{\Psi}(k_x, y)$.

In order to study superradiance phenomena, we impose on top of the uniform condensate a small amplitude ($|\delta\Psi/\Psi_0| \ll 1$) wavepacket with a plane wave shape of wavevector

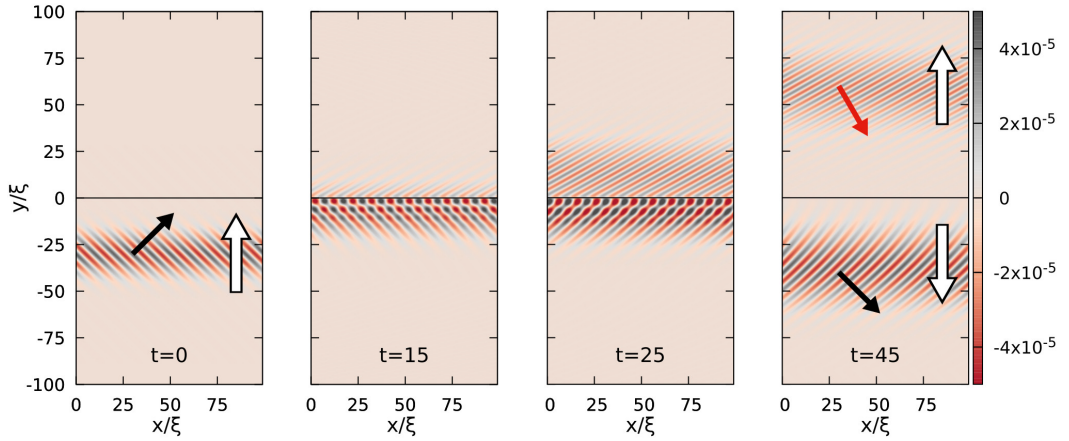

Figure 3.6: Snapshots of the time-evolution of a superradiant scattering process as predicted by a numerical simulation of the GPE. The color plot shows the spatial profile of the density modulation with respect to the uniform unperturbed BEC. We impose a perturbation wavepacket on top of a uniform BEC in the presence of a vector potential $A_x = -\pi M c_s$ in the $y > 0$ half-plane and a compensating external potential as specified in the text. The interaction constant g is spatially uniform, so to give a constant speed of sound c_s. The initial gaussian wavepacket has $k_x = 0.63/\xi$, a central $k_y = 0.63/\xi$ (indicated as dot in the dispersion plot of Fig.3.5(d)) and is spatially centered around $y = -30\xi$ with a variance $\sigma_y = 8\xi$. Times are expressed in units of $\mu/\hbar$. The white arrows indicate the group velocity of the wavepackets along y. The thick black (red) arrows indicate the directions of the wavevector (i.e. of the phase velocity) of the positive (negative) norm wavepackets. One can recognize the negative norm wavepacket from the opposite directions of the group velocity and of the wavevector along y. The simulations have been carried out in an integration box of size $L_x = 20\xi$ along x and $L_y = 200\xi$ along y. Grid spacings $\Delta x = \Delta y = 0.2\xi$ are taken and a time step $\Delta t = 10^{-3}\mu/\hbar$. Thanks to the periodic boundary conditions along x, visibility of the figure was improved by expanding the x domain by repeating the data multiple times.

k_x along x and a Gaussian shape along y with a carrier wavevector k_y. The variance σ_y is taken sufficiently small for the wavepacket to be localized in the $y < 0$ region, but large enough for the momentum distribution to be sharply peaked around the desired k_y. The central wavevector (k_x, k_y) is chosen to be on the positive-norm mode of the slower region with a group velocity directed towards the interface. In order to obtain a clean wavepacket of Bogoliubov excitations, positive and negative frequency components in the atomic basis must be suitably combined to only have positive frequencies in the Bogoliubov quasiparticle basis.

The value of the vector potential is chosen so to satisfy the condition (3.12) for amplification. In particular, the same parameters of Figure 3.5(d) are used; the chosen wavevector (k_x, k_y) is indicated there as a black dot. Since k_x and ω are conserved, we

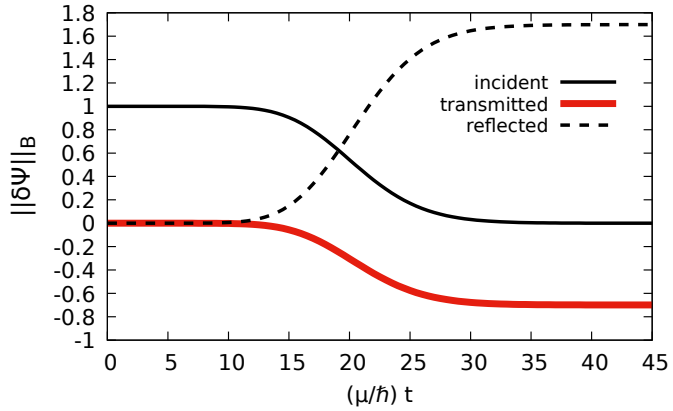

Figure 3.7: Time dependence of the Bogoliubov norm (3.17) of the wavepackets, normalized to the one of the initial in-going wavepacket, for the parameters of the simulation of Figure 3.6. One can see that the reflected wavepacket is amplified by roughly 70%.

expect that the wavepacket is transmitted in the faster region on the mode indicated by a red dot and located on the negative-norm (red) oval. At the same time, the amplified reflected wavepacket is expected to appear at the wavevector indicated by the black empty dot.

Snapshots of the time evolution for parameters for which one expects amplification are shown in Figure 3.6. For each wavepacket, the white arrows indicate the direction of the group velocity along y while the red and black arrows indicate the directions of the phase velocities. We can recognize the negative norm transmitted wavepacket in the upper region of the last snapshot from the fact that the y components of the phase and group velocities have opposite signs, as expected from the dispersion diagram of Fig.3.5(d). For all numerical wavepackets, a Fourier analysis confirms that their central wavevectors match the ones expected from the analytical dispersion relation shown in Fig.3.5(d).

To numerically verify that the expected amplification of the reflected wavepacket is indeed taking place one cannot simply look at the maximum of the wavepackets, since the presence of superluminal dispersion leads to a spreading of the wavepacket. One can instead compute the Bogoliubov norm of the wavepackets

$$||\delta\psi||_B(t) = \int \mathrm{d}k_y \left(|u(t,k_y)|^2 - |v(t,k_y)|^2 \right), \tag{3.17}$$

where u and v are the positive and negative frequency components of the wavepacket in the atomic basis and in the fluid reference frame. In practice, these two components can be isolated by computing the spatial Fourier transform of the two regions separately and identifying the components of wavevector $\pm k_x$. For our choice of a plane-wave along x, the positive and negative k_x wavevector components are in fact directly associated to the positive and negative frequency ones of (3.17). Within each region, the in-going and out-going wavepackets can be isolated since the peak of their momentum

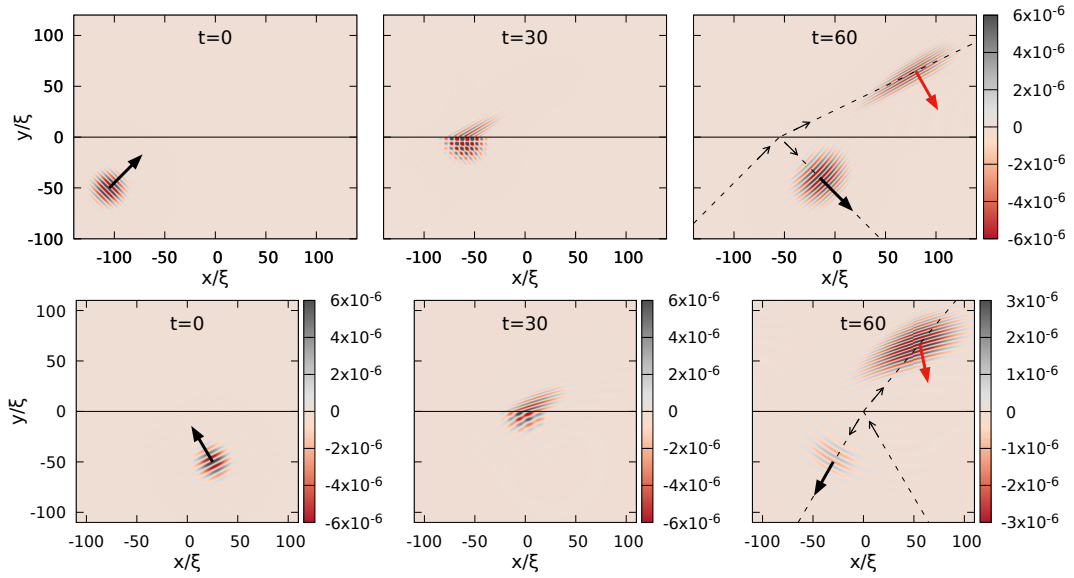

Figure 3.8: Upper panels: snapshots of the scattering process for the same configuration as in Figure 3.6 except for a finite width $\sigma_x = \sigma_y = 10\xi$ of the wavepacket along x. The integration box has the same size $L_y = 200\,\xi$ along y but a wider size $L_x = 200\,\xi$ along x. The color plot shows the spatial profile of the density modulation with respect to the uniform unperturbed BEC. The thick black and red arrows indicate the direction of the wavevector (i.e. of the phase velocity) of the positive-norm and negative-norm wavepackets, respectively. The dashed lines in the rightmost panels are the trajectories of the center of the wavepackets during the scattering and the thin arrows on them indicate the direction of the group velocities. Lower panels: analogous plots in the case of negative refraction. The vector potential in the upper region is $A_x = -1.26\ Mc_s$ and the initial gaussian wavepacket is centered in $k_x = 0.3/\xi$ and $k_y = 0.58/\xi$ and has variances $\sigma_x = \sigma_y = 10\ \xi$. Notice the different scale used in the bottom-right panel, showing the reduced amplitudes of the reflected and negative-refracted wavepackets as compared to the superradiant case shown in the upper-right panel.

distributions is located at values of k_y with opposite signs: for example the in-going initial wavepacket will have its positive frequency peak at (k_x, k_y^s) and its negative frequency one at $(-k_x, -k_y^s)$, while the out-going reflected one will have them respectively at $(k_x, -k_y^s)$ and $(-k_x, k_y^s)$.

The resulting time dependence of the norms of the different wavepackets is shown in Figure 3.7, where one can see that the reflected wavepacket is strongly amplified by approximately 70% as compared to the incident wavepacket. The negative value of the norm of the transmitted wavepacket exactly corresponds to the amplification, so that the total norm and energy are correctly conserved in the scattering process. This confirms the physical interpretation that the amplification of the reflected wavepacket is compensated by the storage of negative energy in the upper region.

While using a plane wave form along x was beneficial to draw the analogy with

the electrostatic problem and perform a quantitative study of the time-evolution of the norm, a clear intuitive picture of the scattering process can be obtained by performing an analogous calculation for a wavepacket of finite width also along x. Even though the mapping onto the electrostatic problem is no longer exact, the same energetic considerations hold. The result is shown in the upper panels of Figure 3.8, where the thick arrows again point in the direction of the phase velocity of the wavepacket while the thin ones along the dashed lines of the last panel indicate the direction of the group velocity. Even though the overall geometry of the scattering process closely resembles standard refraction, a computation the norm of the different wavepackets shows that the reflected wavepacket has indeed been amplified.

It is interesting to compare this scattering process with the negative refraction process [139] that takes place for different values of the incident wavevector and of the vector potential (lower panels). In this case, depicted in Fig.3.5(b), the incident wavepacket has a negative x-component of the group velocity, but the transmitted wavepacket is dragged back by the moving condensate towards the positive-x direction. Since no amplification is taking place, the reflected and transmitted intensities sum up to the incident one and the reflected and transmitted wavepackets are individually weaker than the incident one.

As a final remark, we need to emphasize that these simulations indicate that we are dealing with superradiant scattering from a dynamically stable interface: it is clear from the numerical GPE simulations that the interface quickly returns to its unperturbed state once the wavepackets have moved away from it. This numerical result will be confirmed by the Bogoliubov analysis presented in Sec.4.1.3, where we find no unstable modes on the surface. This is a key difference from the case of tangential discontinuities in hydrodynamics discussed in [95]. In this case, discontinuity surface is typically dynamically unstable and tends to quickly develop ripples that complicate the observation of superradiant amplification.

3.3 Scattering approach and spontaneous superradiance

In the previous Section we studied superradiant scattering in a two-dimensional BEC to which a synthetic vector potential $A_x(y)$ can be applied along x. We now want to give an explicit exact study of the Bogoliubov problem for the fluctuations' scattering in this configuration. We are going to construct the scattering modes and an input-output relation between them, analogously to what was done in [69] (and we summarized in Section 1.5). This will allow us to make predictions about the spontaneous quantum pair creation in the superradiant modes.

Again we consider the system divided in two regions with the synthetic gauge field taking a constant value in each: the *faster* one for $y > 0$ and the *slower* one for $y < 0$. For simplicity we will consider the case in which $A_x^s = 0$, also considering that the physics only depends on the gauge field difference between the two regions.

3.3.1 Kinematics

In each region the linear perturbations ϕ around the stationary state of the shape (1.17)

$$\Psi = \left(\sqrt{n} + \delta\psi\right) e^{-i\mu t/\hbar} \tag{3.18}$$

can be taken as momentum eigenstates, that is the usual Bogoliubov spinor $|\delta\psi\rangle$ can be taken of the form

$$\begin{pmatrix} \delta\psi \\ \delta\psi^* \end{pmatrix}(x,y) = e^{ik_x x + ik_y y} \begin{pmatrix} u_{\mathbf{k}} \\ v_{\mathbf{k}} \end{pmatrix} = |\mathbf{k}\rangle \tag{3.19}$$

The Bogoliubov problem takes the form $\hbar\omega\,|\mathbf{k}\rangle = \mathcal{L}\,|\mathbf{k}\rangle$, with

$$\mathcal{L} = \begin{bmatrix} \frac{\hbar^2}{2M}(k_x^2+k_y^2) + gn - \frac{\hbar}{M}A_x k_x & gn \\ -gn & -\left(\frac{\hbar^2}{2M}(k_x^2+k_y^2) + gn\right) - \frac{\hbar}{M}A_x k_x \end{bmatrix}. \tag{3.20}$$

As usual the dispersion relation in each region is obtained from the characteristic polynomial of this matrix and the result is (3.13)

$$\hbar\omega = -\frac{\hbar}{M}A_x k_x \pm \sqrt{\frac{\hbar^2}{2M}(k_x^2+k_y^2)\left(\frac{\hbar^2}{2M}(k_x^2+k_y^2) + 2gn\right)} = -\frac{\hbar}{M}A_x k_x \pm \mathcal{B}(k_x,k_y), \tag{3.21}$$

where the positive (negative) sign refers to positive (negative) norm modes and we defined the quantity $\mathcal{B}(k_x,k_y)$ for later convenience.

As above, we consider a translationally invariant system along x, so that k_x is a conserved quantity and we can treat the different k_x channels as separate one-dimensional problems along y. Through the identifications of Section 3.2.2 we know that in these one-dimensional problems the transverse momentum k_x plays the role of an effective mass gap in the dispersion and also of the charge coupling to the gauge field, giving a vertical shift of the dispersion curves. For present convenience we show in Figure 3.9 an example of these reduced dispersion relations in the two regions, analogous to the ones shown in Figure 3.4.

In each uniform region at fixed frequency the modes will be a combination of the plane waves written above. Since the Bogoliubov dispersion relation (3.21) is of the fourth-order in the momenta, at fixed ω and k_x, it will generally have 4 roots, that (for real frequencies) can be divided in a pair of real ones and a pair of complex conjugates ones or can all be complex (two pairs of complex conjugates). In the present case there are not frequencies to which four real roots correspond; this can happen for example if a supersonic velocity along y is present.

If we consider an unbound system in the y direction, we need to require for the modes to be bounded at infinity, this means that the imaginary part of the wavevectors must be non-negative in the upper region and non-positive in the lower region. Hence in the case of no real roots there will be two relevant (evanescent) modes while in the case of two real roots there will be one evanescent mode for a total of three physically relevant modes.

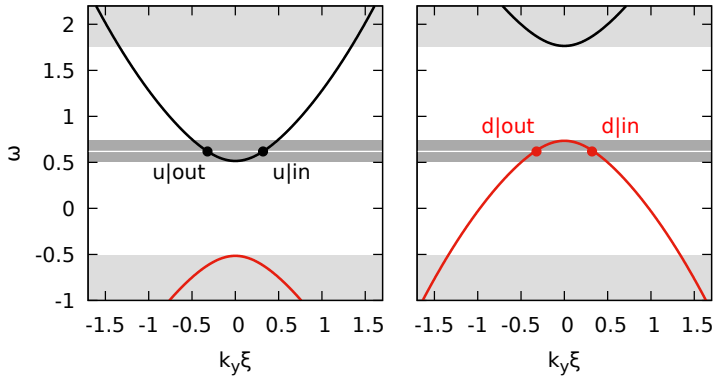

Figure 3.9: Dispersion relations in the two regions (the slower on the left and the faster on the right) for $k_x\xi = 0.5$, $A_x^f = -2.5\ Mc_s$ and $A_x^s = 0$. Black and red lines correspond to positive and negative norm modes. The light gray regions indicate the ordinary scattering ranges and the dark grey one the superradiant scattering range. The white line is an example frequency in the superradiant range individuating the associated scattering modes on the dispersions.

In general, as can be seen in Figure 3.9, there are no real roots in the *mass gap*

$$-\frac{\hbar}{M}A_x k_x - \mathcal{B}(k_x) < \hbar\omega < -\frac{\hbar}{M}A_x k_x + \mathcal{B}(k_x), \tag{3.22}$$

while above (below) it two real roots are present corresponding to positive (negative) norm modes.

We are interested in scattering configurations, that is physical situations in which a plane wave coming from infinity impinges on the interface between the two regions and is reflected and transmitted in other modes. From Figure 3.9 the different kinds of scattering that can occur can be identified, analogously to what we did for the constant-ω cuts of the dispersion relation of Figure 3.5. We focus on ingoing waves from the slower region, the other situation being analogous.

For frequencies above $-\frac{\hbar}{M}A_x^f k_x + \mathcal{B}(k_x)$ positive-norm modes are available in both regions and the incoming wave will be partially transmitted and partially reflected. An analogous behaviour occurs for $\hbar\omega < -\mathcal{B}(k_x)$ where negative-norm modes are available in both regions. We called this kind of same-norm scattering *ordinary scattering* (light gray regions in Figure 3.9).

For frequencies in the faster region mass gap (3.22) there is no available propagating mode to transmit so the incoming wave from the slower region will be *totally reflected*.

The most interesting regime is the one for

$$\mathcal{B}(k_x) < \hbar\omega < -\frac{\hbar}{M}A_x^f k_x - \mathcal{B}(k_x) \tag{3.23}$$

in which the incoming positive-norm mode can be transmitted to a negative energy one. We know that this is *superradiant scattering* (dark gray region in Figure 3.9) and

that it becomes possible when $\hbar|A_x^f|/M > 2c_s$. Also, remember that the superluminal behaviour of the Bogoliubov dispersion relation imposes the upper value (3.16) of the transverse momentum above which superradiant scattering is not possible.

3.3.2 Scattering approach

It is convenient to separate the non-evanescent modes in *ingoing* if their group velocity $v = \partial_y \omega$ is directed towards the interface and *outgoing* if it is directed away from it. In each of the two regions the fluctuation spinor field for frequencies at which there are real roots can hence be written as

$$\begin{pmatrix} u(y) \\ v(y) \end{pmatrix}_{k_x,\omega,I} = \mathcal{A}_I^{in} \begin{pmatrix} u_{k_I^{in}} \\ v_{k_I^{in}} \end{pmatrix} \frac{e^{ik_I^{in} y}}{\sqrt{2\pi|v_I^{in}|}} + \mathcal{A}_I^{out} \begin{pmatrix} u_{k_I^{out}} \\ v_{k_I^{out}} \end{pmatrix} \frac{e^{ik_I^{out} y}}{\sqrt{2\pi|v_I^{out}|}} + \mathcal{A}_I^{ev} \begin{pmatrix} u_{k_I^{ev}} \\ v_{k_I^{ev}} \end{pmatrix} \frac{e^{ik_I^{ev} y}}{\sqrt{2\pi}}, \tag{3.24}$$

where $I = s, f$ and the spinors on the right-hand side are normalized so that $|u_k|^2 - |v_k|^2 = \pm 1$. If instead no propagating modes are present the field will simply be the sum of two evanescent waves.

If not all the modes are evanescent, a scattering solution is obtained by selecting one ingoing mode ($s|in$ or $f|in$) and setting the other ingoing amplitude to zero (if present). For frequencies at which real momenta are present on both sides we can write the input-output relation connecting the outgoing modes amplitudes to the ingoing ones

$$\begin{pmatrix} \mathcal{A}_s^{out} \\ \mathcal{A}_f^{out} \end{pmatrix} = S(k_x, \omega) \begin{pmatrix} \mathcal{A}_s^{in} \\ \mathcal{A}_f^{in} \end{pmatrix}. \tag{3.25}$$

The scattering matrix $S(k_x, \omega)$ is interesting because the square moduli of the elements $|S_{IJ}|^2$ give the reflection or transmission amplitudes in the mode I for an incoming mode J. Moreover it has the following pseudo-unitarity property

$$S^\dagger \eta S = \eta, \tag{3.26}$$

where η is a diagonal matrix having as elements $+1$ for each positive-norm mode and -1 for each negative-energy one; this expresses norm (i.e. energy) conservation during the scattering.

Focusing on an ingoing positive-norm mode from the slower region, $\eta = \sigma_3$ or $\eta = I$ depending on the sign of the norm of the modes in the faster region region. From this one readily sees the occurrence of superradiance for $\eta = \sigma_3$ for which one obtains

$$|S_{ss}|^2 - |S_{fs}|^2 = 1 \tag{3.27}$$

telling us that the reflection coefficient $|S_{ss}|^2$ is greater than one, that is the reflected mode exceeds the incoming one in amplitude.

Notice that the normalization factors of the modes involving the group velocity in equation (3.24) is important to have the correct normalization of the scattering matrix and is obtained by requiring the full mode at fixed frequency is normalized to $\delta(\omega)$.

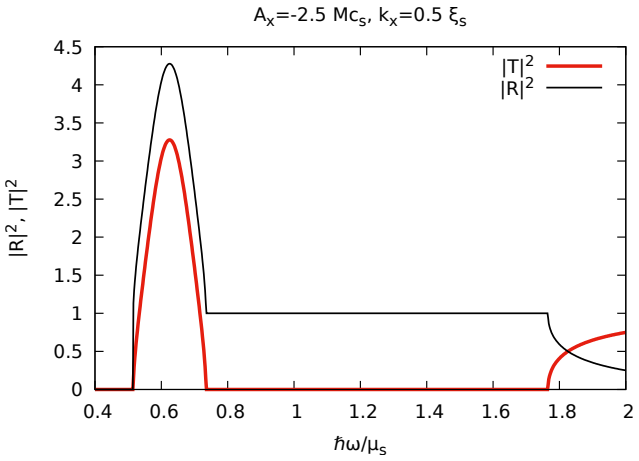

Figure 3.10: Reflection and transmission coefficients for $k_x = 0.5\xi$, $A_x^f = -2.5\ Mc_s$ and ingoing wave from the lower region.

3.3.3 Semi-analytical solution

The scattering formalism is quite general and not restricted to our flat-density and sharp-interface case. In our setup, as was also done in [69], we can however address this problem analytically by matching the analytical modes in the two uniform regions through continuity requirements at the interface.

An ingoing mode chosen, we have four mode amplitudes to determine to solve the scattering problem, divided between outgoing and evanescent modes. These latter do not enter in the scattering matrix relation since they are not relevant in the asymptotic regions, however they are important near the interface. The four conditions needed come from requiring the continuity of the two components of the fluctuation field (3.24) and its first derivative along y at the interface.

We can solve the modes matching linear problem by numerically finding the roots of the dispersion relations (3.21) at fixed ω, computing the group velocities and selecting the desired ingoing channel. We then keep in each region the two physically relevant (outgoing or evanescent) roots and numerically solve the corresponding linear problem for the mode amplitudes $\mathcal{A}_I^{out}$ and $\mathcal{A}_I^{ev}$. The amplitudes of the propagating modes are the coefficients of the scattering matrix.

The result of this procedure for an ingoing (positive-norm) wave from the lower region can be seen in Figure 3.10. The results can be understood by comparison with the dispersion relation plot of Figure 3.9. Below $\hbar\omega/\mu \simeq 0.5$ we are in the mass gap and there is no ingoing mode, while for $0.7 \lesssim \hbar\omega/\mu \lesssim 1.75$ there is no travelling mode in the upper region so one has a total reflection ($S(k_x, \omega) = [S_{ss}]$ with $|S_{ss}|^2 = 1$). For higher frequencies positive-norm travelling modes are available in the upper region and one has an ordinary scattering with reflection and transmission coefficients below one; for these frequencies the scattering matrix is unitary, i.e. $\eta = I$.

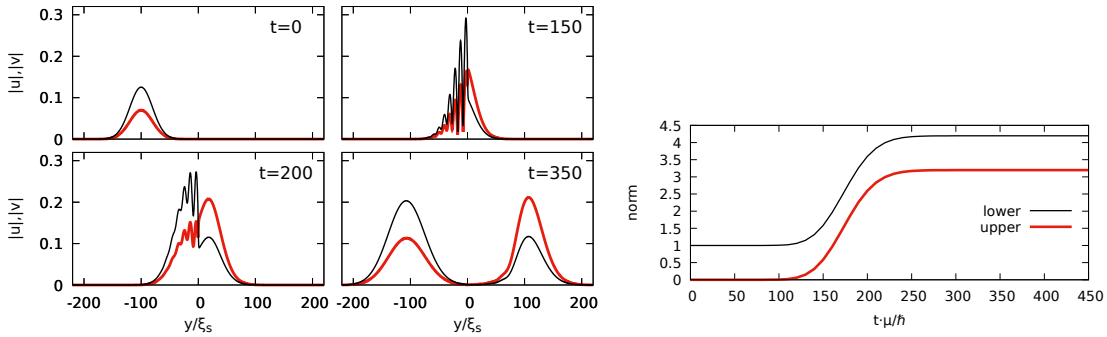

Figure 3.11: Left panels: superradiant scattering for $A_x^f = -2.5\ Mc_s$ of a wavepacket of transverse momentum $k_x\xi = 0.5$ and with momenta centered around $k_y^{in}\xi = 0.32$ ($\hbar\omega = 0.63\ Mc_s^2$). The initial wavepacket is centered in space around $y_0 = -100\ \xi$ with $\sigma = 20\ \xi$. One can clearly see that the positive-norm mode is transmitted to a negative-norm one and reflected with a larger amplitude. The amplification can measured by computing the total Bogoliubov norm (3.17) in the two regions, whose time dependence is shown in the right panel. The amplification coefficient is compatible with the maximum one predicted in Figure 3.10.

Between $\omega \simeq 0.5$ and $\omega \simeq 0.7$ instead negative-norm outgoing modes are available in the upper region: the scattering matrix is hence pseudo-unitary with $\eta = \sigma_3$ and, as expected, one has superradiant scattering with $|S_{uu}|^2 > 1$.

This approach gives us predictions of the amplification coefficients; an example of comparison of this prediction with the time-dependent scattering of wavepackets can be obtained for example by performing a time evolution such as the one of Figure 3.6. To offer a different picture of that process here we chose to evolve the Bogoliubov problem (3.20) in time starting from a wavepacket in the slower region with group velocity directed towards the interface. We performed such simulation with a third-order Runge–Kutta algorithm for the parameters giving Figure 3.10 and for a packet peaked around the frequency of maximum of the reflection coefficient and found a compatible amplification coefficient above 4. This numerical study is summarized in Figure 3.11.

Notice that the solution of the scattering problem with the ingoing (negative-norm) wave from the faster region gives the same reflection coefficient in the superradiant interval, meaning that the magnitude of superradiant amplification does not depend on the direction in which the interface is crossed. This is a consequence of the pseudo-unitarity of the scattering matrix that implies

$$|S_{ud}|^2 = |S_{du}|^2. \tag{3.28}$$

The k_x dependence of superradiant scattering can be investigated by solving the above problem at fixed A_x^f for different values of the transverse momentum. In Figure 3.12 one can see that the maximum of the reflection coefficient decreases when increasing k_x, while the superradiant region widens. For even higher values of the transverse momentum the maxima continue to decrease but the superradiant region shrinks again

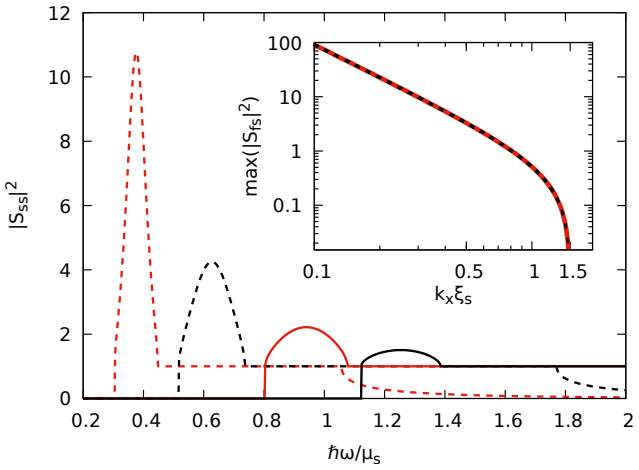

Figure 3.12: Main plot: reflection coefficients for an ingoing wave from the lower region for different values of k_x with $A_x^f = -2.5\ Mc_s$. The maxima from left to right correspond to $k_x\xi = 0.3,\ 0.5\ , 0.75,\ 1$. Inset: log-log plot of the dependence on k_x of the maxima of the transmission coefficient. The solid red line are the numerical data, the superimposed black dashed one is a fit of the shape $\frac{\alpha}{k_x^2} - \beta$, precisely replicating the data.

and vanishes at the dispersive suppression threshold (3.16). Extracting the maxima of the transmission coefficient for each value of k_x gives the plot in the inset of Figure 3.12. The maximum transmission, and hence the maximum superradiant amplification, goes as $1/k_x^2$ minus some constant that makes it vanish at the dispersive suppression threshold, here approximately at $k_x\xi = 1.5$.

3.3.4 Quantum description and spontaneous pair production

In our study of superradiance up to now we treated fluctuations as a classical field, relying on the fact that superradiance, differently from, for example, Hawking radiation, is a classical field effect. As we said in Chapter 2, upon quantization of the field undergoing amplified scattering one expects spontaneous quantum pair production in the modes responsible for superradiance. This is essentially superradiant scattering of vacuum fluctuations, that end up populating the opposite-normed outgoing modes. The prediction of this spontaneous emission can be obtained from the quantum equivalent of the scattering approach we just presented.

We know that fluctuations around a stationary state of a BEC can be described by a bosonic quantum field $\hat{\Psi} = \Psi_0 + \delta\hat{\Psi}$, where the order parameter Ψ_0 describing the condensate continues to be treated as a classical field and the quantum behaviour is encoded in the fluctuations.

After choosing a mode basis for the field, in the second quantization procedure annihilation operators are associated to positive-norm modes and creation operators to

negative-norm ones, as explained in Section 1.1.4. It is convenient for our purposes to quantize the field in the asymptotic regions using, for each ω, the basis of ingoing or outgoing modes.

Given the different kinds of scattering, for different frequency ranges the modes need to be quantized differently. For simplicity we express here only the field component for frequencies in the superradiant range, that we call $\delta\hat{\Psi}^{SR}(y)$, and comment on the other regimes when needed.

The quantum field has two equivalent expressions, one in terms of ingoing modes

$$\delta\hat{\Psi}^{SR}(y) = \int_0^{k_x^{max}} \mathrm{d}k_x \int_{\mathcal{B}(k_x)}^{-A_x k_x - \mathcal{B}(k_x)} \mathrm{d}\omega \; [u_{s|in}(k_x,\omega,x)\hat{a}_s(k_x,\omega) + v^*_{s|in}(k_x,\omega,x)\hat{a}^\dagger_s(k_x,\omega) + u_{f|in}(k_x,\omega,x)\hat{a}^\dagger_f(k_x,\omega) + v^*_{f|in}(k_x,\omega,x)\hat{a}_f(k_x,\omega)], \tag{3.29}$$

and the analogous one in terms of outgoing modes, whose annihilation operators we instead indicate with $\hat{b}_I(\omega)$. A relation between the two sets of operators is given by the input-output relation (3.25) that here becomes

$$\begin{pmatrix} \hat{b}_s(k_x,\omega) \\ \hat{b}^\dagger_f(k_x,\omega) \end{pmatrix} = S(k_x,\omega) \begin{pmatrix} \hat{a}_s(k_x,\omega) \\ \hat{a}^\dagger_f(k_x,\omega) \end{pmatrix} \quad \text{for} \quad \mathcal{B}(k_x) < \hbar\omega < -\frac{\hbar}{M}A_x k_x - \mathcal{B}(k_x). \tag{3.30}$$

The fact that the modes in the faster region appear with a creation operator is a consequence of their negative norm.

Instead, the field component coming from the frequency range of ordinary scattering, where the available modes in the faster region have a positive norm, does not show the exchange of creation and annihilation operators of the second line of (3.29) and the input-output relation given by the (unitary) scattering matrix is simply

$$\begin{pmatrix} \hat{b}_s(k_x,\omega) \\ \hat{b}_f(k_x,\omega) \end{pmatrix} = S(k_x,\omega) \begin{pmatrix} \hat{a}_s(k_x,\omega) \\ \hat{a}_f(k_x,\omega) \end{pmatrix} \quad \text{for} \quad \hbar\omega > -\frac{\hbar}{M}A^f_x k_x + \mathcal{B}(k_x). \tag{3.31}$$

Notice that this last equation expresses the fact that the representations in terms of input and output modes of the quantum field are unitarily equivalent, while in equation (3.30) the mixing of creation and annihilation operators indicates the inequivalence of the two representations. This is the mathematical fact at the basis of particle creation effects in quantum field theories in curved spacetimes (see for example [61]).

As for the case of Hawking radiation presented in Section 1.5, the spontaneous emission is given by the appearance in equation (3.30) of the creation operators for the modes in the faster region. Focusing in particular on the flux of outgoing phonons in the slower region and using the input-output relation one obtains

$$\langle \hat{b}^\dagger_s(k_x,\omega)\hat{b}_s(k_x,\omega)\rangle = |S_{ss}|^2 \langle \hat{a}^\dagger_s(k_x,\omega)\hat{a}_s(k_x,\omega)\rangle + |S_{sf}|^2 \left(1 + \langle \hat{a}^\dagger_f(k_x,\omega)\hat{a}_f(k_x,\omega)\rangle\right), \tag{3.32}$$

where the one in the last term comes from the commutation of the negative-norm operators. Because of this constant term, even if the initial populations of the ingoing modes

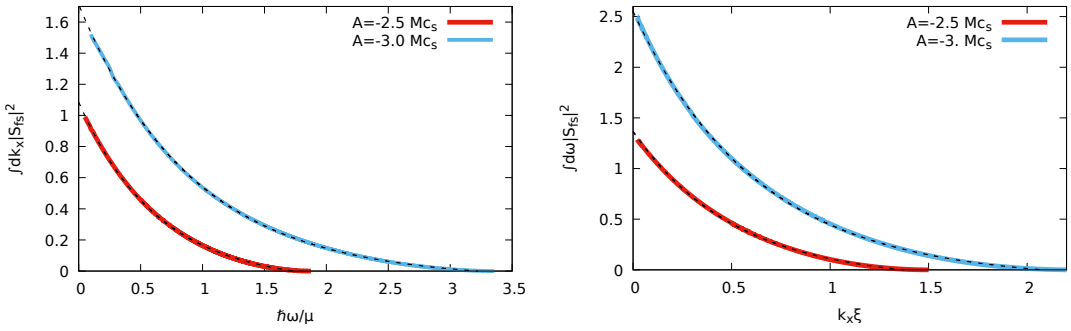

Figure 3.13: Spontaneous emission spectrum (left) and transverse momentum distribution (right) for different values of the gauge field. The superimposed black dashed lines are fits of the numerically obtained data of the shape $f(\omega) = \alpha \exp(-\beta\omega) - \gamma$ (and analogous expression with k_x instead of ω) with α, β, γ positive parameters and describe very well the numerical data. As expected the quantum emission is nonzero only below the dispersive threshold.

is zero (for example at zero temperature), the population of the outgoing modes will be finite. Analogously the outgoing mode in the faster region will have the same zero temperature population because of the symmetry (3.28) of the scattering matrix.

Notice that in the case of ordinary scattering (3.31), since no creation operator enters in the input-output relation, there will be no spontaneous emission. Similarly, in the case of total reflection the input-output relation reduces to $\hat{b}_I(k_x, \omega) = S(k_x, \omega)\hat{a}_I(k_x, \omega)$ and no spontaneous emission can occur.

The emission spectrum for each k_x is hence given by the superradiant *bump* of the transmission coefficient in Figure 3.10. The overall emission spectrum can be obtained by integrating in k_x the transmission coefficient $|S_{sf}(k_x, \omega)|^2$ considering only the superradiant frequency ranges. We computed this with the elements of the scattering matrix obtained from the scattering approach and the result is shown in Figure 3.13, in which one can see that the spectrum of the spontaneous emission has a decreasing exponential behaviour. Analogously, the transverse momentum distribution of the spontaneous emission is obtained by integrating $|S_{sf}(k_x, \omega)|^2$ in ω and shows the same kind of behaviour.

3.3.5 Density-density correlations in position space

As in the case of Hawking radiation, an interesting observable quantity to detect spontaneous pair creation are the correlations between the emitted particles in the two regions. These are usually easier to detect than the emission spectrum, that is easily hidden by noise in the system and were at the heart of the experimental observation of Hawking emission in a BEC [5, 17, 18]

These appear, as a simplest example, as features in density correlation function, that

is expressed in terms of the quantum field $\hat{\Psi} = \Psi_0 + \delta\hat{\Psi}$ as the normal ordered product

$$G^{(2)}(y,y') = \langle \hat{\Psi}^\dagger(y)\hat{\Psi}^\dagger(y')\hat{\Psi}(y')\hat{\Psi}(y)\rangle - \langle \hat{\Psi}^\dagger(y)\hat{\Psi}(y)\rangle \langle \hat{\Psi}^\dagger(y')\hat{\Psi}(y')\rangle . \tag{3.33}$$

Keeping only the terms of the second order in the fluctuation field one obtains

$$G^{(2)}(y,y') = \langle \delta\hat{\Psi}(y')\delta\hat{\Psi}(y)\rangle + \langle \delta\hat{\Psi}^\dagger(y')\delta\hat{\Psi}(y)\rangle + \langle \delta\hat{\Psi}^\dagger(y)\delta\hat{\Psi}(y')\rangle + \langle \delta\hat{\Psi}^\dagger(y)\delta\hat{\Psi}^\dagger(y')\rangle . \tag{3.34}$$

It is convenient for us to expand the correlation function in its ω and k_x components

$$G^{(2)}(y,y') = \int_0^\infty \frac{\mathrm{d}k_x}{2\pi} \int_{-\infty}^{\infty} \mathrm{d}\omega \; G^{(2)}(k_x,\omega,y,y'), \tag{3.35}$$

so that we can use the scattering formalism to evaluate the single components.

We can notice that the emission predicted in equation (3.32) is composed, as expected, by pairs of modes, one in each region. In fact with an analogous argument we find

$$\langle \hat{b}_s^\dagger(k_x,\omega)\hat{b}_f^\dagger(k_x,\omega)\rangle = S^*_{sf}S_{ff}, \tag{3.36}$$

so that we expect to find nontrivial correlations between the density fluctuations in the two regions.

Consider then the correlations between points $y' > 0$ in the faster region and $y < 0$ in the slower region, that are the ones that should bring the signs of superradiant emission, starting from frequencies laying in the superradiant range. We can insert the field expansion (3.29) in (3.34). Since we are interested in the correlations in the outgoing modes due to the quantum fluctuations in the vacuum of the ingoing ones, the idea is to insert the field expansion in terms of outgoing modes and then use the input-output relation (3.30).

Note that for $y < 0$ ($y' > 0$) only the mode of the slower (faster) region will be present, so that

$$\begin{aligned} \delta\hat{\Psi}_{SR}(k_x,\omega,y<0) &= u_{s|out}(k_x,\omega,y)\hat{b}_s(k_x,\omega) + v^*_{s|out}(k_x,\omega,y)\hat{b}_s^\dagger(k_x,\omega) \\ \delta\hat{\Psi}_{SR}(k_x,\omega,y'>0) &= u_{f|out}(k_x,\omega,y')\hat{b}_f^\dagger(k_x,\omega) + v^*_{f|out}(k_x,\omega,y')\hat{b}_f(k_x,\omega). \end{aligned} \tag{3.37}$$

Substituting the input output relation, keeping only the quantum fluctuations terms coming from commutators and using the pseudo-unitarity of the scattering matrix and the u and v components of the plane wave expansion (3.24) we obtain

$$\begin{aligned} G^{(2)}_{SR}(k_x,\omega,y<0,y'>0) =& \frac{r_{k_s^{out}}(k_x,\omega)r^*_{k_f^{out}}(k_x,\omega)}{2\pi\sqrt{|v_s^{out}v_f^{out}|}} \\ & \times S_{sf}(k_x,\omega)S^*_{ff}(k_x,\omega)\; e^{i[k_s^{out}(k_x,\omega)y - k_f^{out}(k_x,\omega)y']} + c.c. \end{aligned} \tag{3.38}$$

where $r_I = u_I + v_I$. This expression is completely analogous to the one obtained for Hawking radiation in [69].

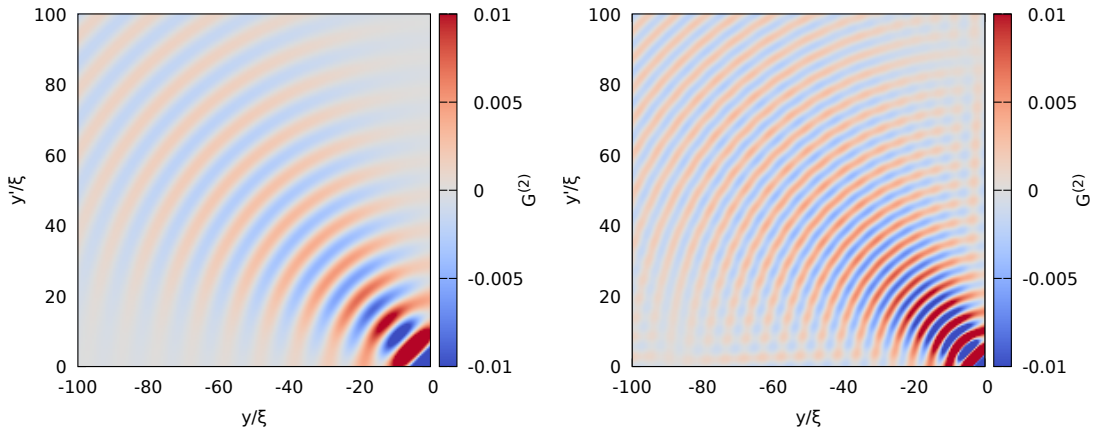

Figure 3.14: Zero temperature density-density correlation functions between the slower $y < 0$ region and the faster $y' > 0$ region computed using the scattering approach. The two panels correspond to $A_x = -2.5\ Mc_s$ and $A_x = -3\ Mc_s$. The oscillating feature is an indication of quantum pair production in the superradiant modes.

The superradiant frequency range is the only source of correlations between the slower and faster regions, since performing the same calculations for ordinary scattering (3.31) shows that its contribution to the correlation function vanishes because of the unitarity of the scattering matrix. This was expected since we saw that pair production only occurs for superradiant frequencies.

Expression (3.38) can hence be used to compute numerically the faster-slower density correlation function starting from the scattering matrix components we obtained in the previous sections. Notice that the use of the scattering approach gives a reliable result only far enough from the interface, since the evanescent modes are not taken into account.

In Figure 3.14 we show the resulting faster-slower correlation pattern, obtained by integrating the result of (3.38) in k_x and ω. This shows an oscillating behaviour with a wavelength decreasing when the gauge field A_x increases. The correlations seem to be nontrivial for all the $y < 0$ and $y' > 0$, decreasing in amplitude while approaching the axes $y = 0$ and $y' = 0$, and maximal for $y = y' = 0$.

In [69] an explanation of the maxima and minima of the density correlations was given in terms of the group velocities of the modes responsible for the correlation feature. In particular extrema of correlation are expected for $y' = (v_f^{out}/v_s^{out})y$. Focusing on a fixed k_x, from the dispersion relations of Figure 3.9 one can see that in the superradiant frequency range, with increasing frequency, v_s^{out} goes from zero to some maximum value, while v_f^{out} goes from the same maximum value to zero. Hence the slope v_f^{out}/v_s^{out} of the lines on which one expects correlation extrema varies from $-\infty$ to 0, thus spanning the whole $(y < 0, y' > 0)$ range, as we observe.

The oscillations in the correlation pattern are instead due to the difference between the outgoing momenta on the two sides. This can be easily understood considering a

simpler version of this problem: the massless Klein paradox of Section 2.1.1. We know that the massive Klein paradox is exactly equivalent to superradiance in our setup in the hydrodynamic limit with the identifications (3.10); by considering the massless case we are removing, together with the dispersive nature of the field, also the mass gap, so that the dispersion relations in the two regions are simply linear, with the one in the faster region being vertically shifted by the electrostatic field.

An estimate of the spatial dependence of the correlation function in this simplified case can be obtained by integrating in frequencies the plane wave factors of equation (3.38). The outgoing wavevectors will be $k_s^{out} = -\omega$ and $k_f^{out} = \omega - eA_0$ and the superradiant frequency range goes from 0 to eA_0, so that

$$G^{(2)}(e, y, y') \sim \int_0^{eA_0} \mathrm{d}\omega \; e^{i(-\omega y - (\omega - eA_0)y')} + c.c \propto \cos\left(\frac{eA_0}{2}(y - y')\right) \mathrm{sinc}\left(\frac{eA_0}{2}(y + y')\right). \tag{3.39}$$

The cardinal sine function gives the localization of the correlation features with the maximum intensity around the line $y' = -y$, as expected from the fact that all excitations have the same group velocity. The cosine instead causes oscillations along that line, and are exactly the ones we observe in the more complex case with mass gaps and nonlinear dispersion.

Also notice that Figure 3.14 is the result of an integration over k_x, each k_x component of the correlation function having a different oscillation wavenumber. The predominant observed oscillations are hence the ones to the transverse momenta dominating the superradiant emission, that is the k_x for which the factors multiplying the plane waves in equation (3.38) are maximal.

We hence have a qualitative understanding of the meaning of this correlation function. However its features are not as easy to look for experimentally as are the ones in the Hawking case in one dimension [69]. In that case in fact the non-gapped sonic dispersion relations (Figure 1.4) result in characteristic straight-line features in the position space density correlations that readily displays the presence of spontaneous pair production.

3.3.6 Two-body correlations in momentum space

As we just discussed, correlations in position space are not the ideal observable for an experimental investigation of *spontaneous superradiant emission*. A perhaps more promising quantity are the two-body correlations in momentum space. The relevant quantity is

$$G^{(2)}(k_y, k'_y) = \langle \delta\hat{\Psi}^\dagger(k_y)\delta\hat{\Psi}^\dagger(k'_y)\delta\hat{\Psi}(k'_y)\delta\hat{\Psi}(k_y)\rangle, \tag{3.40}$$

involving correlations only between non condensed atoms since the condensed ones only live in the zero momentum state (see for example [141] for a complete explanation). These are hence of higher order in the fluctuations but are expected to give a cleaner signal.

We can obtain a semi-analytical formula for this quantity using again the scattering approach. At fixed k_x and ω the dispersion relation fixes the values of the outgoing

momenta $k_s^{out}(k_x,\omega)$ and $k_f^{out}(k_x,\omega)$ so that the correlations will be nonzero only for these value of the momenta: if one measures the momentum k_y in the slower region and the momentum k'_y in the faster one we will have

$$G^{(2)}(k_x,\omega,k_y,k'_y) \propto \delta(k_y - k_s^{out}(k_x,\omega))\delta(k'_y - k_f^{out}(k_x,\omega)). \tag{3.41}$$

Integrating over ω the points in which these correlations are nonzero will hence describe, at fixed k_x a line in the (k_y,k'_y) space and, letting k_x vary, a surface in the (k_y,k'_y,k_x) space that we expect to be the most recognizable feature of spontaneous emission in the superradiant channels.

Through a Wick expansion one can express the quartic correlator (3.40) in terms of products of second order ones (in the following formulas we omit, for simplicity, the fact that we are considering the correlators at fixed k_x and ω)

$$G^{(2)}(k_y,k'_y) = \left|G^{(1)}(k_y,k'_y)\right|^2 + G^{(1)}(k_y,k_y)G^{(1)}(k'_y,k'_y) + \left|A^{(1)}(k_y,k'_y)\right|^2, \tag{3.42}$$

where

$$G^{(1)}(k_y,k'_y) = \langle \delta\hat{\Psi}^\dagger(k_y)\delta\hat{\Psi}(k'_y)\rangle; \qquad A^{(1)}(k_y,k'_y) = \langle \delta\hat{\Psi}(k_y)\delta\hat{\Psi}(k'_y)\rangle. \tag{3.43}$$

Expressions of these correlators at fixed k_x and ω for the momenta showing nonzero correlations can be obtained with a procedure analogous to the one we used for the correlations in position space. As done above, we only keep the terms due to commutators, that are due to vacuum quantum fluctuations at zero temperature. The results are

$$\left|A^{(1)}(k_y,k'_y)\right|^2 = 2\Re\left(u_s^* v_s^* u_f v_f (S_{sf}^* S_{ff})^2\right) + \left(|u_s|^2|v_f|^2 + |v_s|^2|u_f|^2\right)|S_{sf}|^2|S_{ff}|^2 \tag{3.44}$$

$$\left|G^{(1)}(k_y,k'_y)\right|^2 = 2\Re\left(u_s^* v_s^* u_f v_f (S_{sf}^* S_{ff})^2\right) + \left(|u_s|^2|u_f|^2 + |v_s|^2|v_f|^2\right)|S_{sf}|^2|S_{ff}|^2 \tag{3.45}$$

$$G^{(1)}(k_y,k_y)G^{(1)}(k'_y,k'_y) = \left(|u_s|^2\left|S_{sf}^2\right| + |v_s|^2\left|S_{ff}^2\right|\right)\left(|u_f|^2\left|S_{ff}^2\right| + |v_f|^2\left|S_{sf}^2\right|\right). \tag{3.46}$$

We can compute numerically the locus of points in momentum space for which the two-body momentum correlations are nonzero and the value of the correlations there. The result, for the normalized correlation function

$$g^{(2)}(k_y,k'_y) = \frac{G^{(2)}(k_y,k'_y)}{G^{(1)}(k_y,k_y)G^{(1)}(k'_y,k'_y)}, \tag{3.47}$$

is the surface shown in the left plot of Figure 3.15. The fact that the surface folds above itself for higher transverse momenta is due to the superluminal behaviour of the Bogoliubov dispersion, that poses an upper bound on the transverse momenta for which there can be superradiant scattering, and hence spontaneous emission.

One can see that the normalized correlation function is maximal for higher values of k_x. The unnormalized one is instead very much peaked for small k_x. Meaning that,

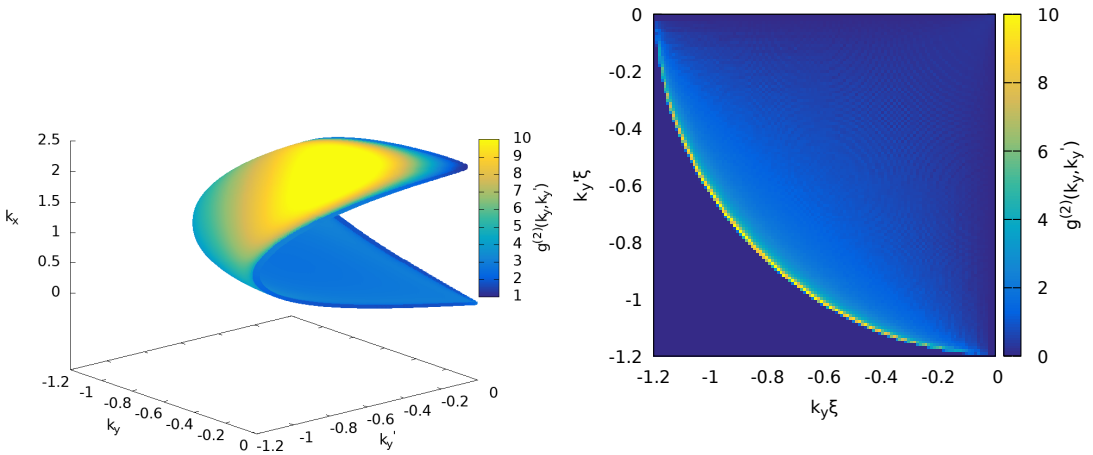

Figure 3.15: Two body correlations in momentum space. On the left the surface described by the points in momentum space between which there is correlation. On the right the same correlations integrated along k_x.

as expected from the behaviour of the scattering matrix elements for small k_x shown in Figure 3.12, the number of emitted couples is much higher for smaller transverse momenta.

Integrating over k_x one obtains the overall correlations for momenta along y, shown in the right part of Figure 3.15. One can see that the normalized correlations are dominated by the *folding* region of the surface of Figure 3.15.

3.4 Superradiant scattering from a lattice region

As a last topic in this Chapter, let us present an alternative setup in which a *planar ergosurface* can be obtained.

Another way to circumvent the irrotationality condition for the velocity of the condensate is to realize that this condition is on the gradient of the phase $\Theta(\mathbf{r})$ of the condensate, while the velocity is $\mathbf{v} = \hbar\nabla\Theta/M$. Hence one can think of modifying the dispersion relation of the atoms so to change their effective mass differently in the two regions, thus changing the velocity while maintaining $\nabla\Theta$ constant along y.

This can be obtained for example by putting an atomic Bose–Einstein condensate inside an optical lattice [19], that is a periodic potential obtained with counterpropagating laser beams. The stationary Gross–Pitaevskii equation in this kind of potentials admits, as in the well known case of the Schrödinger equation in solid state physics, solutions in the form of Bloch waves and results in a band structure of the dispersion relation of the atoms [142]. The stationary states can hence be labeled with the band index and the quasi-momentum K of the condensate (indicated with a capital letter to distinguish it from the one of the perturbations).

Considering the dispersion relation $\varepsilon(K)$ for the atoms of a one-dimensional con-

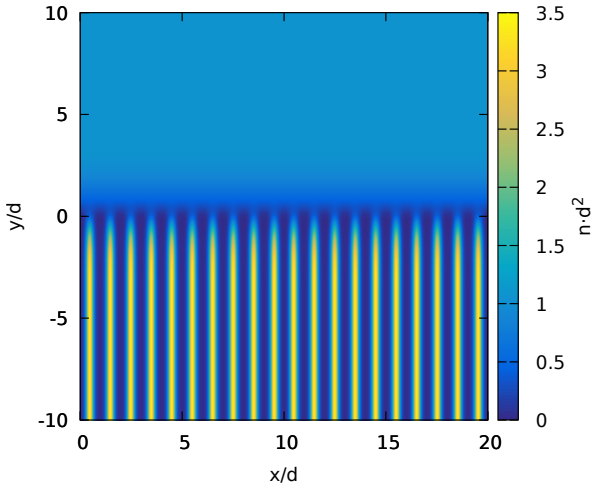

Figure 3.16: Density of a two-dimensional BEC with an optical lattice of depth $s = 12$ in the region $y < 0$ and no external potential for $y > 0$. A constant negative shift of the potential in the lower is applied to keep a constant average density. A smooth transition between the two regions with a hyperbolic tangent profile is used. Lengths are expressed in units of the lattice spacing d.

densate in a given band, the periodic potential results in a K-dependent effective mass $M^*(K)$ and a velocity of the condensate given by

$$\frac{1}{M^*(K)} = \frac{\partial^2 \varepsilon}{\partial K^2} \; ; \qquad v(K) = \frac{\partial \varepsilon}{\partial K}. \tag{3.48}$$

The chemical potential is instead

$$\mu(K) = \frac{\partial [n\varepsilon(K)]}{\partial n}, \tag{3.49}$$

with n the average density of the condensate. From the chemical potential one can get the compressibility and, hence, the speed of sound

$$\kappa^{-1} = n\frac{\partial \mu}{\partial n} \; ; \qquad c = \frac{1}{\sqrt{\kappa M^*}}. \tag{3.50}$$

As discussed in [142], a condensate of quasi-momentum K in an optical lattice has a lower velocity than a free condensate of momentum K, and making the optical lattice deeper makes the condensate velocity decrease, as anticipated from our intuitive considerations regarding the effective mass.

A possible approximate realization of our planar ergosurface is hence a two-dimensional condensate with no external potential for $y > 0$ and subject instead to an optical lattice periodic along x (and uniform along y) for $y < 0$, as in Figure 3.16. By imposing an

overall phase to the condensate order parameter one can obtain a stationary state of the shape

$$\Psi(x,y) = e^{iKx}\ \widetilde{\Psi}(x,y), \tag{3.51}$$

with $\widetilde{\Psi}(x,\cdot)$ a periodic Bloch function for $y<0$ and uniform for $y>0$. The velocity in the uniform part of the system $v_x^f = \hbar K/M$ may be taken to be supersonic and the lattice in the other region deep enough to make this subsonic.

Notice however that, as shown in [142] for the $K=0$ case, also the speed of sound is affected by the periodic potential, decreasing for deeper lattices. To verify the feasibility of our idea a study of the dispersion relation of fluctuations is hence in order, starting from the one in a one-dimensional periodic BEC.

3.4.1 One-dimensional dispersion relation

Consider the one-dimensional GPE describing a condensate in an external periodic potential of the shape

$$V(x) = sE_R \sin^2\left(\frac{\pi x}{d}\right), \tag{3.52}$$

where d is the lattice spacing, $E_R := q_B^2/(2m)$ is the recoil energy (with the Bragg momentum $q_B := \hbar\pi/d$) and s is an adimensional number characterizing the lattice depth.

The dispersion relation of acoustic perturbations on a condensate in an optical lattice is not simply the Bogoliubov one for a uniform medium (1.85) with different condensate velocity and speed of sound, in fact the periodicity introduces a band structure also for the fluctuations (and other features such as peculiar dynamical instabilities [19]). As for the condensate wavefunction, the Bogoliubov vectors can be expressed as Bloch waves, labeled by a band index and a quasi-momentum

$$|\delta\psi_{jk}\rangle = e^{ikx}\begin{pmatrix}\widetilde{u}_{jk}(x)\\ \widetilde{v}_{jk}(x)\end{pmatrix} \tag{3.53}$$

where $\widetilde{u}_{jk}(x)$ and $\widetilde{u}_{jk}(x)$ are periodic with the lattice period. The dispersion relation we are interested in is the one connecting the frequency of the excitations to the quasi-momentum k.

This dispersion relation can be computed numerically. We start with an imaginary-time evolution of the GPE in the periodic potential (3.52) (over a multiple of the potential period with periodic boundary conditions) to find the stationary state $\Psi(x) = e^{iKx}\ \widetilde{\Psi}_K(x)$ at fixed quasi-momentum K. We then evolve in time this wavefunction adding a small ($|\delta\Psi/\Psi| \ll 1$) delta-function perturbation so to sample all the possible momenta. The dispersion relation is then obtained by Fourier-transforming the whole evolution both in space and in time.

Examples of the resulting plots for a condensate at rest, that is with $K=0$, is shown in Figure 3.17, where the effect on the lowest band of the dispersion relation of deepening the lattice at fixed background quasi-momentum is shown. The top-left

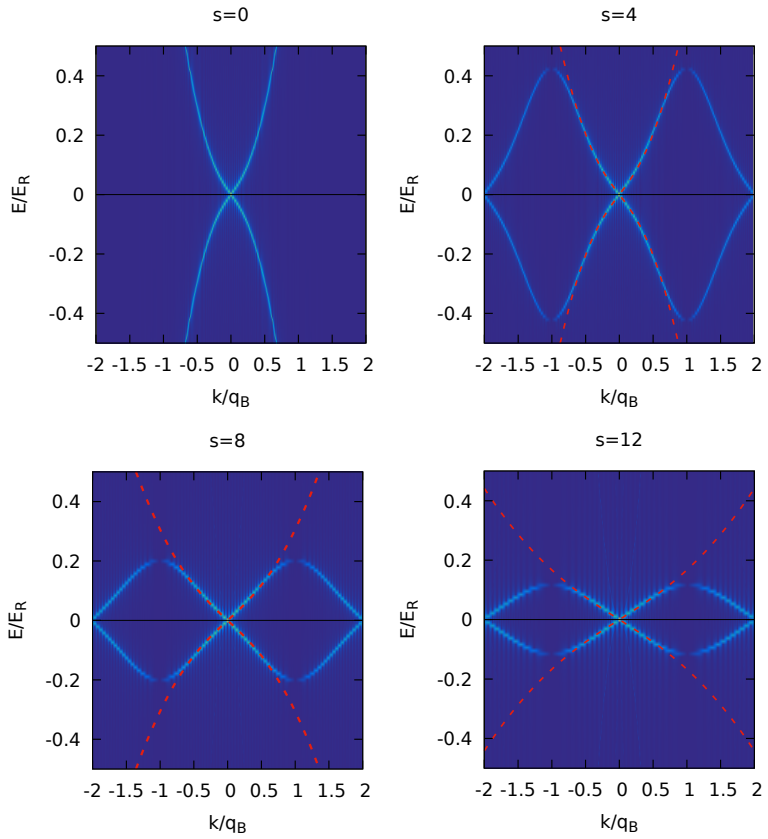

Figure 3.17: Dispersion relations of the elementary excitations for interaction $gn = 0.05\ E_R$ and zero quasi-momentum K of the background condensate for different values of the lattice depth s. The first graph refers to the case without a lattice, that gives simply a Bogoliubov dispersion relation. The dashed red lines are analytical plots of the Bogoliubov dispersion relation in which modified values of the effective atomic mass and of the speed of sound with respect to the uniform case are used. In particular, if M is the *bare* atomic mass and c_0 refers to a uniform condensate, for $s = 4$: $M^* = 1.8M$ and $c = 0.97c_0$, for $s = 8$: $M^* = 4.5M$ and $c = 0.82c_0$, for $s = 12$: $M^* = 12M$ and $c = 0.68c_0$.

plot ($s = 0$) corresponds to no lattice and is evidently a Bogoliubov dispersion in a uniform BEC at rest. In the other panels one can see how the presence of a lattices changes (lowest band of) the dispersion relations. The superimposed red dashed lines are analytical plots of the Bogoliubov dispersion relations in which values of the *effective* atomic mass and of the speed of sound different from the ones of the free condensate are used; in particular when deepening the lattice the effective atomic mass increases and the speed of sound decreases. One can see how these curves approximate well the dispersion relation until the edge of the Brillouin zone is reached.

In Figure 3.18 instead, the same kind of plots are shown in the presence of a nonzero

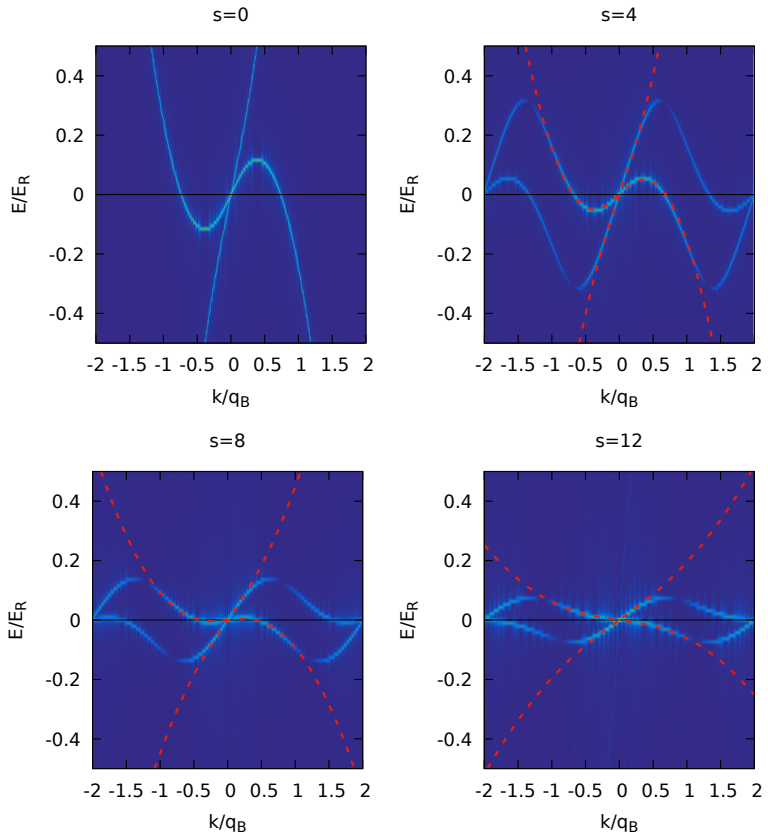

Figure 3.18: Plots analogous to the ones of Figure 3.17 but for nonzero quasi-momentum of the background condensate $K = 0.4\ q_B$. One can see how it is possible to pass from a supersonic to a subsonic regime at fixed quasi-momentum K by increasing the lattice depth. The dashed red lines are again approximations with Bogoliubov dispersion relations with modified mass and reduced speed of sound. For $s = 4$: $M^* = 1.8M$ and $c = 0.85$, for $s = 8$: $M^* = 4.5M$ and $c = 0.70c_0$, for $s = 12$: $M^* = 12M$ and $c = 0.55c_0$.

background quasi-momentum $K = 0.4\ q_B$. The $s = 0$ untrapped case gives a Doppler-shifted Bogoliubov dispersion relation in a supersonic flow. Introducing the lattice makes the effective mass of the atoms increase, correspondingly the velocity of the condensate decreases. While deepening the lattice also the speed of sound decreases, but less than the velocity, so that it is possible to pass from a supersonic flow to a subsonic one. In fact, for a deep enough lattice $s = 12$ the negative-norm branch of the dispersion lowers to negative frequencies and the flow is hence subsonic.

3.4.2 2-dimensional dispersion relation

Now that we know that our idea of passing from a supersonic to a subsonic flow by playing with the lattice depth is feasible, let us consider the two-dimensional dispersion

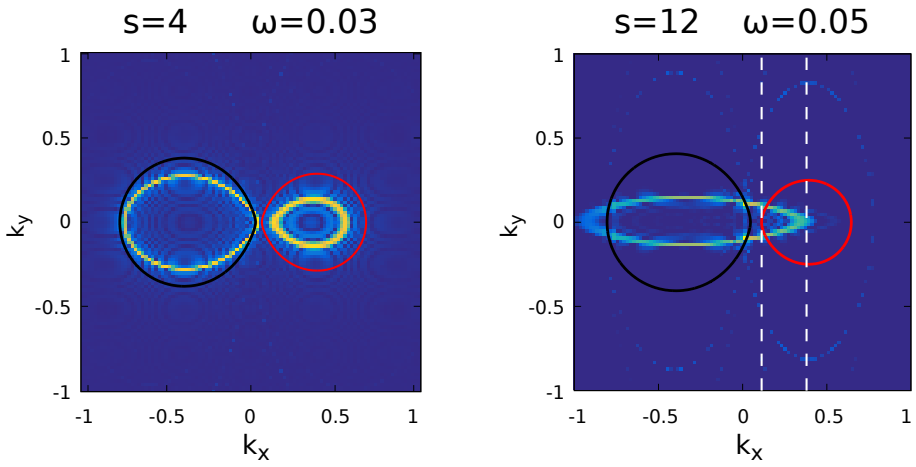

Figure 3.19: Dispersion relation of the elementary excitations at fixed ω for $gn = 0.05\ E_R$, (quasi-)momentum $K = 0.4 q_B$ and lattice depths $s = 4$ and $s = 12$. The black and red lines are respectively the positive- and negative- norm branches of the corresponding Bogoliubov dispersion relation in the uniform condensate; for these values of the parameters the uniform BEC is in a supersonic regime. In the first graph, for $s = 4$, the flow is supersonic also in the lattice region and the ovals are squeezed along y with respect to the free case. In the second graph, for $s = 12$, the regime becomes instead subsonic and the positive-norm oval is further squeezed. For values of k_x between the two dashed white lines mode conversion between upper and lower branches of the dispersion relation is possible.

relation in each of the two regions of Figure 3.16.

Take a two-dimensional region with the lattice along x and uniform along y. The dispersion relation can be numerically measured analogously to the one-dimensional case, by computing the ground state of the two-dimensional condensate (on a range along x multiple of the periodicity of the potential and with periodic boundary conditions in both directions) and by evolving a delta-shaped perturbation in time. The dispersion relation resulting resulting from the Fourier transform both in time and in space can be visualized with constant-ω plots, analogous to the ones of Figure 3.5. A comparison of the resulting plots with the corresponding dispersion curves in the uniform region is shown in Figure 3.19.

The fact that the lattice is only in one direction gives an increased *effective mass* that depends on the direction, so that the ovals are distorted with respect to the uniform case. In the first plot the lattice is not deep enough to make the flow subsonic and positive-norm and negative-norm ovals remain visible. When the lattice is deepened enough, the second oval disappears and the remaining positive-norm oval is highly squeezed. This is shown in second plot of Figure 3.19, that corresponds to the last one of Figure 3.18 for the one-dimensional case.

The superimposed comparison with the dispersion relation of the uniform region

shows intersection with the negative-norm oval. Similarly to what we discussed in Section 3.2, because of the symmetries of the system, stationary scattering on the interface between the two regions can only occur at fixed ω and k_x. We hence know that superradiant scattering is possible at the frequency shown in Figure 3.19 for transverse (quasi-)momenta in the interval delimited by the two white dashed lines.

3.4.3 GPE numerical calculations

We are now ready to test our prediction of superradiant scattering in this setup. We numerically obtain via imaginary-time propagation of the GPE an order parameter of the shape (3.51), with fixed quasi-momentum K. We then construct on top of the condensate a Bogoliubov wavepacket that is a plane wave along x and has a finite width along y, analogously to what we did in Section 3.2.4.

Although with black hole superradiance in mind one would study the scattering from the lattice (subsonic) region to the free (supersonic) region, condition (3.8) tells us that also negative-energy waves coming from the supersonic upper region can be amplified, at the expense of a positive-energy wave transmitted in the lower subsonic lattice region. This is convenient in this case because in the uniform region it is easier to create wavepackets since the Bogoliubov problem can be solved analytically, and it is also easier to measure the packets norms as we did in Section 3.2.4. We can hence measure the norms of the incident packet and of the reflected one, while the one of the transmitted one is difficult to obtain since the Fourier transform of the packet has the periodic structure of the Brillouin zones.

In Figure 3.20 we show snapshots of an example evolution of the GPE displaying the scattering of a wavepacket created in the supersonic uniform upper region of Figure 3.16. The wavepacket is chosen such that it falls between the two dashed lines in Figure 3.19, so that it has a negative norm and one expects an amplified reflection. In the first frame the packet along y has a positive phase velocity and a negative group one. It can be seen that the transmitted packet instead (above the periodicity of the lattice) has an opposite-sign phase velocity while still moving towards negative y. This, as in the uniform case of Section 3.2.4, is an indication of the fact that the two packets have opposite norm.

A Fourier analysis shows that the incident and reflected wavepackets have the same k_x and that the transmitted packet in the lattice region has a peak (repeated in the different Brillouin zones) on the upper half of the ellipse of Figure 3.19, with the k_x of the incident packet. The transmitted packet can also be seen to have a fast modulation given by the periodicity of the lattice

In the last frame the reflected packet is seen to be much wider than the incident one due to dispersion. To assess the amplification we hence compute the integrated Bogoliubov norms (3.17) of the incident and reflected packets in the supersonic region. The variation of the amplitudes in time is shown in the lower panel of Figure 3.20, where one can see that the reflected packet is amplified of circa 20%.

The overall process is very similar to the one illustrated in Figure 3.6. The amplifi-

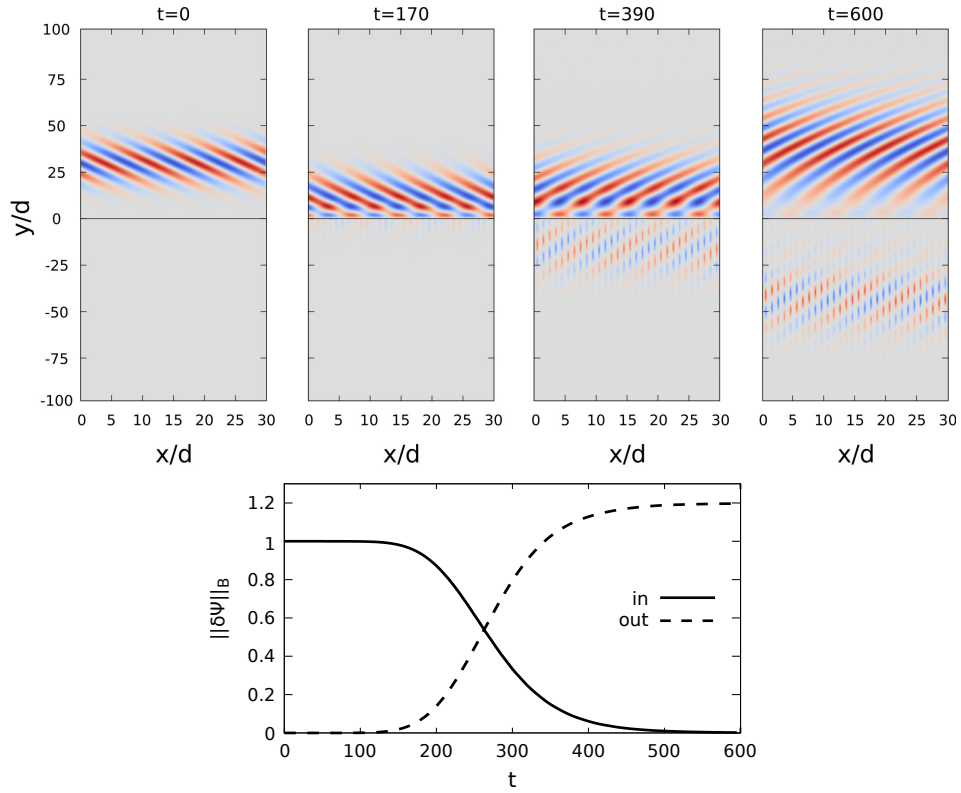

Figure 3.20: Above: snapshots of the scattering of a negative-norm wavepacket in the supersonic region on the interface with the lattice region. The background stationary state has the shape depicted in Figure 3.16, with a constant average density $nd^2 = 1$, interaction $gn = 0.05\ E_R$, (quasi-)momentum $K = 0.4\ q_B$ and lattice depth $s = 12$. The incident wavepacket is chosen with the frequency of the dispersion cut of the right part of Figure 3.19 and with $k_x = 0.25\ q_B$ so that the mode lays in the region in which one expects amplification. The lower panel shows the time dependence of the norms of the incident and reflected packets, showing superradiant scattering.

cation, while being significant, is however in this case smaller than the one we observed with the synthetic vector potential setup. This can be ascribed to the density profile shown in Figure 3.16, in which the density is lower than the average around $y = 0$. This causes a reduced *coupling* between the two regions, that lowers the transmission and hence the amplification.

We can conclude that this setup involving a lattice region is another viable one to observe superradiant scattering, although the uniform density throughout the system makes the configuration involving the synthetic vector potential *cleaner*.

3.5 Summary: a toy model for superradiance

In this Chapter we introduced a simple acoustic metric displaying the essential feature to display superradiance: an ergoregion. A main advantage of the configurations presented here is the geometrical simplicity, that provides an easy to understand and conceptually clear picture of superradiance.

This is permitted by remarkable techniques available to modify the behaviour of a Bose–Einstein condensate, such as a local tuning of the velocity. We showed in fact that the inclusion of a synthetic vector potential breaks the irrotationality constraint on the velocity and expands the class of metrics one can reproduce in a BEC gravitational analogue. Another tool that we showed can be used to this end are periodic potentials that can locally modify the effective mass of the atoms.

Superradiance in our *planar ergosurface* configurations can be explained as a mode-mixing process at the interface between subsonic and supersonic parallel flows and crucially relies on the existence of energetic instabilities. Amplified scattering can be understood simply from plots of the dispersion relations, that also provided a tool to understand the important effects of the superluminal Bogoliubov dispersion on superradiance. The conclusions obtained via analytical and *graphical* means were also confirmed numerically with integrations of the GPE.

The simplicity of the vector-potential-induced planar ergosurface allowed the application of a mode-matching technique that gave a further characterization of superradiant scattering in this setup. This also brought to the prediction of quantum spontaneous pair emission at the ergosurface, that was characterized in terms of density-density and momentum correlations between the excitations inside and outside the ergoregion; these are promising quantities to look for in experimental investigations of this effect.

We saw how superradiant scattering on the planar ergosurface is exactly mappable to the bosonic Klein paradox for a massive charged field in one dimension. As we commented in Chapter 2, the dynamical stability of that configuration is assured by the open boundary conditions in the two asymptotic regions, that we reproduced here by assuming a virtually unbounded system. The next Chapter is devoted to removing this assumption and study the effect of non-open boundary conditions on superradiance and will bring us to the fundamental question of the role of boundary conditions in superradiant scattering.

Chapter 4

Superradiant instabilities with a planar ergosurface

In the previous Chapter we saw that superradiant scattering can be understood as a mode-mixing process at the ergosurface and that it crucially relies on the presence of negative energy modes in some part of the system, that is on the presence of an *energetic instability*. Since the energy of an isolated system is conserved, decreasing the energy from an energetically unstable configuration typically requires the presence of some dissipation mechanism to evacuate the extra energy; superradiance is essentially the simultaneous population of modes of opposite energy. Still, in the case of a single interface considered so far, this process can not happen spontaneously (at the classical level) and it must be stimulated by some incident wave.

We know from our discussion in Section 2.5 that changing the boundary conditions in a system displaying superradiant scattering dramatically changes the physics since dynamical instabilities emerge. In the planar ergosurfaces of the previous Chapter dynamical stability was assured by the absorption provided by the non-Hermitian open boundary conditions of an unbound system on the two sides of the ergosurface. Changing the boundary conditions in our setups based on BECs has a simple operational meaning: we can introduce a reflecting boundary condition for fluctuations by confining the condensate with a trap.

Our setup provides a preciously simple picture of the onset of superradiant instabilities. Take for example a configuration in which, instead of having an unbounded system in both the $\pm y$ directions, we introduce a reflecting boundary condition for fluctuations at the upper system edge. In this case, the transmitted negative norm wavepacket will get reflected and sent back to the interface. Since amplification does not depend on the way the interface is crossed, amplified superradiant reflection will now take place in the upper part, a stronger wavepacket will be generated that propagate upwards, and the process will continue indefinitely. This bouncing back and forth of the wavepacket between the interface and the reflecting boundary is associated to sizable amplification at each bounce on the interface, so that the amplitude of the *trapped* negative-energy mode will increase indefinitely until saturation effects beyond our Bogoliubov reasoning

start taking place.

In the gravitational analogy, this configuration can be seen as an analog of the ergoregion instability of a fast-spinning star with no horizon (Section 2.5.2): the region within the ergosurface shows an exponentially growing perturbation, while correspondingly growing waves get emitted into the outer space. This *dynamical instability* mechanism can occur analogously if the reflecting boundary condition was imposed in the lower part of the system, resulting in an exponential growth of a trapped positive-energy mode; this is the analogous of a black hole bomb instability (Section 2.5.1).

These processes bring us to the fundamental question of superradiance we introduced in Section 2.6: what is the role of absorption and boundary conditions? Here we will answer this question showing that absorption (open boundary conditions) is essential for superradiance only as a stationary equilibrium process, while amplification of finite-width wavepacket can be observed in dynamically unstable systems as a transient phenomenon.

Another aspect of this important question is if horizons do in general assure the necessary *absorption* to prevent dynamical instabilities. To address this second question we include a flow along y in our setup and introduce an analogue horizon with a local change of the speed of sound. This setup is a very flexible *modular* analogue black hole that allows us to shows that the occurrence of ergoregion instabilities is not *in general* avoided by the presence of an horizon and depends on the *smoothness* of this element. In fact we find that a sharp horizon does not work as a perfect absorber and can give sizable reflections of the fluctuations in the ergoregion, thus triggering instabilities as discussed above.

The plan of this Chapter is to focus on the conceptually simpler planar ergosurface obtained with a synthetic vector potential, keeping in mind that analogous physics can be obtained with periodic potentials. First we show that superradiant instabilities occur in our setup by introducing reflection for fluctuations in numerical calculations based on the GPE. We then investigate this physics with the Bogoliubov approach and study the spectra of elementary excitations; this shows that superradiant instabilities in our system are an analogue realization of the Schiff–Snyder–Weinberg (SSW) effect (Section 2.5.3), through the mapping to an electrostatic problem presented in Section 3.2.2. A second approach to the Bogoliubov problem is then presented, based on matching of the modes similar to the one of Section 3.3.3 but for complex frequencies. This provides another way to detect dynamical instabilities and gives the important proof of the fact that our planar ergosurface configuration is dynamically stable. Superradiant scattering from a dynamically unstable configuration is then demonstrated, before discussing the role of horizons.

4.1 Analogue superradiant instabilities and the SSW effect

4.1.1 Evidence from GPE simulations

As a concrete example of the dynamical instability mechanisms sketched above, we consider a finite condensate trapped along the y direction in a box potential; the vanish-

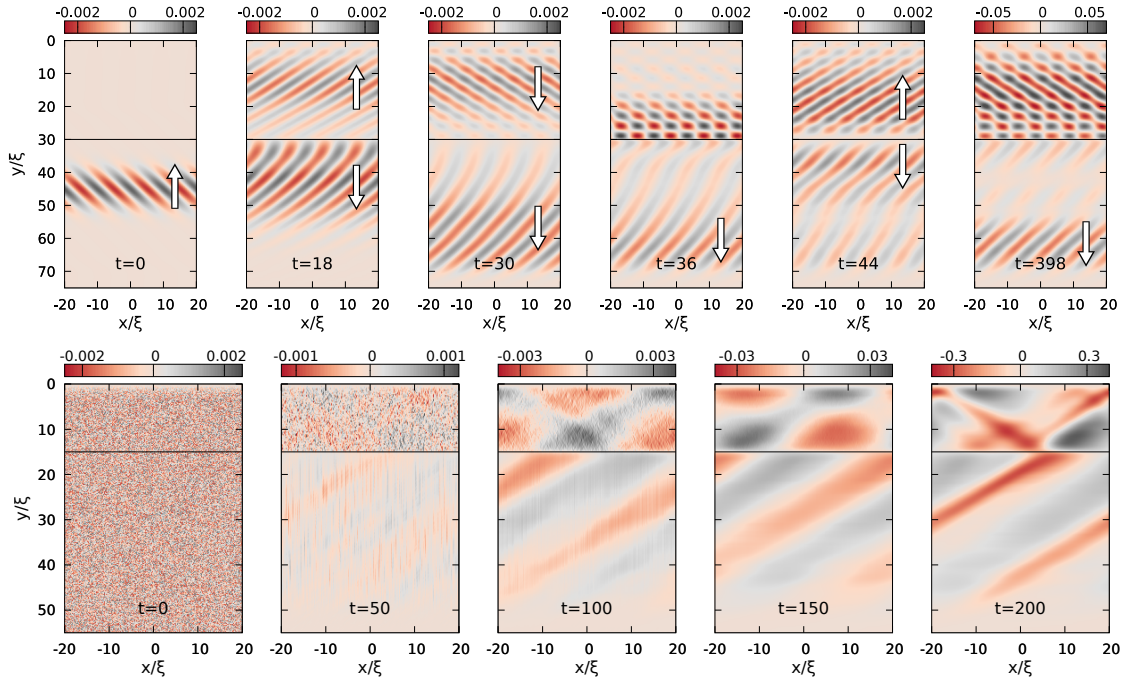

Figure 4.1: Snapshots of the time evolution of a dynamically unstable condensate as predicted by a numerical GPE calculation starting from different initial states. The condensate is confined along y in a box of length $y_{max} = 80\xi$. The interaction constant g is constant, giving a spatially uniform speed of sound c_s. In the $0 \leq y \leq L$ region, a transverse vector potential $A_x = -3Mc_s$ and a compensating external potential $V = -A_x^2/(2M)$ are applied. Fluctuations are absorbed via an imaginary potential when approaching the lower edge at y_{max}, so to mimic an open system geometry along that direction. On the upper row, the initial state features an incident wavepacket traveling in the upwards direction towards the *cavity* of length $L = 30\xi$; the white arrows indicate the directions along y of the group velocities of the wavepackets. On the lower row, the initial state only features a weak white noise and the cavity length is $L = 15\xi$.

ing density at the upper boundary at $y = 0$ introduces reflecting boundary conditions for the Bogoliubov excitations. An absorbing region for fluctuations is introduced around the lower boundary at y_{max} so to simulate an open system geometry in this direction. We then apply a transverse synthetic vector potential field in the upper region $y \in [0, L]$, with $L < y_{max}$.

In the upper panels of Figure 4.1, we display the numerical solution of the Gross–Pitaevskii equation for this configuration starting from an incident wavepacket traveling in the upwards direction with a wavevector in the superradiant amplification range. At the first bounce on the $y = L$ interface, an amplified reflected wavepacket is obtained via superradiant scattering. The negative-norm transmitted wavepacket keeps bouncing back and forth between the interface at $y = L$ and the reflecting boundary at $y = 0$

while its intensity exponentially grows.

In the lower panels of Figure 4.1 we display an analogous numerical simulation starting from a noisy initial state. In this case, the development of the dynamical instability appears qualitatively different. In the $y > L$ lower region, one can see the emergence of a pattern that can be recognized as a *down-going* wave, while a stationary wave coming from superposition of *up-going* and *down-going* waves appears in the upper region with an exponentially growing amplitude. This latter standing wave is the trapped negative-energy mode that gets self-amplified while a positive-energy wave is radiated in the downwards direction.

Qualitatively similar instabilities take place if the reflection occurs in the lower part of the system and also in more complex configurations in which a *stripe*-shaped regions of fast motion is created within a medium at rest. In this last case instead of a reflecting boundary condition one has two planar ergosurfaces, so that amplification of the trapped negative-energy mode will occur at both the *edges of the cavity* resulting in a faster increase of the mode amplitude. This resembles the black hole lasing instability discussed in Section 1.5.2. The present case differs because it occurs in two spatial dimensions and, most importantly, because it does not rely on the superluminal dispersion of the fluctuation field and can also happen for a Klein–Gordon field.

4.1.2 The Bogoliubov spectrum: the SSW effect

Further light on these phenomena is offered by a study of the Bogoliubov eigenmodes. We do this, as explained in Section 1.1.2, by taking fluctuations around some stationary state Ψ_0 of the GPE in the shape (1.17):

$$\Psi(\mathbf{r}, t) = e^{-i\mu t/\hbar} \left[\Psi_0(\mathbf{r}) + \delta\psi(\mathbf{r}, t)\right]. \tag{4.1}$$

Thanks to the translational symmetry along x, we can adopt the one-dimensional perspective and study the spectrum of the excitations for fixed transverse momentum k_x. This corresponds to taking a plane wave form $\delta\psi(x, y, t) = e^{ik_x x}\varphi(y, t)$ for the fluctuations; the field φ then satisfies the one-dimensional Bogoliubov problem

$$i\hbar\partial_t \begin{pmatrix} \varphi \\ \varphi^* \end{pmatrix} = \begin{bmatrix} D_+ & g\,|\Psi_0|^2 \\ -g\,|\Psi_0|^2 & -D_- \end{bmatrix} \begin{pmatrix} \varphi \\ \varphi^* \end{pmatrix}, \tag{4.2}$$

where

$$D_\pm = -\frac{\hbar^2}{2M}\partial_y^2 + \frac{(\pm k_x - A_x)^2}{2M} + 2g\,|\Psi_0|^2 + V - \mu\,. \tag{4.3}$$

The spectrum of this problem can be studied by diagonalizing the equation (4.2) in matrix form. In particular, on a spatial grid of N points, we represent the Bogoliubov spinor as a vector of size $2N$, having as elements the values of the two spinor components at each spatial point. The $2N \times 2N$ matrix is then filled by computing at each spatial point the four elements appearing in (4.2) and by using discretized expressions for the derivatives, that enter in the matrix as elements connecting different spatial points. This matrix is then diagonalized using standard libraries.

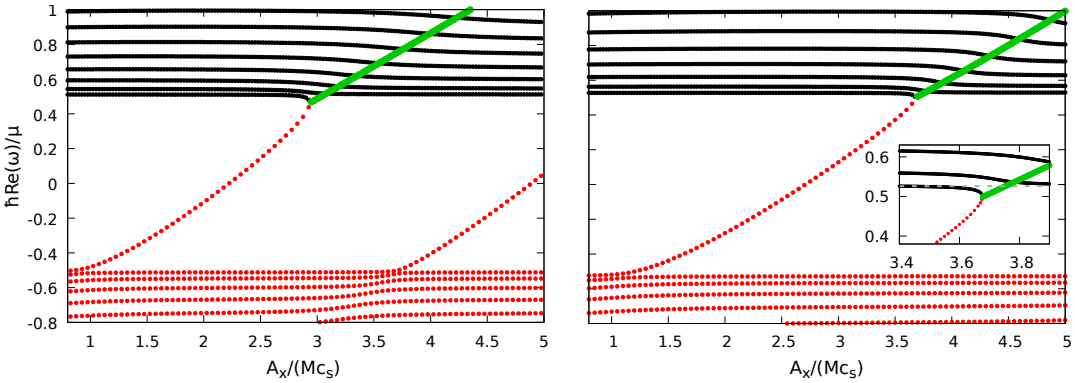

Figure 4.2: Spectra of the effective one-dimensional Bogoliubov problem (4.2) for a condensate confined in a box $0 \leq y \leq y_{max}$ in the presence of a transverse vector potential of variable intensity A_x restricted to the region $y \in [0, L]$ with $L = 2\xi$ and $y_{max} = 30\xi$. The transverse momentum is fixed at $k_x = -0.5/\xi$ and the speed of sound c_s is spatially uniform. Black solid (red dotted) lines indicate the real-valued frequencies of the positive (negative) norm modes; the green thick lines are the real part of the frequencies of dynamically unstable zero-norm modes. The inset is a zoom of the region where dynamical instability emerges. The lower panel show the complete calculation, the upper part is the prediction of the hydrodynamic Klein-Gordon approximation as discussed in the Appendix.

Here we consider a configuration similar to the one that was addressed in Figure 4.1, but imposing Dirichlet boundary conditions both in 0 and y_{max} to the field φ. The right panel in Figure 4.2 shows how the spectrum of this Bogoliubov problem varies as a function of the vector potential intensity A_x for a fixed size L of the moving region and a fixed transverse momentum k_x. In the electrostatic mapping of Section 3.2.2, this corresponds to taking a square box potential for a field of some charge and mass and increasing the amplitude of the electrostatic potential A_0.

One can see that at some point a negative norm state enters the mass gap: in the electrostatic case this corresponds to a bound antiparticle state localized in the positive electrostatic potential box. When the frequency of this state approaches the positive-norm band, opposite-norm states *stick* together and give rise to a zero-norm dynamically unstable modes (as explained in Section 1.1.3 that can be thought as the continuous production of pairs of particles with opposite energies, one falling into the localized negative-norm mode, the other being radiated away on the positive-norm band. This is exactly the mechanism of the SSW effect presented in Section 2.5.3.

Along with the exact solution of the Bogoliubov problem that we just discussed, it is also interesting to consider this problem within the hydrodynamic approximation. As explained in Section 1.4, this approximation corresponds in fact to the Klein–Gordon equation for which the SSW effect was originally derived. To this end we can perform an analogous diagonalization of the matrix of equation (1.84); the result of such calculations

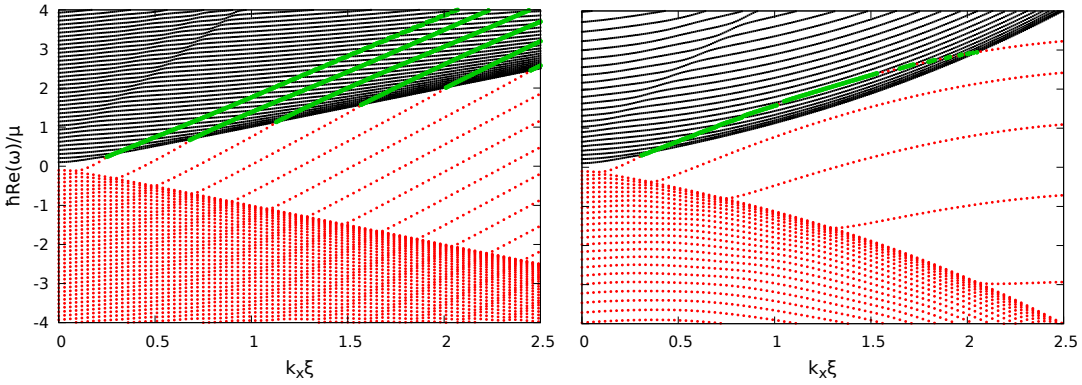

Figure 4.3: k_x-dependent spectra of the same effective one-dimensional Bogoliubov problem (4.2) as studied in Figure 4.2. System parameters: $y_{max} = 30\xi$, $L = 4\xi$ and $A_x = -3Mc_s$. The upper panel shows the result of the hydrodynamical Klein-Gordon approximation, the lower panel one illustrates the complete Bogoliubov problem. The effects of superluminal dispersion are evident in the different spacing of the modes and in their curvature as a function of k_x, which result in the suppression of the instability at high transverse momenta.

is shown in the left panel of Figure 4.2: except for some quantitative differences, the phenomenology is qualitatively identical.

The effects of superluminal nature of the Bogoliubov dispersion can be highlighted by performing an analogous calculation of the spectra as a function of the transverse momentum k_x for fixed values of the size L and of the vector potential intensity A_x. The results for both the exact problem and the hydrodynamic approximation are reported in the right and left panels of Figure 4.3, respectively. One can see that at small transverse momenta k_x the behaviour is, as expected, essentially the same. In contrast, at large k_x the presence of dispersion in the Bogoliubov problem has the consequence that both the mass gap and the bound states energy no longer show a linear dependence on k_x. In particular, for large enough k_x the bound state reenters into the mass gap and the instability is correspondingly suppressed.

This impact of the superluminal dispersion onto the instability is very similar to the suppression of superradiant scattering for high transverse momenta we discussed in Section 3.2.3. Also, condition (3.12) for superradiance is the same for the occurrence of instabilities. In the upper plot of Figure 4.3, this condition can be graphically understood in terms of the slope of the bound state. This slope is proportional to $|A_x|$ and for $|A_x| < 2Mc_s$ is smaller than the slope of the k_x-dependent mass gap, that is of the lowest positive-norm state. As a result, instabilities can not develop in this case.

Our reasoning so far assumed open boundary conditions for large-y, so radiative waves can be emitted in this direction and nothing can come back. Actually, the spectra shown in Figures 4.2 and 4.3 were calculated for finite size systems with Dirichlet boundary conditions. While the considered system size is generally large enough that

the geometry can be considered as effectively open in the large-y direction, still some remnants of the finite size are visible in some specific parts of the spectra. For instance, a suppression of the instability is possible for specific parameter values: the dynamical instability is due to the coupling of two modes of opposite norm that are close to resonance. For a finite system the spectrum is discrete so that such pairs of modes may not be available. This is what happens in the right panel of Figure 4.3 around $k_x\xi \sim 2$, where the instability is absent for some intervals of the transverse momenta: even though the energetically unstable negative-norm mode is above the mass gap, it is far from resonance with positive-norm modes and the instability is effectively quenched. As we will see in full detail in the next Chapter, increasing the system size reduces the spacing between modes and removes the stability islands.

4.1.3 Detection of dynamical instabilities via mode-matching

The discussion on dynamical instabilities carried out in the previous Sections was based on a combination of numerical GPE simulations and a semi-analytical study of a standard Bogoliubov problem in a finite-size system with Dirichlet boundary conditions. In this Section, we introduce a variant of the Bogoliubov approach that naturally includes the open boundary conditions and is able to identify the intrinsic dynamical instabilities of an unbounded system without the need of artificially restricting to a finite size and then taking an infinite-size limit.

The idea is the following. For a fixed (real) k_x and different (complex) frequencies ω, we look for the roots of the dispersion relations (3.13) in each of the two uniform regions and we construct the associated plane-wave modes. Among all these modes, we focus on the ones that display an exponential decay away from the interface. The existence of global modes of the whole system at a given (complex) ω satisfying the desired boundary conditions is then checked by trying to match the plane waves at the interface under the required continuity conditions. This imposes a linear set of equations to the mode amplitudes and the existence of non-trivial solutions at specific ω is signalled by a vanishing determinant. This approach was used to prove the dynamical stability of a white-hole configuration in [143].

One advantage of this method is that we can treat exactly open systems in the y direction by selecting the appropriately decaying modes in each of the two regions. At fixed k_x and ω the Bogoliubov dispersion relation will in general have four k_y roots. For non-real frequencies, all roots are complex, two with a positive imaginary part and two with a negative one. If open boundary conditions are considered, and since we are considering an isolated system with no driving, exponentially growing modes have to be discarded. This leaves us with only two relevant asymptotically bounded modes in each region, namely the ones with $\Im(k_y) > 0$ in the faster upper region and the ones with $\Im(k_y) < 0$ in the slower lower region.

In the fast/slow region the plane wave expansion of the modes will hence be

$$|\phi^{f/s}\rangle = \sum_j \mathcal{A}_j^{f/s} \begin{pmatrix} 1 \\ \beta_j^{f/s} \end{pmatrix} e^{ik_{y,j}^{f/s} y}, \tag{4.4}$$

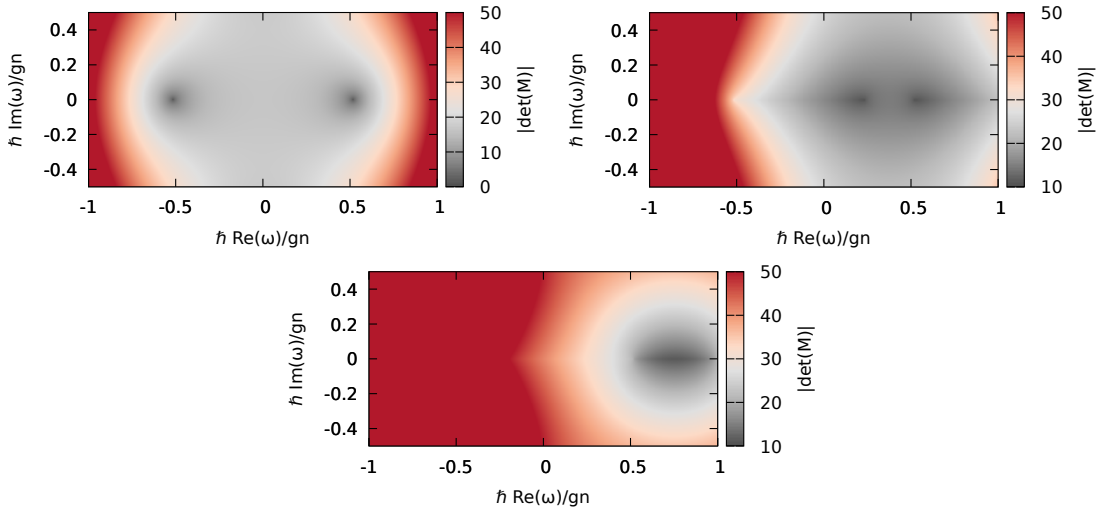

Figure 4.4: Log-scale color plots of the absolute value of the determinant (arbitrary units) of the linear matching problem with open boundary conditions on both sides of the interface for $k_x = 0.5/\xi$. The three plots correspond to $A_x^f = 0$, $A_x^f = -1.5\ Mc_s$ and $A_x^f = -3\ Mc_s$. A vanishing value of the determinant at a positive imaginary part of the frequency $\Im(\omega)$ is a necessary (but not sufficient) condition for instability. Here, zeros of the determinant are present only in the first (trivial) case and only for real values of the frequency; these correspond to the only real-frequency modes compatible with our boundary conditions, that are plane waves along x and constant along y. These plots show that the single interface configuration is dynamically stable.

where the sum runs over the physically relevant modes and $\beta_j^{f/s}$ is the proportionality constant between the two components of the Bogoliubov spinor that can be obtained from the linear problem (4.2) for a homogeneous system with the parameters of the fast/slow region.

Consider first the configuration with open boundary conditions on both sides. In this case, we have two relevant modes per side. The continuity conditions at the interface for the two spinor components of the fluctuation field and of their first derivative give four linear conditions that can be used to determine the four mode amplitudes. The existence of non-trivial solutions requires that the determinant be zero at some frequency ω. Dynamical instabilities are associated to roots with a positive imaginary part $\Im(\omega) > 0$. Notice that this is a necessary but not sufficient condition for instabilities: zeros of the determinant may in fact also occur for frequencies for which the roots of the dispersion relation become degenerate within one of the two homogeneous regions. These zeros do not correspond to dynamical instabilities and can be easily identified by looking at the corresponding values of the two relevant k_y roots in each region, to see that they coincide in at least one region. In our configuration, such zeros are found for $\omega = \pm i\mu/\hbar$ and $\omega = -A_x k_x/M \pm i\mu/\hbar$.

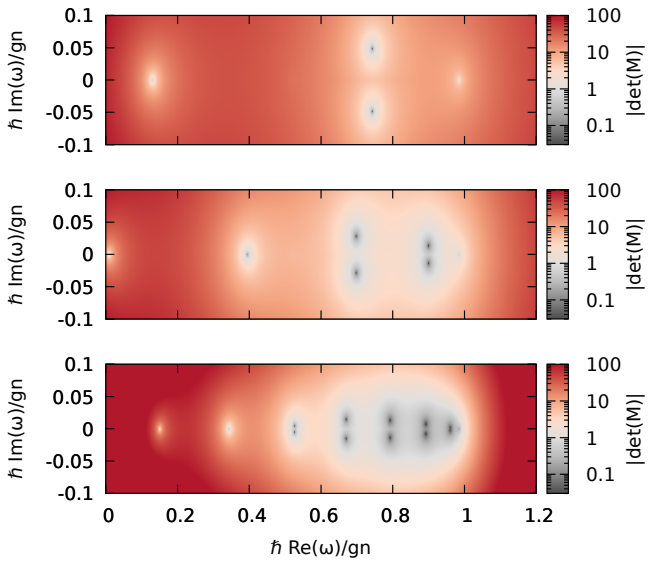

Figure 4.5: Log-scale plots of the absolute value of the determinant (arbitrary units) in the case of a reflecting boundary condition in the faster region at a distance L from the interface. Here $k_x = 0.5/\xi$ and $A_x^f = -3\ Mc_s$ and the tree plots correspond to $L = 5\ \xi$, $L = 10\ \xi$ and $L = 20\ \xi$. Dynamical instabilities are signalled by the presence of roots in the upper half complex plane $\Im(\omega) > 0$.

Beyond these spurious roots that must be discarded from the outset, in the case of a single interface no other solutions are found except for purely real frequencies in the case of a vanishing vector potential, as one can see in Figure 4.4. This proves that the condensate is dynamically stable and, in particular, does not show localized instabilities along the ergosurface, in stark contrast to classical hydrodynamic systems, such as the one discussed in Section 2.1.2, where analogous velocity fields are generally unstable against the generation of ripples at the interface.

Things of course change if we introduce reflecting boundary conditions on either side. Let us focus on the simplest case with a reflecting boundary condition in the fast region at a distance L from the interface as discussed in the previous Section. In this case, we need to keep all the four roots of the dispersion relations in the upper region, corresponding to waves that propagate back and forth between the interface and the upper reflecting boundary. We then have six amplitudes to determine, the two extra conditions being provided by the condition that the field vanishes on the upper boundary. A plot of the resulting determinant in the complex-ω plane is shown in Figure 4.5: as expected, the dynamical instabilities associated to the SSW effect discussed in the previous Section emerge as a series of zeros of the determinant in the $\Im(\omega) > 0$ half-plane. Their frequency $\Re(\omega)$ lies within the superradiant frequency range, here located between $0.5 \lesssim \hbar\omega/gn \lesssim 1$.

As expected, the number of the unstable modes depends on the size of the faster

region. The momenta of the trapped modes giving rise to instability must in fact satisfy a *quantization* condition given by the finite size of the *electrostatic* potential box. This is clearly visible in the growing number of zeros when increasing L from the top to the bottom panel of Figure 4.5. On the other hand, the instability rate $\Im(\omega)$ decreases while increasing the cavity size. Physically, this is also easily understood since amplification occurs upon bouncing on the ergosurface and the *round trip time* of the excitations increases with L.

4.1.4 Discussion

Based on our findings so far, let us summarize the connection between our predictions for flowing condensates and the dynamics of rotating spacetimes in gravitational physics. As we saw in the previous Chapter the fluctuations of the condensate around the stationary state describing our setup can be described in the hydrodynamic limit via the simple curved-spacetime metric (3.5) displaying an ergosurface that is a line at constant y in an unbound system in that direction.

This can be compared to a massless scalar field in the spacetime of an asymptotically flat Kerr black hole. The radial reduction of the problem for fields with a fixed azimuthal number is formally equivalent to our mapping to an electrostatic problem at fixed transverse momentum, except for the cylindrical instead of planar geometry.

In the black hole case, the ergoregion is surrounded by the unbounded space on one side and by the black hole horizon on the other side, both providing an open (or radiative) boundary condition whose non-hermiticity provides an effective *absorption*. As a result, the Kerr black hole is dynamically stable against scalar field perturbations [10] even though it is energetically unstable since energy extraction is possible via superradiant scattering processes. In our analogy, this corresponds to a single ergosurface in an unbounded condensate on both sides along y, for which we have predicted superradiant scattering in Section 3.2 and proved its dynamical stability in Section 4.1.3.

As we discussed in Section 2.5, removing (part of) the absorption on one of the two sides gives rise to dynamical instabilities, just as we have just seen for our analog model. If a strong enough reflection occurs inside the ergoregion (corresponding to a reflection at the upper edge of our setup), one has an *ergoregion instability*, that can happen for *ergostars* that have an ergoregion but no horizon (Section 2.5.2). On the other hand, if the reflection occurs on the outside (corresponding to the lower part of our setup), the instability is known as a *black-hole-bomb* (Section 2.5.1).

Our analogue model summarizes this physics in a simple way, without the complications of the circular geometry and of the greater complexity of *real* black hole spacetimes. It also shows the direct link between superradiant instabilities and the SSW effect [15], besides the one between superradiant scattering and the bosonic Klein paradox. Moreover, our setup provides a system in which these *toy models* can be investigated also experimentally, besides being a conceptual guide as we will also see in the following of this chapter.

4.2 Superradiant scattering without dissipation

The discussion of the previous Chapter made it clear that superradiant scattering can be understood in the analogue model as mode conversion happening at the ergosurface, similarly to the analogue interpretation of Hawking radiation as scattering on the horizon (Section 1.5). The discussion of the previous Section showed instead how changing the boundary conditions in a system displaying superradiant scattering can result in dynamical instabilities. But does superradiant scattering remain possible in systems displaying dynamical instabilities? It is sometimes stated (see for example [90]) that in black holes superradiance cannot occur without an horizon, as the approach in terms of the conservation of the Wronskian presented in Section 2.2 seems to suggest.

That approach refers to *stationary* processes (involving plane waves) and real frequencies, so that it correctly predicts no superradiance when waves are not evacuated from the system; we know in fact that the correct *stationary* description involves complex frequencies. Still, we know that superradiant scattering can be seen as a process occurring at the ergosurface, that may also be very far from the regions where boundary conditions for the problem are imposed. This suggests that as a *time-dependent transient* effect involving finite-width wavepackets, superradiance can occur without elimination of the involved waves from the system, in other words without a dissipation assuring the absence of dynamical instabilities. In the case of black holes, this means that amplification of radiation through superradiant mechanisms can also occur without an horizon.

In the case here under detailed study this can be easily understood from the GPE calculation summarized in the upper row of Figure 4.1: the initial incident packet can be measured to be amplified in the first scattering with the ergoregion, even if this eventually ends up triggering an instability at later times. Amplification is in fact due to the coupling between opposite-norm modes in a restricted region of space around the interface; if this process is well separated in space from the reflecting element, the positive feedback mechanism responsible for the instability only occurs after a sizable time-interval set by the round-trip time of the transmitted wavepacket. In the meanwhile, only the amplified wavepacket is visible.

Such a superradiant scattering in a dynamically unstable system is shown in a more intuitive way in Figure 4.6, where a time evolution of the Bogoliubov problem (4.2) at fixed transverse momentum of a configuration similar to the one of the upper simulation of Figure 4.1 is performed; the one-dimensional perspective and the use of the Bogoliubov spinor components give here an immediate picture of the norm of the packets and of their amplification. The initial wavepacket is chosen with a frequency in the superradiant interval and can be seen to undergo superradiant scattering exactly as in Figure 3.11: a negative-norm wavepacket is transmitted and the reflected packet is bigger. This is quantitatively checked in bottom left panel.

The subsequent evolution reflects instead the dynamical instability of the system. The transmitted packet is reflected by the boundary condition and is sent back to the interface where it undergoes amplified scattering *at the expense* of a transmitted positive-norm packet; this amplification is again visible in the time dependence of the packets

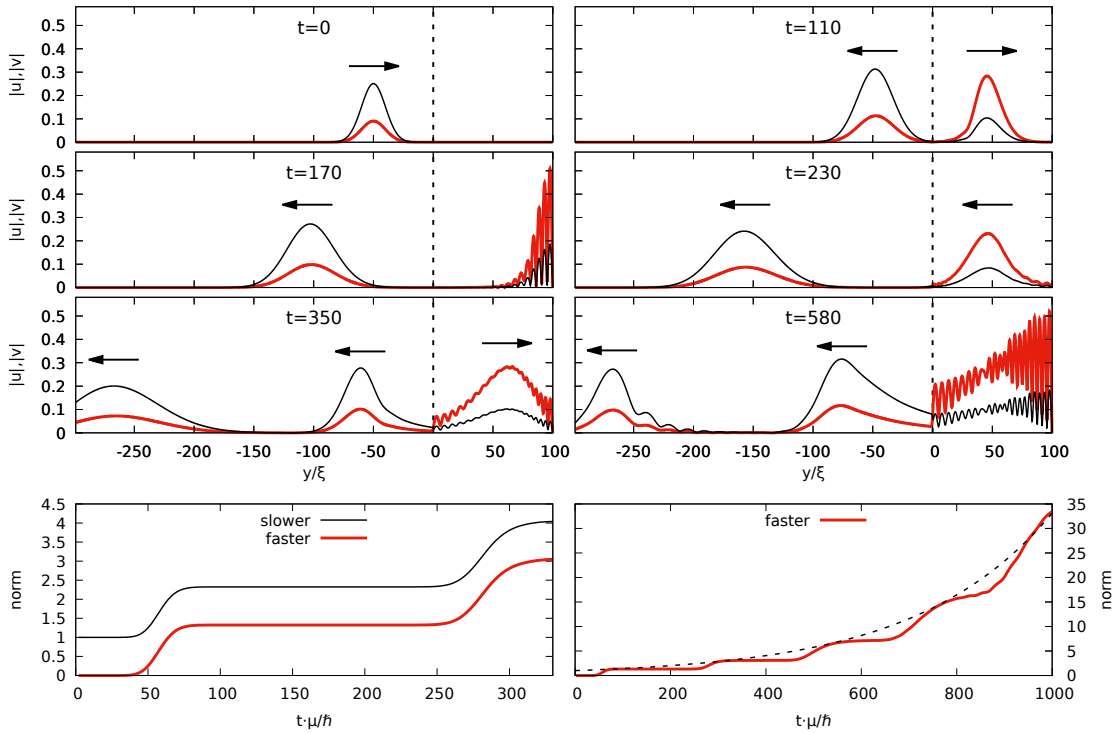

Figure 4.6: Upper panels: time evolution of the Bogoliubov problem for a constant-density condensate with a synthetic vector potential $A_x^f = 3\,Mc_s$ applied for $y > 0$. The initial condition is taken with Gaussian wavepacket (of transverse momentum $k_x = 0.8/\xi$ and centered around $k_y = 0.7/\xi$ with a variance $\sigma_y = 10\xi$) in the slower region and group velocity towards the interface. Absorbing boundary conditions are imposed via a smooth absorbing potential for large and negative y. Black thin lines indicate the u component of the Bogoliubov spinor and the red thick lines the v part. The arrows indicate the directions of the group velocities of the wavepackets. Lower panels: on the left time-dependence of the overall Bogoliubov norm in the two regions for *short* times. Superradiant scattering of the initial packet and of the transmitted packet are clearly visible. On the right time-dependence of the norm in the faster region for longer times. The behaviour is clearly dynamically unstable and the dashed line shows a similar exponential growth for comparison.

norm plotted in the bottom left panel of 4.6. This bouncing continues with an ever increasing amplitude of the trapped mode, that is compared with an exponential growth in the bottom right panel of Figure 4.6. The trapped packet is eventually very distorted by the nonlinearity of its dispersion relation.

This time evolution is a clear example of what we said above: superradiant scattering as a stationary *time-independent* process requires dissipation, whose absence results in dynamical instabilities in the *time-independent* spectrum of the system. Nonetheless, superradiance as a *time-dependent* transient phenomenon can still be observed.

The experimental observation of a mechanism of this kind for a one-dimensional condensate displaying acoustic black-hole and white hole horizons was reported in [87]. In that case initially spontaneous Hawking emission from the black hole horizon was observed at early times, and was then followed by the developing of a black hole lasing instability.

4.3 The effect of horizons: a *modular* black hole

As we just discussed, *stable* amplified reflection requires some absorption inside the ergoregion to avoid dynamical instabilities due to the repeated amplification of the negative-energy waves. As we mentioned in Section 2.4, in the standard treatments of superradiance it is pointed out how such an absorption mechanism is naturally provided in black hole spacetimes by the horizon, which acts as an open boundary condition, prohibiting the reflection of radiation towards the ergosurface.

In this Section, we show how the behaviour at horizons can be much richer than this: besides showing that the superluminal dispersion relation can make superradiance to occur at a horizon, we will discuss instabilities that are triggered by the presence of an horizon, that can provide a sizable reflection of perturbations determining the onset of an ergoregion instability. This is done by introducing a third region in our setup, working as the interior of a black hole horizon; we thus have a *modular* black hole whose different features can be tuned to study their effect on the propagation of fields.

4.3.1 Scattering at a horizon

As a first step, consider an interface at $y = 0$ separating a slow region of subsonic flow $v^s < c_1$ in the lower half-plane $y < 0$ from a fast region of supersonic flow $v^f > c_2$. In contrast to the previous sections, we do not assume that the speed of sound is spatially uniform, in particular we focus on the $c_1 > c_2$ case. As compared to our discussion of superradiance in Sec.3.2, the flow velocities $\mathbf{v}^{s,f}$ are no longer assumed to be oriented along the direction x parallel to the interface, but can be oriented in different directions. For generic flow velocity directions, the dispersion of the modes in each region can be obtained by rotating the plots in Fig.3.2 in the (k_x, k_y) plane.

Let us start from the hydrodynamic Klein-Gordon regime. In the upper region of supersonic $v^f > c_2$ flow, the asymptotes of the hyperbolas are oriented in a different way depending on whether the y component of the velocity v^f_y is smaller or larger than the

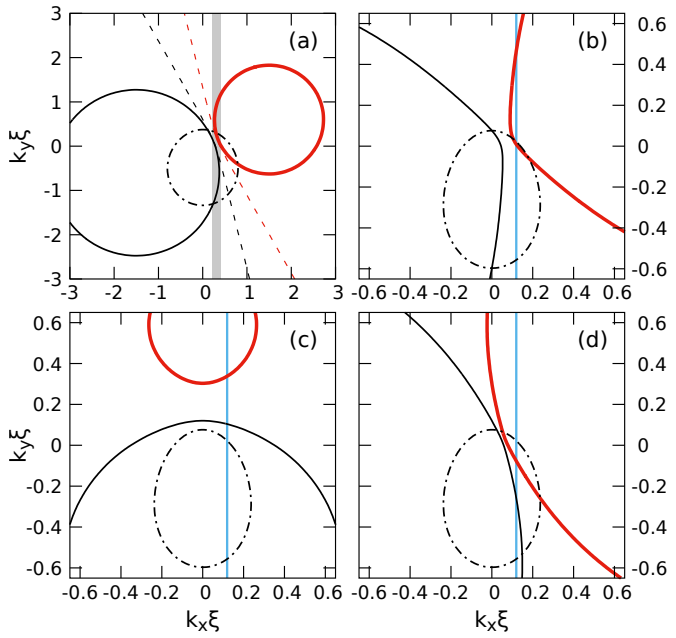

Figure 4.7: (a) Comparison of the cuts at $\hbar\omega/Mc_1^2 = 1$ of the Bogoliubov dispersion relations inside (solid lines) and outside (dash-dotted lines) the *horizon* for $v_x^s = 0$, $v_x^f = 2.12Mc_1$, $v_y^s = v_y^f = 0.85c_1$ and $c_2 = 0.1c_1$. Dashed lines are instead the cut of dispersion relation of the corresponding Klein-Gordon problem inside the horizon. (b)-(d) Referring to the configuration of Figure 4.8: comparison of the $\hbar\omega/Mc_1^2 = 0.2$ cut of the Bogoliubov dispersion relations in the exterior region (dash-dotted lines) with the one in the ergoregion (b) and with the ones inside a region of supersonic longitudinal flow $v_y^f > c_2$ (c,d). Parameters: $A_E = -2.12Mc_1$, $v_y^s = v_y^f = 0.85c_1$, $c_2 = 0.1c_1$. In panel (c), $A_H = 0$. In panel (d), $A_H = A_E$. The blue lines in (b-d) indicate the value $k_x\xi = 0.1$ considered in the following Figs.4.8 and 4.9.

speed of sound c_2, which gives rise to different scattering processes. In the former case, one has a slight rotation of Fig.3.2, namely there still exist two windows of k_x values in which one only has a positive or a negative norm mode and the two regions are separated by an interval with no available mode. As a result, the same superradiance physics takes place: depending on k_x, an incident wavepacket coming from the subsonic region at $y < 0$ can either be totally reflected (region II in Fig.3.2, or be partially transmitted and reflected (regions III and IV), or undergo superradiant scattering (region I).

In the latter $v_y^f > c_2$ case, the orientation of the asymptotes is the one displayed by the dashed lines in Fig.4.7(a). As expected for a horizon, all the modes have a positive y-component of the group velocity, so they can not travel back through the horizon. In particular, both a positive and a negative norm mode are available for any value of k_x: as a result the incident wavepacket will split in a pair of transmitted and reflected positive-norm components in addition to the negative-norm transmitted one. In spite of the

amplification given by the negative-norm mode, because of this multi-partite splitting, the intensities of the wavepackets are not necessarily larger than the incident one and superradiance in the sense of amplified reflection does not generically occur.

The situation changes dramatically when the superluminal Bogoliubov dispersion is considered. In this case, illustrated by the solid lines in Fig.4.7(a), there exist again regions of k_x values in which a single negative norm mode is available, which leads to the unexpected behaviour of a superradiant scattering occurring directly at the horizon in the absence of an isolated ergosurface. GPE simulations of the wavepacket dynamics (not shown) give results qualitatively identical to the ones in Sec.3.2.

Solid lines in panel (c) of the same figure show an analogous dispersion for $v_x^f = 0$ case: in this case, there are no k_x values for which negative-norm modes only exist, so no purely superradiant scattering is possible. This shows how a lateral flow is anyway an essential ingredient of superradiance.

4.3.2 Dynamical instabilities triggered by a horizon

Inspired from general-relativistic black holes, let us now focus on configurations displaying an external ergosurface and an internal horizon like the one sketched in the upper part of Figure 4.8. This configuration consists of three layers and displays a finite longitudinal velocity along y in addition to the synthetic vector potential directed along x. In the outermost layer (left), the speed of sound c_1 exceeds all components of the velocity and the flow is subsonic. In the central layer, the vector potential A_E is large enough to give a super-sonic flow along x, but the inward radial velocity v_y is still subsonic. Except for the small longitudinal speed, the first interface is expected to behave very similarly to the ergosurface discussed in the previous Sections. In the third layer (right), the longitudinal velocity v_y exceeds the speed of sound c_2, so the second interface behaves as a horizon for long-wavelength waves. The synthetic vector potential A_H in the third region is drawn with a dashed line to indicate that we are going to consider both the $A_H = A_E$ case (which resembles a vortex with drain) and the $A_H = 0$ one.

In Figure 4.7 we show comparisons between the fixed-ω cuts of the Bogoliubov dispersion relations in the left, subsonic region (dash-dotted lines) and in the supersonic central and right regions (solid lines). Panel (b) shows the comparison between the left and the central ergoregion: the flow along y is responsible for a *tilt* of the curves in the ergoregion with respect to the $v_y = 0$ case shown in Figure 3.5(d) but the structure of the available modes remains essentially the same. Panels (c) and (d) show instead the comparison with the third region inside the horizon, in respectively the $A_H = 0$ and $A_H = A_E$ cases.

The blue lines in the panels (b-d) indicate a value of the transverse wavevector $k_x\xi = 0.1$ at which, for the chosen frequency value $\hbar\omega/Mc_1^2 = 0.2$, the central region behaves as an ergoregion and the right one as the interior of a black hole. Focusing on this specific value of k_x, in the lower part of Figure 4.8 we show constant-k_x cuts of the dispersion relations. The choice of parameters is such that, for all the values between $A_H = 0$ and $A_H = A_E$ of the vector potential in the third region, the interface

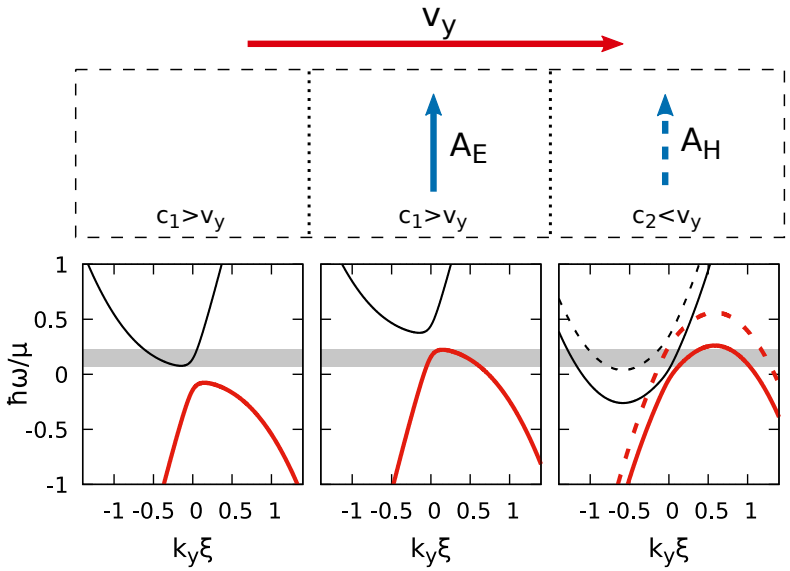

Figure 4.8: Top row: scheme of a configuration including both an ergoregion and an horizon. The ergoregion is included by means of a vector potential oriented along x. The horizon is created by changing the speed of sound in the third region. Here, the vector potential A_H may or may not be present. Bottom row: plots of the dispersion relations at fixed transverse momentum $k_x\xi = 0.1$ for the same parameters considered in Fig.4.7(a-c), namely $A_E = -2.12Mc_1$, $v_y = 0.85c_1$, $c_2 = 0.1c_1$, $A_H = A_E$ (dashed) or 0 (solid). The gray region indicates the frequency interval in which superradiant scattering can occur.

between the second and third regions behaves as an horizon (that is inside the horizon both positive- and negative-norm modes are available at the same frequency) at all frequencies for which amplified reflection at the ergosurface is possible (gray region).

Based on general arguments of black hole physics [114,115], we could expect that the horizon behaves as an absorbing element so that all the negative-norm modes created by superradiant processes at the ergosurface is dumped into the black hole. From a different perspective and inspired from studies of analog black holes [69], one could also expect that the horizon may provide some significant reflection. Depending on the relative magnitude of the reflection coefficient at the horizon and of the amplification at the ergosurface, this mechanism may give rise to a self-amplification process leading to a dynamical instability.

This conjecture can be numerically tested by performing a numerical simulation of the time-dependent one-dimensional Bogoliubov–de Gennes equation (4.2). In order to create the horizon we also spatially vary the speed of sound in addition to the vector potential. As done in [17, 18, 69], this is obtained by means of a suitable spatial profile of the interaction constant and of the external potential, so to maintain a constant density for the background condensate $\Psi_0(y) = \sqrt{n_0}e^{i(Mv_y/\hbar)y}$ as summarized in the following table. As usual, the interaction constant is related to the speed of sound via

$c_{1,2} = \sqrt{g_{1,2} n_0 / M}$ and, with the parameters specified in Figure 4.8, we have the following configuration.

	$A_x(y)$	$g(y)$	$V(y)$
$y < y_E$	0	g_1	0
$y_E < y < y_H$	A_E	g_1	$-\dfrac{A_E^2}{2M}$
$y > y_H$	A_H	g_2	$-\dfrac{A_H^2}{2M} + (g_1 - g_2) n_0$

While the ergosurface is created via a sharp jump of the vector potential, a smooth spatial variation of the interaction constant around the horizon is considered, of the form

$$g(y) = g_1 + \frac{g_2 - g_1}{2} \left(1 + \tanh \left(\frac{y - y_H}{\ell_0} \right) \right) . \tag{4.5}$$

Here, y_H is the position of the horizon and l_0 regulates the smoothness of the transition. An analogous analytical form is taken for the vector potential $A_x(y)$ crossing from A_E to A_H.

In order to offer a seed to the instabilities, we start from an initial noisy configuration. A pair of absorbing regions are included well outside the ergoregion and well inside the horizon so to mimic open boundary conditions. This guarantees that all spurious instabilities that may come from the backfeeding of excitations from the outside (black hole bomb) and from the inside (black hole lasing) of the black hole are fully suppressed.

Even though the structure of the modes is the same in all cases, the numerical results turn out to be qualitatively different depending on the *smoothness* of the horizon, that is on the thickness l_0 of the transition region and on the difference between A_H and A_E.

In the presence of a second jump of vector potential from $A_x = A_E$ to $A_x = A_H = 0$, the behaviour depends strongly on the thickness l_0 of the transition (4.5). For very sharp horizons (that is for small l_0) dynamically unstable modes localized on the horizon and independent on the size of the ergoregion are observed; these do not seem to be directly related to superradiant phenomena but depend on the microscopic physics of the condensate. In the next Subsection we will give more details on these instabilities, that we plan to investigate in future work.

For smoother horizons, such localized instabilities are no longer present, and a spatially extended dynamical instability of completely different nature takes place, as signalled by the fast temporal growth of a spatially oscillating pattern that extends all the way between the ergosurface and the horizon. An example of such an temporal evolution is shown in Figure 4.9. The origin of this instability can be traced to the self-amplification of the excitations trapped in the ergoregion according to a mechanism similar to the one illustrated in Fig.3.6: excitations bounce between the ergosurface, where they get amplified, and the horizon where they are partially reflected with a sufficiently high amplitude to give an overall increase of the excitation intensity during a round-trip. These are the typical features of an *ergoregion instability*: interestingly enough, such instability occurs here in spite of the presence of a horizon. Note that here

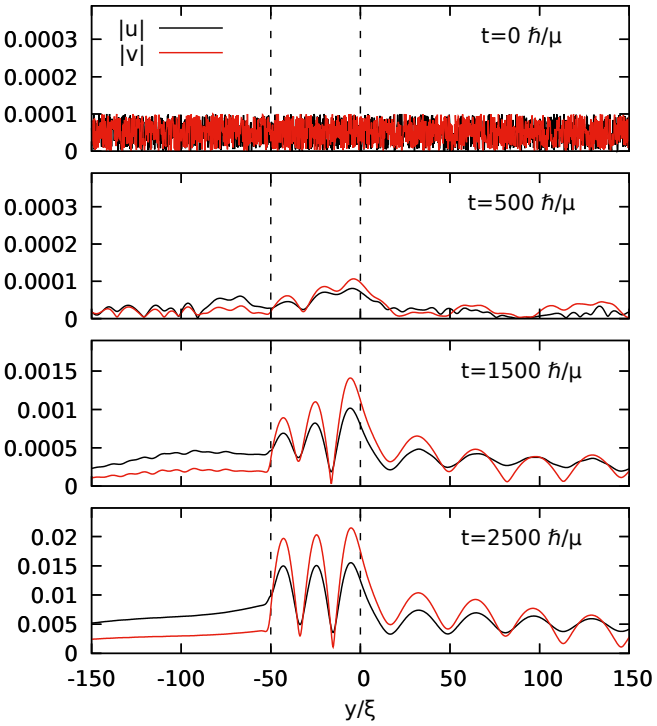

Figure 4.9: Snapshots of the time evolution of the moduli of the fluctuation spinor components given by the reduced one-dimensional Bogoliubov problem at a fixed transverse wavevector $k_x\xi = 0.1$ for the configuration sketched in Figure 4.8 with $A_H = 0$ and $l_0 = 5\xi$. The evolution starts from a noisy configuration and absorbing regions are included at the boundary of the integration box to avoid spurious reflections. The black and red lines show the modulus of the u, v components of the Bogoliubov spinor. Time is measured in units of the external $\mu = mc_1^2$.

the radiative wave that enter the horizon is composed of two k_y components of opposite norms whose beating is responsible for the oscillating behaviour seen in the figure for $y > 0$.

In order to verify our interpretation, we need to check that the ergoregion instability disappears when smoother transitions are considered for which reflection is negligible. While increasing l_0 is observed to determine a reduction of the instability rate given by a smaller refection at the horizon, a further increase would require a substantial change of the configuration to properly accommodate the transition region. We hence chose to obtain a smoother transition by reducing the second jump of the vector potential $A_H - A_E$. In particular, we performed simulations for A_H ranging from zero to a flat vector potential profile across the horizon interface $A_H = A_E$, so to pass from a sharper horizon to a smoother one. For A_H approaching A_E, reflections at the horizon interface are indeed well suppressed, so that the initial noisy configuration smoothly decays in time and only displays some long-lived *quasinormal modes*. This configuration is thus

close to the standard astrophysical case where reflection of waves traveling towards the black hole horizon are typically excluded.

Further confirmation of this physical picture is provided by a spectral analysis of the growing perturbation. This shows that the frequencies of all unstable modes fall in the superradiant interval (gray region of Figure 4.8). As a final evidence, we checked that increasing the size of the ergoregion causes the number of unstable modes to increase and their instability rates to decrease according to the increased round-trip time within the ergoregion.

On the basis of this analysis, we can conclude that the presence of an horizon does not *in general* guarantee the absence of ergoregion instabilities. Observable ergoregion instabilities may in fact arise for strong enough reflection around the horizon. The fact that no such instabilities have been ever found in *real* general-relativistic black holes [10] or in vortices [109] suggests that in all these cases the horizon region is smooth enough to suppress reflection. Still, as our calculations show, this feature does not appear to be a general property of horizons and may not be satisfied in other configurations.

4.3.3 Surface instabilities at the horizon

In the previous Subsection we mentioned that, when changing sharply in space both the vector potential and the speed of sound, dynamical instabilities localized on the interface can develop. To give more details about these instabilities, we consider here, instead of a configuration with three zones as we did in the rest of this Section, a single interface dividing a region with no synthetic vector potential and subsonic longitudinal flow from one with a (large enough) transverse vector potential and a lower speed of sound, making the longitudinal flow supersonic.

In other words horizon and ergoregion occur at the same point, similarly to the Schwarzschild black hole or to the one-dimensional setup of Subsection 1.5, but with the added complexity of a nontrivial flow in the extra spatial dimension. This is very different to what happens in *real* rotating black holes, where the ergosurface is always outside of the horizon, but serves here merely an example to show how these surface instabilities can occur; a more comprehensive study of this interesting physics is planned in future work.

A time evolution of the Bogoliubov problem in such a configuration with absorbing regions at the edges of the numerical box, starting from a noisy initial state, results in the exponential increase of the mode shown in the upper plot of the left part of Figure 4.10; the quick decrease of the mode above $y \sim 150\xi$ is due to the presence of the absorbing potential. This exponential growth is reflected in the spectrum of excitations: performing a diagonalization of the Bogoliubov problem with Dirichlet boundary conditions at the edges of a numerical box large enough to reduce finite-size effects, one finds a dynamically unstable mode of essentially identical shape, shown in the lower plot; notice the smoother decrease of the mode in the absence of an absorbing potential. In the slower $y < 0$ region the mode has a smooth exponential decay, while in the faster $y > 0$ one the decay is slower and there are spatial oscillations in the moduli of the Bogoliubov spinor components;

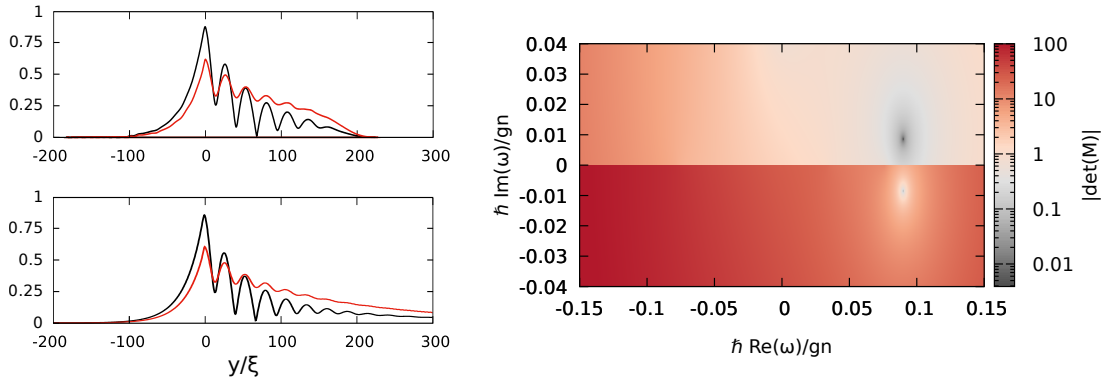

Figure 4.10: Different investigations of the surface instabilities that can develop in the presence of a simultaneous jump in the value of the synthetic vector potential and in the one of the speed of sound (i.e. of the interaction constant). In the top left panel a plot of the dynamically unstable modes as obtained from the time evolution of the Bogoliubov problem with absorbing boundary conditions at the edges of the numerical domain. In the bottom left panel a plot of the dynamically unstable mode found with a diagonalization of the Bogoliubov problem for a finite-size system. On the right log-scale plot of the determinant of the linear problem given by the matching of the modes of the two uniform regions with the procedure presented in Subsection 4.1.3; the zero of the determinant for positive imaginary parts of the frequencies corresponds to the dynamically unstable mode detected with the other two methods. The parameters used are longitudinal flow $v_y = 0.85\ c_1$, vector potential in the upper region $A_x^f = -2.12\ Mc_1$ and zero in the lower region, speed of sound in the upper region $c_2 = 0.1\ c_1$. The problem is solved at fixed transverse momentum $k_x = 0.14/\xi_1$.

this signals that the mode is composed by multiple (two) momentum components with different real parts of the wavenumbers, that results in beating.

The spatially decreasing profile of the mode in both the regions suggests that it is a localized *surface* dynamical instability. As we will discuss in the next Chapter, the fact that the mode obtained with diagonalization appears *localized* is an indication of the fact that this instability remains in an unbound system. Notice however that the effect of the finite size of the system used for the diagonalization remains as very small oscillations on the long right tail of the mode in the bottom left panel. The time dependent simulations with absorbing boundary conditions mimics the behaviour of an unbound system and confirms this picture. In the next Chapter we will give a complete discussion of the effects on dynamical instabilities of the finite size of the system.

Here we can get further confirmation by applying the procedure presented in Subsection 4.1.3, that allows to treat exactly an unbound system. By matching the asymptotically bound modes in the two regions at the interface at different frequencies one obtains the determinant shown in the right part of Figure 4.10. Zeros of the determinant corresponding to a dynamically unstable mode and its decaying pseudo-degenerate

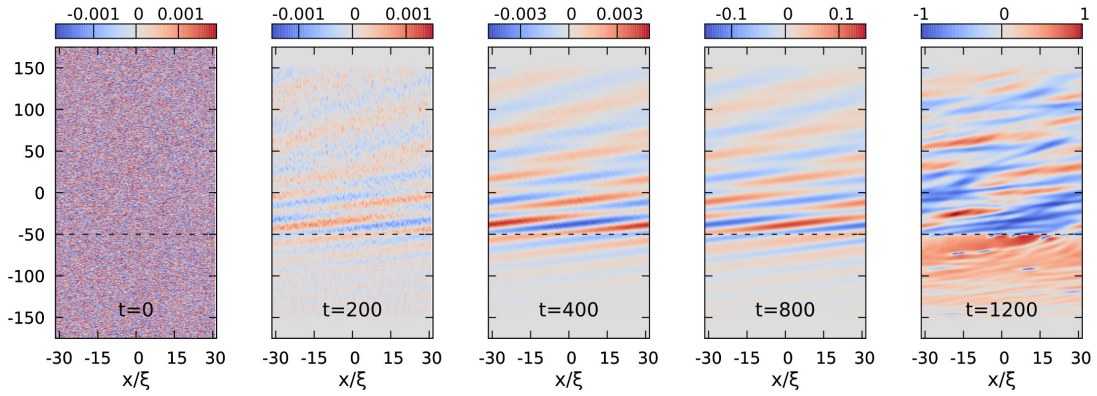

Figure 4.11: Time evolution of the density variations around the constant-density stationary state for a condensate with a uniform vertical flow $v_y = 0.85\ c_1$, vector potential in the upper region $A_x^f = -2.12\ Mc_1$ and zero in the lower region and speed of sound in the upper region $c_2 = 0.1\ c_1$. An initial weak noise is added to serve as a seed for dynamical instabilities. Periodic boundary conditions are used and two absorbing regions are included at the y edges, so to mimic an open system in that direction. The exponentially growing mode corresponds to the one observed in the one-dimensional approach of Figure 4.10.

partner are clearly visible. The real and imaginary parts of the frequency corresponding to the dynamically unstable mode are compatible with the values obtained from the time evolution and the diagonalization of the Bogoliubov problem.

Another visualization of this instability can be obtained by performing a numerical time evolution of the corresponding two-dimensional GPE with absorbing boundary conditions at the edges of the y range of the numerical integration box. In Figure 4.11 snapshots of such a simulation starting from a noisy perturbation around the uniform stationary state are shown. One can see that an exponentially growing mode dominates the dynamics; this mode decreases in a fast way *outside of the horizon* ($y < -50\ \xi$) and has instead a longer tail inside the horizon, exactly as the one of Figure 4.10. The exponential growth of this mode saturates at long times, when nonlinear effects come into play; in the last snapshots one can in fact see a substantial modification of the stationary states, with also the creation of vortices.

The numerical analyses presented here clearly show that a simultaneous jump in the synthetic vector potential and in the speed of sound can lead to dynamical instabilities localized on the surface, that is also present in an unbound system. As we underlined in the previous Subsection, these disappear for *smooth enough* transitions, that seems to be the case of general-relativistic black holes.

4.4 Summary: superradiance and dynamical instabilities

Following the general theory of superradiance presented in the previous Chapter, in the present one we analyzed the role of boundary conditions in superradiant effects. In particular we focused on a planar ergosurface obtained with the application of a synthetic vector potential and we changed the boundary conditions on its two sides by confining the condensate or by changing the speed of sound.

The presence of reflection brought, as expected, the emergence of dynamical instabilities. In our geometrically simple setup the analogue of black hole bomb and ergoregion instabilities of rotating spacetimes are obtained with reflections outside or inside the ergoregion. Through the exact mapping with a one-dimensional charged scalar field these instabilities turn out to be a realization of the SSW effect for an electrostatic potential box. Predicted in a toy model for nuclear physics, this effect finds here a first possible experimental implementation. Away from this ideal *dispersionless* analogy, when the superluminal behaviour of excitations in BECs was taken into account, important suppressions of the instability at high momenta were found, analogous to the ones we demonstrated for amplified scattering. The behaviour at small momenta is however not affected by these dispersive effects.

While studying these instabilities via the Bogoliubov problem, we also proved the dynamical stability of the planar ergosurface in an unbound system. Our setup is hence a system in which amplified scattering is the only relevant physical mechanism, differently from analogous flows in hydrodynamics, that display dynamical instabilities of the interface. We will return to these surface instabilities in Chapter 6, where we will study their interplay with superradiant effects in a BEC setup.

A conclusion of the previous Chapter was that superradiance can be understood as a mode mixing at the ergosurface. Here we showed that this implies that, while without *dissipation* superradiant instabilities emerge, in the presence of reflections amplified scattering can still occur as a *transient time-dependent* effect concerning finite-width wavepackets. This means that in black holes superradiant scattering can also occur in the absence of an horizon, that only determines the unstable behaviour at late times. This answers the important question we put forward at the end of Chapter 2 on the role of boundary conditions for amplified scattering.

Regarding horizons, we also showed how they do not *in general* provide the necessary absorption to avoid ergoregion instability, but it depends on the smoothness of the spacetime around them. This does probably not apply to black hole solutions of the Einstein equations, for which horizons were found to provide an open boundary condition and hence dynamical stability, but may be important for analogue models and more peculiar spacetimes.

This Chapter closes the *lessons* we derived *from* BEC analogues for the understanding of superradiance. The following Chapters will deal with the opposite arrow of the analogy, using the concepts emerging from superradiance to understand the physics of BECs, starting with the important problem of the stability of quantized vortices in BECs.

Chapter 5

Ergoregion instabilities in quantized vortices

Our investigation of superradiance so far has focused on proposing and analyzing analogue configurations in which the basic mechanisms of the phenomenon appear in a simple way and with which superradiance and superradiant instabilities can hopefully be investigated experimentally, also at the quantum level. The *flow of information* has hence been, as usual in Analogue Gravity, mainly from the well-known and well-controlled microphysics of Bose–Einstein condensates to the less approachable one of curved spacetimes.

In this Chapter our path will instead be the opposite and we will try to get insight into the fundamental physics of BECs from the gravitational analogy and what is known about the physics of rotating spacetimes. This perspective was adopted for example in [144], where schemes to exploit analog Hawking processes to entangle collective phonon modes were proposed, and in [88], where a one-dimensional superfluid flow instability was reinterpreted as a black hole lasing effect.

The concepts we are interested in applying are the ones we developed in the previous Chapters, and in particular what we learned about superradiant instabilities in Chapter 5. We will consider with this perspective the stability properties of one of the most important features of superfluids and BECs: quantized vortices. These share with our planar ergosurfaces a purely *tangential* flow that passes from subsonic to supersonic when moving towards the core of the vortex.

These objects have received a great deal of attention in the last decades, both theoretically and experimentally [16,130], beginning with the very introduction of the Gross–Pitaevskii equation in early 1960's in [145], where singly quantized vortices in an infinite condensate were considered. Since the experimental realization of atomic BECs in optical and/or magnetic traps, extensive studies on the properties of vortices in trapped gases have been performed [40, 146–152]. The *idealized* case of quantized vortices in spatially infinite geometries was instead much less considered and only recently a convincing evidence that doubly quantized vortex are dynamically unstable in a spatially uniform BEC was in fact reported [152], while dynamical stability of such configurations

had been previously claimed by several authors [149, 153]. More in general, a full understanding of the microscopic mechanisms determining the stability of quantized vortices in generic geometries is still missing.

From our analogue gravity point of view it is natural to start by asking what is the acoustic geometry provided by a quantized vortex. Their irrotational flow is purely azimuthal and has a radial dependence $v_\theta \propto 1/r$, and hence becomes supersonic in the vicinity of the vortex core. With respect to the vortex geometry presented in Section 1.3.3, the absence of a radial flow implies that there can be no horizon, so that the acoustic spacetime has only an ergoregion. This naturally suggests the possibility of *ergoregion instabilities* (Section 2.5.2). Also, when considering trapped geometries the vanishing density of the condensate at the border of the system imposes a reflecting boundary condition on the fluctuation field, so that for quantized vortices in a trapped BEC also the black hole bomb mechanism of Section 2.5.1 can occur. Unraveling the different instability mechanisms at play in different geometries is the main subject of this Chapter.

Notice however that this picture of the possible instability mechanisms for a vortex relies on the gravitational analogy, that only holds in the hydrodynamic limit, and attention must be paid to the microscopic features of the BEC. In particular the sudden density drop in the vortex core falls outside the validity of the hydrodynamic vortex and the superluminal dispersion of excitations can, as we saw in the previous Chapters, modify superradiant phenomena with respect to the predictions based on the Klein–Gordon equation.

In this Chapter we carry out a microscopic study of the Bogoliubov collective excitations around vortices of different charge in spatially homogeneous two-dimensional BECs beyond the hydrodynamic approximation. With a careful consideration of the boundary conditions, we confirm that singly quantized vortices are stable in an otherwise uniform condensate, whereas doubly quantized ones are rendered dynamically unstable by an intrinsic instability of the vortex core, analogous to an ergoregion instability. We then extend our analysis to vortices with higher charge to further characterize the instabilities in the different angular momentum channels and additional similarities with ergoregion instabilities in hydrodynamic vortices (studied in [125]) are found, from which we conclude that the dynamical instabilities of multiply quantized vortices are condensed matter analogues of the ergoregion instabilities of rotating spacetimes, with some modifications due to dispersive effects.

Our results also shine new light on the known results for trapped BECs, showing that the instability is not induced by the trap and, thus, is not related to black-hole-bomb type mechanisms. The only effect of the trap is rather to modulate the instability rate via interference mechanisms and even suppress it in specific regimes. Application of our formalism to singly quantized vortices brings the unexpected consequence that their celebrated dynamical stability is not a general fact, but a consequence of the spatially homogeneous or harmonic trap geometries usually considered in the literature: more complex configurations showing an inner density bump followed by a constant density plateau turn out to be dynamically unstable against the vortex spiralling out even at

zero temperature.

As a final point, we show that multiply quantized vortices provide another example of how superradiant scattering can also occur in the presence of ergoregion instabilities. This is further evidence on the fact that dissipation is not an essential ingredient for superradiance.

The work presented in this Chapter was published in [22].

5.1 Vortices and the linear Bogoliubov problem

Let us start from the Gross–Pitaevskii equation (1.5) describing a dilute Bose-Einstein condensate at zero temperature

$$i\hbar\partial_t\Psi(\mathbf{r},t) = \left[-\frac{\hbar^2\nabla^2}{2M} + g|\Psi(\mathbf{r},t)|^2 + V_{\rm ext}\right]\Psi(\mathbf{r},t), \tag{5.1}$$

where g is the interparticle interaction constant, M is the atomic mass and $V_{\rm ext}(\mathbf{r})$ is an external trapping potential. As in the previous Chapters we consider the case of two spatial dimensions, which simplifies the treatment and is a good approximation for a pancake-shaped condensate tightly confined in the third direction.

Vortices located at the center of a cylindrically-symmetric system are stationary solutions of the GPE of the form

$$\Psi_\ell(\mathbf{r},t) = f(r)e^{i\ell\theta}e^{-i\mu t/\hbar}, \tag{5.2}$$

where μ is the chemical potential of the condensate and ℓ is a number that, for the order parameter to be single valued, must be an integer. This expresses the *quantization of the circulation* of the vortex and we refer to ℓ as the *charge* of the vortex. Vortices of charge ℓ have a purely azimuthal velocity profile of the form

$$v_\theta(r) = \frac{\hbar}{M}\frac{\ell}{r}, \tag{5.3}$$

which turns supersonic in the vicinity of the vortex core.

To avoid singularities at $r = 0$, the (real-valued) amplitude $f(r)$ of the order parameter must go to zero for $r \to 0$ so that in the center of vortex the density is depleted. For a vortex in an otherwise infinite and spatially homogeneous condensate the order parameter tends to a constant $f(r) \to f_\infty$ at large distances, while the chemical potential is $\mu = gn_\infty = g|f_\infty|^2$. For a vortex of charge ℓ, the current becomes supersonic at a radius $r_E \sim \ell\xi$, where the healing length $\xi = \hbar/(mgf_\infty^2)^{1/2}$ is calculated for the asymptotic value of the density. The healing length can also be seen as the distance at which the density reaches approximately half of the value at infinity [16]. Near the core of the vortex we are hence away from the hydrodynamic regime.

The stability of vortices can be studied with the Bogoliubov approach of Section 1.1.2, where one linearizes the GPE around the stationary state Ψ_ℓ and looks for the eigenmodes of the linearized dynamics. In the cylindrically symmetric geometries under

consideration, we can decompose the perturbation vector (1.19) in its angular momentum m components

$$\begin{pmatrix}\delta\Psi\\ \delta\Psi^*\end{pmatrix}(r,\theta,t)=e^{im\theta}\begin{pmatrix}e^{i\ell\theta}e^{-i\mu t/\hbar}u_\phi(r,t)\\ e^{-i\ell\theta}e^{i\mu t/\hbar}v_\phi(r,t)\end{pmatrix}. \tag{5.4}$$

and focus our attention on the radial dynamics. For each m component, the time evolution for the radial spinor $|\phi\rangle(r,t):=(u_\phi(r,t),v_\phi(r,t))^T$ is given by the Bogoliubov–de Gennes (BdG) equation

$$i\hbar\partial_t|\phi\rangle=\mathscr{L}_{\ell,m}|\phi\rangle \tag{5.5}$$

with the radial Bogoliubov operator

$$\mathscr{L}_{\ell,m}=\begin{bmatrix}D_+ + V_{\rm ext}+2gf^2-\mu & gf^2\\ -gf^2 & -(D_- + V_{\rm ext}+2gf^2-\mu)\end{bmatrix} \tag{5.6}$$

and

$$D_\pm=\frac{\hbar^2}{2M}\left(-\partial_r^2-\frac{\partial_r}{r}+\frac{(\ell\pm m)^2}{r^2}\right). \tag{5.7}$$

As discussed in Section 1.1.2 for the general case, the evolution (5.5) is σ_3-pseudo-unitary, i.e. $\sigma_3\mathscr{L}_{\ell,m}^\dagger\sigma_3=\mathscr{L}_{\ell,m}$, and the associated conserved non-positive definite inner product (1.23) becomes here

$$\langle\psi|\,\sigma_3\,|\psi\rangle=2\pi\int{\rm d}r\;r\left[u_\psi^*(r)u_\psi(r)-v_\psi^*(r)v_\psi(r)\right]. \tag{5.8}$$

Remember that the energy of an eigenmode $|\psi_i\rangle$ of the BdG matrix (5.6) with frequency ω_i is given by

$$E_i=\langle\psi_i|\,\sigma_3\,|\psi_i\rangle\,\hbar\omega_i, \tag{5.9}$$

so that, for example, negative-norm (positive-norm) modes with a positive (negative) real frequency have negative energy, and that complex-frequency modes come in *pseudo-degenerate* (sharing the same real part) pairs of decaying and dynamically unstable zero-norm modes. According to (5.9), zero norm implies zero energy: in physical terms the exponential growth of unstable modes corresponds to the simultaneous creation of particles and antiparticles with opposite energies, which leaves the total energy unchanged.

Another property of the BdG matrix important for the present analysis is the *particle-hole symmetry* (1.26), that in our cylindrically symmetric geometry, with the choice (5.4), is expressed by the fact that the spectrum at $-m$ is specular to the one at m. In detail, there exist pairs i,j of eigenvectors and eigenvalues at $\pm m$ that are related to each other by

$$\begin{pmatrix}u_{-m,j}\\ v_{-m,j}\end{pmatrix}=\begin{pmatrix}v_{m,i}\\ u_{m,i}\end{pmatrix};\qquad \omega_{-m,j}=-\omega_{m,i}, \tag{5.10}$$

so that both the sign of the frequency and the norm of the mode are inverted. In what follows, we can thus restrict our attention to positive values of m only with no loss of information.

In what follows, it will be useful to also consider the shape (1.82) of the radial BdG equations in terms of density and phase perturbations $\delta\widetilde{n} := \delta n/n$ and $\delta\Theta$

$$\partial_t \begin{pmatrix} \delta\Theta \\ \delta\widetilde{n} \end{pmatrix} = \begin{bmatrix} -i\dfrac{\hbar}{M}\dfrac{\ell m}{r^2} & -\dfrac{\widetilde{D}}{2} - \dfrac{Mc_s^2}{\hbar} \\ 2\widetilde{D} & -i\dfrac{\hbar}{M}\dfrac{\ell m}{r^2} \end{bmatrix} \begin{pmatrix} \delta\Theta \\ \delta\widetilde{n} \end{pmatrix} \tag{5.11}$$

with

$$\widetilde{D} = \frac{\hbar}{2M}\left(-\partial_r^2 - \frac{\partial_r}{r} - \frac{\partial_r f^2}{f^2}\partial_r + \frac{m^2}{r^2}\right). \tag{5.12}$$

As we discussed in Section 1.4, for slowly spatially varying (*long-wavelength*) perturbations the derivative term in the upper right element is negligible and the resulting equation has the shape of a Klein–Gordon (KG) equation in a curved spacetime with the local speed of sound $c_s = \sqrt{gf^2/m}$ playing the role of the speed of light.

The spectral properties of the BdG equations summarized above are shared by the KG equation, but we know that the two equations differ for the associated dispersion relations, with the BdG one deviating from the linear behaviour of the KG one. In spite of this difference, it is useful to look at the problem of the vortex stability starting from what is known for gravitational systems and look for possible modifications due to the deviations from the linear dispersion of the hydrodynamic limit and to the microscopic structure of the vortex core.

Notice that, while the hydrodynamic approximation on the background condensate automatically implies taking the long-wavelength limit for the fluctuations, leading to the non-dispersive KG problem, the long-wavelength approximation for the perturbation field can formally be performed even for background density profiles outside of the hydrodynamic regime. This will allow us in Section 5.4 to discriminate between the modifications to the gravitational effects due to dispersion and those due to the microscopic behaviour of the density.

5.2 Stability of vortices in trapped BECs: what is known

In an infinite condensate, the energy of a charge ℓ vortex is higher than the one of an array of ℓ singly charged vortices [36]: this means that multiply quantized vortices are *energetically unstable*.

Concerning harmonically trapped condensates, extensive studies within the Bogoliubov approach [146, 147] have shown that vortices – even singly quantized ones – are always *energetically unstable* since they possess a negative-energy $m = 1$ mode localized around the vortex core, corresponding to precession around the trap center. Actual spiraling of the vortex out of the condensate requires some mechanism to dissipate the extra energy, for example via interaction with thermal atoms at finite temperatures [154]. As a result, the vortex position remains *dynamically stable* under the purely conservative dynamics (5.5).

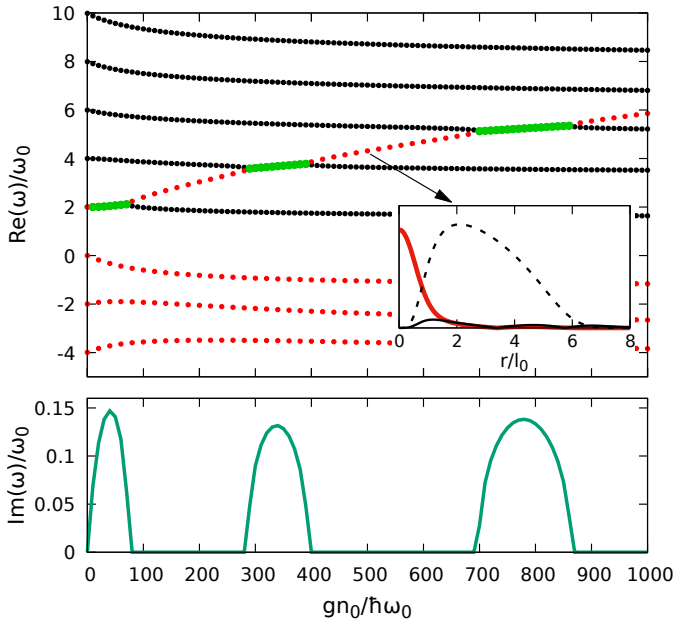

Figure 5.1: Real (upper plot) and imaginary (lower plot) parts of the BdG eigenfrequencies for modes of azimuthal number $m = 2$ on a charge $\ell = 2$ vortex in an harmonic trap for different values of the interparticle interaction energy. Here $n_0 = N/l_0^2$ with N number of atoms and $l_0 = \sqrt{\hbar/(2M\omega_0)}$. Black (solid), red (dotted) and green (thicker) lines correspond to positive-, negative- and zero-norm modes. In the inset a plot of the energetically unstable mode for $gn_0/\hbar\omega_0 = 500$: the black (thinner) and red (thicker) lines show the modulus of the u and v components of the BdG spinor, the dashed line is a rescaled plot of the condensate density.

While all other excitation modes of singly charged vortices are energetically (and thus dynamically) stable, multiply quantized ones display alternate intervals of dynamical instability and stability as the nonlinear interparticle interaction is varied with respect to the trap frequency. An example of this behaviour for $m = 2$ perturbations on a charge $\ell = 2$ vortex, reproducing the conclusions of [148], is shown in Figure 5.1. After numerically finding the radial profile $f(r)$ of the GPE ground state at fixed circulation ℓ with an external trapping potential $V_{\rm ext}(r) = M\omega_0^2 r^2/2$, we diagonalize the corresponding BdG matrix (5.6) for a fixed azimuthal number m but different values of the nonlinear parameter of the GPE, i.e. for different values of the interparticle interaction constant or for different numbers of atoms in the trap.

One can see that the system has a negative energy mode (negative norm and positive frequency) for all values of the parameters and is thus energetically unstable. This energetically unstable mode is localized near the vortex core, as can be seen in the inset. As discussed also in [40], dynamically unstable modes can emerge from the crossing of this negative-norm band with a positive-norm one. This is a consequence of the symplec-

tic [42] nature of the BdG problem and in the Hamiltonian systems language is known as the mixing of modes of opposite Krein norm. This gives rise to the characteristic mode sticking visible in the upper panel, associated to the instability bubbles that are visible in the lower panel.

Even though the literature agrees on the occurrence of these instabilities and unambiguous experimental evidence is available [151], the situation is much less clear for what concerns the physical origin of the instability. The fundamental question that we plan to address in this article is to understand whether the dynamical instability is induced by the trapping, as some authors suggest [153, 155], or whether it is instead an intrinsic instability of the vortex core, as recently argued in [152].

What is sure is that vortices of any charge in trapped condensates have some angular momentum channels with energetically unstable modes localized in the core. In the language of the gravitational analogy, these modes corresponds to negative-energy modes localized in the ergoregion of a rotating spacetime. The energetic instability can then be turned into a dynamical one if enough reflection happens on either side of the ergoregion: if it happens on the outer side, one has the so-called black-hole-bomb effect; if it happens on the inner side, an ergoregion instability occurs.

As it has been pointed out in [152] and we are going to show in the next sections, the instability of multiply charged vortices in condensates persists in spatially unbounded geometries where no reflection from the outer side can occur, so it can be classified of the ergoregion instability type. The effect of the trapping is rather the opposite, since it tends to suppress the instability within some specific regions of parameters as already visible in Figure 5.1.

5.3 A charge 2 vortex in an infinite BEC

5.3.1 Large system limit $R \to \infty$

As a first step, we follow the path of [152] and investigate the stability of a doubly quantized vortex in an infinite BEC by looking how the spectrum of a finite system of size R evolves in the infinite size limit $R \to \infty$. To this purpose, we numerically find the radial profile $f(r)$ of the GPE ground state Ψ_ℓ with a given circulation ℓ on a wide but finite interval $[0, R]$. In order to mimic a spatially homogeneous BEC, Neumann boundary conditions $\partial_r f|_{r=R} = 0$ are imposed on the BEC wavefunction. The BdG spectrum is then obtained imposing Dirichlet boundary conditions at $r = R$ onto the perturbation, $u_\phi(r = R) = v_\phi(r = R) = 0$. The calculation is repeated for growing values of the size R.

The resulting discrete spectra of modes are shown in the left panels of Figure 5.2 as a function of R for an $m = 2$ perturbation on a charge $\ell = 2$ vortex. An energetically unstable mode (with negative norm and positive frequency) is clearly visible in panel (a) at an (almost) R-independent frequency around $0.44\,\mu/\hbar$. This R-independence is a strong indication that the mode is localized in the core region, which is further verified in the exponential decay of the envelope of u_ϕ and v_ϕ of the unstable mode (panel

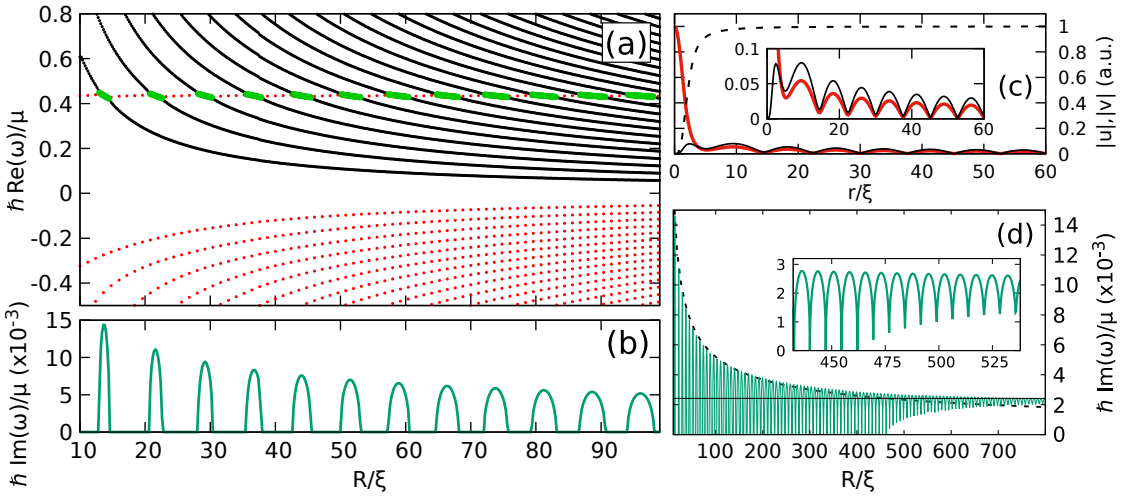

Figure 5.2: Real (a) and imaginary (b) parts of the Bogoliubov eigenfrequencies for modes of azimuthal number $m = 2$ on a charge $\ell = 2$ vortex in a BEC of size R. Black (solid), red (dotted), green (thicker) lines corresponds to positive-, negative-, and zero-norm modes. A wider view of the imaginary part is given in panel (d). Here, the $1/\sqrt{R}$ dashed line envelopes the instability maxima up to moderate R. The horizontal line indicates the instability rate extracted from the time-dependent simulation with absorbing boundary conditions shown in Figure 5.3. Panel (c): spatial shape of the dynamically unstable core mode for the case with $R = 60\xi$. The black (thin) and red (thick) lines respectively show the moduli of the u_ϕ and v_ϕ components of the Bogoliubov spinor. The dashed line shows the (rescaled) density profile of the vortex. In the inset the mode on a shorter amplitude range is plotted to highlight the structure at large r.

(c)). As for the trapped BEC case, dynamical instabilities emerge from the crossing of this negative norm core mode with the positive-norm collective modes; the resulting instability bubbles are shown in Figure 5.2(b).

More insight in the instability mechanism is visible in the spatial profile of the dynamically unstable mode shown in panel (c): here, one recognizes a localized part at the vortex core which contributes with a negative norm and an extended part that penetrates deep in the bulk with a positive norm (better visible in the zoom in the inset). The two add up to a total zero norm, as expected for a dynamically unstable mode. This spatial structure indicates that the instability is due the coupling of a localized negative-energy excitation to a propagating positive-norm one. The oscillations that are visible at large r are due to the interference of the outgoing waves with their reflection at the system edge $r = R$.

Looking at Figure 5.2(d), an important distinction between the moderate-R and large-R regimes jumps to the eyes. In the former case, the positive-norm collective modes of the condensate are well distinct in energy and the stability islands (instability peaks) are well separated as a function of R: stability (instability) occurs whenever the phase of the reflected waves at the $r = R$ boundary destructively (constructively)

interferes with the oscillation of the core mode. This same mechanism is the cause of the finite stability windows that are also visible in the trapped condensate case of Figure 5.1. A time-dependent insight on this destructive interference will be given in Section 5.6, where we discuss the temporal evolution of the system in response to a initial perturbation. In contrast, for large R the instability bubbles merge with each other and the instability rate tends to a R-independent value.

Some qualitative understanding about this crossover can be obtained by analytical means. As mentioned in [11], the instability stems from the mixing of a spatially extended positive-norm mode with a localized negative-norm one, so the matrix element $\mathcal{M}$ of the mixing scales as the normalization of the spatially extended mode. In our cylindrical geometry, this normalization scales as $R^{-1/2}$, which determines the scaling $\mathcal{M}(R) \sim R^{-1/2}$ of the matrix element. This scaling reflects in an analogous scaling for the envelope of the instability rate maxima in the moderate-R regime where modes are well discrete, see the dashed line in Figure 5.2(d).

The width of the instability bubbles is instead determined by the width of the regions around the crossing point for which the detuning of the positive- and negative-norm modes is not larger than the matrix element $\mathcal{M}$. The width in R is hence proportional to the ratio between the matrix element and the derivative $d\omega/dR$, namely $\delta R \sim \mathcal{M}/|d\omega/dR|$.

Since the positive-norm modes have a phononic nature, the frequency of the j-th mode (with j integer) scales approximately as $\omega_j \sim j\, c_s/R$, so that the derivative at the crossing point with the frequency ω_- of the trapped mode is given by $|d\omega_j/dR| \sim \omega_-/R$. Hence the width δR of the instability bubbles increases as $\sqrt{R}$ for growing R, as visible in Fig.5.2(b). Given the scaling of ω_j on R, the spacing ΔR between modes at the same frequency is instead a constant, so that neighboring instability bubbles eventually merge with each other into a broad continuum for large values of R.

More in detail, the spacing ΔR along R can be related to the frequency spacing $\Delta\omega$ between modes at a given R by $\Delta R = \Delta\omega/|d\omega/dR|$. Since the mode spacing $\Delta\omega$ is related by $\Delta\omega = 2\pi/T_{\rm rt}$ to the round-trip time $T_{\rm rt}$ of phonons from the core to the $r = R$ boundary and back, the merging condition $\delta R \gtrsim \Delta R$ can be reformulated as $\mathcal{M}(R)\, T_{\rm rt} \gtrsim 1$ which has a transparent physical interpretation: the instability bubbles due to the spatially finite geometry disappear into a structureless continuum when the round-trip time exceeds the characteristic time of the instability, so that finite-size effects can no longer affect the dynamics of the instability.

5.3.2 Outgoing boundary conditions

While this way of taking the infinite-size limit may seem a sound way of describing a spatially infinite system, one must not forget that the eigenmodes of finite systems have a standing-wave shape and necessarily involve a reflected in-going wave, while for a truly infinite system no reflection is possible and the eigenmodes must have a purely outgoing character. As a consequence, the spectrum of a finite system is generally very different (even in the infinite-size limit) from the one in the asymptotic outgoing

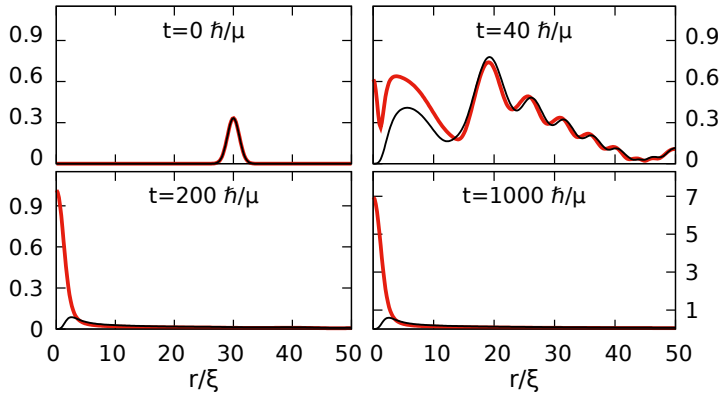

Figure 5.3: Snapshots of the time evolution of a $m = 2$ perturbation scattering on a $\ell = 2$ vortex. Black (thin) and red (thick) lines respectively show the u_ϕ and v_ϕ components of the Bogoliubov spinor. Outgoing boundary conditions are imposed by including a wide and smooth imaginary potential of Gaussian spatial shape centered at the edge of the integration box $r = 700\xi$, of variance 120ξ and amplitude 0.15μ, so to effectively absorb the perturbation spinor $|\phi\rangle$ and suppress the reflected waves.

boundary conditions case. Because of this crucial difference, well highlighted for the Klein–Gordon case in [44], it is thus essential to put any conclusion on the infinite system on solid grounds by implementing radiative boundary conditions where all reflected waves are removed from the outset. The approach we used in Section 4.1.3 to treat directly the open system is not practicable here because the system is not simply composed by uniform regions and neither an eikonal approximation is possible due to the rapid density variations near the vortex core. We hence resort to time-dependent simulations.

In Figure 5.3 we summarize a numerical study of the time-dependent BdG equations (5.5) where such radiative boundary conditions are implemented by adding an effective absorption at large distances. A series of snapshots of the evolution of a perturbation in the $m = 2$ channel in the presence of a $\ell = 2$ vortex are shown, starting from a (arbitrarily chosen) real and Gaussian perturbation equally affecting the u and v components of the BdG spinor (upper-left panel). At early times (not shown) the perturbation splits in a pair of in- and out-going wavepackets the in-going one is then reflected by the vortex core and ends up propagating in the outwards direction as well, albeit with a strongly deformed shape because of the superluminal dispersion (upper-right panel). Eventually, the spatial shape of the perturbation is characterized at long times by an exponentially growing, negative-norm unstable core mode and a positive-norm excitation current propagating to infinity (bottom panels). Compared to Figure 5.2(c), the outgoing boundary conditions remove the interference-induced oscillations at large distance, leaving only the exponential spatial decay typical of unstable modes. The complex profile visible in the upper-right panel is a transient effect due to interference between the incident and the reflected wavepackets at the vortex core and disappears at late times as shown in the bottom row panels.

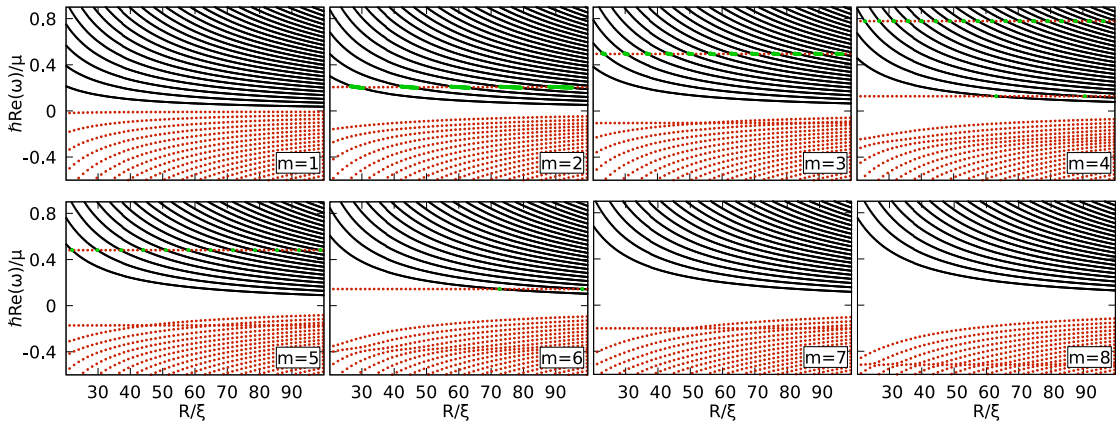

Figure 5.4: R-dependence of the Bogoliubov spectrum of a $\ell = 4$ vortex for different azimuthal m. Black (solid), red (dotted) and green (thicker) lines correspond to positive-, negative- and zero-norm modes.

The temporal growth of the core mode can be precisely fitted with an exponential law (not shown) of instability rate $\Im(\omega) \simeq 0.00242\,\mu/\hbar$, indicated by the horizontal line in Figure 5.2(d) and in perfect agreement with the rate found for the finite system in the $R \to \infty$ limit. As a conclusion of this Section, our rigorous way of directly dealing with an infinite system perfectly confirms the results of [152] and offers further understanding of the validity of their infinite-size-limit procedure.

5.4 Higher charge vortices

Based on this important general result on the instabilities of a spatially infinite system, we are now entitled to apply the numerically simpler $R \to \infty$ infinite-size-limit procedure to more general cases, starting from $\ell > 2$ charge vortices in uniform condensates. As an example, we display in Figure 5.4 the R-dependence of the different-m spectra for a given charge $\ell = 4$. Independently from ℓ, the $m = 1$ spectrum always shows a negative-norm mode around zero energy. This core mode corresponds to the zero energy mode found in [145] and associated to the translation of the vortex core. For large but finite R, the frequency of this $m = 1$ negative-norm core mode is very small and negative, meaning that the system is energetically stable. As expected, this frequency tends to 0 in the $R \to \infty$ limit where translational invariance is recovered.

While the $m = 1$ mode is the only core mode for $\ell = 1$ vortices, for larger $\ell \geq 2$ other negative norm core modes appear for increasing m at both negative and positive BdG frequencies, corresponding thus to positive and negative energies. Interestingly, the energy of the lowest energy (highest frequency) core mode decreases until $m = \ell$ and then starts increasing again until it becomes positive and energetic stability is recovered for all $m > 2\ell - 2$. Since dynamical instabilities result from negative norm modes crossing the positive norm ones, this means that instabilities can only occur in the finite range

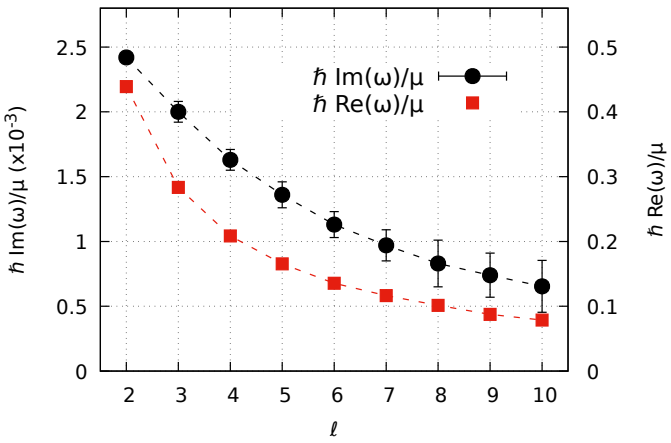

Figure 5.5: Imaginary (black circles) and real (red squares) parts of the $m = 2$ unstable mode frequency for growing vortex charge ℓ. The meaning of the error bars on the black circles is explained in the text.

of m values

$$2 \leq m \leq 2\ell - 2. \tag{5.13}$$

Notice that this result differs from what is reported in previous literature: Ref. [148] reports dynamical instabilities only for $m \leq \ell$, while Ref. [40] claims that they exist for all $m \geq 2$.

For what concerns the rate of the different instability channels, we find the quite unexpected result that for all values of ℓ the rate is strongest for $m = 2$ and then decreases with m. Since the instability of multiply charged vortices is associated to their splitting into an assembly of ℓ singly charged vortices, one may have expected the most unstable mode to be at $m = \ell$. However our analysis shows that the vortex decay begins with lower-m deformations of the core and the splitting in ℓ parts only appears during the later dynamics dominated by nonlinear effects.

To investigate instead the ℓ dependence of the instability, we focus on the (most unstable) $m = 2$ channel and for each ℓ we perform the infinite-size-limit procedure until the instability bubbles have fully merged into the large-R unstructured continuum illustrated in Figure 5.2(d). To further remove numerical artifacts, we take the average of the last few R-dependent oscillations as the instability rate and the corresponding variance as an estimate of the error on this value. The result for vortices up to charge $\ell = 10$ is shown in Figure 5.5, where also the real part of the frequency of the unstable modes is shown. Surprisingly the instability rate is highest for the lowest $\ell = 2$ charges and decreases continuously while increasing ℓ. This implies that the first stages of the vortex splitting process are slower for higher charge vortices.

It is now interesting to compare our results to the recent work [125] carried out for a purely hydrodynamic system for which the gravitational analogy holds exactly. With the aim of studying ergoregion instabilities, this work considers the case of a vortex

without a drain and, since the hydrodynamic description breaks down near $r = 0$, the KG equation must be supplemented with a reflecting boundary condition at a finite radius. For a given size of the ergoregion, the authors then find that all the high-enough m modes are dynamically unstable, but the instability rate is stronger for the lower-m unstable modes. The fact that this overall hierarchy of the instability rates of the different m-channels is shared by the Bogoliubov and the hydrodynamic calculations confirms that the nature of the instability is indeed the same in the two cases.

The main difference between the two calculations lies in the upper bound on the m instability range. Also this feature is however compatible with the interpretation of the instability in terms of an ergoregion instability: it can in fact be ascribed to the superluminal dispersion that pushes the energy of the high-wavevector excitations modes towards high energies. This physical interpretation was numerically confirmed by solving the linearized problem for the excitation modes in the long-wavelength approximation. To this purpose we applied the same diagonalization procedure used for the BdG problem to the corresponding KG problem, that is equation (5.11) without the derivative term in the upper-right element. This removes the dispersive effects. As expected, in this case we find no upper bound on m for the occurrence of instabilities, so that unstable modes are also present for $m > 2\ell - 2$.

The fact that the same conclusions were obtained in the hydrodynamic calculations for a spatially homogeneous density profile of [125] suggests that the specific profile of the density around the vortex core does not have any substantial effect on the m-dependence of the instability rates. On the other hand, the density depletion around the vortex core seems to play an important role in the ℓ dependence of the instability rate: an increase of the instability rates with the vortex circulation was in fact observed in the hydrodynamic case of [125], in stark contrast with the decrease found in our calculations shown in Figure 5.5. Since the same decrease of the instability rate was observed in the corresponding KG calculations where the dispersive effects are not present but the density depletion in the core remains, this difference can not be ascribed to the superluminal dispersion of Bogoliubov excitations, but rather to the density depletion around the vortex core.

As a main conclusion of this and the previous Sections, our joint numerical and analytical analysis fully confirms that the instability of multiply quantized vortices in BECs is a dispersive version of the ergoregion instability of rotating acoustic spacetimes and has no relation with the black hole bomb effect.

5.5 On the stability of singly charged vortices

In the previous Section we saw how, for all the vortex charges, the $m = 1$ channel shows a core mode at zero frequency in the infinite system corresponding to a translation of the core: thanks to translational invariance, this displacement does not alter the energy of the system. Based on ergoregion instability arguments, the stability of charge $\ell = 1$ vortices can be attributed to the dispersive effects that do not allow the presence of localized negative-energy modes at higher $m > 1$.

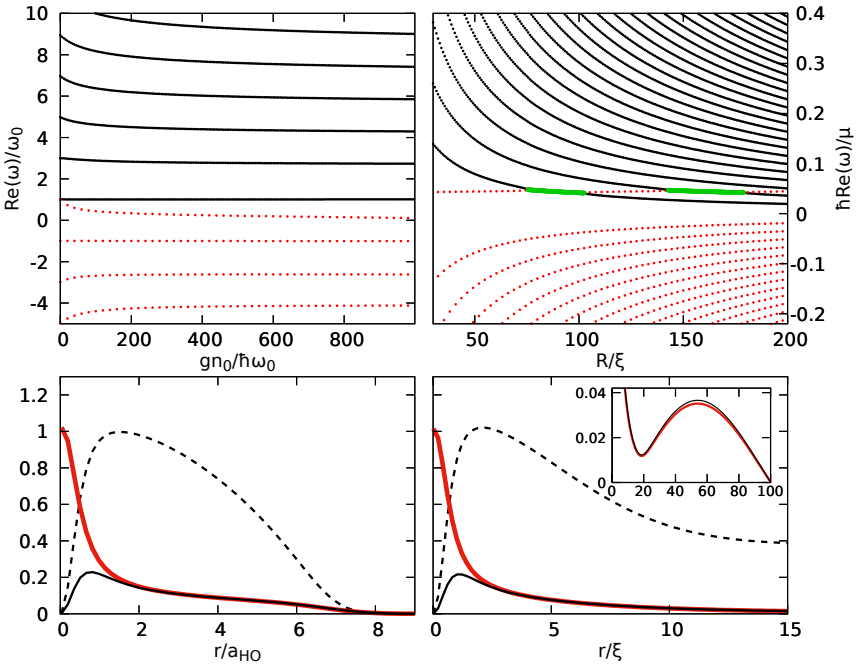

Figure 5.6: Left column: BdG spectra of a $\ell = 1$ vortex in a harmonically trapped condensate as a function of the interparticle interaction energy (top). Spatial profile of the energetically unstable mode for $gn_0 = 1000\hbar\omega_0$ (thin black and thick red lines correspond to the moduli of the u_ϕ and v_ϕ components of the Bogoliubov spinor in arbitrary units) along with (dashed line) a rescaled version of the condensate density profile (bottom). Right column: BdG spectra of a $\ell = 1$ vortex in the presence of an attractive Gaussian potential of the form (5.14) of strength $A = 2gn_\infty$ and spatial size $\sigma = 5\xi$ (with n_∞ asymptotic density and ξ the associated healing length) as a function of the total radius R of the condensate (top). Spatial profile of the dynamically unstable mode for $R = 100\xi$ along with (dashed line) the condensate density profile (bottom).

In contrast to what is often claimed, the stability (both energetic and dynamical) of $\ell = 1$ vortices in trapped geometries is not a general fact. For example, as we already said, vortex translation is energetically unstable in harmonically trapped BEC [146], whose inverted-parabola-shaped density profile favours expulsion of the vortex. The spectra for varying nonlinear interaction is visible in the top-left part of Figure 5.6, where one can see that a negative-energy core mode (whose spinor components are plotted in the lower panel) approaches zero frequency from above while increasing the number of atoms. The fact that this energetically unstable negative-norm mode is always located in frequency below the lowest positive-norm collective mode guarantees that the energetic instability never becomes dynamical.

Quite unexpectedly, if the density profile shows instead a bump surrounded by a wide region of lower density, this ordering of the modes is no longer guaranteed and collective modes satisfying the resonance condition for dynamical instability may be

available for $m = 1$, leading to a *dynamical* instability of singly-charged vortices. This feature is illustrated in the right part of Figure 5.6, where the infinite-size-limit procedure is applied to a condensate subjected to an inverted-Gaussian-shaped potential

$$V_{\rm ext} = -A \exp[-r^2/(2\sigma^2)] \tag{5.14}$$

with a positive chemical potential $\mu > 0$. The corresponding density profile is plotted with a dashed line in the lower panel: it displays a bump at short distances $r \lesssim \sigma$, then it tends to a non-vanishing constant value for large $r \gg \sigma$. In this configuration, instability regions appear as shown by the green lines in the top-right panel. In this parameter regions, the vortex starts precessing around the center with an ever-increasing radius, while its periodic rotatory motion leads to the emission of outward propagating sound waves in the external flat region. As usual, the positive energy of the emitted sound compensates for the negative energy associated to the vortex motion. In the harmonically trapped condensate, this sound emission process would not be possible as the cut-off frequency for collective modes in the condensate lies above the precession frequency of the vortex.

Further insight on this physics is obtained by comparing the spatial shape of the $m = 1$ core modes plotted in the bottom panels for the two cases. This graphs show how these modes share the same shape near the core but, while the one in the harmonic trapped BEC quickly decays to zero as it has no collective mode to couple with (bottom-left panel), the one in the Gaussian potential couples to a long-wavelength collective mode that extends throughout the whole condensate, as it can be seen from the non-vanishing weight at large r (bottom-right panel).

As a final point, it is interesting to note in the inset of this plot how the u_ϕ part of the spinor slightly exceeds the v_ϕ one at large r. This is in contrast to the harmonically trapped case, in which u_ϕ and v_ϕ simultaneously vanish when the density approaches zero, and shows that the long-distance part of the excitation indeed contributes with a positive energy and norm and confirms that the instability results from the mixing of a localized negative-norm mode with an outward-propagating positive-norm mode.

5.6 A time-dependent perspective: superradiant scattering and destructive interference

As we mentioned in Section 1.1.3, dynamical instabilities are associated to the presence of energetic instabilities and, as we stressed throughout this thesis, the localization of negative-energy modes in some part of the system is the basic ingredient of amplified scattering. These localized modes, that are here the core modes, are the origin of the dynamical ergoregion instabilities if they remain in the system and get further amplified in a stimulated way while emitting positive-energy excitations outside.

We already discussed in the previous Chapter that the presence of an *absorption* mechanism for these modes, although guaranteeing dynamical stability, is not an essential ingredient of superradiant scattering, that just depends on the presence of an

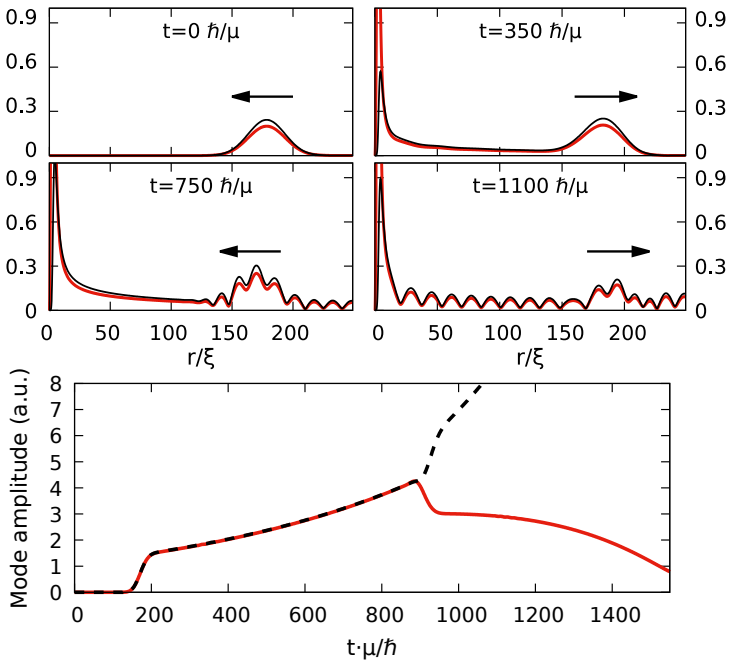

Figure 5.7: First and second row: Snapshots of the evolution of a Gaussian Bogoliubov wavepacket of $m = 2$ incident waves hitting a charge $\ell = 4$ vortex. The frequency of the incident wavepacket is centered around $\omega = 0.2\hbar/\mu$, namely the frequency of the core mode visible in the spectra shown on the top-left panel of Figure 5.4. Dirichlet boundary conditions are imposed to the Bogoliubov modes at $R = 380\xi$. The arrows indicate the direction of the radial group velocity. The bottom panel shows the time-dependence of the core mode amplitude (red solid line), as measured by the $r = 2\xi$ value of the v_ϕ component of the BdG spinor. The black dashed line is the time-dependence of the same core mode amplitude for a slightly different size $R = 388.4\xi$, for which the system is dynamically unstable. Around $t = 900\mu/\hbar$, the two curves show clear signature of the destructive vs. constructive interference between the reflected wavepacket and the core mode.

ergosurface and not on the boundary conditions of the problem, that may be specified even very far from the ergosurface itself.

The present case of quantized vortices provides another example in which superradiance in the presence of dynamical instabilities can be demonstrated. Superradiant amplified scattering is illustrated in Figure 5.7 where we show snapshots of the evolution of a Gaussian wavepacket of azimuthal number $m = 2$ incident onto a $\ell = 4$ vortex in a spatially homogeneous condensate. In practice, we have numerically obtained the condensate profile as done in Section 5.3. We have then constructed a wavepacket of Bogoliubov excitations centered at the frequency of the core mode found in Figure 5.4 and with a group velocity directed towards the vortex core.

The wavepacket reaches the vortex core between the first ($t = 0$) and the second

($t = 350\mu/\hbar$) snapshots. While being reflected from it, it populates the (negative energy) core mode as visible in the narrow excitation peak on the left edge of the second to fourth panels. Even though pulse distortion effects make it hardly visible by eye, a quantitative comparison of the BdG norm (5.8) of the wavepacket before and after the scattering process shows that the reflected packet is amplified by approximately 18%. This is a clear evidence of the occurrence of superradiant scattering in the short-time dynamics.

At later times, after being triggered by the superradiant scattering process, the amplitude of the core mode keeps exponentially increasing between $t = 200\hbar/\mu$ and $t = 800\hbar/\mu$, as it is visible in the time-dependence shown in the bottom panel. Of course, this increasing amplitude is associated to an analogous exponential growth of the excitations in the bulk behind the amplified wavepacket.

While this first stage of the evolution does not depend on the actual size of the system and is well captured by the theory for an infinite condensate, the long-time dynamics crucially depends on the specific value of the system size R. In the simulation of Figure 5.7, this was chosen to fall within one of the stability windows. In the third snapshot at $t = 750\hbar/\mu$, the amplified packet has been already reflected by the Dirichlet boundary condition at the end of the system at $R = 380\,\xi$ (outside the plot) and is approaching again the vortex core. The complex oscillatory profile visible in this third snapshot is due to the interference of the reflected wavepacket with the exponentially growing emission by the unstable core mode. A second scattering process occurs when this reflected wavepacket hits the vortex: during this scattering process, the incident wavepacket interferes with the excitation amplitude left in the core mode after the first scattering and, since then, exponentially growing. For the chosen value of the condensate radius R, destructive interference occurs and the amplitude of the reflected wavepacket is suppressed, as shown in the last snapshot at $t = 1100\hbar/\mu$.

The complete time dependence of the negative norm core mode amplitude is shown in the bottom panel. As a signature of the destructive interference effect (solid red line), the exponential increase of the core mode amplitude suddenly stops around $t = 900\hbar/\mu$ and is replaced by a strong decrease at later times. After this first back-and-forth motion, the core mode evolution keeps displaying alternate intervals of increasing and decreasing amplitude.

This complex time-dependent behaviour reflects the dynamical stability of the system as predicted by the time-independent calculation of the spectrum and is a clear illustration of how the finite size of the system is able to quench the ergoregion instability that would instead appear in an infinite geometry. In agreement with the results presented in Sec.IV for the large R behaviour, the interference effect ceases being relevant for $\gamma(R)T_{\rm rt} \gtrsim 1$, that is when the round-trip time $T_{\rm rt}$ is so large that the core mode amplitude has time to grow to such large values that the reflected wavepacket no longer has any significant effect on the exponential growth of the instability.

In the dynamically unstable regions, the interference at each scattering event would instead be constructive, leading to a ever increasing core mode amplitude with an even higher rate than in the infinite system. The effect of this constructive interference on the core mode amplitude for a slightly different system size $R = 388.4\xi$ is plotted in the

lower panel of Figure 5.7. As expected, in this case (black dashed line) the constructive interference leads to a sudden upwards jump of the core mode amplitude, which then keeps exponentially increasing.

5.7 Summary: rotating spacetimes and quantized vortices

In this Chapter we applied the analogy with rotating spacetimes to investigate the physical origin of the instabilities of multiply charged vortices in two-dimensional Bose–Einstein condensates. The instabilities can be directly associated to the presence of energetically unstable modes in the vortex core region where the flow is supersonic; as we discussed in the introductory Chapter 2 and showed in detail in Chapter 4, this is typical of ergoregion instabilities occurring in curved spacetimes. The differences with gravitational systems and analogue models in the hydrodynamic regime – in particular the suppression of instabilities at high values of the angular momentum – can be ascribed to the superluminal dispersion of Bogoliubov waves in condensates.

In contrast to the black-hole bomb instabilities triggered by reflections outside the ergoregion, here the finite size of the system rather leads to a quench of the instability via a destructive interference effect. This explains the peculiar stability properties of vortices in trapped condensates and also proves that the dynamical instabilities are not, as it is sometimes claimed, induced by the trapping. Based on our novel understanding of these instability phenomena, exotic geometries where singly quantized vortices are also dynamically unstable were identified.

From the analogue gravity point of view, our calculations show the robustness of superradiant phenomena against the superluminal corrections to the linear sonic dispersion and give an example of how the gravitational analogy can provide qualitatively correct results even outside its hydrodynamical regime of validity. Quantized vortices also provide another example of how superradiant scattering can also occur in the absence of dissipation (e.g. of an horizon), as we concluded in the previous Chapter. We showed this here with time-dependent simulations of the BdG equations for perturbations on a dynamically unstable multiply quantized vortex, that also illustrated once more how finite size effects can stabilize the system.

Here we dealt with the stability of single vortices in a cylindrically-symmetric system; a step forward to the consideration of the dynamics of multiple vortices is made in the following Chapter, where the ideas coming from superradiance are applied in a different configuration.

Chapter 6

Kelvin–Helmholtz and *superradiant* instabilities of a quantized shear layer

In Chapters 3 and 4 we studied superradiant scattering and superradiant instabilities from an analogue-gravity point of view by introducing a *minimal* and geometrically simple configuration in which the essential elements involved in these phenomena can be distinguished and tuned. We said that the flow of the condensate in our *planar ergosurface* is analogous to the one of tangential discontinuities in hydrodynamics, for which amplification of acoustic waves can be predicted as we reviewed in Subsection 2.1.2. However, while we showed that the interface is dynamically stable in our case, hydrodynamic tangential discontinuities are well-known to be dynamically unstable to the formation of ripples along the interface.

An example is the Kelvin–Helmholtz (KH) instability (see for example [95,156]), that is known to happen not only for sharp tangential discontinuities, but also for smoother *shear layers* between parallel flows. The effect of this instability is to amplify perturbations of the transition layer between the two flows that end up to mix in a turbulent way. An example can be seen in Figure 6.1, where the shear layer is seen to *roll up* creating the characteristic vortices that can also be observed in atmospheric clouds. This is an inviscid instability, meaning that the phenomenon is mainly determined by inertial effects and not by viscosity [156].

Superfluids are known to display inviscid flow and KH instability was experimentally observed at an interface between the two superfluid phases of ^{3}He [157,158]. Also Bose–Einstein condensates (BECs) were considered for the study of this phenomenon; in particular in [159] KH instability was shown to develop in phase-separated two-component BECs, while in [160] a *quantized vortex sheet* in a single component condensate was considered. We are here more interested in this last work, in which a potential barrier between two counterpropagating flows is progressively lowered to create a shear layer. In contrast to our planar ergosurfaces, involving *tricks* such as a synthetic vector potential or the inclusion of a periodic trapping potential, in this configuration the irrotationality constraint on the velocity is not broken; hence the only way in which the vorticity that is intrinsic to the transition between the two flows can enter the system is through the

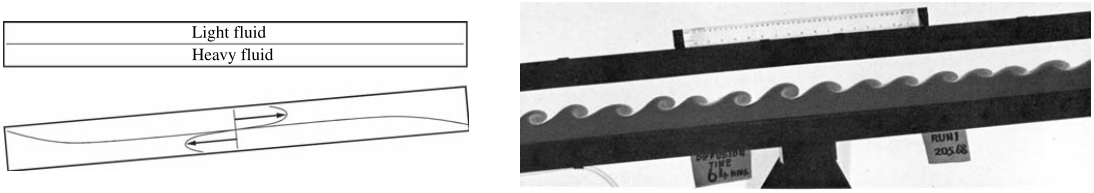

Figure 6.1: On the left representation of a possible realization of the Kelvin–Helmoltz instability in an hydrodynamic context. Two liquids of different densities are posed on top of each other and the container is then tipped so that the heavier fluid falls and the lighter one rises, thus creating a shear layer. On the right a photograph of the experimental realization of [161], in which the interface can be seen to *roll up*, creating a characteristic pattern. The pictures are taken from [156].

creation of quantized vortices. In the KH instability, the vortices are then seen to *roll up* and clusterize, with a behaviour that is the analogous of the one of the classical vortex sheet shown in Figure 6.1 but with quantized vorticity.

While from this configuration one can expect superradiant scattering with the arguments of Section 3.2 based on the *asymptotic* dispersion relations, the focus of this Chapter will be on surface dynamical instabilities. We will see that the physics changes qualitatively with the relative velocity of the two flows and ranges from the quantized version of the Kelvin–Helmholtz instability we just described [160], to a new regime of slower instability for *superradiant* relative velocities between the two parallel flows $\Delta v > 2c_s$. We will call this *radiative instability* (RI) since the unstable modes are not localized in the shear layer and display instead an emission of phonons in the two regions of uniform flow.

The transition to this second regime is given by the emergence of energetic instabilities in the two (supersonic) flows and bears resemblances both with superradiant instabilities discussed in Chapter 4 and with vortex instabilities of Chapter 5 and may be of relevance also for classical hydrodynamics. While the velocity field of this configuration resembles the one giving rise to the SSW instabilities of Section 4.1, the radiative instabilities in the present case do not disappear in an unbound system and are hence similar to multiply quantized vortices that, as we saw in the previous Chapter, maintain their instability in the unbound system.

In the following we attack the problem by numerically studying the time evolution of the Gross–Pitaevskii equation and by solving the linearized Bogoliubov problem on top of the *quantized vortex sheet* configuration with a Bloch-waves approach. Besides confirming the occurrence of the quantized KH instability for relative flow speeds $\Delta v < 2c_s$, for which the hydrodynamic low-wavelength physics seems to dominate, we display and characterize the new radiative instability regime at large $\Delta v > 2c_s$ and another regime at very small velocities in which instead the *short-wavelength* physics of the quantized shear layer dominates. The work presented in this Chapter is under completion and will be object of a future publication.

6.1 GPE simulations

As in the rest of this Thesis, we describe a BEC at $T = 0$ tightly confined in one direction (in a *pancake* shape) with the GPE in two spatial dimensions [16]:

$$i\hbar\partial_t\Psi(t,x,y) = \left[-\frac{\hbar^2\nabla^2}{2M} + g|\Psi(t,x,y)|^2 + V_{\text{ext}}(t,y)\right]\Psi(t,x,y). \tag{6.1}$$

As indicated in this equation, we consider an external potential constant along x and possibly dependent on time.

As was done in [160], we consider periodic boundary conditions along x and a potential composed by two hard walls at $y = \pm L_y/2$ and by a repulsive Gaussian potential centered in $y = 0$. The Gaussian potential is initially strong enough so that the condensates in the two region are separated and independent, as shown in the leftmost panels of Figure 6.2. The ground state of the GPE with this potential in computed via imaginary-time propagation and at $t = 0$ the two condensates are given equal and opposite *momentum kicks* so that they develop equal and opposite velocities[1] $\pm v$ along x.

The intensity of the central Gaussian potential is then linearly decreased in time so to vanish at $t = 100$, after which the external potential is composed only by the time-independent hard walls. After the central barrier is lowered the only way for the condensate to satisfy the irrotationality of the velocity vector field is to create an array of (singly) quantized vortices along $y = 0$, in numbers equal to the difference of the winding numbers of the phase in the two channels. This can be understood from plots of the phase of the order parameter as shown in Figure 6.3. In other words, given a relative velocity Δv between the two condensates, the number of vortices per unit length will be

$$n_{\text{vort}} = \frac{M}{\hbar}\frac{\Delta v}{2\pi}. \tag{6.2}$$

For values of x that do not correspond to a vortex, the y dependence of the transverse velocity v_x can be in good approximation fitted with a functional form of the shape $v_x(y) = v\tanh(y/\delta_v)$, with δ_v width of the transition region between the two counter-propagating uniform flows. This is a well-known velocity profile in hydrodynamics, whose inviscid (Kelvin–Helmholtz) instability was studied in [162]. Fits of the numerical data obtained from the GPE show that while increasing the velocity the width of the shear layer decreases approximately as

$$\delta_v \simeq \frac{\hbar}{M}\frac{1}{2v}. \tag{6.3}$$

In Figure 6.2 we show, for two different relative velocities, snapshots of the time-evolution of the GPE following this procedure and including a small noise on the order parameter Ψ as a seed for instabilities. In the first example, for $\Delta v < 2c_s$ (or $v < c_s$),

[1] Remember that, differently from what we did in Chapters 3 and 4, here the physical velocity corresponds with the canonical velocity $\hbar\nabla\Theta/M$, since no synthetic vector potential is used.

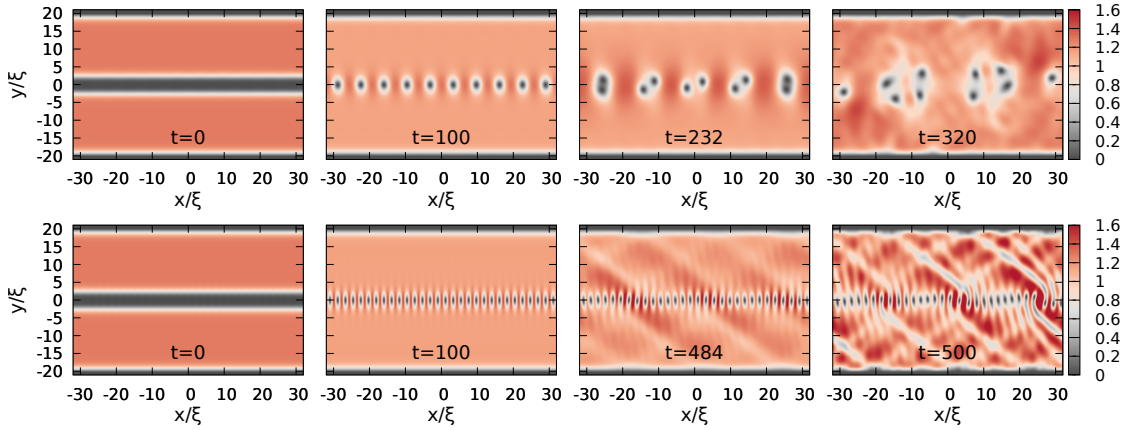

Figure 6.2: Time evolutions (obtained by solving the GPE) of the density of a condensate confined along y by hard walls and with a central Gaussian potential $V_G = A\exp(-y^2/2\sigma^2)$ with $A = 5\mu$ and $\sigma = \xi$. As shown in Figure 6.3, opposite velocities are imposed for the two parts of the system and when the Gaussian potential is progressively lowered (between $t = 0$ and $t = 100\ \mu/\hbar$) an array of quantized vortices develops. The upper plots show the case $v = 0.491\ c_s$ (i.e. $\Delta v < 2c_s$) and the lower ones $v = 1.473\ c_s$ (i.e. $\Delta v > 2c_s$). The first case shows the KH behaviour presented in [160], in which vortices clusterize and co-rotate. The second one is an example of the RI regime, in which the instability is slower and the unstable mode is not localized on the vortex line, but spreads all over the system.

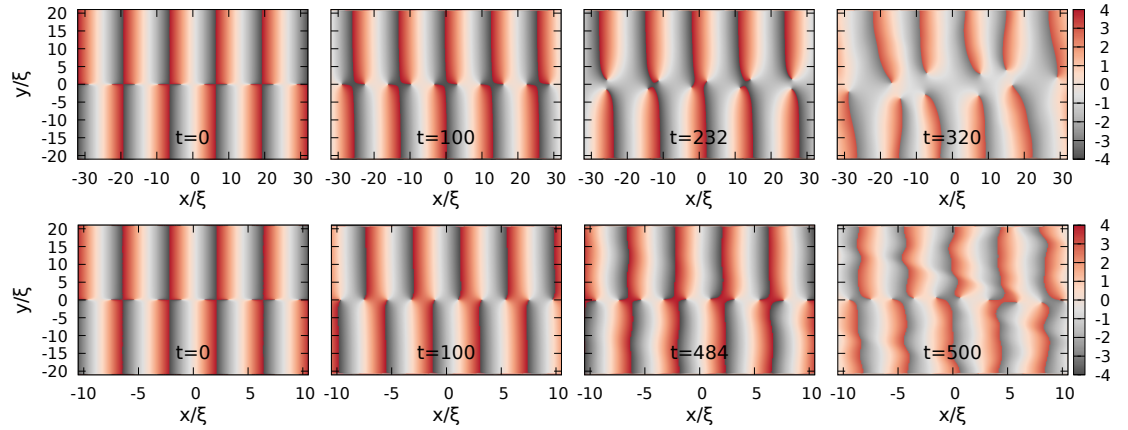

Figure 6.3: Time evolutions of the phase of the condensate associated to the density evolutions shown in Figure 6.2. The x range in the second case is reduced to improve visibility. In the leftmost panels one can see how opposite gradients of the phase result in the creation vortices, corresponding to each *open end* of a branch cut. While in the upper KH case the branch cuts are mostly displaced around $y = 0$, in the lower RI case they are significantly distorted on their whole length.

the vortex line is unstable with a surface instability similar to the KH instability of hydrodynamic. After some time vortices start to move from the horizontal $y = 0$ line and begin to co-rotate in clusters of growing size. In the second example instead, in which $\Delta v > 2c_s$, even if the vortices are much closer, they do not move initially from the horizontal line and an unstable growing mode develops in the whole system, as can be seen from the emerging pattern. Surprisingly, the vortices take a longer time to move and do so together with significant density variations in the *bulk* of the system. This behaviour also reflects in the behaviour of the phase of the condensate shown in Figure 6.3, whose branch cuts are in the first case significantly deformed only in the central part of the system, while in the second case become wiggly on their whole length. The fact that the emerging pattern in the second case resembles a superposition of up-going and down-going waves suggests that phononic propagating modes are involved; we hence call this *radiative instability* (RI).

Further evidence on the difference of localization of the unstable modes in the two cases is obtained by varying the vertical size of the system L_y, that is the separation between the two hard walls. We observe that for $\Delta v < 2c_s$ the time for the vortex line to deform is essentially independent from L_y, while for $\Delta v > 2c_s$ the instability rate decreases while increasing L_y.

All these features suggest that the instability resembles the analogue SSW effect as depicted in the GPE simulations of Figure 4.1; in fact the $\delta_v > 2c_s$ threshold for this kind of instability is the same in the two cases, and also the SSW instabilities strongly depends on the system size. However we will see in the following that, despite the similarities, the radiative instability is also present in an unbound system along y, while we know that the SSW one relies on the finite size.

While strikingly showing the different instability mechanisms, time evolutions of the GPE are not the best tool to obtain a complete picture of the phenomenon. The relatively long time the instability takes to significantly deform the line of vortices suggests that the configuration obtained when the central Gaussian potential is lowered is a stationary state $\Psi_v(x, y)$ of the GPE. This is confirmed by the fact that imaginary time evolutions of the GPE with fixed winding numbers in the two channels converge to states of the shape we found with the above time-dependent procedure. In the following we hence resort to a study of the linear stability of this stationary state with a Bogoliubov approach.

6.2 Bloch functions for the Bogoliubov problem

The natural approach to the study of the Bogoliubov problem in this configuration is to take advantage of the periodic structure of the stationary states we are interested in; the vortices along $y = 0$ are in fact equispaced along x (as can be seen in the second ($t = 100$) panels of Figure 6.2). As usual we consider a small deviation from the stationary state

$$\Psi(t, x, y) = e^{-i\mu t/\hbar} \left(\Psi_v(x, y) + \delta\psi(t, x, y)\right), \tag{6.4}$$

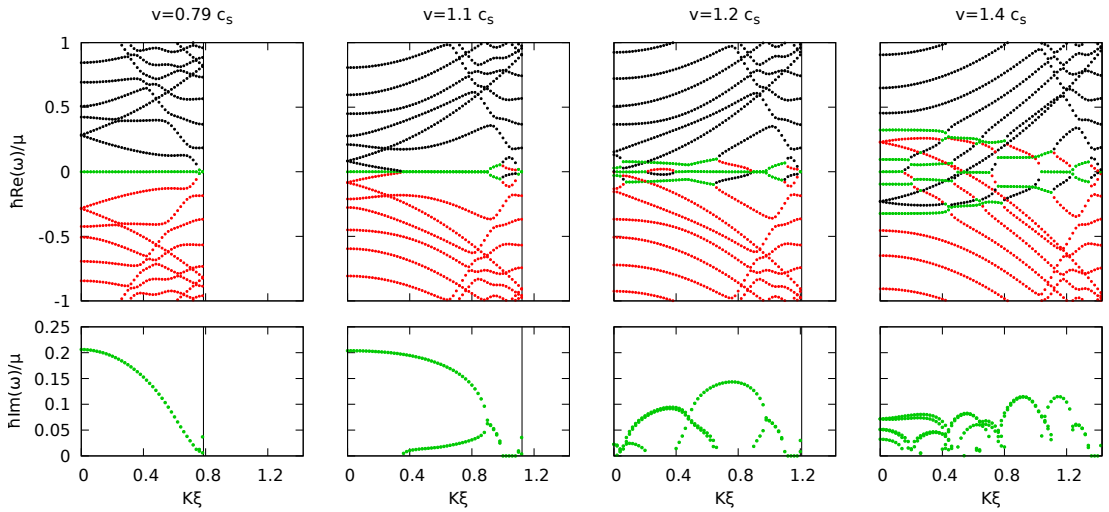

Figure 6.4: Real (top panels) and imaginary (bottom panels) parts of the eigenfrequencies of the Bogoliubov problem for varying Bloch momentum K for vertical size $L_y = 20\xi$ and for four different values of the velocity v in each parallel flow. The K range is truncated at the edge of each Brillouin zone. Black lines correspond to positive-norm modes, red lines to negative-norm ones and green lines to zero-norm dynamically unstable modes, giving rise to the *bubbles* of instability in the lower plots. At the crossing of the $v = c_s$ threshold, energetic instabilities begin to be present. One can see the transition between a regime in which the zero-frequency KH instability dominates to a regime of RI, in which the instability maxima occur at finite K.

where the stationary state Ψ_v relative to a given velocity v in each channel has the periodicity

$$\Psi_v\left(x + \frac{1}{n_{\text{vort}}}, y\right) = \Psi_v\left(x, y\right). \tag{6.5}$$

The Bogoliubov spinor describing perturbations can hence be decomposed in decoupled Bloch waves of the shape

$$\begin{pmatrix} \delta\psi \\ \delta\psi* \end{pmatrix}(x,y) = e^{iKx} \begin{pmatrix} \phi_K \\ \phi_K^* \end{pmatrix}(x,y), \tag{6.6}$$

where ϕ_K has the same periodicity (6.5) of the stationary state, and K belongs to the first Brillouin zone $-\frac{M}{\hbar}v \leq K \leq \frac{M}{\hbar}v$. The resulting Bogoliubov equations at fixed v and K are

$$i\hbar\partial_t \begin{pmatrix} \phi_K \\ \phi_K^* \end{pmatrix} = \begin{bmatrix} D & g\Psi_v^2 \\ -g\left(\Psi_v^*\right)^2 & -D \end{bmatrix} \begin{pmatrix} \phi_K \\ \phi_K^* \end{pmatrix}, \tag{6.7}$$

with

$$D = -\frac{\hbar^2\nabla^2}{2M} - \frac{i\hbar K}{M}\partial_x + \frac{\hbar^2 K^2}{2M} + 2g|\Psi_v|^2 + V_{\text{ext}} - \mu. \tag{6.8}$$

To solve this problem we first compute the *lattice cell* of Ψ_v, that is the portion of the stationary state containing one vortex, that for each v has a length along x of $1/n_{\rm vort}$, where the linear density of vortices is given by (6.2). Notice that, since the lowest possible winding number in each channel is one, one cannot obtain less than two vortices; in other words, because of its phase, the periodicity of the complex order parameter Ψ_v is $2/n_{\rm vort}$. However, in the Bogoliubov problem (6.7) only the square of the order parameter enters, so that the *physical* periodicity of the system is actually $1/n_{\rm vort}$.

We hence compute, for a fixed v, the order parameter with an imaginary-time propagation of the GPE on a numerical x range of $2/n_{\rm vort}$, imposing unit winding number in each channel, and then construct the Bogoliubov matrix with half of the x range of the obtained Ψ_v.

We then diagonalize this matrix, for a given Bloch momentum K, that we compute using discretized expressions for the derivatives. We repeat this diagonalization sampling all the transverse momenta K in the first Brillouin zone[2] for the given v. Examples of the obtained spectra for different values of the velocity of the two opposite parallel flows are shown in Figure 6.4.

One can see that for $\Delta v < 2c_s$ the spectra are composed of positive-energy modes (positive-norm at positive frequencies and negative-norm at negative ones) and by a zero-frequency dynamically unstable branch, whose instability rate increases while approaching $K = 0$. For $\Delta v > 2c_s$ instead the positive- and negative-norm parts of the spectra merge, reflecting the energetic instability associated to the supersonic flows in both the upper and the lower part of the system. As we already saw in multiple occasions, when energy bands of opposite norm sign approach, they become pseudo-degenerate, giving rise to dynamically unstable branches.

One can see here that the emergence of these new dynamical instabilities perturbs the zero-frequency KH unstable branch, suppressing it. For high enough velocities in fact the KH behaviour dominated by small momenta is replaced by (lower) maxima at finite K. The suppression of the KH instability in favor of a *slower* radiative instability is hence to be attributed to the coupling of the degrees of freedom responsible for the local deformation of the vortex array with the ones of the excitation modes in the two uniform flows.

A quick picture of the different instability regimes can be obtained by looking at Figure 6.5 in which we show, for two different L_y, the maximum instability rate for different values of v and the corresponding Bloch momentum. Three distinct regimes are apparent. For small velocities the maximum instability rate is approximately independent from v, changes with the vertical size of the system and occurs at the edge of the Brillouin zone; this *small velocities* regime was not included in the GPE simulations of the previous Section, since the large spacing between the vortices requires a large integration box and the small instability rate requires long times of evolution. For higher velocities (but below $v = c_s$) the maximum instability occurs for $K = 0$, increases linearly with

[2]Actually, because of the symmetries of the system, the positive-momenta half of the Brillouin zone is enough.

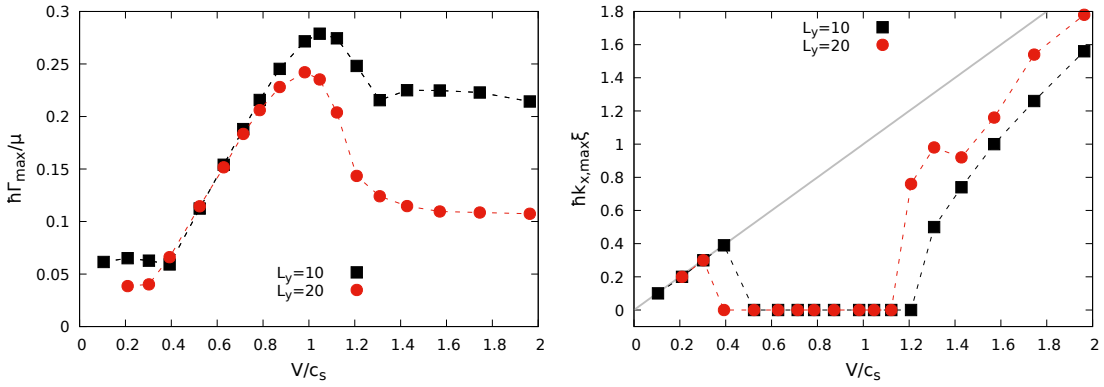

Figure 6.5: Maxima (left plot) and the corresponding transverse momentum values (right plot) of the instability for different values of v and for two different vertical sizes of the system L_y. Dashed lines are simply a guide for the eye and the gray line in the right plot indicates the edge of the Brillouin zone. Three regimes are distinguishable, differing for the v dependence, the L_y dependence and the transverse momentum corresponding to the maximum (see main text).

the velocity and is independent on the system size; this is the KH regime. Finally, for higher velocities the maximum instability rate occurs for finite values of K (increasing with v), is approximately constant for increasing velocities and strongly depends on the system size; this is the RI regime.

In the next Section we consider in detail these three regimes, starting from the most known one displaying the quantized Kelvin–Helmholtz instability

6.3 Instability regimes

6.3.1 Small velocities: Kelvin–Helmholtz regime

In hydrodynamics the KH instability for a (continuous) vortex sheet, i.e. a tangential discontinuity between two parallel flows v_1 and v_2, is known to have the *dispersion relation* (see [156] Section 4.3.1)

$$\omega = \frac{v_1 + v_2}{2} k_T \pm i \frac{v_1 - v_2}{2} k_T, \tag{6.9}$$

where k_T is the wavevector of the perturbation tangential to the discontinuity (parallel to the flows). This result is modified if instead of a tangential discontinuity a finite-width vorticity layer is present, for example for a piecewise-linear profile such as the one depicted in Figure 6.6(a) the dispersion relation becomes (see [156] Section 4.3.2)

$$\omega = \frac{v_1 + v_2}{2} k_T \pm i \frac{v_1 - v_2}{4\delta} \sqrt{e^{-4k_T\delta} - (2k_T\delta - 1)^2}; \tag{6.10}$$

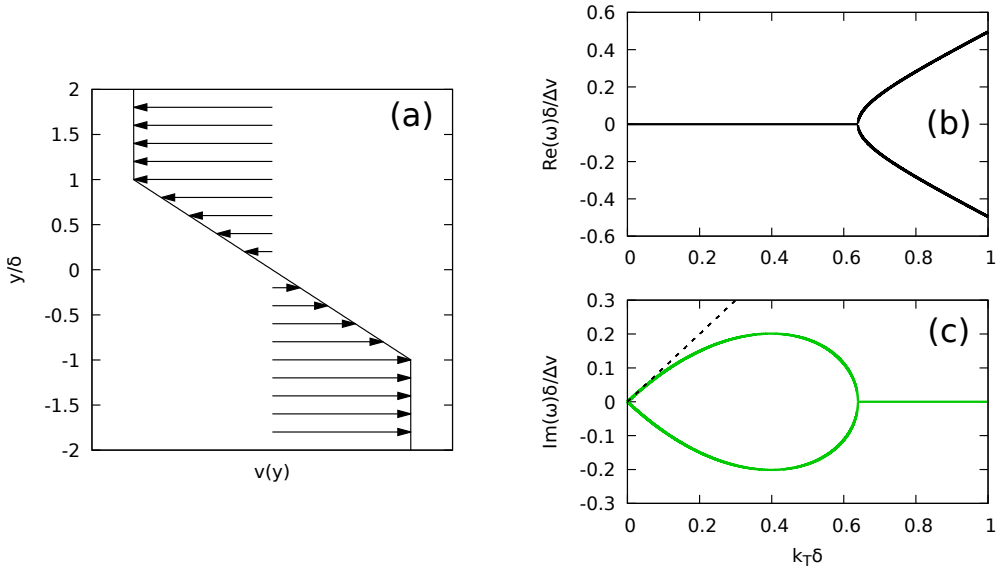

Figure 6.6: Plots describing the hydrodynamic prediction for the Kelvin–Helmholtz instability for a vorticity layer of finite width. Panel (a) displays a piecewise parallel flow where two uniform flows are connected by a linear transition region of finite width 2δ. In panels (b) and (c) the real and imaginary parts of the frequency of the unstable modes of this parallel flow, as expressed by the dispersion relation (6.10). The dashed line in panel (c) shows the result for a zero-width tangential discontinuity (6.9). A suppression of the instability for high transverse momenta due to the finite-width shear layer is visible. Analogous plots are shown in Section 4.3.2 of [156]. Qualitatively similar results are found for a parallel flow with an hyperbolic tangent profile, similar to the velocity field of our condensate.

our case corresponds to $v_1 = -v_2 = v$. Panels (b) and (c) of Figure 6.6 show the real and imaginary parts of the frequency of the KH modes. At low transverse momenta the instability rate increases linearly, as in the zero-thickness case (6.9), while at higher transverse momenta (above $k_T\delta \sim 0.6$) the instability is quenched. An analogous suppression of the instability was found in [162] for an hyperbolic tangent velocity profile, that we said is similar to the one of our case.

Because of our choice of the shape of fluctuations (6.4), in which the phase of the stationary state is not taken as an overall factor, our Bloch momentum K differs from the hydrodynamic transverse momentum k_T. In particular our choice implies that momenta are measured with respect to the *laboratory frame*, while the above result for the hydrodynamic Kelvin–Helmholtz instability is obtained by measuring the momenta with respect to the fluid, as we did for example in Chapter 5 for the study of vortices with the choice (5.4). For this reason the Bloch momentum is related to k_T by

$$K = \frac{M}{\hbar} v - k_T. \tag{6.11}$$

Hence in the present case we expect an instability rate with a behaviour *specular* to the one of Figure 6.6(c); that is, while going from the edge of the Brillouin zone towards decreasing Bloch momenta, a linear increase of the instability rate that then *bends* because of the finite width of the vorticity layer. This is exactly what we observe in the lower plot of the first case in Figure 6.4. The suppression of the instability we see in the hydrodynamic case is instead not observed here. Our result is however consistent with the hydrodynamic prediction, in fact the threshold for the suppression $k_T \gtrsim 0.6/\delta$ is fixed by the width of the shear layer, that in our case is velocity-dependent and given by (6.3). According to that scaling $0.6/\delta_v > (M/\hbar)v$, so that the hydrodynamic suppression threshold lies outside of the Brillouin zone.

Also the zero real part of the frequency of the unstable KH modes is in accordance with the hydrodynamic prediction (6.10) for $v_1 = -v_2$ and, finally, from the left plot of Figure 6.5 we see that between $v \sim 0.4\ c_s$ and $v \sim 0.8\ c_s$ the maximum instability rate increases linearly with v, corresponding to the linear dependence on the velocity difference of the imaginary part of the frequency of the hydrodynamic prediction (6.9).

Despite these striking similarities, notice that the imaginary part of the frequencies of the first case in Figure 6.4 has an additional structure of modes at the edge of the Brillouin zone, corresponding to real parts of the frequencies slightly displaced from zero. Since momenta at the edge of the Brillouin zone correspond to periodicities equal to the ones of the vortices *lattice*, these are modes in which the *quantized* nature of our vorticity layer becomes very important and hence one does not expect similarities with the hydrodynamic case. We will see that these modes play crucial roles in the other two instability regimes.

6.3.2 High velocity: radiative instability regime

As we already discussed, the transition from the KH regime to the RI one by increasing the flow velocity can be seen in the last three plots of Figure 6.4, in which the emergence of energetic instabilities associated to the supersonic flows above $\Delta v = 2c_s$ suppresses the $Re(\omega) = 0$ unstable KH branch. Correspondingly, the instability rate maxima move to finite values of the Bloch momentum, reflecting the patterns of up-going and down-going waves visible in the second GPE simulation of Figure 6.2.

We also already noticed how this behaviour and the $2c_s$ threshold are reminiscent of the SSW effect we discussed in Section 4.1. In that case the relative velocity between the two regions was obtained was obtained with a synthetic vector potential, so that the lower part of the system was at rest and the upper one was moving. It is now interesting to repeat the Bogoliubov calculations of Subsection 4.1.2 in a configuration more similar to the present one, that is with equally-sized upper and lower regions and with equal and opposite uniform synthetic vector fields in the two regions. The result for $|v| = |A_x|/M = 1.5c_s$ in each region is shown in Figure 6.7.

One can see that, apart for the folding of the bands, this is similar to the rightmost plot of Figure 6.4 (also see the following Figure 6.8) with inverted momenta K. As we commented for the KH regime, this inversion is due to the choice of expression

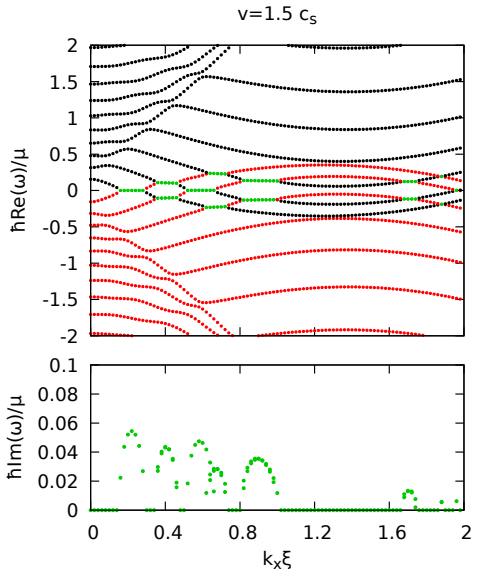

Figure 6.7: Spectra of the analogue SSW effect studied in Section 4.1 in a slightly different configuration. Instead of applying a synthetic vector potential only in one region, equal and opposite vector potentials $A_x = \pm 1.5\ c_s$ are applied in the two regions. Moreover, instead of considering a potential box in a wider system, we take the two regions of the same size $L_y/2 = 10\xi$.

for the fluctuation field: in the case in which the velocity is induced with a synthetic vector potential, the momenta of the modes of the resulting Bogoliubov problem (4.2) are automatically measured with respect to the condensate and a relation analogous to (6.11) holds. The finite-K instability maxima dominating the RI regime in a finite system along y can hence be attributed to the analogue SSW effect, that is to the continuous production of phonons with opposite energies in the two regions.

The present radiative instability however substantially differs in its behaviour when the vertical size of the system is increased. Remember that in the SSW case the instability decreases when the two regions are made larger and eventually disappear in the infinite-size system (corresponding to the bosonic Klein paradox). The dependence on L_y of the RI can instead be tested by performing diagonalizations analogous to the ones of Figure 6.4 but for a fixed velocity and various values of the vertical size of the system.

In Figure 6.8 the result of such a procedure is shown in the upper panels. One can see that while L_y is increased the density of the modes grows and correspondingly the instability *bubbles* increase in number. The maxima of instability rate move instead always more towards the edge of the Brillouin zone and their value decreases. As can be seen from the red dots in the lower plot, showing the maximum instability rate for various values of L_y, instead of decreasing to zero, the greatest imaginary part of the frequencies tends towards a constant value for large enough systems, suggesting the permanence of the instability in an infinite system.

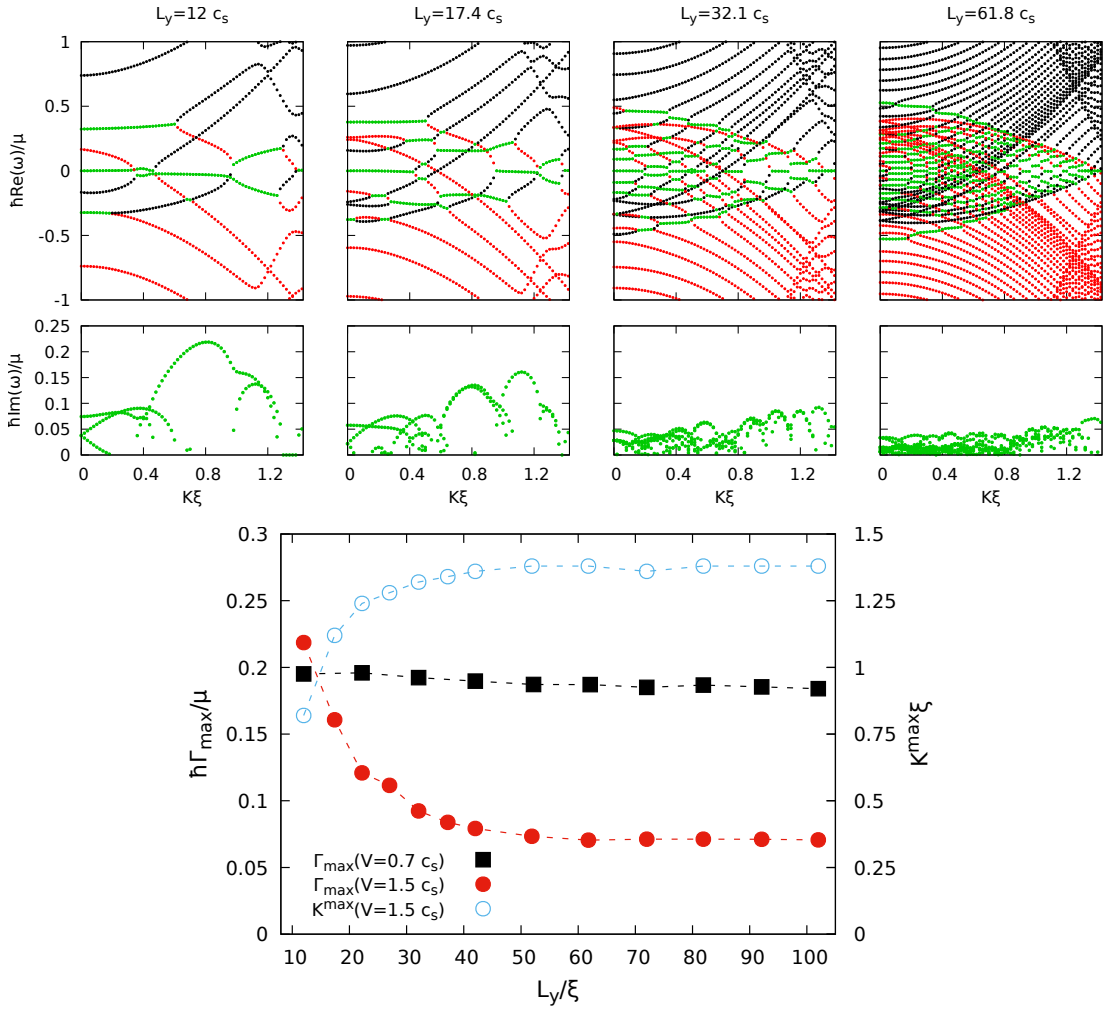

Figure 6.8: Upper plots: real and imaginary parts of the Bogoliubov spectra for $v = 1.5\ c_s$ and varying vertical size of the system. One can see the transition from a SSW behaviour to an instability localized on the edge of the Brillouin zone that is size-independent. In the lower plots the dependence of the instability maxima on the system size are shown. Red dots indicate the maximum instability rate in the RI regime, with the empty blue circles being the K corresponding to the instability maxima. Black squares show instead the result for a velocity in the KH regime case, that results to be essentially size-independent. The maximal instability in this case always occurs for $K = 0$.

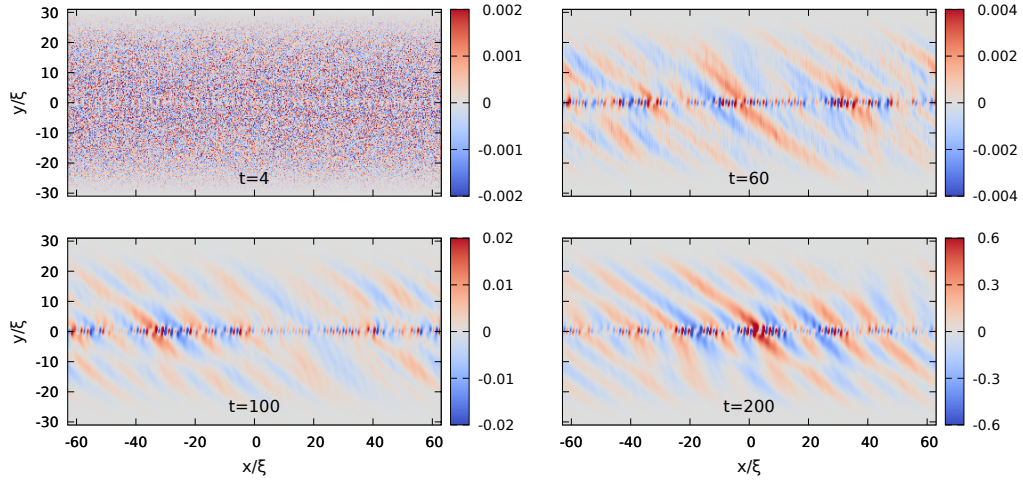

Figure 6.9: Snapshots of the time evolution of the density variations obtained by evolving in time the Bogoliubov equations for $v = 1.496\ c_s$ starting from a noisy configuration. Two gaussian absorbing regions around $\pm L_y/2$ are included to simulate an infinite system. This confirms that in the RI regime also the unbound system is unstable.

From the point of view of the spectra of the upper part of Figure 6.8, for sizes larger than the ones shown the amplitude of bubbles of instability continues to decrease, except for the rightmost bubble visible in the plot for $L_y = 61.8\ c_s$, corresponding to $\Re(\omega) = 0$) that remains essentially constant for growing system sizes and is responsible for the leftover instability for large L_y. Its invariant position is shown by the empty blue circles in the lower panel.

The permanence of the instability in the infinite system can be confirmed by a time-dependent simulation of the Bogoliubov problem, as we did in Subsection 5.3.2 for a doubly-quantized vortex. We performed a time evolution of the two-dimensional Bogoliubov equations (6.7) for $K = 0$ and on a background composed by many *lattice cells*, so to sample many Bloch momentum values together, and starting from a noisy configuration. Regions of absorbing potential are included near $\pm L_y/2$ to simulate open boundary conditions. The resulting time evolution of the density variations is shown in Figure 6.9. One can see that the system continues to be dynamically unstable, with the responsible mode being peaked around the positions of the vortices and radiating away in both regions. With respect to the patterns emerging in the lower panels of Figure 6.2, the absorbing boundary conditions remove the down-going waves.

This shape of the mode suggests that the propagating modes on the two sides of the interface are coupled to a mode localized around the vortices. This gives rise to a dynamical instability that does not depend on extended modes trapped in one of the two regions, but instead on modes localized around vortices coupling to outgoing modes in the two regions. This instability is hence similar in nature to the ones of multiply quantized vortices in unbound systems studied in the previous Chapter, in which modes localized in the core couple to radiating phonons in the rest of the condensate.

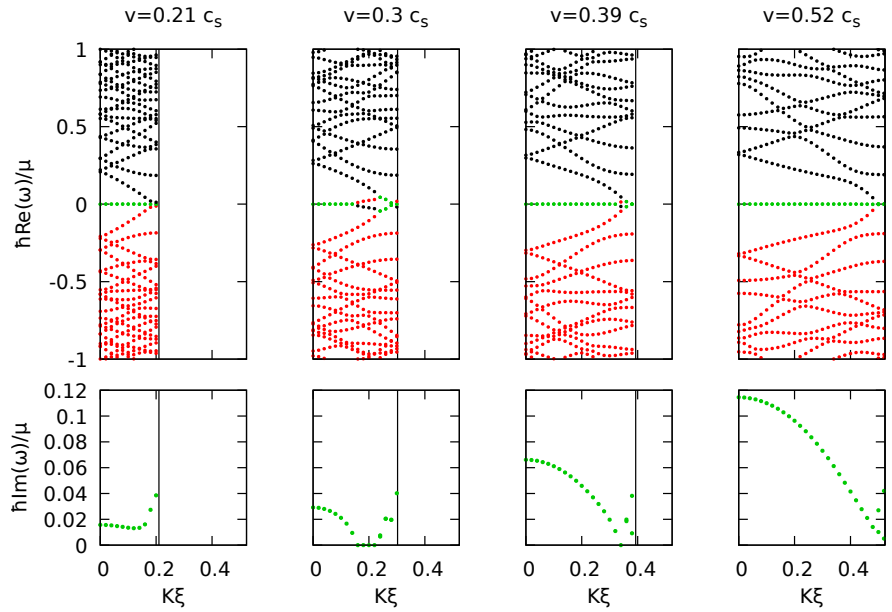

Figure 6.10: Plots analogous to the ones of Figure 6.4, for $L_y = 20\xi$, but for small velocities. One can see the transition from the KH instability of the last plot to a regime in which the instability is dominated by the modes near the edge of the Brillouin zone, that are essentially independent from the velocity.

We can summarize the conclusions of this subsection by saying that, for large enough velocity differences above $\Delta v = 2c_s$, the KH instability is suppressed by a different kind of instability involving propagating phonons in the two regions of uniform flow. This suppression can be ascribed to the mixing of the modes responsible for the KH instability with phononic modes. For small enough systems in the vertical direction the instability is dominated by a SSW-like effect, while for large enough and unbound systems this instability is substituted by continuous (and growing) emission of outgoing phonons.

6.3.3 Very small velocities regime

From Figure 6.5 we identified a third regime occurring for small velocities $v \lesssim 0.4\ c_s$. This regime is more difficult than the other to study since the low velocities are associated to a large *elementary cell* of the discrete shear layer, making diagonalizations computationally slow. Moreover the small instability rates require long times for a real-time detection of the instabilities.

In Figure 6.10 one can see the transition from a KH instability regime (rightmost plot) to a regime in which the instabilities are dominated by momenta exactly at the edge of the edge of the Brillouin zone $K = \frac{M}{\hbar}v$. Unstable modes for this value of K are present for all values of v, and for all the system sizes, as can be also seen in Figures 6.4 and 6.8, but are usually subleading with respect to the other instability mechanisms.

However for small velocities the maximum of the KH unstable branch falls below this velocity-independent instability.

These Bloch momenta correspond exactly to the length separating the vortices, i.e. to the microscopic structure of the shear layer. Moreover the velocity-independence implies that the instability does not depend on the spacing between the vortices. These two facts indicate that the unstable mode is associated to the motion of single vortices, instead of to a collective motion of the whole array as in the KH case.

The fact that the instability rate decreases for larger systems along y suggests an interpretation: due to the finite size the background density of the condensate is non-uniform and drops to zero towards the hard walls at $\pm L_y/2$, so that the single vortices will have energetic instabilities associated to their motion to a lower-density region. Due to the specific density profile this energetic instability may become dynamical, with a mechanism similar to the one presented in Section 5.5. One hence expects that this instability will vanish for large L_y, leaving only the KH one.

A full characterization of this regime, for example of its size dependence, to get further proof of its physical origin is left for a completion of this work.

6.4 Summary: interface instabilities and superradiant effects

In this Chapter we saw how a configuration of parallel flows similar to our planar ergosurfaces but with an irrotational velocity field is subject to the generation of an array of quantized vortices. This is a *quantized* analogue of shear layers in hydrodynamics, and also shows an instability analogous to the Kelvin–Helmholtz instability, in which the vortices of the shear layer move from the interface and begin to co-rotate.

Quite surprisingly, when the relative velocity between the two parallel flows is larger than twice the speed of sound, this instability is replaced by a slower instability involving excitations that spread on the whole system, and are not localized around the interface excitations. The threshold and the features of this new instability indicate that it is of the kind occurring in the SSW effect, that we studied for a planar ergosurface with no interface instabilities in Chapter 4. We called this new instability regime *radiative instability*. However, differently from superradiant instabilities that disappear when unbound regions on the two sides of the interface are considered, the radiative instability was here shown to remain also in an infinite system. In this case a continuous emission of phonons from the vortex array is observed, and the instability can be interpreted as emerging from the interplay between modes living in the quantized shear layer and propagating *superradiant* modes.

The physics presented in this Chapter displays a novel connection between concepts coming from classical hydrodynamics and concepts coming from superradiant effects, and is a new example of a surprising effect in the physics of BECs predicted through the gravitational analogy.

Conclusions and future perspectives

In this Thesis we focused of the phenomenon of superradiance with two perspectives. On the one hand we exploited the remarkable tools that have been developed to manipulate Bose–Einstein condensates to consider (possibly realizable) *toy model spacetimes* that helped us to get a simple picture of superradiance. On the other hand we used the ideas emerged from the study of superradiance to reconsider from a different point of view problems concerning fundamental aspects of the physics of Bose–Einstein condensates. The generality of superradiant phenomena manifested in a rich network of physical analogies, ranging from quantum fields on curved spacetimes, to classical and quantum hydrodynamics, to charged relativistic fields, to electromagnetism. These connections are based on the fact that the phenomena addressed here essentially rely on the interplay between modes of positive and negative energies of classical and quantum fields in open or closed geometries, with the various realizations differing in the physical origin of these modes.

The first part of this work was aimed at obtaining lessons *for* superradiance from an analogue gravity perspective. In Chapters 3 and 4 we proposed a new type of analogue model, based on a BEC in which a local tuning of the velocity is obtained with a synthetic vector potential field or with a periodic lattice potential. This makes it possible to go beyond the irrotationality condition for the velocity field on which the gravitational analogy is based and hence widens the spectrum of the spacetime geometries that can be studied. This brought us to consider a *planar ergosurface*, a minimal setup displaying superradiant scattering in a planar geometry, more intuitive and tunable than the traditional vortex geometry. This has allowed us to disentangle the different effects at play in superradiant phenomena and provide new intuitive insight on some delicate issues.

In this setup boundary conditions for the fluctuation field can be easily changed by putting the condensate in a trap. This allowed us to study dynamical instabilities associated to self amplification of superradiant field modes. In particular the black hole bomb and ergoregion instabilities occurring in black hole spacetimes simply occur by imposing reflecting boundary conditions on either side of the planar ergosurface.

The picture of superradiant effects that emerges is based on a spatially localized mode mixing process and implies that the presence of dissipation is not a necessary ingredient for amplified scattering to occur: a wavepacket impinging on the ergosurface will in fact undergo amplification regardless of the presence of additional reflecting or absorbing elements in the neighborhood of the ergosurface and of the global dynamical

stability of the configuration. Nevertheless, dissipation is a fundamental ingredient to avoid all those dynamical instabilities that emerge at later times when the amplified wave is fed back to the amplifying element.

In general-relativistic black hole spacetimes this stabilization is provided by an horizon. The role of such an element was here studied by adding a flow perpendicular to the ergosurface and a third region in which this flow is supersonic. This adds an acoustic horizon to the setup, that hence provides a toy model black hole in which the different elements can be tuned. By studying this configuration we have found that the presence of an horizon is not in general able to remove instabilities. Depending on the specific geometry, back-scattering of waves traveling towards a black hole horizon may in fact provide a sufficient reflection to turn the superradiant scattering into a dynamical instability and therefore destabilize the ergoregion.

Throughout the study of the planar ergosurface, the effects of the superluminal behaviour of the Bogoliubov dispersion relation on superradiant phenomena were studied and we found that, with respect to the corresponding dispersionless Klein–Gordon field, it provides suppression of both amplified scattering and superradiant instabilities at high momenta. Phenomena at low momenta are however not affected by dispersive effects, so that one can investigate superradiance in a Bose–Einstein condensate with success.

Besides being effective toy models, these configurations are interesting for possible experimental investigations of superradiant effects. Differently from analogous hydrodynamic flows displaying amplification of fluctuations, the ergosurface is here free from surface instabilities and hence leaves superradiant scattering as the only relevant phenomenon. As further advantage, in this system experimental investigations could also be performed at the quantum level, in fact the quantum features of sound in Bose–Einstein condensates allows the study of spontaneous pair production effects happening at the ergosurface, an effect predicted for rotating spacetimes that has however no experimental evidence. Here we studied this phenomenon and showed that it can conveniently be detected by looking at the momentum correlations of fluctuations between the inside and outside of the ergosurface, similarly to what was recently done for the first detection of Hawking radiation [4, 5, 18].

Besides the connection with rotating spacetimes, we highlighted the exact mapping of the physics of the planar ergosurface to the physics of a one-dimensional massive charged bosonic field in an electrostatic potential. Superradiant scattering and instabilities in these setups are hence also analogue realizations of the bosonic Klein paradox and of the Schiff–Snyder–Weinberg effect. These effects were always considered as toy models and find here a platform where they can be addressed experimentally.

The second part of this Thesis dealt with the application of the concepts of superradiance to obtain a new perspective on aspects of the physics of BECs, that is to obtain lessons *from* superradiance. In Chapter 5 we considered the fundamental problem of the instabilities of quantized vortices in a BEC. The interpretation of these as superradiant instabilities allowed to get a novel perspective on the problem and to solve some misconceptions that remained despite the extensive studies on the subject in the literature. In particular we showed that the dynamical instabilities associated to the splitting of

multiply quantized vortices originate in the vortex core and are not due to the presence of a trapping potential; in other words they are ergoregion instabilities and not black hole bombs. The identification with ergoregion instabilities came with a surprising quantitative correspondence with the results obtained in the hydrodynamic regime, that does not describe well the core region of quantized vortices. The deviations from these hydrodynamic predictions were found to be analogous to dispersive effects encountered in the study of planar ergosurfaces, with a suppression of the instabilities at high angular momenta.

As a last topic we considered the instabilities of a quantized shear layer between two parallel flows in a BEC, an example in which the rich physical connections displayed in the rest of this work come into play. Differently from the planar ergosurface, here the physics is dominated by surface instabilities. We in fact found, when the relative velocity of the flows is increased, a transition from a *hydrodynamic* behaviour analogous to the Kelvin–Helmholtz instability to a slower *superradiant* Schiff–Snyder–Weinberg-like instability. However, differently from superradiant instabilities, in this second regime the dynamical instability is also present when open boundary conditions are imposed on the two sides of the interface; in this case the unstable mode is composed by a part localized in the quantized shear layer and by a part propagating away from the interface in the two uniform flows.

The different realizations of superradiant phenomena explored in this thesis lay the basis for future works on superradiance and studies of related phenomena. First of all, specific platforms and experimental setups to measure the phenomena we analyzed here have to be considered in detail. Even though our discussion has been carried out with a special eye to atomic condensates, the general ideas developed in this context are of direct applicability also to analog models based on quantum fluids of light [23, 31, 35] for which synthetic magnetic fields are under active study [132]. Configurations providing a planar ergosurface in this different platform are currently being considered.

The *superradiant* physics of vortices may also be of direct experimental addressability, given the large experience of the experimental community working on cold gases in manipulating and probing these objects [130]. Again, another experimental platform in which these effects can be tested is provided by quantum fluids of light, that have been shown to display quantized vortices [163]. Quantized vortices may also be an interesting building block for different configurations interesting for analogue gravity. For example, instead of the scattering on a single vortex, one could consider superradiance involving a lattice of singly quantized vortices. The lattice structure adds the degrees of freedom of the relative positions of the vortices, from which the extra energy associated to amplified scattering can be drawn and whose modification due to the scattering are an example of back-reaction of the fluctuation field on the background *acoustic spacetime*.

Another extension of our present analysis we are actively considering is the case of two-component condensates, that can be obtained by using two different species or by selecting different internal states of the atoms (see for example Chapter 21 of [16]). In these mixtures collective excitations separate in *density* and *spin* modes, describing the *in* and *out* of phase oscillations of the two components [164]. The advantage offered by

this physics for our purposes is given by the fact that spin excitations can have a speed of sound much slower than the density one. In the particular case of vortices the size of the non-hydrodynamic vortex core is fixed by the density healing length, while the size of the *analogue ergosurface* for spin modes is given by the much larger spin healing length, that hence extends in a region of the vortex where the hydrodynamic approximation (and so the gravitational analogy) is accurate. One can hence think of obtaining a *hydrodynamic* quantum rotating acoustic spacetime considering a highly quantized vortex in the both the condensate components. This can be made dynamically stable in the density modes by adding a repulsive *pinning* potential in the core of the vortex, or stable also in the spin modes by adding a *drain* of the atoms in the core of the vortex, thus creating an acoustic horizon and, hence, a quantum rotating acoustic black hole. Additional freedom in the design of analogue setups is given by the possibility of coupling the two species of the condensates in a coherent way; this tool was recently exploited to investigate black hole lasing [83].

From a more theoretical point of view, the toy models involving planar ergosurfaces provide an interesting tool to ask further questions about the physics of curved spacetimes. While our present work has focused on the dynamics in a small excitations regime, well describing superradiant scattering and the first stages of dynamical instabilities, a natural next step is to extend the analysis to large-amplitude perturbations, for which nonlinear effects become important. This has been explored for analogue modes in the context of the late-time evolution of black hole lasers [165–168]. This physics is of high interest for gravitational physics as it provides an analogue of the back-reaction effect of the superradiant instability on the underlying metric, e.g. of rotating or charged black holes in anti-de Sitter spacetimes [169–171], and is related to the existence of so-called *hairy* black holes.

As a last intriguing point, the *modular* planar black hole we introduced to study the effect of horizons on superradiant instabilities provides a powerful toy model to address unexplored aspects of the physics of black holes. Extending the study on quantum pair production at the ergosurface, we can ask what are the modifications to Hawking emission from the horizon in the presence of an ergoregion. What we expect is that the presence of the ergoregion *cavity* provides additional spectral features to Hawking emission due to the *quasinormal modes* [109]. This would connect the Hawking effect, usually investigated in a *fixed* spacetime, and time-dependent dynamical behaviours of black holes, such as the ones described by quasinormal modes, aspects that are usually investigated in separate routes [172].

Bibliography

[1] C. Barcelo, S. Liberati, and M. Visser, "Analogue gravity," *Living reviews in relativity*, vol. 14, no. 1, p. 3, 2011.

[2] S. W. Hawking, "Particle creation by black holes," *Communications in mathematical physics*, vol. 43, no. 3, pp. 199–220, 1975.

[3] W. G. Unruh, "Experimental black-hole evaporation?," *Physical Review Letters*, vol. 46, no. 21, p. 1351, 1981.

[4] J. Steinhauer, "Observation of quantum Hawking radiation and its entanglement in an analogue black hole," *Nature Physics*, vol. 12, no. 10, p. 959, 2016.

[5] J. R. M. de Nova, K. Golubkov, V. I. Kolobov, and J. Steinhauer, "Observation of thermal Hawking radiation and its temperature in an analogue black hole," *Nature*, vol. 569, no. 7758, pp. 688–691, 2019.

[6] M. Visser, "Essential and inessential features of Hawking radiation," *International Journal of Modern Physics D*, vol. 12, no. 04, pp. 649–661, 2003.

[7] R. Penrose and R. Floyd, "Extraction of rotational energy from a black hole," *Nature Physical Science*, vol. 229, no. 6, p. 177, 1971.

[8] Y. B. Zel'dovich *Pis'ma Zh. Eksp. Teor. Fiz.*, vol. 14, pp. 270 [JETP Lett. **14**, 180 (1971)], 1971.

[9] Y. B. Zel'dovich *Zh. Eksp. Teor. Fiz*, vol. 62, pp. 2076 [Sov.Phys. JETP **35**, 1085 (1972)], 1972.

[10] R. Brito, V. Cardoso, and P. Pani, "Superradiance," *Lect. Notes Phys*, vol. 906, no. 1, p. 18, 2015.

[11] M. Visser, "Acoustic black holes: horizons, ergospheres and Hawking radiation," *Classical and Quantum Gravity*, vol. 15, no. 6, p. 1767, 1998.

[12] T. Torres, S. Patrick, A. Coutant, M. Richartz, E. W. Tedford, and S. Weinfurtner, "Rotational superradiant scattering in a vortex flow," *Nature Physics*, vol. 13, no. 9, p. 833, 2017.

[13] C. A. Manogue, "The Klein paradox and superradiance," *Annals of Physics*, vol. 181, no. 2, pp. 261–283, 1988.

[14] L. Schiff, H. Snyder, and J. Weinberg, "On the existence of stationary states of the mesotron field," *Physical Review*, vol. 57, no. 4, p. 315, 1940.

[15] S. A. Fulling, *Aspects of quantum field theory in curved spacetime*, vol. 17. Cambridge university press, 1989.

[16] L. Pitaevskii and S. Stringari, *Bose-Einstein condensation and superfluidity*, vol. 164. Oxford University Press, 2016.

[17] R. Balbinot, A. Fabbri, S. Fagnocchi, A. Recati, and I. Carusotto, "Nonlocal density correlations as a signature of Hawking radiation from acoustic black holes," *Physical Review A*, vol. 78, no. 2, p. 021603, 2008.

[18] I. Carusotto, S. Fagnocchi, A. Recati, R. Balbinot, and A. Fabbri, "Numerical observation of Hawking radiation from acoustic black holes in atomic Bose–Einstein condensates," *New Journal of Physics*, vol. 10, no. 10, p. 103001, 2008.

[19] O. Morsch and M. Oberthaler, "Dynamics of Bose-Einstein condensates in optical lattices," *Reviews of modern physics*, vol. 78, no. 1, p. 179, 2006.

[20] J. Dalibard, F. Gerbier, G. Juzeliūnas, and P. Öhberg, "Colloquium: Artificial gauge potentials for neutral atoms," *Reviews of Modern Physics*, vol. 83, no. 4, p. 1523, 2011.

[21] L. Giacomelli and I. Carusotto, "Understanding superradiant phenomena with synthetic vector potentials in atomic Bose-Einstein condensates," *arXiv preprint arXiv:2011.01736*, 2020.

[22] L. Giacomelli and I. Carusotto, "Ergoregion instabilities in rotating two-dimensional Bose-Einstein condensates: Perspectives on the stability of quantized vortices," *Physical Review Research*, vol. 2, no. 3, p. 033139, 2020.

[23] I. Carusotto and C. Ciuti, "Quantum fluids of light," *Rev. Mod. Phys.*, vol. 85, pp. 299–366, Feb 2013.

[24] I. Carusotto, "Superfluid light in bulk nonlinear media," *Proceedings of the Royal Society A: Mathematical, Physical and Engineering Sciences*, vol. 470, no. 2169, p. 20140320, 2014.

[25] L. J. Garay, J. Anglin, J. I. Cirac, and P. Zoller, "Sonic analog of gravitational black holes in Bose-Einstein condensates," *Physical Review Letters*, vol. 85, no. 22, p. 4643, 2000.

[26] L. J. Garay, J. Anglin, J. I. Cirac, and P. Zoller, "Sonic black holes in dilute Bose-Einstein condensates," *Physical Review A*, vol. 63, no. 2, p. 023611, 2001.

[27] C. Barcelo, S. Liberati, and M. Visser, "Analogue gravity from Bose-Einstein condensates," *Classical and Quantum Gravity*, vol. 18, no. 6, p. 1137, 2001.

[28] M. H. Anderson, J. R. Ensher, M. R. Matthews, C. E. Wieman, and E. A. Cornell, "Observation of Bose-Einstein condensation in a dilute atomic vapor," *science*, vol. 269, no. 5221, pp. 198–201, 1995.

[29] K. B. Davis, M.-O. Mewes, M. R. Andrews, N. J. van Druten, D. S. Durfee, D. Kurn, and W. Ketterle, "Bose-Einstein condensation in a gas of sodium atoms," *Physical review letters*, vol. 75, no. 22, p. 3969, 1995.

[30] M. Novello, M. Visser, and G. E. Volovik, *Artificial black holes*. World Scientific, 2002.

[31] H. S. Nguyen, D. Gerace, I. Carusotto, D. Sanvitto, E. Galopin, A. Lemaître, I. Sagnes, J. Bloch, and A. Amo, "Acoustic Black Hole in a Stationary Hydrodynamic Flow of Microcavity Polaritons," *Phys. Rev. Lett.*, vol. 114, p. 036402, Jan 2015.

[32] D. D. Solnyshkov, H. Flayac, and G. Malpuech, "Black holes and wormholes in spinor polariton condensates," *Phys. Rev. B*, vol. 84, p. 233405, Dec 2011.

[33] D. Gerace and I. Carusotto, "Analog Hawking radiation from an acoustic black hole in a flowing polariton superfluid," *Phys. Rev. B*, vol. 86, p. 144505, Oct 2012.

[34] D. Solnyshkov, C. Leblanc, S. Koniakhin, O. Bleu, and G. Malpuech, "Quantum analogue of a Kerr black hole and the Penrose effect in a Bose-Einstein condensate," *Physical Review B*, vol. 99, no. 21, p. 214511, 2019.

[35] M. Jacquet, T. Boulier, F. Claude, A. Maître, E. Cancellieri, C. Adrados, A. Amo, S. Pigeon, Q. Glorieux, A. Bramati, *et al.*, "Polariton fluids for analogue gravity physics," *Philosophical Transactions of the Royal Society A*, vol. 378, no. 2177, p. 20190225, 2020.

[36] C. J. Pethick and H. Smith, *Bose–Einstein condensation in dilute gases*. Cambridge university press, 2008.

[37] Y. Castin, "Bose–Einstein condensates in atomic gases: simple theoretical results," in *Coherent atomic matter waves*, pp. 1–136, Springer, 2001.

[38] Y. Castin and R. Dum, "Low-temperature Bose-Einstein condensates in time-dependent traps: Beyond the U (1) symmetry-breaking approach," *Physical Review A*, vol. 57, no. 4, p. 3008, 1998.

[39] L. Landau, "Theory of the superfluidity of helium ii," *Physical Review*, vol. 60, no. 4, p. 356, 1941.

[40] E. Lundh and H. M. Nilsen, "Dynamic stability of a doubly quantized vortex in a three-dimensional condensate," *Physical Review A*, vol. 74, no. 6, p. 063620, 2006.

[41] Y. Nakamura, M. Mine, M. Okumura, and Y. Yamanaka, "Condition for emergence of complex eigenvalues in the Bogoliubov–de Gennes equations," *Physical Review A*, vol. 77, no. 4, p. 043601, 2008.

[42] V. I. Arnol'd, *Mathematical methods of classical mechanics*, vol. 60. Springer Science & Business Media, 2013.

[43] V. I. Arnol'd and A. Avez, "Ergodic problems of classical mechanics," 1968.

[44] A. Coutant, F. Michel, and R. Parentani, "Dynamical instabilities and quasi-normal modes, a spectral analysis with applications to black-hole physics," *Classical and Quantum Gravity*, vol. 33, no. 12, p. 125032, 2016.

[45] A. L. Fetter, "Nonuniform states of an imperfect Bose gas," *Annals of Physics*, vol. 70, no. 1, pp. 67–101, 1972.

[46] D. Petrov, "Quantum mechanical stabilization of a collapsing Bose-Bose mixture," *Physical review letters*, vol. 115, no. 15, p. 155302, 2015.

[47] G. Kang, "Quantization of scalar field in the presence of imaginary frequency modes," *arXiv preprint hep-th/9603166*, 1996.

[48] U. Leonhardt, T. Kiss, and P. Öhberg, "Theory of elementary excitations in unstable Bose-Einstein condensates and the instability of sonic horizons," *Physical Review A*, vol. 67, no. 3, p. 033602, 2003.

[49] G. Kang, "Quantum aspects of ergoregion instability," *Physical Review D*, vol. 55, no. 12, p. 7563, 1997.

[50] S. Butera and I. Carusotto, "Mechanical backreaction effect of the dynamical Casimir emission," *Physical Review A*, vol. 99, no. 5, p. 053815, 2019.

[51] R. P. Kerr, "Gravitational field of a spinning mass as an example of algebraically special metrics," *Physical review letters*, vol. 11, no. 5, p. 237, 1963.

[52] M. Visser, "The Kerr spacetime: A brief introduction," *arXiv preprint arXiv:0706.0622*, 2007.

[53] R. M. Wald, *General relativity*. University of Chicago press, 2010.

[54] E. Poisson, *A relativist's toolkit: the mathematics of black-hole mechanics*. Cambridge university press, 2004.

[55] S. Chandrasekhar, *The mathematical theory of black holes*, vol. 69. Oxford University Press, 1998.

[56] R. Penrose, ""Golden Oldie": Gravitational collapse: the role of general relativity," *General Relativity and Gravitation*, vol. 34, no. 7, pp. 1141–1165, 2002.

[57] H. Feshbach and F. Villars, "Elementary relativistic wave mechanics of spin 0 and spin 1/2 particles," *Reviews of Modern Physics*, vol. 30, no. 1, p. 24, 1958.

[58] S. W. Hawking, "Black hole explosions?," *Nature*, vol. 248, no. 5443, pp. 30–31, 1974.

[59] R. Brout, S. Massar, R. Parentani, and P. Spindel, "A primer for black hole quantum physics," *Physics Reports*, vol. 260, no. 6, pp. 329–446, 1995.

[60] L. H. Ford, "D3: Quantum field theory in curved spacetime," in *General Relativity and Gravitation*, pp. 490–493, World Scientific, 2002.

[61] T. Jacobson, "Introduction to quantum fields in curved spacetime and the Hawking effect," in *Lectures on Quantum Gravity*, pp. 39–89, Springer, 2005.

[62] T. Jacobson, "Black-hole evaporation and ultrashort distances," *Physical Review D*, vol. 44, no. 6, p. 1731, 1991.

[63] R. Brout, S. Massar, R. Parentani, and P. Spindel, "Hawking radiation without trans-Planckian frequencies," *Physical Review D*, vol. 52, no. 8, p. 4559, 1995.

[64] S. Corley and T. Jacobson, "Hawking spectrum and high frequency dispersion," *Physical Review D*, vol. 54, no. 2, p. 1568, 1996.

[65] A. Coutant, R. Parentani, and S. Finazzi, "Black hole radiation with short distance dispersion, an analytical S-matrix approach," *Physical Review D*, vol. 85, no. 2, p. 024021, 2012.

[66] R. Balbinot, I. Carusotto, A. Fabbri, C. Mayoral, and A. Recati, "Understanding hawking radiation from simple models of atomic Bose-Einstein condensates," in *Analogue Gravity Phenomenology*, pp. 181–219, Springer, 2013.

[67] S. J. Robertson, "The theory of Hawking radiation in laboratory analogues," *Journal of Physics B: Atomic, Molecular and Optical Physics*, vol. 45, no. 16, p. 163001, 2012.

[68] U. Leonhardt, T. Kiss, and P. Öhberg, "Bogoliubov theory of the Hawking effect in Bose–Einstein condensates," *Journal of Optics B: Quantum and Semiclassical Optics*, vol. 5, no. 2, p. S42, 2003.

[69] A. Recati, N. Pavloff, and I. Carusotto, "Bogoliubov theory of acoustic Hawking radiation in Bose-Einstein condensates," *Physical Review A*, vol. 80, no. 4, p. 043603, 2009.

[70] J. Macher and R. Parentani, "Black-hole radiation in Bose-Einstein condensates," *Physical Review A*, vol. 80, no. 4, p. 043601, 2009.

[71] I. Carusotto, R. Balbinot, A. Fabbri, and A. Recati, "Density correlations and analog dynamical Casimir emission of Bogoliubov phonons in modulated atomic Bose-Einstein condensates," *The European Physical Journal D*, vol. 56, no. 3, pp. 391–404, 2010.

[72] P.-É. Larré, A. Recati, I. Carusotto, and N. Pavloff, "Quantum fluctuations around black hole horizons in Bose-Einstein condensates," *Physical Review A*, vol. 85, no. 1, p. 013621, 2012.

[73] D. Boiron, A. Fabbri, P.-É. Larré, N. Pavloff, C. I. Westbrook, and P. Ziń, "Quantum signature of analog Hawking radiation in momentum space," *Physical review letters*, vol. 115, no. 2, p. 025301, 2015.

[74] G. Rousseaux, C. Mathis, P. Maïssa, T. G. Philbin, and U. Leonhardt, "Observation of negative-frequency waves in a water tank: a classical analogue to the Hawking effect?," *New Journal of Physics*, vol. 10, no. 5, p. 053015, 2008.

[75] W. G. Unruh, "Sonic analogue of black holes and the effects of high frequencies on black hole evaporation," *Physical Review D*, vol. 51, no. 6, p. 2827, 1995.

[76] O. Lahav, A. Itah, A. Blumkin, C. Gordon, S. Rinott, A. Zayats, and J. Steinhauer, "Realization of a sonic black hole analog in a Bose-Einstein condensate," *Physical review letters*, vol. 105, no. 24, p. 240401, 2010.

[77] S. Corley and T. Jacobson, "Black hole lasers," *Physical Review D*, vol. 59, no. 12, p. 124011, 1999.

[78] U. Leonhardt and T. G. Philbin, "Black hole lasers revisited," in *Quantum Analogues: From Phase Transitions to Black Holes and Cosmology*, pp. 229–245, Springer, 2007.

[79] A. Coutant and R. Parentani, "Black hole lasers, a mode analysis," *Physical Review D*, vol. 81, no. 8, p. 084042, 2010.

[80] S. Finazzi and R. Parentani, "Black hole lasers in Bose–Einstein condensates," *New Journal of Physics*, vol. 12, no. 9, p. 095015, 2010.

[81] F. Michel and R. Parentani, "Saturation of black hole lasers in Bose-Einstein condensates," *Physical Review D*, vol. 88, no. 12, p. 125012, 2013.

[82] J. De Nova, S. Finazzi, and I. Carusotto, "Time-dependent study of a black-hole laser in a flowing atomic condensate," *Physical Review A*, vol. 94, no. 4, p. 043616, 2016.

[83] S. Butera, P. Öhberg, and I. Carusotto, "Black-hole lasing in coherently coupled two-component atomic condensates," *Physical Review A*, vol. 96, no. 1, p. 013611, 2017.

[84] J. Steinhauer, "Observation of self-amplifying Hawking radiation in an analogue black-hole laser," *Nature Physics*, vol. 10, no. 11, pp. 864–869, 2014.

[85] M. Tettamanti, S. Cacciatori, A. Parola, and I. Carusotto, "Numerical study of a recent black-hole lasing experiment," *EPL (Europhysics Letters)*, vol. 114, no. 6, p. 60011, 2016.

[86] M. Tettamanti, I. Carusotto, and A. Parola, "On the role of interactions in transsonically flowing atomic condensates," *arXiv preprint arXiv:2010.07613*, 2020.

[87] V. I. Kolobov, K. Golubkov, J. R. M. de Nova, and J. Steinhauer, "Spontaneous Hawking radiation and beyond: Observing the time evolution of an analogue black hole," *arXiv preprint arXiv:1910.09363*, 2019.

[88] S. Finazzi, F. Piazza, M. Abad, A. Smerzi, and A. Recati, "Instability of the superfluid flow as black-hole lasing effect," *Physical review letters*, vol. 114, no. 24, p. 245301, 2015.

[89] J. D. Bekenstein and M. Schiffer, "The many faces of superradiance," *Physical Review D*, vol. 58, no. 6, p. 064014, 1998.

[90] M. Richartz, S. Weinfurtner, A. Penner, and W. Unruh, "Generalized superradiant scattering," *Physical Review D*, vol. 80, no. 12, p. 124016, 2009.

[91] F. Hund, "Materieerzeugung im anschaulichen und im gequantelten Wellenbild der Materie," *Zeitschrift für Physik*, vol. 117, no. 1-2, pp. 1–17, 1941.

[92] H. S. Ribner, "Reflection, transmission, and amplification of sound by a moving medium," *The Journal of the Acoustical Society of America*, vol. 29, no. 4, pp. 435–441, 1957.

[93] J. R. Booker and F. P. Bretherton, "The critical layer for internal gravity waves in a shear flow," *Journal of Fluid Mechanics*, vol. 27, no. 3, pp. 513–539, 1967.

[94] J. F. McKenzie, "Reflection and amplification of acoustic-gravity waves at a density and velocity discontinuity," *Journal of Geophysical Research*, vol. 77, no. 16, pp. 2915–2926, 1972.

[95] L. D. Landau and E. M. Lifshitz, "Fluid mechanics," *Fluid Mechanics. Second Edition. 1987. Pergamon, Oxford*, 1987.

[96] M. C. Braidotti, A. Vinante, G. Gasbarri, D. Faccio, and H. Ulbricht, "Zel'dovich amplification in a superconducting circuit," *arXiv preprint arXiv:2005.03705*, 2020.

[97] A. Prain, C. Maitland, D. Faccio, and F. Marino, "Superradiant scattering in fluids of light," *Physical Review D*, vol. 100, no. 2, p. 024037, 2019.

[98] V. Ginzburg and I. Frank, "Radiation of a uniformly moving electron due to its transition from one medium into another," *Journal of Physics (USSR)*, vol. 9, pp. 353–362, 1945.

[99] V. Ginzburg, "Radiation by uniformly moving sources," in *The lesson of quantum theory*, 1986.

[100] J. Marino, A. Recati, and I. Carusotto, "Casimir forces and quantum friction from Ginzburg radiation in atomic Bose-Einstein condensates," *Physical Review Letters*, vol. 118, no. 4, p. 045301, 2017.

[101] I. Carusotto, S. Hu, L. Collins, and A. Smerzi, "Bogoliubov-Cherenkov radiation in a Bose-Einstein condensate flowing against an obstacle," *Physical review letters*, vol. 97, no. 26, p. 260403, 2006.

[102] A. Starobinski, "Amplification of waves during reflection from a rotating black hole," *Zh. Eksp. Teor. Fiz*, vol. 64, p. 48, 1973.

[103] W. G. Unruh, "Second quantization in the Kerr metric," *Physical Review D*, vol. 10, no. 10, p. 3194, 1974.

[104] A. Starobinsky and S. Churilov, "Amplification of electromagnetic and gravitational waves scattered by a rotating black hole," *Zh. Eksp. Teor. Fiz*, vol. 65, no. 3, pp. 3–11, 1973.

[105] S. A. Teukolsky, "Rotating black holes: Separable wave equations for gravitational and electromagnetic perturbations," *Physical Review Letters*, vol. 29, no. 16, p. 1114, 1972.

[106] S. A. Teukolsky, "Perturbations of a rotating black hole. I. Fundamental equations for gravitational, electromagnetic, and neutrino-field perturbations," *The Astrophysical Journal*, vol. 185, pp. 635–648, 1973.

[107] S. Basak and P. Majumdar, "Superresonance from a rotating acoustic black hole," *Classical and Quantum Gravity*, vol. 20, no. 18, p. 3907, 2003.

[108] S. Basak and P. Majumdar, "Reflection coefficient for superresonant scattering," *Classical and Quantum Gravity*, vol. 20, no. 13, p. 2929, 2003.

[109] E. Berti, V. Cardoso, and J. P. Lemos, "Quasinormal modes and classical wave propagation in analogue black holes," *Physical Review D*, vol. 70, no. 12, p. 124006, 2004.

[110] T. R. Slatyer and C. Savage, "Superradiant scattering from a hydrodynamic vortex," *Classical and Quantum Gravity*, vol. 22, no. 19, p. 3833, 2005.

[111] F. Federici, C. Cherubini, S. Succi, and M. Tosi, "Superradiance from hydrodynamic vortices: A numerical study," *Physical Review A*, vol. 73, no. 3, p. 033604, 2006.

[112] M. Richartz, A. Prain, S. Liberati, and S. Weinfurtner, "Rotating black holes in a draining bathtub: superradiant scattering of gravity waves," *Physical Review D*, vol. 91, no. 12, p. 124018, 2015.

[113] V. Cardoso, A. Coutant, M. Richartz, and S. Weinfurtner, "Detecting rotational superradiance in fluid laboratories," *Physical review letters*, vol. 117, no. 27, p. 271101, 2016.

[114] E. Berti, V. Cardoso, and A. O. Starinets, "Quasinormal modes of black holes and black branes," *Classical and Quantum Gravity*, vol. 26, no. 16, p. 163001, 2009.

[115] J. M. Bardeen, W. H. Press, and S. A. Teukolsky, "Rotating black holes: locally nonrotating frames, energy extraction, and scalar synchrotron radiation," *The Astrophysical Journal*, vol. 178, pp. 347–370, 1972.

[116] S. A. Teukolsky and W. Press, "Perturbations of a rotating black hole. III-Interaction of the hole with gravitational and electromagnetic radiation," *The Astrophysical Journal*, vol. 193, pp. 443–461, 1974.

[117] W. H. Press and S. A. Teukolsky, "Floating orbits, superradiant scattering and the black-hole bomb," *Nature*, vol. 238, no. 5361, pp. 211–212, 1972.

[118] S. W. Hawking and H. Reall, "Charged and rotating AdS black holes and their CFT duals," *Physical Review D*, vol. 61, no. 2, p. 024014, 1999.

[119] V. Cardoso, O. J. Dias, J. P. Lemos, and S. Yoshida, "Black-hole bomb and superradiant instabilities," *Physical Review D*, vol. 70, no. 4, p. 044039, 2004.

[120] T. Damour, N. Deruelle, and R. Ruffini, "On quantum resonances in stationary geometries," *Lettere al Nuovo Cimento (1971-1985)*, vol. 15, no. 8, pp. 257–262, 1976.

[121] J. L. Friedman, "Ergosphere instability," *Communications in Mathematical Physics*, vol. 63, no. 3, pp. 243–255, 1978.

[122] N. Comins and B. F. Schutz, "On the ergoregion instability," *Proceedings of the Royal Society of London. A. Mathematical and Physical Sciences*, vol. 364, no. 1717, pp. 211–226, 1978.

[123] M. Richartz and A. Saa, "Superradiance without event horizons in general relativity," *Physical Review D*, vol. 88, no. 4, p. 044008, 2013.

[124] L. Di Menza, J.-P. Nicolas, and M. Pellen, "A new type of charged black hole bomb," *General Relativity and Gravitation*, vol. 52, no. 1, p. 8, 2020.

[125] L. A. Oliveira, V. Cardoso, and L. C. Crispino, "Ergoregion instability: The hydrodynamic vortex," *Physical Review D*, vol. 89, no. 12, p. 124008, 2014.

[126] E. G. Broadbent and D. W. Moore, "Acoustic destablilization of vortices," *Philosophical Transactions of the Royal Society of London. Series A, Mathematical and Physical Sciences*, vol. 290, no. 1372, pp. 353–371, 1979.

[127] S. Fulling, "Varieties of instability of a boson field in an external potential," *Physical Review D*, vol. 14, no. 8, p. 1939, 1976.

[128] E. Ching, P. Leung, A. M. van den Brink, W. Suen, S. Tong, and K. Young, "Quasinormal-mode expansion for waves in open systems," *Reviews of Modern Physics*, vol. 70, no. 4, p. 1545, 1998.

[129] J. Dalibard, "Introduction to the physics of artificial gauge fields," *Quantum Matter at Ultralow Temperatures*, 2015.

[130] A. L. Fetter, "Rotating trapped Bose-Einstein condensates," *Reviews of Modern Physics*, vol. 81, no. 2, p. 647, 2009.

[131] N. R. Cooper, J. Dalibard, and I. B. Spielman, "Topological bands for ultracold atoms," *Rev. Mod. Phys.*, vol. 91, p. 015005, Mar 2019.

[132] T. Ozawa, H. M. Price, A. Amo, N. Goldman, M. Hafezi, L. Lu, M. C. Rechtsman, D. Schuster, J. Simon, O. Zilberberg, and I. Carusotto, "Topological photonics," *Rev. Mod. Phys.*, vol. 91, p. 015006, Mar 2019.

[133] I. B. Spielman, "Raman processes and effective gauge potentials," *Physical Review A*, vol. 79, no. 6, p. 063613, 2009.

[134] Y.-J. Lin, R. L. Compton, A. R. Perry, W. D. Phillips, J. V. Porto, and I. B. Spielman, "Bose-Einstein condensate in a uniform light-induced vector potential," *Physical Review Letters*, vol. 102, no. 13, p. 130401, 2009.

[135] Y.-J. Lin, R. L. Compton, K. Jimenez-Garcia, J. V. Porto, and I. B. Spielman, "Synthetic magnetic fields for ultracold neutral atoms," *Nature*, vol. 462, no. 7273, p. 628, 2009.

[136] L. J. Leblanc and I. B. Spielman, *Bose-Einstein Condensates in Artificial Gauge Fields*, p. 299–321. Cambridge University Press, 2017.

[137] S. Butera, N. Westerberg, D. Faccio, and P. Öhberg, "Curved spacetime from interacting gauge theories," *Classical and Quantum Gravity*, vol. 36, no. 3, p. 034002, 2019.

[138] P. S. J. Russell, T. A. Birks, and F. D. Lloyd-Lucas, *Photonic Bloch Waves and Photonic Band Gaps*, pp. 585–633. Boston, MA: Springer US, 1995.

[139] V. Veselago, "Electrodynamics of substances with simultaneously negative electrical and magnetic permeabilities," *Soviet Physics Uspekhi*, vol. 10, no. 4, pp. 504–509, 1968.

[140] M. Richartz, A. Prain, S. Weinfurtner, and S. Liberati, "Super-radiant scattering of dispersive fields," *Classical and Quantum Gravity*, vol. 30, no. 8, p. 085009, 2013.

[141] S. Butera, D. Clément, and I. Carusotto, "Position-and momentum-space two-body correlations in a weakly interacting trapped condensate," *arXiv preprint arXiv:2008.13039*, 2020.

[142] M. Kraemer, C. Menotti, L. Pitaevskii, and S. Stringari, "Bose-Einstein condensates in 1D optical lattices," *The European Physical Journal D-Atomic, Molecular, Optical and Plasma Physics*, vol. 27, no. 3, pp. 247–261, 2003.

[143] C. Mayoral, A. Recati, A. Fabbri, R. Parentani, R. Balbinot, and I. Carusotto, "Acoustic white holes in flowing atomic Bose–Einstein condensates," *New Journal of Physics*, vol. 13, no. 2, p. 025007, 2011.

[144] S. Finazzi and I. Carusotto, "Entangled phonons in atomic Bose-Einstein condensates," *Physical Review A*, vol. 90, no. 3, p. 033607, 2014.

[145] L. Pitaevskii, "Vortex lines in an imperfect Bose gas," *Sov. Phys. JETP*, vol. 13, no. 2, pp. 451–454, 1961.

[146] R. Dodd, K. Burnett, M. Edwards, and C. W. Clark, "Excitation spectroscopy of vortex states in dilute Bose-Einstein condensed gases," *Physical Review A*, vol. 56, no. 1, p. 587, 1997.

[147] D. Rokhsar, "Vortex stability and persistent currents in trapped Bose gases," *Physical review letters*, vol. 79, no. 12, p. 2164, 1997.

[148] H. Pu, C. Law, J. Eberly, and N. Bigelow, "Coherent disintegration and stability of vortices in trapped Bose condensates," *Physical Review A*, vol. 59, no. 2, p. 1533, 1999.

[149] A. A. Svidzinsky and A. L. Fetter, "Stability of a vortex in a trapped Bose-Einstein condensate," *Physical review letters*, vol. 84, no. 26, p. 5919, 2000.

[150] M. Möttönen, T. Mizushima, T. Isoshima, M. Salomaa, and K. Machida, "Splitting of a doubly quantized vortex through intertwining in Bose-Einstein condensates," *Physical Review A*, vol. 68, no. 2, p. 023611, 2003.

[151] Y. Shin, M. Saba, M. Vengalattore, T. Pasquini, C. Sanner, A. Leanhardt, M. Prentiss, D. Pritchard, and W. Ketterle, "Dynamical instability of a doubly quantized vortex in a Bose–Einstein condensate," *Physical Review Letters*, vol. 93, no. 16, p. 160406, 2004.

[152] H. Takeuchi, M. Kobayashi, and K. Kasamatsu, "Is a doubly quantized vortex dynamically unstable in uniform superfluids?," *Journal of the Physical Society of Japan*, vol. 87, no. 2, p. 023601, 2018.

[153] I. Aranson and V. Steinberg, "Stability of multicharged vortices in a model of superflow," *Physical Review B*, vol. 53, no. 1, p. 75, 1996.

[154] P. Fedichev and G. Shlyapnikov, "Dissipative dynamics of a vortex state in a trapped Bose-condensed gas," *Physical Review A*, vol. 60, no. 3, p. R1779, 1999.

[155] D. V. Skryabin, "Instabilities of vortices in a binary mixture of trapped Bose-Einstein condensates: Role of collective excitations with positive and negative energies," *Physical Review A*, vol. 63, no. 1, p. 013602, 2000.

[156] F. Charru, *Hydrodynamic instabilities*, vol. 37. Cambridge University Press, 2011.

[157] G. E. Volovik, "On the Kelvin-Helmholtz instability in superfluids," *Journal of Experimental and Theoretical Physics Letters*, vol. 75, no. 8, pp. 418–422, 2002.

[158] R. Blaauwgeers, V. Eltsov, G. Eska, A. Finne, R. P. Haley, M. Krusius, J. Ruohio, L. Skrbek, and G. Volovik, "Shear flow and Kelvin-Helmholtz instability in superfluids," *Physical review letters*, vol. 89, no. 15, p. 155301, 2002.

[159] H. Takeuchi, N. Suzuki, K. Kasamatsu, H. Saito, and M. Tsubota, "Quantum Kelvin-Helmholtz instability in phase-separated two-component Bose-Einstein condensates," *Physical Review B*, vol. 81, no. 9, p. 094517, 2010.

[160] A. Baggaley and N. Parker, "Kelvin-Helmholtz instability in a single-component atomic superfluid," *Physical Review A*, vol. 97, no. 5, p. 053608, 2018.

[161] S. Thorpe, "Experiments on the instability of stratified shear flows: miscible fluids," *Journal of Fluid Mechanics*, vol. 46, no. 2, pp. 299–319, 1971.

[162] A. Michalke, "On the inviscid instability of the hyperbolictangent velocity profile," *Journal of Fluid Mechanics*, vol. 19, no. 4, pp. 543–556, 1964.

[163] K. G. Lagoudakis, M. Wouters, M. Richard, A. Baas, I. Carusotto, R. André, L. S. Dang, and B. Deveaud-Plédran, "Quantized vortices in an exciton–polariton condensate," *Nature physics*, vol. 4, no. 9, pp. 706–710, 2008.

[164] M. Abad and A. Recati, "A study of coherently coupled two-component Bose-Einstein condensates," *The European Physical Journal D*, vol. 67, no. 7, p. 148, 2013.

[165] F. Michel and R. Parentani, "Saturation of black hole lasers in Bose-Einstein condensates," *Phys. Rev. D*, vol. 88, p. 125012, Dec 2013.

[166] F. Michel and R. Parentani, "Nonlinear effects in time-dependent transonic flows: An analysis of analog black hole stability," *Phys. Rev. A*, vol. 91, p. 053603, May 2015.

[167] J. R. M. de Nova, S. Finazzi, and I. Carusotto, "Time-dependent study of a black-hole laser in a flowing atomic condensate," *Phys. Rev. A*, vol. 94, p. 043616, Oct 2016.

[168] J. R. M. de Nova, P. F. Palacios, I. Carusotto, and F. Sols, "Long time universality of black-hole lasers," 2020.

[169] P. Bosch, S. R. Green, and L. Lehner, "Nonlinear Evolution and Final Fate of Charged Anti–de Sitter Black Hole Superradiant Instability," *Phys. Rev. Lett.*, vol. 116, p. 141102, Apr 2016.

[170] N. Sanchis-Gual, J. C. Degollado, P. J. Montero, J. A. Font, and C. Herdeiro, "Explosion and Final State of an Unstable Reissner-Nordström Black Hole," *Phys. Rev. Lett.*, vol. 116, p. 141101, Apr 2016.

[171] W. E. East and F. Pretorius, "Superradiant Instability and Backreaction of Massive Vector Fields around Kerr Black Holes," *Phys. Rev. Lett.*, vol. 119, p. 041101, Jul 2017.

[172] J. W. York Jr, "Dynamical origin of black-hole radiance," *Physical Review D*, vol. 28, no. 12, p. 2929, 1983.